Development of a Six-Field Two-Phase Model for use in Reactor System Codes

A Dissertation

Presented in Partial Fulfilment of the Requirements for the

Degree of Doctor of Philosophy

with a

Major in Mechanical Engineering

in the

College of Graduate Studies

University of Idaho

by

Glenn A. Roth

Major Professor: Fatih Aydogan, Ph.D.

Committee Members: Sule Ergun, Ph.D.; Fred Gunnerson, Ph.D.; George Mesina, Ph.D.

Department Administrator: Steven Beyerlein, Ph. D.

August 2017

Authorization to Submit Dissertation

This dissertation of Glenn Anderson Roth, submitted for the degree of Doctor of Philosophy with a major in Mechanical Engineering and titled "Development of a Six-Field Two-Phase Model for use in Reactor System Codes," has been reviewed in final form. Permission, as indicated by the signatures and dates given below, is now granted to submit final copies to the College of Graduate Studies for approval.

Major Professor: _____Date_____
Fatih Aydogan, Ph.D.

Committee Members: _____Date_____
Sule Ergun, Ph.D.

_____Date_____
Fred Gunnerson, Ph.D.

_____Date_____
George Mesina, Ph.D.

Department Administrator: _____Date_____
Steven Beyerlein, Ph.D.

Abstract

The design and analysis of the thermal/hydraulic systems of nuclear power plants necessitates system codes that can be used in the analysis of steady-state and transient conditions. Due to the dispersed development of system codes over many laboratories and universities, there are several system codes available for use. Many of the available codes have multiple similar versions developed for specific user needs.

System codes are used to analyze nuclear reactor systems during steady state and transient operations. These codes can predict pressure drop, void fraction distributions and temperature distributions for various coolants, heated flow geometries, and heat configurations. They also include models for various two-phase flow regimes, but extreme flow conditions that involve significant phase change can tax the current code capabilities.

Current system codes have mass, momentum, and energy conservation equations for two fields (liquid and vapor), resulting in a model with six conservation equations. Recent developments in limited applications of a few of these codes have added a separate droplet field from the continuous liquid. This is part of a trend toward the inclusion of more fields (and requisite conservation equations) in system codes.

Two-phase flows are divided into flow regimes based on their appearance and the flow structure. The regimes are used to select appropriate closure relationships to model heat transfer, interfacial drag, and other flow conditions.

The representation of two-phase flow phenomena is improved by increasing the number of fields. Conservation equations based on six fields (liquid, vapor, small bubble, large bubble, small droplet and large droplet) have been derived as part of this dissertation.

The conservation equations for mass, momentum, and energy increase the amount of information that is needed to model the flow field. This dissertation shows how several new variables are added to the system of conservation equations. These variables include source terms for physical interactions between the droplets and the vapor, droplet entrainment

and break-up. In addition, heat transfer across the many interfaces must be described or the governing equations cannot be solved. Closure models that can be used to solve the expanded system of conservation equations have been identified in this work.

The solution of a system of governing equations for six fields is complex. There are 18 equations that must be solved - six field equations each for the mass, momentum, and energy conservation. This dissertation describes how the primary variables are selected, and how the 18 equations are solved in a two-step process - first the momentum equations, then the remaining 12 mass and energy conservation equations.

This dissertation is a compilation of papers that have been published or submitted for publication by the author.

Acknowledgements

I would like to thank my advisor, Dr. Fatih Aydogan for his guidance and support throughout what became a very long process toward completion of this study. I also owe a special thanks to Dr. George Mesina, who not only served on my committee, but provided a great deal of assistance in understanding the RELAP5 code and the approach to the solution of a complex system of equations.

In addition, I would also like to thank Dr. Fred Gunnerson and Dr. Sule Ergun for serving on my committee and providing their support through valuable comments and suggestions.

Dedication

I am certain that I will never fully understand the sacrifices made by my wife and children during my studies. It is with humility and gratitude that I dedicate this work to them for their significant patience during all the times that Daddy was studying.

Table of Contents

List of Tables

List of Figures

Nomenclature

Greek

α Volume fraction

α_{BS} Void fraction of transition between inverted annular and the inverted annular, inverted slug transition region

$\alpha_{diff,f}$ Thermal diffusivity for liquid two-phase flow boiling

α_e Volume fraction of entrained droplets

α_f Volume fraction occupied by continuous liquid

α_g Vapor/Gas volume fraction

α_i Area fraction face i - area of phase/total area

α_k Void fraction of phase k

α_{LB} Volume fraction of large group bubbles

α_{LD} Volume fraction of large droplets

α_{lrgdrp} Volume fraction for large droplet field

α_l Continuous liquid fraction

α_{SA} Void fraction marking change from inverted slug to mist flow

$\alpha_{SBu,max}$ Maximum volume fraction for small group bubbles

α_{SBu} volume fraction of small bubbles

α_{Tb} Taylor bubble void fraction in slug flow

α_{totdrp} Total volume fraction for both droplet fields

α_t Total void fraction

α_v Volume fraction of vapor field

β Added mass coefficient

χ Turbulent kinetic energy dissipation rate per unit mixture mass

χ Turbulent kinetic energy dissipation rate per unit mixture mass ($^{m^2}/_{s^3}$)

χ Wetted perimeter

ΔT_{sf} Subcooling of liquid phase $T^{sat} - T_f$

ΔT_{sg} "Subcooling" of vapor phase $T^{sat} - T_g$

Δ Volume fraction oversize

δ Thickness of interface region between phases/fields

δ_{1or2} Thickness of interface region on one side of the interface

ΔD Diameter bin width (m)

ϵ =1 for $\Gamma_w \geq 0$, =0 for $\Gamma_w \leq 0$

ϵ Fraction of droplets broken up by spacer that are "small"

ϵ Wall vapor generation/condensation flag. ϵ=1 for boiling in the boundary layer, ϵ=-1 for condensation.

ϵ_p "Pumping" term - $\frac{\rho_f\left[h_f^s - \min\left(h_f, h_f^s\right)\right]}{\rho_g h_{fg}}$

η Fraction of total vapor generation coming from entrained liquid field

η Fraction of vapor generation from large and small droplet fields

η_e Grid efficiency factor - portion of drop shattered into microdroplets

η_e Grid efficiency factor

η_{LD} Fraction of vapor generation from large droplets

Γ Interfacial mass transfer rate

Γ Interfacial phasic mass transfer

Γ Mass generation rate per unit volume

Γ Vapor generation rate per unit volume ($^{kg}/_{m^3 s}$)

Γ Volumetric mass exchange rate ($^{kg}/_{m^3 \cdot s}$)

Γ''' Average rate of vapor generation per unit volume

Γ'''_e Average rate of vapor generation per unit volume from entrained liquid

Γ'''_l Average rate of vapor generation per unit volume from continuous liquid

Γ^+ Maximum of Γ and 0

Γ^- Minimum of Γ and 0

Γ_k Mass generation for phase k

Γ_g Average rate of vapor generation per unit volume from all liquid fields

Γ_{ig} Vapor generation rate due to energy exchange in the bulk fluid

Γ_{ik} Mass transfer at phase interface

Γ_k Generation rate of phase k

Γ_w Inter-phase mass transfer at wall boundary layer

Γ_w Vapor generation rate due to energy exchange at the wall

Λ Interfacial thermal energy transfer term

λ Wavelength (m)

λ Wavelength

λ_{crit} Characteristic wavelength for droplet formation (m)

$\langle\alpha\rangle$ Void fraction averaged over the cross-sectional area

$\mathbb{T}$ Stress tensor

$\mathfrak{T}$ Viscous stress tensor

$\mathfrak{T}_k^T$ Turbulent stress tensor

μ Dynamic viscosity

μ_g Vapor viscosity $(Pa\cdot s)$

μ_L Liquid viscosity $(Pa\cdot s)$

μ_L Liquid viscosity

μ_m Mixture viscosity

μ_m Mixture viscosity

ν Parameter in calculation of small droplet fraction in vertical flows

$\overline{\alpha}$ α_g for bubbles and α_f for droplets

$\overline{\sigma}$ Viscous stress gradient

ϕ Body source of quantity ψ

Φ_k^μ Viscous dissipation term

Φ_k^T Turbulent work effect source

ψ	Any quantity or property per unit mass
ψ	Interphase mass exchange per unit volume ($kg/s/m^3$)
ρ	Density
ρ	Mass density of the radionuclide specie (kg/m^3)
ρ	Mass density
ρ_a	Noncondensable gas density = $\rho_a = \rho_g - \rho_v$
ρ_b	spatial boron (solute) density
ρ_c	Density of continuous phase
ρ_c	Density of continuous phase
ρ_d	Liquid density of droplet ($^{kg}/_{m^3}$)
ρ_f	Liquid density ($^{kg}/_{m^3}$)
ρ_G	Density of gas
ρ_g	Density of vapor ($^{kg}/_{m^3}$)
ρ_g	Density of vapor and noncondensable gas mixture
ρ_i	Density face i
ρ_k	Density of phase k
ρ_l	Density of liquid phase
ρ_l	Liquid density
ρ_{mdl}	Model density
ρ_m	Mixture density = $\alpha_g \rho_v + (1 - \alpha_g)\, \rho_l$

ρ_{NC} Density of noncondensable gas

ρ_v Density of vapor phase

σ Surface Tension

σ Surface tension $(^{kg}/_{s^2})$

τ Drag force to compute droplet relative velocity $(^{1}/_{s})$

τ_i Interfacial shear per unit volume (N/m^3)

$\tau_{w,cv}$ Period of entrainment phenomena in control volume (s)

τ_{Wk} Wall to phase k friction term

θ Angle of flow channel

θ Angular position within pipe $\theta = 0$ at bottom

Υ =1 for $\Gamma_{ig} \geq 0$, =0 for $\Gamma_{ig} \leq 0$

ς Pipe diameter dependent coefficient

ς Pipe diameter-dependent coefficient

ζ Droplet turbulent diffusivity $(^{m^2}/_{s})$

ζ Droplet turbulent diffusivity

$\overline{\rho_k}$ Time-averaged density of phase k

$\underline{\underline{\sigma}}_g$ Average gas phase viscous stress tensor

$\underline{\underline{\sigma}}_l$ Average continuous liquid phase viscous stress tensor

$\underline{\tau}_{i,ge}$ Average drag force per unit volume by the gas on the entrained liquid

$\underline{\tau}_{i,gl}$ Average drag force per unit volume by the gas on the continuous liquid

$\underline{\tau}_{w,e}$ Force exerted by the wall on the entrained liquid

$\underline{\tau}_{w,g}$ Force exerted by the wall on the combined gas

$\underline{\tau}_{w,l}$ Force exerted by the wall on the continuous liquid

English

$-\int_{S_c} \vec{q} \cdot \vec{n}\, dA$ Rate of heat addition to phase at surfaces other than $S_i\,(t)$. This term includes the conduction contribution where S_c is occupied by the phase, and the heat addition by walls where S_c is a solid bounding wall

ΔC Drop concentration gradients for the channel

Δt Change in time from one timestep to the next (timestep size)

ΔX Cell height (m)

ΔX Cell height

$\dot{q}$ Local instant body heating (W/m^3)

$\hat{v}_{fg}$ Average velocity of annular film and entrained droplets

$\mathbb{I}$ Unity tensor

$\mathbb{J}$ Efflux of the quantity ψ

$\mathbb{J}_a^{l\cdot}$ Surface flux $\mathbb{J}_a$ in space coordinates

$\mathbb{J}_k^T$ Turbulent flux of phase k

$\mathcal{L}_m$ Model length scale

$\overline{f}$ External forces per unit mass

$\overline{u_f}$ Average film velocity $(^m/_s)$

$\overline{u_{gc}}$	Average velocity of gas core ($^m/_s$)
$\overline{u}_l$	Averaged liquid film velocity ($^m/_s$)
$\overline{u}_{tc}$	Critical eddy velocity for bubble breakup ($^m/_s$)
$\overline{u}_t$	Average turbulent eddy velocity ($^m/_s$)
$\overline{u}_t$	average turbulent eddy velocity
$\overline{v}_{gj}$	Weighted area-average of the drift flux velocity
$\overline{V}_k$	Void-weighted area average velocity for phase k
$\vec{g}$	Body force field
$\vec{N}$	Outward normal of surface Σ_i (tangent to phase interface)
$\vec{n}$	Normal vector to boundary surface A_m
$\vec{n}_k$	Normal vector to surface k
$\vec{q}$	Surface heat flux
$\vec{v}$	Bulk velocity vector
$\vec{v}$	Velocity of fluid within interface region
$\vec{v}_{i,k}$	Velocity of phase k near the interface
$\vec{v}_i$	Velocity of interface
A	Channel flow area
A	Flow area
A	Interfacial area
A	Interfacial area

$A^{\alpha\beta}$ Surface metric tensor

A_c Channel area (m^2)

A_g Projected grid blockage area (m^2)

A_m Surface surrounding the material volume V_m

A_c Area of the channel

A_d Total interfacial area of the drops (m^2)

a_{fr} Ratio of diameter of largest drop from breakup to diameter of drop that broke up

A_f Flow area (m^2)

A_f Flow area of pipe

$a_{gf,ann}$ Vapor interfacial area concentration for annulus

$a_{gf,Tb}$ Area concentration - control-volume based

$a_{gf,Tb}$ Volumetric interfacial area

a_{gf} Interfacial area per unit volume

a_{gf} Particle (bubble or droplet) surface area per unit volume

A_g Area of the grid

$A_{i,6}$ Interfacial area concentration for small bubbles

$A_{i,d}$ Droplet interfacial area concentration ($1/m$)

$A_{i,d}$ Droplet interfacial area concentration

$A_{i,SBu}$ Interfacial area concentration - Small bubbles ($1/m$)

$a_{i,SBu}$ Small Bubble interfacial area concentration ($1/m$)

A_i Area of interface between phases/fields

A_i Total area of face i for volume V

a_i Interfacial area concentration (area per unit volume)

A_{ki} Total area of A_i for flowing fluid phase under consideration

A_k Area of interface of phase k

A_w Wall surface area

B Body forces (gravity)

b Empirical constant

B_s Balance of a quantity on a surface

B_v Balance of a quantity in a unit volume

B_x Body force in x coordinate direction

B_x Body forces (gravity)

C Coefficient of virtual mass (from momentum equations)

C The concentration of the radionuclide in atoms per unit volume (atoms/m^3)

C_B Bulk concentration of drops

C_0 Distribution parameter

C_1 Shear lift coefficient

$C_{D,i}$ Interfacial drag coefficient

$C_{D,k}$ Drag coefficient of leading group k bubble in wake entrainment

$C_{D,SBu}$ Drag coefficient of the leading small group bubble in wake entrainment

C_{D2} Bubble drag coefficient for a bubble in large bubble group

C_D Drag coefficient

C_d Empirical constant - 4.8 based on air/water results

C_d Empirical constant - 4.8

C_i Line tracing the perimeter of the interface between surfaces

C_L, C_G Wall friction coefficient for liquid (L) and gas (G)

C_m Model constant

C_{pf} Liquid specific heat at constant pressure

$C_{RC,k}$ Proportionality constant

C_{RC1} Proportionality constant = 3.0 [9]

C_{RC2} Proportionality constant

C_{RC} Empirical coefficient for small bubble coalescence

$C_{RC}^{(2)}$ Empirical coefficient for large bubble coalescence

$C_{RC}^{(k)}$ Empirical coefficient for bubble coalescence

C_{SO} Shear off coefficient - 3.8×10^{-5}

C_{SO} Shear off coefficient determined by experiment

C_s Empirical constant for horizontal convective boiling

$C_{TI,SBu}$ Small bubble turbulent impact coefficient

$C_{TI}^{(k)}$ Adjustable coefficient - 0.03

C_{WE} Wake entrainment coefficient for bubble coalescence - 0.002 for water/air

$C_{WE}^{(k)}$ Experimental determined coefficient for wake entrainment between two large bubbles

$C_{WE}^{(k)}$ Wake entrainment coefficient for bubble coalescence

$C_{WE}^{(11,2)}$ Coefficient for wake entrainment where two group 1 bubbles combine to make a group 2 bubble

$C_{WE}^{(2)}$ Experimentally determined coefficient for wake entrainment between two group 2 (large) bubbles

C_{wk} Wall shear coefficient for phase k

C_W Droplet concentration near wall

D Diameter of pipe (m)

D Diameter

d Particle diameter

d' Most probable particle diameter

$D^{'}$ Large (Taylor) bubble diameter

d^* Nondimensional particle diameter

D_b Bubble diameter (m)

d_b Average bubble diameter - Sauter mean diameter

D_{cl}^* Nondimensional measure of average size of bubble in small bubble group

D_c Volume equivalent diameter of bubble with volume V_c (m)

d_d Droplet diameter

D_{hy} Hydraulic Diameter

D_{hy} Hydraulic diameter of pipe (m)

D_h Hydraulic diameter

D_I Diameter of drop impacting spacer grid (m)

D_I Diameter of droplet impacting spacer grid

D_i Representative drop size for group i (m)

D_{max} Maximum droplet diameter (m)

d_{max} Maximum particle (bubble or droplet) diameter

D_o Initial Droplet Diameter (m)

D_o Initial droplet diameter

d_o Average bubble diameter

d_o Average particle diameter

D_{SBu} Sauter mean diameter of small bubbles (m)

D_{SM} Sauter Mean Diameter (m)

D_s Viscous dissipation rate per unit volume

D_t Diameter of transition between large and small droplets (m)

D_{vm} Volume median droplet diameter (m)

$DISS$ Energy dissipation term

$DISS_k$ Energy dissipation function of phase k

e Apparent internal energy

E_i Rate of energy transfer per unit volume across phase interfaces

E_k Energy gain in phase k through interfaces

e_l, e_g Internal energy of liquid ($_l$) or gas/vapor ($_g$)

F Function F

f Functional definition of a mathematical surface $f(\vec{x}, t) = 0$

F_b Buoyancy force

F_i''' Interfacial drag force per unit volume

$f_k \frac{\partial A}{\partial z}$ Term for variable cross-sectional duct - phase k

FI_k Interphase drag coefficient for phase k

FW Wall drag coefficient in energy dissipation and momentum equations ($^1/_{sec}$)

FW_k Wall drag coefficient for phase k

G Gap of the flow channel (m)

G Gap of the flow channel

G Mass flow rate (kg/s)

g Gravitational acceleration ($^m/_{s^2}$)

g Gravity

g Gravity

g Gravity

g_{ln} Space metric tensor

G_s Dimensionless fluid velocity gradient

h^* Phasic specific enthalpy (for bulk interface mass transfer)

$h^{\backprime}$ Phasic specific enthalpy for wall (thermal boundary layer) interface mass transfer

$h_{\psi,l}$ Enthalpy of interphase mass exchange

h_{CL} Collapsed liquid level calculated for the whole liquid in the pipe cross-section

h_{cr} Critical specific enthalpy for net voids - from Saha-Zuber [10]

h_{fg} Specific enthalpy of vaporization

h_f^s Liquid enthalpy at saturation

H_{gf} Sensible (direct) heat transfer coefficient per unit volume

H_g Average gas phase enthalpy

H_g^i Enthalpy of gas phase associated with interfacial mass transfer

h_g^s Vapor enthalpy at saturation

$H_{if,Tb}$ Volumetric interfacial heat transfer coefficient for Taylor bubbles - $^W/_{m^3K}$

H_{if} Volumetric heat transfer coefficient - interface to liquid

H_{ig} Volumetric heat transfer coefficient - interface to vapor

h_i $U + P/\rho$ on S_i

h_i Enthalpy of face i

$H_{k,m}$ Heat transfer coefficient from field k to field m per unit volume

h_k Enthalpy of phase k

h'_k Specific enthalpy for interface mass transfer in the thermal boundary layer

h_k^* Specific enthalpy in phase k

H_l Average liquid phase enthalpy

H_L, H_G Liquid (L) or gas (G) enthalpy

h_l, h_v Liquid ($_l$) or vapor ($_v$) enthalpy

$h_l^{'}$ Liquid enthalpy of the bulk liquid if it is vaporizing; liquid saturation enthalpy if vapor is condensing

H_l^i Enthalpy of liquid phase associated with interfacial mass transfer

$H_{m,k}$ Heat transfer coefficient from field m to field k per unit volume

H_V Enthalpy for vapor

$h_v^{'}$ Vapor enthalpy of the bulk vapor if vapor is condensing; vapor saturation enthalpy if liquid is vaporizing

h_v^* Vapor enthalpy

$HLOSS$ Dynamic flow loss in liquid phase resulting from abrupt area changes. Code-computed or user-input values.

$HLOSSG$ Dynamic flow loss in vapor phase resulting from abrupt area changes. Code-computed or user-input values.

I Interfacial exchange of momentum

i_{fg} Heat of vaporization (latent heat)

J Mixture superficial velocity

j^* Larger of phase superficial velocities

$j_{g,crit}$ Critical gas velocity for the onset of entrainment - just sufficient to levitate a drop with the Sauter mean diameter (m/s)

j_g Volumetric flux of vapor phase (m/s)

Ja Jacob number

Ja_e Effective Jacob number

$k_A^{'}$ Empirically selected constant

k_σ Mass transfer coefficient

$k_A^{'}$ Empirical Constant

$k_{D\theta}$ Local deposition velocity at angle θ ($^m/_s$)

k_D Local droplet deposition velocity ($^m/_s$)

k_D Local droplet deposition velocity

K_e Geometry dependent constant

k_f Thermal conductivity of liquid

L_{cell} Length of calculational cell (m)

L_{cell} Length of computational cell

m Solute concentration ($mass_{solute}/unit_m ass_{liquid_water}$) in the liquid phase

m_{DB} Mass of small drops generated after grid breakup (kg)

m_E Mass of droplets entering the grid

m_E Mass of drops entering the spacer grid (kg)

M_{ik} Generalized interfacial drag

M_i Interfacial drag force per unit volume

M_k k-th phase momentum source from interfacial transfer

M_k State density function

M_{ni} mass of i-th noncondensable gas

M_n total mass of noncondensable gas in the vapor/gas phase

M_s mass of vapor in the vapor/gas phase

Mw Molecular weight of the radionuclide specie (kg/kg-mole)

N number of noncondensables

$N_{\mu g}$ Viscosity number for vapor phase, $N_{\mu g} = \mu_g / \left[\rho_g \sigma \sqrt{\frac{\sigma}{g\Delta\rho}}\right]^{\frac{1}{2}}$

N_μ Viscosity number

N_a Avogadro's number (atoms/kg-mole)

n_i Number of droplets in group i

n_T Total number of droplet groups

$N_{w,cv}$ Number of waves in the control volume

N_{wav} Number of wavelengths within annular control volume - L_{cv}/λ

NG Number of droplet groups containing similar-sized droplets

P Average Pressure

P Perimeter of the pipe (m)

P Pressure (Pa)

P System pressure

p Bulk partial pressure

p^* Probability of particles (bubbles or drops) with nondimensional diameter d^*

P_w Wetted perimeter (m)

P_{crit} Critical pressure

P_H Heated Perimeter

P_H Heated perimeter (m)

P_i Pressure of noncondensable gas i

P_k Instant, local physical, or flow variable for phase k

P_n Noncondensable gas partial pressure

P_p Perimeter of pipe

P_w Wetted Perimeter

$Perim_i$ Interface perimeter

Pr_f Liquid Prandtl number

Q Volumetric heat addition rate ($^W/_{m^3}$)

q_{dl}, q_{dg} Power deposited directly to liquid ($_{dl}$) or vapor ($_{dg}$)

Q_{GI} Energy exchange between gas phase and interface

q_{GI} Heat Flux between gas phase and interface

q_{gl} Liquid to gas sensible heat transfer

Q_G Gas volumetric flow ($^{m^3}/_s$)

Q_G Gas volumetric flow

$q'''_{i,g}$ Heat flow to gas phase

$q'''_{i,l}$ Heat flow to liquid phase

q_{ig} Interfacial heat transfer to vapor

Q_{ik} Interface heat transfer per unit volume to phase k

q_{il} Interfacial heat transfer to liquid

Q_i $-\frac{1}{V}\int_{S_i(t)} \vec{q}\cdot\vec{n}\,dA$ rate of heat addition to phase per unit volume at the interface

$q'''_{l,NC}$ Heat transfer between liquid and noncondensable gas

q_{Le}, q_{Ge} Interface to liquid (L) and to gas (G) heat fluxes

Q_{LI} Energy exchange between liquid phase and interface

q_{LI} Heat Flux between liquid phase and interface

q'_l, q'_g Heat flux to liquid ($_l$) or vapor ($_g$)

q_{pL}, q_{pG} Wall to liquid (L) and to gas (G) heat fluxes

$q_{SBu,i}$ heat lost from small bubbles to liquid

$Q'''_{w,g}$ Wall heat transfer rate per unit volume to vapor

$Q'''_{w,l}$ Wall heat transfer rate per unit volume to liquid

q_{wg} Wall heat flow to vapor

q_{wi} Wall-to-interface heat flux

Q_{Wk} Energy exchange from wall to phase k

Q_{wk} Wall heat transfer per unit volume to phase k

q_{wl} Wall heat flow to liquid

q'''_w Heat transferred from the wall to the continuous liquid per unit volume (W/m^3)

q''_w Total wall heat flux (W/m^2)

R Pipe radius (m)

R Rate of direct heating per unit volume

R Rate of stratification

r Radius

r_b Bubble radius

R_c^* Dimensionless radius of curvature for cap bubble

R_c^* Dimensionless radius of curvature of a cap bubble

r_{LB} Large bubble radius (m)

$R_{m,LB}$ Maximum radius of curvature of a bubble in group 2 (m)

r_{SBu} Radius of small bubble (m)

$R_{SO,c}$ Critical radius of curvature for bubble shear off

$R_{SO,c}$ Critical radius of curvature for bubble shear-off (m)

Rc Radius of curvature

Re_p Particle (bubble or drop) Reynolds number

Re_p Particle Reynolds number

S Ratio of drop velocity to gas velocity

S Ratio of drop velocity to gas velocity

S Source term

S Suppression factor

S The source of the radionuclide in units of atoms per unit volume per second (atoms/m^3-sec)

s Sheltering coefficient (ATHLET used 0.01)

S'''_{ent} Average rate of entrainment per unit volume

$S'''_{LB,DE}h_{LB}$ large bubble de-entrainment to vapor field

$S'''_{LB,FB}h_{LB}$ large bubble breakup from flow

$S'''_{LB,SB}h_{LB}$ large bubble breakup from spacer grid

$S'''_{SBu,C}h_{SBu}$ small bubble to large bubble field (from coalescence)

$S'''_{SBu,DE}h_{SBu}$ small bubble de-entrainment

$S'''_{SBu,E}h_g$ small bubble entrainment from cont. vapor

$S'''_{SD,E}h_f$ small droplet entrainment from cont. liquid

$S_{e,l}$ External energy source terms

S_E Droplet entrainment flux ($^{kg}/_{m^3 s}$)

S_F Shape factor (assumed to be unity -1.0)

$S_{i,l}$,$S_{i,v}$ External momentum source terms (e.g. pumps)

S_i Source term for noncondensable gases

s_k Liquid or vapor multiplier. Set to 1 for vapor phases and -1 for liquid phases

SE_G, SE_L Energy source term for liquid (L) and vapor (G)

SM_G, SM_L Momentum source term for liquid (L) and gas (G)

T Temperature

t Time for two-phase flow boiling

t Time

t_α^n Hybrid tensor

T^s Saturation temperature

T^s Saturation temperature

t_{ann} Thickness of annulus (m)

t_{brk} Break-up time required for bag-type droplet breakup (s)

t_{film} Annular film thickness (m)

T_f Liquid temperature

T_g Vapor temperature

$t_{StripBU}$ Break-up time required for stripping-type droplet breakup (s)

U Internal energy

u Bulk phase internal energy

U_d Relative drop velocity $(^m/_s)$

U_G Vapor velocity $(^m/_s)$

U_k Specific internal energy for phase k

$u_{r,SBu}$ Relative velocity of the leading small bubble in wake entrainment $(^m/_s)$

u_{ro} Initial vapor velocity relative to droplet $(^m/_s)$

u_r Relative bubble velocity to liquid phase

u_T Droplet terminal velocity $(^m/_s)$

$U_{vap,bqf}$ Characteristic vapor velocity for vapor generated below quench front ($^m/_s$)

$U_{vap,crit}$ Critical vapor velocity ($^m/_s$)

V Total volume of both phases

V Volume of the hydro cell

V Volume

v Magnitude of bulk velocity

v The velocity of the transporting phase (m/s)

v Velocity

v^* Friction velocity ($^m/_s$)

V_i Interface velocity

V_m Material volume

V_{ann} Volume of annulus liquid within the control volume (m^3)

V_{cell} Volume of computational cell (m^3)

V_{cell} Volume of computational cell

V_c Critical volume (m^3)

V_c Critical volume

V_{dI} Velocity of drop impacting spacer grid

V_d Total volume of the drops (m^3)

$V_{entr,w}$ Volume of liquid entrained from a wave crest (m^3)

v_{fg} Relative velocity $(v_g - v_f)$

V_f Liquid volume within control volume (m^3)

v_f velocity of the liquid phase

$V_{g,j}$ Drift velocity

v_{in} Normal component of velocity vector on face i

V_i Volume of the interfacial region of thickness δ around the phase/field interface

V_k Volume of phase of interest

v_k Velocity of phase k

$V_{L,disp}$ Volume of liquid dispersed in flow

$V_{L,nd}$ Volume of liquid not dispersed in flow

V_l, V_g Magnitude of velocity of liquid $(_l)$ or gas/vapor $(_g)$ phase

v_L, v_G Liquid (L) or gas (G) velocity

$V_{m,LB}$ Maximum volume for large group bubbles (m^3)

v_m $\frac{G_m}{\rho_m}$

v_{ni} Normal (to interface) component of interfacial velocity

v_{rb} Relative velocity of a cap bubble W.R.T. the liquid around the bubble base in axial direction $(^m/_s)$

V_r Relative velocity (m/s)

v_r Velocity of phase r

v_{SB} Small bubble velocity

$V_{SO,c}$ Critical volume for bubbles sheared off of a larger bubble (m^3)

v_{ti} Tangential (to interface) component of interfacial velocity

VIS_k Artificial viscosity term for field k, where k is 1 or 4.

W Longer width of flow duct

W Longer width of the flow duct (m)

W_G Mass flow of vapor ($^{kg}/_{s}$)

w_i Interface velocity

W_{ki}^T Turbulent flux of work due to drag force

W_{LE} Mass flow of entrained drops ($^{kg}/_{s}$)

W_{LE} Mass flow of entrained drops

W_{LFC} Critical film flow for droplet entrainment ($^{kg}/_{s}$)

W_{LFC} Critical mass flow liquid film

W_{LF} $W_L - W_{LE}$ - difference between total liquid and droplet mass flows ($^{kg}/_{s}$)

W_{LF} Difference between total liquid mass flow and droplet mass flow ($^{kg}/_{s}$)

W_{LF} Mass flow liquid film

W_L Mass flow of liquid ($^{kg}/_{s}$)

w_l Liquid phase velocity

w_r Cross sectional average relative velocity

$w_{V,e}$ Vapor velocity required to suspend a droplet

$w_{V,s}$ Minimum gas velocity for slug formation

$w_{V,w}$ Minimum gas velocity for wave formation

w_v Vapor phase velocity

We Critical Weber number

$We_{c,SO}$ Critical Weber number for bubble shear-off

$We_{c,TI,k}$ Critical Weber number for turbulent breakup of small bubbles - 6.5

$We_{c,TI}$ Critical Weber number for turbulent impact

We_c Critical Weber number for bubble breakup

$We_{m,LB}$ Weber number for largest large group bubble

x Direction of flow

X_i Specific fraction of noncondensable gas i

X_n Noncondensable quality

X_n total noncondensable mass fraction in the vapor/gas phase

y Vertical position within horizontal pipe flow area - $y = 0$ at bottom of pipe (m)

$\dot{q}_i$ Heat flow at the phase interface

$\dot{q}_{wl}$ Heat flow through structures

$\vec{f}_w$ Wall friction

$\vec{g}$ Gravity vector

$\vec{V}_g$ Velocity vector of vapor phase (time-averaged)

$\vec{V}_l$ Velocity vector of liquid phase (time-averaged)

$\vec{w}_\Gamma$ Velocity of interphase mass exchange

$\vec{w}_\psi = \vec{w}_l$ For evaporation

$\vec{w}_\psi = \vec{w}_v$ For condensation

$\vec{w}_l$ Liquid velocity vector

$\vec{w}_m$ $\frac{1}{\rho_m}\left(\alpha\rho_v\vec{w}_v + (1-\alpha)\,\rho_l\vec{w}_l\right)$

$\vec{w}_R$ Relative liquid velocity $=\vec{w}_v - \vec{w}_l$

$\vec{w}_v$ Vapor velocity vector

$\underline{q}_g$ Average gas phase conduction vector

$\underline{q}_l$ Average liquid phase conduction vector

$\underline{U}_\Gamma$ Phase velocity of the source of the mass being transferred

$\underline{U}_{Se}$ Velocity of the entrainment source

$\underline{g}$ Acceleration of gravity

$\underline{U}_e$ Phase velocity vector of the entrained liquid

$\underline{U}_g$ Phase velocity vector of the gas

$\underline{u}_k$ Velocity of phase k

$\underline{U}_l$ Phase velocity vector of the liquid

Subscripts

1 Continuous liquid field

2 Large Droplet

3 Small Droplet

4 Continuous vapor field

5	Large Bubble
6	Small Bubble
a	Interfacial surface parameter per unit surface area
b	Bubble value (field numbers 5 or 6)
C	Coalescence
CV	Continuous vapor
d	Droplet value (field numbers 2 or 3)
DE	De-entrainment
E	Entrainment
f	Liquid
FB	Flow-caused breakup
g	Vapor
I	Interface
i	Field interface
i	Interface
K	Center of volume upstream of calculation volume
k	Field subscript - any of the 6 fields
k	Phase or field
L	Center of current calculational volume
L	Continuous liquid field

l	Leading (bubble field)
LB	Large bubble
LD	Large droplet field
max	Maximum value
ni	Interface normal
o	Reference
RC	Random Collision
rel	Relative value
s	Interfacial surface parameter
SB	Spacer-caused breakup
SD	Small droplet field
SI	Surface Instability
SO	Shear off
T	Trailing (bubble field)
t	Total value
w	Value at the wall, wall
WE	Wake Entrainment

Superscripts

$'$	Indication of phasic specific enthalpy for heat transfer in the thermal boundary layer near the wall

$*$ Indication of phasic specific enthalpy for bulk heat transfer

$\dot{}$ "Donored" value - volume weighted average at a junction from adjacent volumes

$\sim$ Provisional value

n "Old" time value

$n+1$ "New" time value

(1) Group 1 bubble interactions

(11,2) Group 1 bubble coalesces with a group 1 bubble to make a group 2 bubble

(12,2) Group 1 bubble coalesces with a group 2 bubble to make a group 2 bubble

(2) Group 2 bubble interactions

(2,1) Group 2 bubble breaks up to make group 1 bubbles

(2,11) Group 2 bubble breaks up to make two group 1 bubbles

(2,12) Group 2 bubble breaks up to make a group 1 bubble and a group 2 bubble

(2,2) Group 2 bubble breaks up to make group 2 bubbles

$()_{,\beta}$ Surface covariant derivative [11]

$\overline{X}$ Time average of X

∇ Mathematic gradient

$\overline{\overline{X}}$ Phase average of X (phase density function weighted time average)

$\sum_j$ Summation over j interfaces

$\widehat{X}$ Mass weighted time average of X

CHAPTER 1

Introduction

Nuclear reactor systems are complex, and require detailed analysis to evaluate reactor performance during normal operations as well as accident or transient conditions. Nuclear Pressurized Water Reactor (PWR) systems include steam generators, pressurizers, vessels where the reactor fuel is utilized, pumps, valves, and many pipe fittings and components. Boiling Water (BWR) systems such as that as depicted schematically in Figure 1.1 are similar to PWR systems, but do not require pressurizers (or steam generators, for some BWR designs). Computer codes that are used to analyze these complex reactor systems are called "system codes".

System codes include detailed models of reactor components, such as pipes, pressurizers, valves, and pumps. These hydrodynamic models have frequently been extended to include a code capability to model multiple phase flows [12, 13]. The interaction between phases in the coolant is modeled in order to capture heat transfer properties and mass exchange between the phases.

Conservation equations are used to balance the mass, momentum, and energy within a control volume or phase. Mass, momentum, and energy balances are computed to account for convective effects, heat added to or removed from the control volume or phase, and other characteristics such as energy loss to diffusion or viscous effects. For two-phase systems, mass, momentum, and energy may also be exchanged by a change in phase. Jump models are often used to capture these effects. Complete characterization of a phase requires an equation for the mass, momentum, and energy balance, along with the closure relationships for that phase. Some system codes include the capability to model noncondensable gas mixed with the vapor or dissolved solutes (such as boron) mixed with the liquid [13]. However, these additional phases are often only represented by a single mass balance equation, effectively assuming that the solute or gas is at the same temperature and moves at the same velocity as the surrounding phase [12].

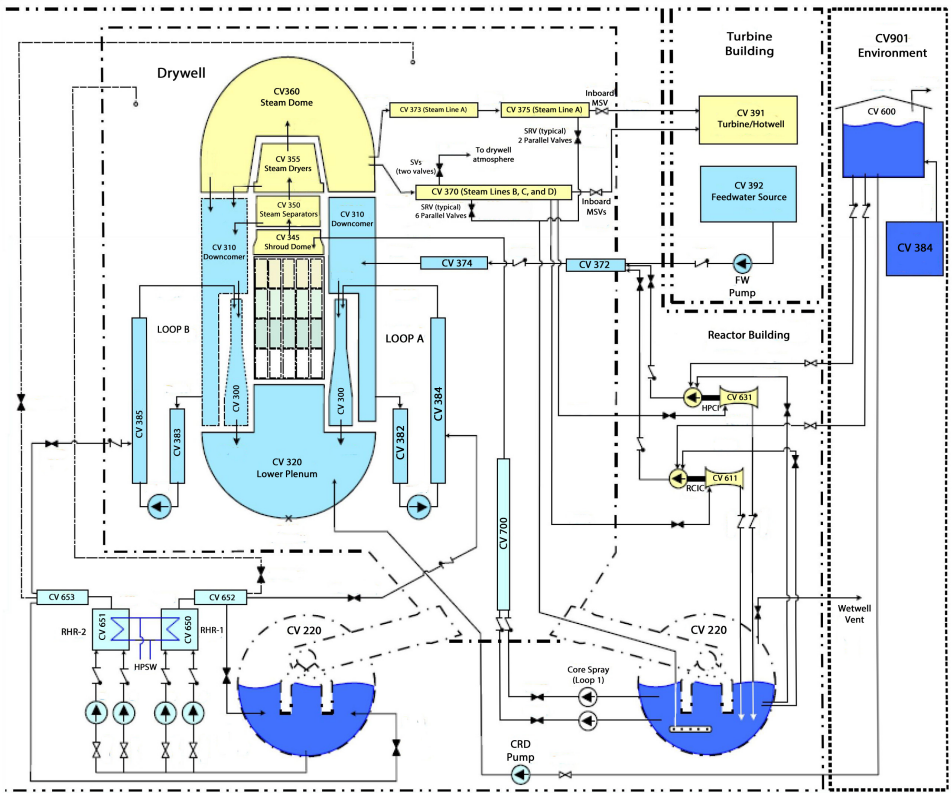

Figure 1.1: Nuclear Reactor System

System codes begin to differentiate when considering the number of modeled fields. Generally, the code models include just two fields, one for each phase. Such a model is limited to capturing the characteristics of a liquid and vapor by using the lumped capacitance approximation. This approximation applies to two fields by assuming that all the liquid (continuous liquid and droplets) are only one field having the same temperature, pressure, and velocity. The same approximation applies to the vapor field, where the continuous vapor and the bubbles are both covered by a single field and share a single velocity, temperature, and pressure.

Almost all system codes have a two-phase, two-field model that is adequate for many anticipated flow regimes [12]. Vertical flow regimes that are present before the point of Critical Heat Flux (CHF) are shown in Figure 1.2. Some nuclear reactor designs, in particular Boiling Water Reactors (BWRs), operate at steady state with coolant that ranges from single phase liquid to high vapor fraction. Other reactor designs can experience severe

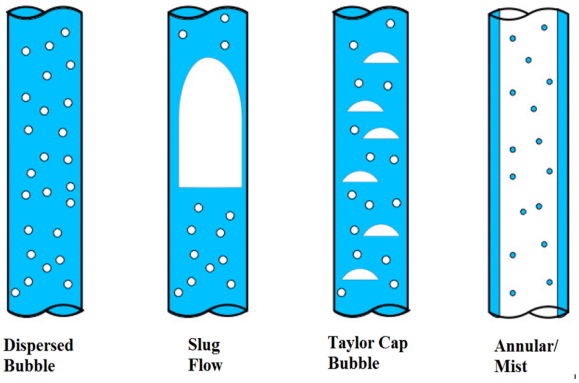

Figure 1.2: Pre-CHF Vertical Two-Phase Flow Regimes

accident scenarios (such as core reflood, blowdown, or rapid depressurization) where rapid and extreme changes in coolant vapor content will tax the capabilities of a two-field model. The steady state BWR conditions and severe accident scenarios can involve bubbles and droplets of varying size. Reactor system characteristics and accident progress are affected by the heat transfer between these additional fields. For example, droplet formation and evaporation removes significant amounts of heat from the bulk coolant. Small droplets leaving the large droplet field increase the effective surface area, which increases the thermal activity of the droplets. As these small droplets evaporate, they increase the steam flow and convective heat transfer while reducing the total liquid volume.

More recent developments in nuclear system codes have included updates to the number of fields modeled by the governing equations. It was found that two fields are insufficient for modeling some transients effectively. The addition of a droplet field helps to model the transition to superheat conditions, as well as the complex heat transfer of a reflood condition. The W-COBRA/TRAC-TF2 code now includes a droplet field that is available in the 3D vessel component [3], though there is a single energy equation for the liquid film and the droplet field, which implies that both fields share the same temperature. The TRACE code will soon include a droplet field to improve reflood modeling [1]. COBRA-TF is a subchannel code for rod bundle analysis that has three fields: continuous liquid, continuous vapor, and large droplets. An additional field for small droplets was added as described in [7]. The

capability of the CATHARE code to predict dryout and rewetting is improved by increasing the number of fields that are modeled [14].

The limitations of a two-fluid six-equation model were cited as a weakness of current system codes during the development of the NEPTUNE code [15]. Multifield models are being developed for the NEPTUNE code, since they were found to be necessary for key applications, including steam generators and heat exchangers [15].

Addition of a droplet field improves the results for reflood conditions. The NRC is also considering development of a bubble field for the TRACE code for further transient model improvements [16, 17]. Specialized TRACE versions have been developed that include bubble fields [18]. Increasing the number of fields improves the results for transient reactor analysis. Kunz et. al. [19] developed a multi-field two-phase model and showed that increasing the number of fields improves the results for transient two-phase analysis.

Further progress in system codes is expected to come from multifield modeling [15]. The current trends in system code development include the improvement of the two-phase models by increasing the number of fields. This dissertation shows the development of two-phase, six-field conservation equations for the following six fields:

1. Continuous Liquid
2. Continuous Vapor

} Fields currently included in many system codes [12, 13]

3. Large Bubble
4. Small Bubble
5. Large Droplet
6. Small Droplet

} Four proposed fields

The interactions between these six fields are represented graphically in Figure 1.3.

Governing (conservation) equations are generated from a balance of the mass, momentum,

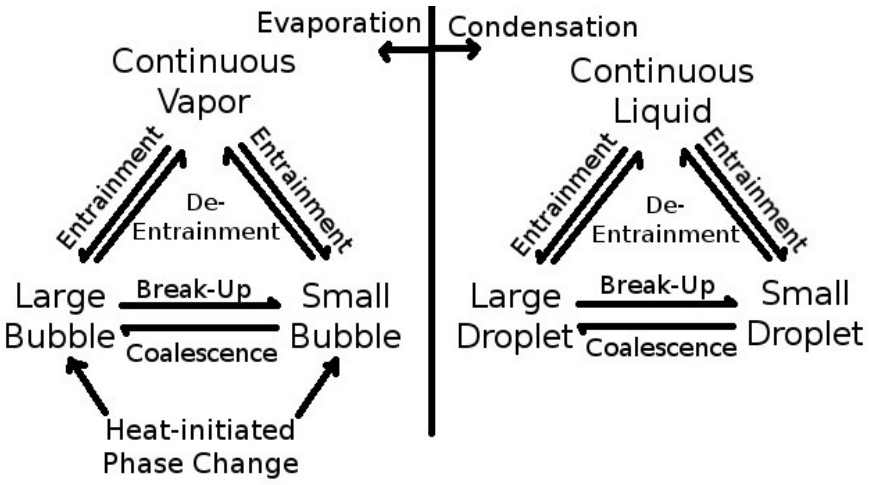

Figure 1.3: Interactions between 6 fields

and energy within a control volume or field. Mass, momentum, and energy balances are computed to account for convective effects, heat added to or removed from the control volume or phase, and other characteristics such as energy loss to diffusion or viscous effects. The interactions between fields in the coolant are modeled in order to evaluate heat transfer properties and mass exchange between the phases. For systems that involve two phases, mass, momentum, and energy may also be exchanged by a change in phase. Complete characterization of a field requires an equation for the mass, momentum, and energy balance, along with the closure relationships for that field.

This work will show a full set of mass, momentum, and energy equations for each of the proposed fields. The inclusion of the energy equations will allow the separate fields to have different temperatures from one another. This is a new idea that has not been done for previous codes. This change makes it difficult to predict the amount of improvement in model fidelity that can be expected for six fields in comparison to three. The three field codes currently available do not include the energy equation, so they are not expected to show the same improvement as if the equation were included.

In realistic flows, all six fields will not be present in all flow regimes. For example, bubbly flow will be made up mostly of smaller bubbles, while slug flow will consist of large bubbles. Droplets will most likely not be present in bubbly flow. The six field equations developed

in this dissertation establish a framework for balancing the interactions between the six fields. The volume fraction of each field is tracked by the governing equations. For a bubbly regime, the effect of the droplet field will be reduced by the balance equations, until it can be eliminated from the calculation.

Each field included in the model requires additional conservation equations and closure relationships to be modeled effectively by the code. The mass governing equations cannot be solved without these closure models. The six-field equations add several new variables to the system of governing equations, and the closure models solve for these variables. The closure relationships track interactions between the fields, allowing the code to determine when a particular field will no longer be included in the flow.

The first nuclear system codes for reactor analysis were limited to very basic models that were able to model only a single fluid field [20]. A single fluid field does not allow for very detailed modeling of reactor transients. Developments in the RELAP code in the late 1960's and early 1970's included the addition of a second field to allow for calculation of 2-phase transients, along with the accompanying boiling heat transfer models [20]. Like other system codes, RELAP models the performance of reactor systems for transient and steady state conditions. RELAP has a complete set of governing equations for two-phase flows, and includes mass balance equations for both noncondensable gases and dissolved solutes [12]. The closure relationships utilized in RELAP consider several flow regimes, including slug, annular, and bubbly flows. The two-field model has been used by many system codes since that time [1, 21].

Although RELAP5-3D and other RELAP codes include closure models for various flow regimes, currently only two fields are modeled by the governing equations [12]. The closure relationships are limited to heat transfer correlations between pipe walls and the coolant field. The interactions of droplets that may be in the vapor field or bubbles within the liquid field are not physically modeled by the code. So, while RELAP5-3D will differentiate the heat transfer between the wall and a bubbly flow or continuous liquid regime, the presence

of the bubbles will not affect the calculation of the fluid velocity, temperature, or the vapor generation rate.

Several of the features associated with the proposed six-field model are new to the field of nuclear reactor analysis. The six fields have been identified and justified in this work, and the primary variables have been identified for those six fields. This has not been done for six fields previously. In addition, correlations for the mechanisms of mass, momentum, and energy transfer have been identified for each of the six fields. These correlations are essential to the development of a viable six-field model, and have not been identified previous to this work. in some cases, the correlations required adaptations in order to work within the framework of the proposed six-field model. These adaptations are also new to the field, and an expanson of the work that developed the original correlations. Finally, the solution technique used in the RELAP5-3D code has been adapted to work for a six-field model.

This dissertation presents a six-field model and a solution scheme that can be applied to RELAP5-3D or other system codes to improve accuracy of transient modeling. The chapters of this dissertation consist of journal articles written by the author and Dr. Fatih Aydogan and Dr. George Mesina. These papers were not altered significantly for inclusion in this dissertation in order to preserve continuity with the published works. The papers included herein are:

- Chapter 2:
  - G. Roth and F. Aydogan, "Theory and implementation of nuclear safety system codes - Part I: Conservation equations, flow regimes, numerics and significant assumptions", Progress in Nuclear Energy, 76, 2014, 160-182
  - G. Roth and F. Aydogan, "Theory and implementation of nuclear safety system codes - Part II: System code closure relations, validation, and limitations", Progress in Nuclear Energy, 76, 2014, 55-72

- Chapter 3:
  - G. Roth and F. Aydogan, "Derivation of new mass, momentum, and energy conservation equations for two-phase flows", Progress in Nuclear Energy, 80, 2015, 90-101
  - G. Roth and F. Aydogan, "Development of Governing Equations Based on Six Fields for the RELAP code", Nuclear Science and Engineering, Vol 182, No. 1, Jan 2016, Pg 71-82
- Chapter 4:
  - G. Roth and F. Aydogan, "Mass Closure Models for a system code based on six fields", Progress in Nuclear Energy 94 (2017), 147-161
- Chapter 5:
  - G. Roth and F. Aydogan, "Momentum and energy closure relationships for two-phase flow six-field model", Submitted for publication
- Chapter 6:
  - G. Roth, G. Mesina, F. Aydogan, "Solution of governing equations for six-field system code", Proceedings of the ASME 2017 Power and Energy Conference, June 26-30, 2017, Charlotte, NC, USA
  - G. Roth, G. Mesina, F. Aydogan, "Solving the governing equations for a six field system code", Submitted for publication

CHAPTER 2

Current System Code Capabilities

This chapter consists of the results of a literature search into the capabilities of current system codes. It provides detailed comparisons of several codes to include the governing equations, closure relationships, limitations and solution methods for codes including ATHLET, CATHARE, RELAP, and TRAC.

2.1 Conservation Models

Conservation equations vary between the system codes, but the basic equations for conservation of mass, momentum and energy are consistent. The mass, momentum, and energy conservation equations can be written for each phase in the system. Doing this for the vapor and liquid phases results in the what is referred to as the six-equation model. Figure 2.1 shows a simplified characteristic hydraulic system and illustrates the challenges in modeling two-phase hydrodynamic systems. The complexity can be demonstrated by considering the exchange of mass, momentum, and energy between the phases shown in Figure 2.1. Although the system depicted in Figure 2.1 is simplified, more complex flow regimes are often modeled by system codes, and will be addressed later.

The interactions between the liquid phase and the vapor phase take several forms. Droplet entrainment is one method for mass transfer between the liquid and vapor phase. Liquid droplet entrainment is due to:

- Interactions with hydraulic structures (such as rector fuel bundle spacer grids)
- Viscous effects (droplets "breaking off" into the vapor flow)

Droplets are re-entrained when they impact the liquid/vapor interface or coalesce into larger droplets that form a large enough volume to no longer be considered droplets. The vapor phase may also be entrained in the liquid phase in the form of bubbles by similar mechanisms.

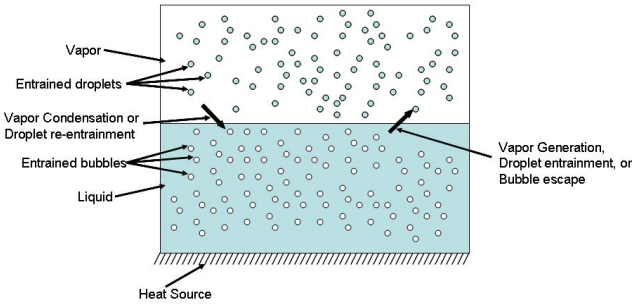

Figure 2.1: Generic Two-Phase System

Different shapes and sizes of bubbles must be represented by different governing equations in reality, but modeling simplifications use just a few equations to represent them. Mass exchange between the phases is also accomplished by converting one phase to the other. This exchange of mass is accompanied by energy transfer, which is added to or removed from the liquid or vapor phase by:

- Direct contact with the container walls
- Radiation heat transfer from the liquid or wall surface to the entrained droplets
- Convection to/from the vapor phase at the phase interface or at the bubble or droplet interfaces

These heat transfer mechanisms can increase the temperature in the liquid phase until it reaches the saturation temperature, and the liquid begins to transition to the vapor phase. The same is true in reverse, where the vapor phase can condense into liquid. This can occur at the liquid/vapor interface, as well as at droplet or bubble interfaces. The droplets and bubbles will grow or shrink, depending on the direction of heat flow. The conservation equations used by the system codes attempt to model the exchange of mass and energy in the two-phase system. The RELAP5 codes (MOD3, MOD3.3, 3D, SCDAP) model two phases (liquid and vapor) for each of the three conservation equations. The resulting six equations give this model its name; the "six-equation model". The conservation equations for one-dimensional components are shown in the following sections.

2.1.1 RELAP5 Governing Equations

1D Component Mass Conservation

$$\frac{\partial}{\partial t}\left(\alpha_k \rho_k\right) + \frac{1}{A}\frac{\partial}{\partial x}\left(\alpha_k \rho_k v_k A\right) = \Gamma_k \tag{2.1}$$

Where the subscript k indicates the phase, either vapor (g) or liquid (f). The first term on the left-hand side of Equation 2.1 is the time rate of change of the mass of phase k. The second term is the change in mass of phase k due to the mass entering or leaving the control volume. The Γ_k is the volumetric mass exchange rate of phase k. The mass conservation equation formulation does not consider mass sources or sinks. This results in a requirement that the mass lost from one phase must be acquired by the other. Thus, $\Gamma_f = -\Gamma_g$. The momentum equation has been written in "area-average" notation. RELAP assumes that the total mass transfer can be partitioned into contributions from mass transfer at the vapor/liquid interface near the wall (Γ_w) and interfacial mass transfer in the bulk fluid (Γ_{ig})

1D Component Momentum Conservation

$$\begin{gathered}\alpha_k \rho_k A \frac{\partial v_k}{\partial t} + \frac{1}{2}\alpha_k \rho_k A \frac{\partial v_k^2}{\partial x} = -\alpha_k A \frac{\partial P}{\partial x} + \alpha_k \rho_k B_x A - \\ \left(\alpha_k \rho_k A\right) FW_k \cdot v_k + \Gamma_k A \left(v_{kI} - v_k\right) - \left(\alpha_k \rho_k A\right) FI_k \cdot \left(v_k - v_r\right) - \\ C \alpha_k \alpha_r \rho_m A \left[\frac{\partial \left(v_k - v_r\right)}{\partial t} + v_r \frac{\partial v_k}{\partial x} - v_k \frac{\partial v_r}{\partial x}\right]\end{gathered} \tag{2.2}$$

Note that the momentum conservation equation is written in terms of momentum per unit volume using the velocity variables v_g and v_f. The spatial variation of the momentum terms is expressed in terms of v_g^2 and v_f^2. The momentum conservation written this way can be reduced to the Bernoulli equation for steady, incompressible, and frictionless flow.

The momentum equation has a reduced effect on the solution when compared to the mass and energy equations. This is due to the fact that reactor flows are dominated by large

sources and sinks of momentum (pumps and abrupt area changes).

This formulation of momentum conservation assumes that the phasic pressures are equal, and that the interfacial pressure is the same as the phasic pressures (except for stratified flows). Phasic viscous stresses are neglected, but are considered at the interface. Interface force terms include both the viscous and pressure stresses. Wall forces are assumed to be modeled by the variable area momentum flux formulation.

1D Component Energy Conservation

$$\frac{\partial}{\partial t}\left(\alpha_k \rho_k U_k\right) + \frac{1}{A}\frac{\partial}{\partial x}\left(\alpha_k \rho_k U_k v_k A\right) = -P\frac{\partial \alpha_k}{\partial t} - \frac{P}{A}\frac{\partial}{\partial x}\left(\alpha_k v_k A\right) + Q_{wk} + Q_{ik} + \Gamma_{ig} h_k^* + \Gamma_w h_k^{'} + DISS_k \tag{2.3}$$

The energy conservation model implemented in RELAP simplifies the calculation by neglecting Reynolds heat flux, interfacial energy storage and internal phasic heat transfer. The conservation equations are written for the liquid and vapor phases only; no distinction is made for droplets or bubbles. Thus, the conservation equations as implemented in the RELAP5 series of codes model the exchange of mass, energy, and momentum between the phases, but do not explicitly model the entrained droplets or vapor bubbles. Changes in droplet and bubble sizes are not captured by this limited model, except by a change in the void fraction reported for the control volume in question.

3D Component Conservation equations

The RELAP5-3D code includes a multidimensional component that was developed to better model the multi-dimensional features in reactor systems. The multi-dimensional effects are important in the vessel (core and downcomer regions) and the steam generator components. The multidimensional component can model one, two or three-dimensional arrays of volumes with internal junctions to connect the volumes. These volumes can be arranged in Cartesian or cylindrical geometries. The mass, momentum, and energy equations are documented

in the RELAP5-3D manual [22]. Mass conservation in the multidimensional component is computed as shown in Equation 2.4 for phase k (liquid or vapor).

$$V\left(\rho\frac{\partial\alpha_k}{\partial t}+\alpha_k\frac{\partial\rho}{\partial t}\right)+\sum_i A_i\alpha_i\rho_i v_{in}=V\Gamma \tag{2.4}$$

where α_i and α_V are defined:

$$\alpha_i=\frac{A_{ki}}{A_i} \tag{2.5}$$

$$\alpha_k=\frac{V_k}{V} \tag{2.6}$$

The conservation of momentum is computed as shown in Equation 2.7.

$$\rho_k\left(\frac{\partial\overline{v_k}}{\partial t}+\overline{v_k}\cdot\nabla\overline{v_k}\right)=-\nabla P+\overline{\sigma}+\rho_k\overline{f} \tag{2.7}$$

Internal energy conservation is computed as shown in Equation 2.8.

$$\begin{aligned}V\left(\rho U\frac{\partial\alpha_k}{\partial t}+\alpha_k U\frac{\partial\rho}{\partial t}+\alpha_k\rho\frac{\partial U}{\partial t}\right)+\sum_i A_i\alpha_i\rho_i U_i v_{in}=\\ -\int_{S_c}\vec{q}\cdot\vec{n}\,dA+Q_iV-P\left[\frac{\partial\alpha_k V}{\partial t}+\sum_i A_i\alpha_i v_{in}\right]\\ +h_i\Gamma V+D_sV+RV\end{aligned} \tag{2.8}$$

Noncondensable Gas and Dissolved Solutes

Reactor systems are not always limited to just two phases. Often, solutes are dissolved in the reactor coolant (e.g. boron to aid in reactor control). Noncondensable gasses (e.g. nitrogen) are also frequently present as part of the vapor phase or in solution with the liquid phase.

The effects of these added phases on the flow field are modeled by the RELAP5 codes with some simplifying assumptions. It is assumed that:

- The noncondensable gas or the solute are at the same temperature and pressure as their surroundings
- That the solute or noncondensable gasses do not affect the properties of the liquid or vapor, and
- That the solute or gas moves at the same velocity as the fluid

These assumptions simplify the modeling of the additional phases to a single mass conservation equation for each phase. If the assumptions can be considered valid, it is not necessary to add energy and momentum conservation equations to track the dissolved solute and gasses.

The RELAP5 codes add two mass conservation equations. One (Equation 2.9) is used to track the mass of dissolved solute in the liquid coolant (usually boron), and the other (Equation 2.11) is used to track noncondensable gases in the vapor phase. If more than one type of noncondensable gas is present, Equation 2.11 can be modified to include an additional term, X_{ni} in each paranthetical term. X_{ni} is the noncondensable gas phase for the i-th noncondensable species. The additional terms in Equation 2.11 allow for a separate mass conservation equation for each additional noncondensable gas. In this way, RELAP can account for more than one noncondensable gas in the model.

$$\frac{\partial \rho_b}{\partial t} + \frac{1}{A}\frac{\partial (\rho_b v_f A)}{\partial x} = 0 \tag{2.9}$$

$$\rho_b = \alpha_f \rho_l C_b = \rho_m \left(1 - X\right) C_b \tag{2.10}$$

$$\frac{\partial}{\partial t}\left(\alpha_g \rho_g X_n\right) + \frac{1}{A}\frac{\partial}{\partial x}\left(\alpha_g \rho_g X_n v_g A\right) = 0 \tag{2.11}$$

$$X_n = \frac{\sum_{i=1}^{N} M_{ni}}{\sum_{i=1}^{N} M_{ni} + M_s} = \frac{M_n}{M_n + M_s} \tag{2.12}$$

Although the assumptions of the noncondensable gas conditions do not require a separate energy conservation equation for the gas, the liquid energy equation must still be modified

when noncondensable gasses are modeled. The sensible heat transfer rate per unit volume (Q_{gf}) is subtracted from the energy balance for the vapor phase, and added to the liquid energy balance equation. This sensible heat transfer rate is the heat transfer at the noncondensable gas-liquid interface. This term must be included since the interfacial terms use a saturation temperature that is based on the bulk vapor partial pressure instead of the saturation temperature based on the local vapor partial pressure. The sensible heat transfer rate is computed as shown in Equation 2.13.

$$Q_{gf} = \left(\frac{P - P_s}{P}\right) H_{gf} \left(T_g - T_f\right) + \frac{P_n}{P} H_{gf} \left(T_g - T_f\right) \tag{2.13}$$

The interfacial heat transfer and mass transfer terms (Q_{ig} and Γ_g) also change slightly when noncondensable gasses are present.

Radionuclide Tracking

RELAP5-3D and RELAP5-3D/SCDAP include a third additional mass balance equation to track radionuclides. The radionuclide model assumes:

- That the fluid properties (liquid or vapor/gas) are not affected by the presence of the radionuclides,
- Energy absorbed by the fluid from decay of the radionuclides is negligible,
- Radionuclides are well-mixed with the transporting phase, implying that they are transferred at the phase velocity.

As with the noncondensable gasses, these assumptions reduce the required conservation equations. Mass conservation for the radionuclides is the only required continuity equation. The mass conservation equation for the radionuclide specie is:

$$\frac{\partial C}{\partial t} + \frac{1}{A} \frac{\partial}{\partial x} \left(CvA\right) = S \tag{2.14}$$

Number density (C) may be converted to the mass density using Equation 2.15.

$$\rho = \frac{C \cdot Mw}{N_a} \tag{2.15}$$

2.1.2 RELAP-7 Governing Equations

RELAP-7 is currently under development at the Idaho National Laboratory (INL) [23, 24]. It has recently added some two-phase functionality. The work is ongoing to fully incorporate and qualify governing equations for the vapor phase, using methods outlined in Reference [25]. The six equations used for the RELAP-7 mass, momentum, and energy balances are similar to those previously described for the RELAP5 series of codes, with the differences noted. An additional equation is included to calculate the volume fraction. This section presents the set of RELAP-7 governing equations documented in Reference [24].

Mass Conservation

The mass conservation equations for RELAP-7 are shown below. Note the conspicuous inclusion of the interfacial area term (A_{int}) that is not included in the RELAP5 formulation. In addition, the mass balance equations presented here are not volume-averaged, as was done with the RELAP5 formulation.

$$\frac{\partial \alpha_l \rho_l A}{\partial t} + \frac{\partial \alpha_l \rho_l u_l A}{\partial x} = -\Gamma A_{\text{int}} A \tag{2.16}$$

$$\frac{\partial \alpha_g \rho_g A}{\partial t} + \frac{\partial \alpha_g \rho_g u_g A}{\partial x} = \Gamma A_{\text{int}} A \tag{2.17}$$

As before, the first term on the left-hand size of the equation is the mass rate of change. The second term represents the mass crossing the volume boundary, and the right-hand side of the equation is the volumetric mass exchange rate.

Momentum Conservation

The momentum balance equations for liquid and vapor are shown here. Note the additional terms for interfacial area, pressure, and velocity.

$$\begin{aligned}\frac{\partial \alpha_l \rho_l u_l A}{\partial t} + \frac{\partial \alpha_l A\left(\rho_l u_l^2 + p_l\right)}{\partial x} = p_{\text{int}} A \frac{\partial \alpha_l}{\partial x} + \\ p_l \alpha_l \frac{\partial A}{\partial x} + A\lambda\left(u_g - u_l\right) - \Gamma A_{\text{int}} u_{\text{int}} A - \\ f_l \alpha_l \rho_l \left(u_l - u_w\right)^2 (\pi A)^{\frac{1}{2}} - f_l^{'} \frac{1}{2} \rho_l \left(u_l - u_{\text{int}}\right)^2 A_{\text{int}} A + \alpha_l \rho_l \vec{g} \cdot \hat{n}_{axis} A\end{aligned} \tag{2.18}$$

The first two terms of Equation 2.18 are the same as those from Equation 2.3. The third and fourth terms make up the pressure gradient from Equation 2.3. The next term $(A\lambda\left(u_g - u_l\right))$ is a velocity relaxation term, and the next term accounts for interfacial mass transfer effects. The next two terms incorporate interphase viscous drag, and the last term includes gravity forces. The components of Equation 2.19 below follow the same pattern.

$$\begin{aligned}\frac{\partial \alpha_g \rho_g u_g A}{\partial t} + \frac{\partial \alpha_g A\left(\rho_g u_g^2 + p_g\right)}{\partial x} = p_{\text{int}} A \frac{\partial \alpha_g}{\partial x} + \\ p_g \alpha_g \frac{\partial A}{\partial x} + A\lambda\left(u_l - u_g\right) - \Gamma A_{\text{int}} u_{\text{int}} A - \\ f_g \alpha_g \rho_g \left(u_g - u_w\right)^2 (\pi A)^{\frac{1}{2}} - f_g^{'} \frac{1}{2} \rho_g \left(u_g - u_{\text{int}}\right)^2 A_{\text{int}} A + \alpha_g \rho_g \vec{g} \cdot \hat{n}_{axis} A\end{aligned} \tag{2.19}$$

Energy Conservation

The total energy balance equations are shown below. Notice again the inclusion of the interfacial terms that are not present in the RELAP5 formulation.

$$\begin{aligned}\frac{\partial \alpha_l \rho_l E_l A}{\partial t} + \frac{\partial \alpha_l u_l A \left(\rho_l E_l + p_l\right)}{\partial x} = p_{\text{int}} u_{\text{int}} A \frac{\partial \alpha_l}{\partial x} - \overline{p}_{\text{int}} A \mu \left(p_l - p_g\right) + \\ \overline{u}_{\text{int}} A \lambda \left(u_g - u_l\right) + \Gamma A_{\text{int}} \left(\frac{p_{\text{int}}}{\rho_{\text{int}}} - H_{l\ \text{int}}\right) A + A_{\text{int}} h_{Tl} \left(T_{\text{int}} - T_l\right) A + \\ \alpha_l h_{lw} \left(T_w - T_l\right) \left[4\pi A + \left(\frac{\partial A}{\partial x}\right)^2\right]^{\frac{1}{2}} + \alpha_l \rho_l u_l \vec{g} \cdot \hat{n}_{axis} A\end{aligned} \tag{2.20}$$

As with the momentum conservation equations, the first two terms are to capture the same effects as the first two terms used in the RELAP5 formulation (Equation 2.1.1. The third term in Equation 2.20 captures the pressure effects that are addressed by the fourth term in Equation 2.1.1. The fourth term in the RELAP-7 formulation is a pressure relaxation term. The fifth term is a velocity relaxation term. Interfacial mass transfer is captured by the sixth term, and the seventh term models direct interfacial heat transfer. Simple wall heat transfer is modeled by the eighth term, and gravity effects are again modeled in the ninth term. Similar explanations apply for the terms in Equation 2.21.

$$\begin{aligned}\frac{\partial \alpha_g \rho_g E_g A}{\partial t} + \frac{\partial \alpha_g u_g A \left(\rho_g E_g + p_g\right)}{\partial x} = p_{\text{int}} u_{\text{int}} A \frac{\partial \alpha_g}{\partial x} - \\ \overline{p}_{\text{int}} A \mu \left(p_g - p_l\right) + \overline{u}_{\text{int}} A \lambda \left(u_l - u_g\right) - \Gamma A_{\text{int}} \left(\frac{p_{\text{int}}}{\rho_{\text{int}}} - H_{g\ \text{int}}\right) A + \\ A_{\text{int}} h_{Tg} \left(T_{\text{int}} - T_g\right) A + \alpha_g h_{gw} \left(T_w - T_g\right) \left[4\pi A + \left(\frac{\partial A}{\partial x}\right)^2\right]^{\frac{1}{2}} + \\ \alpha_g \rho_g u_g \vec{g} \cdot \hat{n}_{axis} A\end{aligned} \tag{2.21}$$

Volume Fraction

This is the seventh equation in the "seven-equation model". This allows for the computation of the volume fraction to be used in the six-equation model. These equations allow for the

use of a volume fraction computed in parallel with the rest of the governing equations and is dependent on time and location. Note that the first term on the right hand side of the equation provides pressure relaxation. The second term on the right-hand side is simply the interfacial mass transfer effect.

$$\frac{\partial \alpha_l A}{\partial t} + u_{\text{int}} A \frac{\partial \alpha_l}{\partial x} = A\mu \left(p_l - p_g\right) - \frac{\Gamma A_{\text{int}} A}{\rho_{\text{int}}} \tag{2.22}$$

$$\frac{\partial \alpha_g A}{\partial t} + u_{\text{int}} A \frac{\partial \alpha_g}{\partial x} = A\mu \left(p_g - p_l\right) - \frac{\Gamma A_{\text{int}} A}{\rho_{\text{int}}} \tag{2.23}$$

Only one of these equations is needed for two-phase flow, since the volume fractions in two-phase flows sum to 1. For single-phase flows, the appropriate equation (vapor or liquid) should be used.

2.1.3 TRACE Governing Equations

TRACE also uses the six-equation model, solving the conservation of mass, momentum, and energy equations for each phase (liquid or vapor) in the coolant. As with the RELAP codes, the TRACE fluid model makes no distinction between droplets or bubbles.

Mass Conservation

$$\frac{\partial [(1-\alpha_g)\,\rho_l]}{\partial t} + \nabla \cdot \left[(1-\alpha_g)\,\rho_l \vec{V}_l\right] = -\Gamma_g \tag{2.24}$$

$$\frac{\partial (\alpha_g \rho_v)}{\partial t} + \nabla \cdot \left[\alpha_g \rho_v \vec{V}_g\right] = \Gamma_g \tag{2.25}$$

Note the similarities between Equations 2.24, 2.25, and Equation 2.1. The structure of the RELAP equation is similar to that of the TRACE code, and the terms in the TRACE

equations capture the same model characteristics that are described by the RELAP equation. The TRACE formulation uses a single variable for the generation rate (interfacial mass transfer), which results in the negative sign seen in 2.24. This is reproduced by the RELAP formulation when Equation 2.1 is written for both phases and then making the substitution of $\Gamma_f = -\Gamma_g$. The representation of phase volume fraction is done in much the same way. The TRACE formulation uses a single variable for (in this case) vapor volume fraction (α_g), while the RELAP formulation uses a variable representing void fraction of each phase. The void fraction of one phase can be written in terms of the void fraction of the other phase:

$$\alpha_f = 1 - \alpha_g \tag{2.26}$$

If Equation 2.1 is written for both phases and then Equation 2.26 is substituted into those equations, a formulation that is very similar to TRACE is obtained. There are two significant differences between the RELAP and TRACE formulations of the mass conservation equations.

The first is that RELAP casts the time and volume averaged equations in area average notation. TRACE uses volume and time averaging alone. The second difference is that RELAP is shown to apply to a single coordinate direction (indicated by the partial derivative with respect to x), while the TRACE equation is formulated for three dimensions (as indicated by the ∇ terms). Although the formulation allows for three dimensions, in actual application, most of the TRACE components are one-dimensional.

Both system codes average the flow over the cross-section of the flow channel. This averaging scheme makes it possible to model flow changes resulting from changes in cross sectional area, but it does not allow for flow structure effects to be captured. Thus, recirculation zones are not modeled using this technique.

Momentum Conservation

$$\frac{\partial\left[(1-\alpha_g)\,\rho_l\vec{V}_l\right]}{\partial t}+\nabla\cdot(1-\alpha_g)\,\rho_l\vec{V}_l\vec{V}_l+ \\ (1-\alpha_g)\,\nabla P=\vec{f}_i+\vec{f_{wl}}+(1-\alpha_g)\,\rho_l\vec{g}-\Gamma\vec{V}_i \tag{2.27}$$

$$\frac{\partial\left[\alpha_g\rho_g\vec{V}_g\right]}{\partial t}+\nabla\cdot\alpha_g\rho_g\vec{V}_g\vec{V}_g+\qquad\alpha_g\nabla P=-\vec{f}_i+\vec{f_{wg}}+\alpha_g\rho_g\vec{g}+\Gamma\vec{V}_i \tag{2.28}$$

In the above equations, f_i is the force per unit volume due to shear at the phase interface, f_{wl} is the wall shear force per unit volume acting on the liquid, and f_{wg} is the shear force per unit volume acting on the gas. The method for computing the force terms in shown in the following equations.

$$f_i=C_{D,i}\left(\vec{V}_g-\vec{V}_l\right)|\vec{V}_g-\vec{V}_l| \tag{2.29}$$

$$f_{wg}=-C_{wg}\vec{V}_g|\vec{V}_g| \tag{2.30}$$

$$f_{wl}=-C_{wl}\vec{V}_l|\vec{V}_l| \tag{2.31}$$

The TRACE momentum conservation formulations use Reynolds averaging and split the velocities into mean and fluctuating contributions, in much the same way as is often done with turbulence flow modeling. The equations shown here do not include all the terms and notation from the classic turbulence formulation since contributions from the Reynolds stress and many of the right-hand side terms in the energy and momentum conservation equations are captured by engineering correlations.

There are differences between the formulation for the momentum conservation between the RELAP codes (Equation 2.2) and the formulation used in TRACE. These differences stem from the averaging scheme, and the overall formulation. The RELAP code uses a

formulation that reduces to a simplified Bernoulli equation. TRACE has modeled the momentum conservation using similar techniques to those used in common turbulence modeling schemes.

Energy Conservation

$$\frac{\partial[(1-\alpha_g)\,\rho_l\,(e_l+V_l^2/2)]}{\partial t}+\nabla\cdot\left[(1-\alpha_g)\,\rho_l\left(e_l+\frac{P}{\rho_l}+\frac{V_l^2}{2}\right)\vec{V_l}\right]= q_{il}+q_{wl}+q_{dl}+(1-\alpha_g)\,\rho_l\vec{g}\cdot\vec{V_l}-\Gamma h_l^{'}+\left(\vec{f_i}+\vec{f_{wl}}\right)\cdot\vec{V_l} \tag{2.32}$$

$$\frac{\partial\left[\alpha_g\rho_g\left(e_g+V_g^2/2\right)\right]}{\partial t}+\nabla\cdot\left[\alpha_g\rho_g\left(e_g+\frac{P}{\rho_g}+V_g^2/2\right)\vec{V_g}\right]= q_{ig}+q_{wg}+q_{dg}+\alpha_g\rho_g\vec{g}\cdot\vec{V_g}+\Gamma h_v^{'}+\left(-\vec{f_i}+\vec{f_{wg}}\right)\cdot\vec{V_g} \tag{2.33}$$

The $\Gamma h_v^{'}$ and $\Gamma h_l^{'}$ terms in the energy equation are the product of the mass transfer and the applicable interface stagnation enthalpy. The terms represent the energy that moves with the mass transfer at the interface. The only portions of the work terms that are kept in the energy equations are those that change the bulk kinetic energy. Heating due to viscous effects is not considered, except when included as part of a special pump model to capture heating by the pump rotor. These contributions are included through the source term q_{dl}

Noncondensable Gas and Dissolved Solutes

Like RELAP, TRACE has the capability to model noncondensable gasses with the assumptions that the gasses move at the same velocity and have the same temperature as the vapor/gas phase. These assumptions mean that with the inclusion of a single mass conservation equation, the effects of noncondensable gasses can be included. An additional mass conservation equation must be provided for each additional gas. Dissolved boron can also be tracked in the TRACE code, subject to the assumption that the boron mass does not affect the liquid momentum equation, and it does not affect the thermodynamic or other physical

properties of the liquid. These assumptions are similar to those used in the RELAP code. Boron tracking is enabled by use of a model for solubility of boric acid. Additional solutes (besides boron) could be modeled if the user provides a different solubility curve (through a user option).

2.1.4 WCOBRA/TRAC-TF2 Governing Equations

The WCOBRA/TRAC-TF2 code uses a six-equation model for all 1D components, with two additional equations to capture the mass conservation of a noncondensable gas phase and concentration of a solute. The 1D components include pipes, pumps and valves [3]. The vessel (3D) component uses a slightly different formulation that considers the two-phase flow differently than in the 1D components. The 3D component uses a two-fluid, three-field formulation of the conservation equations [3]. The conservation equations for both component types are discussed here.

1D Component Mass Conservation

$$\frac{\partial(\alpha_k \rho_k)}{\partial t} + \nabla\left[(\alpha_k \rho_k)\cdot \underline{u}_k\right] = \Gamma_k \tag{2.34}$$

When written for each phase, Equation 2.34 is identical to the TRACE Equations 2.24 and 2.25. The first term of Equation 2.34 represents the time rate of change of the mass, the second term is the rate of mass efflux from the volume, and the Γ_k term is the rate of mass transfer to phase k from the other phases.

1D Component Momentum Conservation

$$\begin{aligned}\frac{\partial \underline{u}_l}{\partial t} + \underline{u}_l \cdot \nabla \underline{u}_l = -\frac{1}{\rho_l}\cdot \nabla P - \frac{C_{D,i}}{\alpha_l \rho_l}\cdot |\underline{u}_l - \underline{u}_g|\cdot \left(\underline{u}_l - \underline{u}_g\right) + \\ \frac{\Gamma^-}{\alpha_l \rho_l}\cdot \left(\underline{u}_l - \underline{u}_g\right) - \frac{C_{wl}}{\alpha_l \rho_l}\cdot |\underline{u}_l|\cdot \underline{u}_l - \underline{g}\cdot \cos(\theta)\end{aligned} \tag{2.35}$$

$$\frac{\partial \underline{u}_g}{\partial t} + \underline{u}_g \cdot \nabla \underline{u}_g = -\frac{1}{\rho_g} \cdot \nabla P - \frac{C_{D,i}}{\alpha_g \rho_g} \cdot |\underline{u}_g - \underline{u}_l| \cdot \left(\underline{u}_g - \underline{u}_l\right) - \frac{\Gamma^+}{\alpha_g \rho_g} \cdot \left(\underline{u}_g - \underline{u}_l\right) - \frac{C_{wg}}{\alpha_g \rho_g} \cdot |\underline{u}_g| \cdot \underline{u}_g - \underline{g} \cdot \cos(\theta) \tag{2.36}$$

Equations 2.35 and 2.36 do not immediately resemble Equations 2.27 and 2.28 used in TRACE. If α and ρ_g are assumed to be constant in time and space, they can be moved out of the derivative terms in the TRACE equations, which can be rearranged to resemble the equations in

WCOBRA/TRAC-TF2. Recall from Equations 2.29, 2.30 and 2.31 that the force terms f can be written in terms of the drag coefficients. When these substitutions are made in the TRACE equations, the formulation shown above becomes apparent.

1D Component Energy Conservation

$$\frac{\partial(\alpha_g \rho_g e_g + \alpha_l \rho_l e_l)}{\partial t} + \nabla \left[(\alpha_g \rho_l e_l) \cdot \underline{u}_g + (\alpha_l \rho_l e_l) \cdot \underline{u}_l\right] = -P \cdot \left[\nabla \left(\alpha_g \cdot \underline{u}_g + \alpha_l \cdot \underline{u}_l\right)\right] + q_{wg} + q_{wl} + q_{dg} + q_{dl} \tag{2.37}$$

$$\frac{\partial(\alpha_g \rho_g e_g)}{\partial t} + \nabla \left[(\alpha_g \rho_g e_g) \cdot \underline{u}_g\right] = -P \cdot \left[\frac{\partial \alpha_g}{\partial t} + \nabla \left(\alpha_g \cdot \underline{u}_g\right)\right] + q_{wg} + q_{dg} - (q_{ig} + q_{gl}) + \Gamma \cdot h_v^* \tag{2.38}$$

The energy equations above have a different formulation than the TRACE Equations (2.32, 2.33). Equation 2.37 is formulated for a mixture of liquid and vapor, while Equation 2.32 is formulated for liquid only. Equation 2.38 is formulated for a gas energy balance.

Noncondensable Gas and Dissolved Solutes

Reactor system coolant can be made up of more than a simple fluid. Often, noncondensable gases are introduced by radiation effects or from pressurized equipment utilizing inert gas. In addition, dissolved components (such as boron) can be used to balance the chemistry of the reactor coolant or control reactivity. These additional coolant components are modeled using separate governing equations within the code. These equations are discussed below.

Noncondensable Mass Conservation As with the RELAP code, the noncondensable gas is assumed to move at the same velocity and be at the same temperature as the vapor that is present in the system. This eliminates the need for the momentum and energy conservation equations for the noncondensable gases. The WCOBRA/TRAC-TF2 code assumes that the noncondensable gas is air, and uses corresponding thermal properties. The user is also able to select hydrogen or helium as an alternative.

$$\frac{\partial(\alpha_g \rho_a)}{\partial t} + \nabla \left[(\alpha_g \rho_a) \cdot \underline{u}_g \right] = 0 \tag{2.39}$$

Dissolved Solid Conservation It is common for reactor systems to include boron salts or other dissolved solutes to maintain desirable reactor coolant chemistry or provide additional reactivity control. During normal operation, the solute can come out of solution, dependent upon coolant temperatures. When the solute precipitates out of solution, it will plate out on the internal surfaces of the coolant piping. This changes the hydrodynamic performance of the reactor. The fluid properties of the coolant are also affected, though slightly, by the presence of the dissolved solute. The WCOBRA/TRAC-TF2, TRAC-M and TRACE solute models do not capture the hydrodynamic effects of the presence of the solute. However, the code does track the solubility curve, and maintains the concentration of solute at or

below the solubility limit, which is affected by temperature. If more fluid enters the cell, the code assumes that the solute that has plated out in that location instantly dissolves to the solubility limit. The user can specify a mass/reactivity-coefficient table to capture the effects of boron concentration on the reactivity of the reactor. Since the hydrodynamics are not affected by the presence of the solute, users are able to use the solute variable as a tag to track fluid from a specific source throughout the coolant system.

$$\frac{\partial(\alpha_l m \rho_l)}{\partial t} + \nabla \left[(\alpha_l m \rho_l) \cdot \underline{u}_l\right] = S_m \tag{2.40}$$

The 3D vessel component in WCOBRA/TRAC-TF2 includes a three-field representation of two-phase flow. The three fields are: 1) combined gas/vapor, 2) continuous liquid, and 3) entrained liquid (droplet) [3]. The combined gas/vapor field includes noncondensable gasses as well as vapor resulting from boiling. The entrained liquid field captures the droplets that may be entrained in the vapor/gas flow. The conservation equations for the three-field model are shown below. There is a single energy conservation equation for the liquid film and liquid droplet field. This implies the assumption that the liquid droplet and liquid film are at the same temperature.

3D Component Mass Conservation

The 3-D mass conservation equations are more detailed than those that were used for 1-D flows. These equations can be grouped into the following three sections:

Combined-Gas Field (Vapor Field)

$$\frac{\partial}{\partial t}\left(\alpha_g \rho_g\right) + \nabla \cdot \left(\alpha_g \rho_g \underline{U}_g\right) = \Gamma''' \tag{2.41}$$

The 3D vapor field mass conservation equation above is the same as the 1D mass conservation Equation 2.34, except that the vapor generation rate is a per unit volume quantity in the 3D equation.

$$\frac{\partial}{\partial t}\left(\alpha_l \rho_l\right) + \nabla\cdot\left(\alpha_l \rho_l \underline{U}_l\right) = -\Gamma_l^{'''} - S_{ent}^{'''} = -\left(1-\eta\right)\Gamma^{'''} - S_{ent}^{'''} \tag{2.42}$$

The 3D components include an additional liquid field to model the entrained liquid droplets. The additional liquid field requires that a second liquid mass conservation equation be developed. This equation represents the continuous liquid, and includes extra terms on the right-hand side of the equation to reduce the liquid generation rate ($\Gamma_l^{'''}$) by the average rate of entrainment per unit volume ($S_{ent}^{'''}$), since the entrained liquid reduces the volume of the continuous liquid.

Entrained Liquid Field

$$\frac{\partial}{\partial t}\left(\alpha_e \rho_l\right) + \nabla\cdot\left(\alpha_e \rho_l \underline{U}_e\right) = -\Gamma_e^{'''} + S_{ent}^{'''} = -\eta\Gamma^{'''} + S_{ent}^{'''} \tag{2.43}$$

As in Equation 2.42, this formulation is very similar to the 1D mass conservation equation for liquid. In this case, the entrainment rate per unit volume is added to the liquid generation rate, since this increases the volume of entrained liquid.

Noncondensable Gas Field The noncondensable gas momentum conservation Equation (2.44) for the 3D component is identical to that used for 1D components.

$$\frac{\partial}{\partial t}\left(\alpha_g \rho_{NC}\right) + \nabla\cdot\left(\alpha_g \rho_{NC} \underline{U}_g\right) = 0 \tag{2.44}$$

3D Component Momentum Conservation

The three equations in this section are the momentum conservation equations for the 3D component. As for the formulation of the 3D mass conservation, the 3D component includes a third equation for the entrained liquid momentum conservation. Note that the equations shown here are similar to the 1D momentum conservation equations, but the 3D formulation includes terms to balance the momentum lost by the entrainment of water droplets in the vapor phase. The interfacial forces are also expressed as variables here where the 1D equations showed the forces as an expression. The 3-D momentum equations can be grouped into the following categories based on the flow field:

Combined-Gas Field (Vapor Field)

$$\begin{aligned}\frac{\partial}{\partial t}\left(\alpha_g \rho_g \underline{U}_g\right) + \nabla\cdot\left(\alpha_g \rho_g \underline{U}_g^2\right) = -\alpha_g \nabla P + \alpha_g \rho_g \vec{g} + \\ \nabla\cdot\left[\alpha_g\left(\underline{\underline{\sigma}}_g\right)\right] - \underline{\tau}_{w,g}''' - \underline{\tau}_{i,gl}''' - \underline{\tau}_{i,ge}''' + \Gamma''' \underline{U}_r\end{aligned} \tag{2.45}$$

Continuous liquid field

$$\begin{aligned}\frac{\partial}{\partial t}\left(\alpha_l \rho_l \underline{U}_l\right) + \nabla\cdot\left(\alpha_l \rho_l \underline{U}_l^2\right) = -\alpha_l \nabla P + \alpha_l \rho_l \vec{g} + \\ \nabla\cdot\left[\alpha_l\left(\underline{\underline{\sigma}}_l\right)\right] - \underline{\tau}_{w,l} + \underline{\tau}_{i,gl} - (1-\eta)\,\Gamma''' \underline{U}_\Gamma - S_{ent}''' \underline{U}_{Se}\end{aligned} \tag{2.46}$$

Entrained Liquid Field

$$\begin{aligned}\frac{\partial}{\partial t}\left(\alpha_e \rho_l \underline{U}_e\right) + \nabla\cdot\left(\alpha_e \rho_l \underline{U}_e^2\right) = -\alpha_e \nabla P + \alpha_e \rho_l \vec{g} - \\ \underline{\tau}_{w,e} + \underline{\tau}_{i,ge} - \eta\Gamma''' \underline{U}_\Gamma + S_{ent}''' \underline{U}_{Se}\end{aligned} \tag{2.47}$$

3D Component Energy Conservation

The 3D formulation of the three-field energy conservation equations is shown in this section. Note that for this derivation, the third field (entrained liquid) is included in a single equation with the continuous liquid field. Thus, there are only two energy balance equations for the 3D component:

Combined-Gas Field

$$\frac{\partial}{\partial t}\left(\alpha_g \rho_g H_g\right) + \nabla\cdot\left(\alpha_g \rho_g H_g \underline{U}_g\right) = -\nabla\cdot\left[\alpha_g\left(\underline{q}_g\right)\right] + \Gamma''' H_g^i + q_{i,g}''' + q_{l,NC}''' + Q_{w,g}''' + \alpha_g \frac{\partial P}{\partial t} \tag{2.48}$$

Liquid Fields

$$\frac{\partial}{\partial t}\left[\left(\alpha_l + \alpha_e\right)\rho_l H_l\right] + \nabla\cdot\left(\alpha_l \rho_l H_l \underline{U}_l\right) + \nabla\cdot\left(\alpha_e \rho_l H_l \underline{U}_e\right) = -\nabla\cdot\left[\alpha_g\left(\underline{q}_l + \underline{q}_l^T\right)\right] - \Gamma''' H_l^i + q_{i,l}''' + q_{l,NC}''' + Q_{w,l}''' + \left(\alpha_l + \alpha_e\right)\frac{\partial P}{\partial t} \tag{2.49}$$

2.1.5 TRAC-M Governing Equations

This system code is similar to the others already presented. The TRAC-M code has a two-fluid model for both one- and three-dimensional

components [4]. Models for the typical reactor system components (pipes, valves, pressurizers, etc.) are included in the code.

Older versions of TRAC (such as TRAC-PD2), used a simplified, five-equation model that had a single momentum equation for both liquid and vapor phases. A drift flux model was used to determine the velocity of each phase, since the solution of a single momentum equation cannot provide separate velocity results for the phases.

Mass Conservation

The TRAC-M mass conservation equations are shown below. Equation 2.50 is the mass balance for the combined gas field, and Equation 2.51 is for the liquid field.

$$\frac{\partial(\alpha\rho_v)}{\partial t} + \nabla\cdot\left(\alpha\rho_v\vec{V}_g\right) = \Gamma \tag{2.50}$$

$$\frac{\partial[(1-\alpha)\,\rho_l]}{\partial t} + \nabla\cdot\left[(1-\alpha)\,\rho_l\vec{V}_l\right] = -\Gamma \tag{2.51}$$

The TRAC-M mass conservation equations shown in this section are identical to those used in the TRACE code (2.1.3).

Momentum Conservation

The combined gas momentum conservation equation is shown in Equation 2.52. Equation 2.53 is for the liquid field.

$$\begin{aligned}\frac{\partial\vec{V}_g}{\partial t} + \vec{V}_g\cdot\nabla\vec{V}_g = &-\frac{1}{\rho_v}\nabla P - \frac{C_{D,i}}{\alpha\rho_v}\left(\vec{V}_g - \vec{V}_l\right)\\ &|\vec{V}_g - \vec{V}_l| - \frac{\Gamma^+}{\alpha\rho_v}\left(\vec{V}_g - \vec{V}_l\right) - \frac{C_{wv}}{\alpha\rho_v}\vec{V}_g|\vec{V}_g| + \vec{g}\end{aligned} \tag{2.52}$$

$$\begin{aligned}\frac{\partial\vec{V}_l}{\partial t} + \vec{V}_l\cdot\nabla\vec{V}_l = &-\frac{1}{\rho_l}\nabla P + \frac{C_{D,i}}{(1-\alpha)\,\rho_l}\left(\vec{V}_g - \vec{V}_l\right)|\vec{V}_g - \vec{V}_l|\\ &-\frac{\Gamma^-}{(1-\alpha)\,\rho_l}\left(\vec{V}_g - \vec{V}_l\right) - \frac{C_{wl}}{(1-\alpha)\,\rho_l}\vec{V}_l|\vec{V}_l| + \vec{g}\end{aligned} \tag{2.53}$$

The momentum conservation equations shown above are quite similar to those used in WCOBRA/TRAC-TF2 and described in section 2.1.4. As described in that section, the

momentum conservation equations are also very similar to those used in TRACE, though TRACE makes the substitutions that are shown in Equations 2.29, 2.30 and 2.31.

Energy Conservation

The energy conservation equations are grouped into a gas field and combined internal energy field containing both the liquid and vapor phases.

Combined Gas Field

$$\begin{aligned}\frac{\partial(\alpha\rho_g e_g)}{\partial t} + \nabla\left(\alpha\rho_g e_g \vec{V}_g\right) = -P\frac{\partial\alpha}{\partial t} - \\ P\nabla\cdot\left(\alpha\vec{V}_g\right) + q_{wg} + q_{dg} + q_{ig} + q_{gl} + \Gamma h_v^{'}\end{aligned} \tag{2.54}$$

Combined Internal Energy (Liquid and Vapor Field)

$$\begin{aligned}\frac{\partial[(1-\alpha)\,\rho_l e_l + \alpha\rho_v e_g]}{\partial t} + \nabla\left[(1-\alpha)\,\rho_l e_l \vec{V}_l + \alpha\rho_v e_g \vec{V}_g\right] = \\ -P\nabla\cdot\left[(1-\alpha)\,\vec{V}_l + \alpha\vec{V}_g\right] + q_{wl} + q_{wg} + q_{dl} + q_{dg}\end{aligned} \tag{2.55}$$

The phase-change rate (Γ) required in the above equations is evaluated using a simple energy jump relationship.

$$\Gamma = \frac{-\left(q_{ig} + q_{il}\right)}{\left(h_v^{'} - h_l^{'}\right)} \tag{2.56}$$

The energy conservation equations are very similar to those used in the WCOBRA/TRAC-TF2 code (2.1.4). The only differences are in the consideration of the volume fraction and the direction assumed for the heat transfer from the interface. The WOBRA/TRAC-TF2 formulation shows separate volume fraction variables for the liquid and combined gas fields. The WCOBRA/TRAC-TF2 formulation assumes a different direction for the vapor to interface

and vapor to liquid heat transfer. This is evident from the change in sign.

2.1.6 ATHLET Governing Equations

The ATHLET code offers two different models for hydrodynamic simulation. The first that will be discussed here is a six-equation model similar to those already presented. The second option is a five-equation model. Both models are documented in Reference [26].

Mass Conservation

Equation 2.57 is the liquid mass conservation equation. The vapor mass conservation equation is Equation 2.58. The ATHLET mass conservation equations shown here are identical to those shown in the TRACE mass conservation section (2.1.3) with the exception for the variables used.

$$\frac{\partial[(1-\alpha)\,\rho_l]}{\partial t} + \nabla\left[(1-\alpha)\,\rho_l \vec{w}_l\right] = -\psi \tag{2.57}$$

$$\frac{\partial(\alpha\rho_v)}{\partial t} + \nabla\left(\alpha\rho_v \vec{w}_v\right) = \psi \tag{2.58}$$

Momentum Conservation

The ATHLET momentum conservation is solved in one of two ways. The first method uses two momentum equations, one for each field (liquid and vapor). This results in a six-equation model much like that used in the other system codes already presented. The second method combines the liquid and vapor momentum conservation into a single equation, resulting in a five-equation model. The next two sections discuss these two models in more detail.

Six-Equation Model (Two Momentum Equations) Equation 2.59 shown below is the ATHLET liquid phase momentum conservation equation.

$$\begin{aligned} \frac{\partial[(1-\alpha)\,\rho_l\vec{w}_l]}{\partial t} + \nabla\left[(1-\alpha)\,\rho_l\vec{w}_l\vec{w}_l\right] + \nabla\left[(1-\alpha)\,P\right] = \\ \vec{\tau}_i - (1-\alpha)\,\vec{f}_w - \psi\vec{w}_\Gamma - (1-\alpha)\,\rho_l\vec{g} + \alpha\,(1-\alpha)\,(\rho_l-\rho_v)\,\vec{g}D_h\nabla\alpha + \\ \alpha\,(1-\alpha)\,\rho_m\left(\frac{\partial\vec{w}_R}{\partial t} + \nabla\vec{w}_R\right) + S_{i,l} \end{aligned} \tag{2.59}$$

The ATHLET vapor phase momentum conservation equation is:

$$\begin{aligned} \frac{\partial(\alpha\rho_v\vec{w}_v)}{\partial t} + \nabla\left(\alpha\rho_v\vec{w}_v\vec{w}_v\right) + \nabla\left(\alpha P\right) = \\ -\vec{\tau}_i - \alpha\vec{f}_w + \psi\vec{w}_\Gamma - \alpha\rho_v\vec{g} - \alpha\,(1-\alpha)\,(\rho_l-\rho_v)\,\vec{g}D_h\nabla\alpha - \\ \alpha\,(1-\alpha)\,\rho_m\left(\frac{\partial\vec{w}_R}{\partial t} + \nabla\vec{w}_R\right) + S_{i,v} \end{aligned} \tag{2.60}$$

Five-Equation Model (One Momentum Equation) The ATHLET code offers two different models for hydrodynamic simulation. The second model is called the five-equation model. The five-equation model is very similar to the six-equation model in that it solves the mass and energy balances in the control volumes separately for liquid and vapor phases in the same way that is shown above, yielding four equations. The fifth equation is a momentum balance that is solved for a mixture of liquid and vapor at the control volume junctions.

The momentum balance equation is generated by combining the separate momentum equations into an overall momentum equation for the two-phase mixture.

$$\begin{aligned} \frac{\partial(\rho_m\vec{w}_m)}{\partial t} - \vec{w}_m\frac{\partial\rho_m}{\partial t} + \rho_m\vec{w}_m\nabla\vec{w}_m + \\ \nabla\left(\alpha\,(1-\alpha)\,\frac{\rho_v\rho_l}{\rho_m}\vec{w}_r\vec{w}_r\right) + \nabla P = \vec{f}_w + \rho_m\vec{g} + S_{i,m} \end{aligned} \tag{2.61}$$

This single momentum balance equation neglects the phase interface shown in Figure 2.1, which makes it difficult to compute separate phase velocities. A drift-flux formulation

is used to give the relative velocity between the phases. The phase velocities are calculated by the following equations:

$$w_l = \frac{G}{A\rho_m} - \frac{\alpha_g \rho_g w_r}{\rho_m} \tag{2.62}$$

$$w_v = \frac{G}{A\rho_m} - \frac{(1-\alpha_g)\,\rho_l w_r}{\rho_m} \tag{2.63}$$

Energy Conservation

The ATHLET energy conservation equations bear some similarities to the equations for TRACE shown in section 2.1.3. Some of the differences stem from the internal energy included in the TRACE formulation (see Equation 2.32), which is expressed as enthalpy in the ATHLET formulation. The first equation shown here is the ATHLET energy conservation for the liquid field. Equation 2.65 is the same, but for the vapor field.

$$\begin{aligned} \nabla\left[(1-\alpha)\,\rho_l \vec{w}_l \left(h_l + \frac{1}{2}\vec{w}_l\vec{w}_l\right)\right] = -P\frac{\partial(1-\alpha)}{\partial t} + \vec{\tau}_i\vec{w}_l + (1-\alpha)\,\vec{\tau}_i \\ (\vec{w}_v - \vec{w}_l) + (1-\alpha)\,\rho_l\vec{g}\vec{w}_l + \dot{q}_{wl} + \dot{q}_i + \psi\left(h_{\psi,l} + \frac{1}{2}\vec{w}_\psi\vec{w}_\psi\right) + S_{e,l} \end{aligned} \tag{2.64}$$

$$\frac{\partial\left[(1-\alpha)\,\rho_l\left(h_l + \frac{1}{2}\vec{w}_l\vec{w}_l - \frac{P}{\rho_l}\right)\right]}{\partial t} +$$

Where:

- $(1-\alpha)\,\rho_l\vec{g}\vec{w}_l$ = Gravitational work
- $(1-\alpha)\,\vec{\tau}_i\,(\vec{w}_v - \vec{w} - l)$ = Dissipation due to interfacial shear
- $\psi\left(h_{\psi,l} + \frac{1}{2}\vec{w}_\psi\vec{w}_\psi\right)$ = Energy flow due to phase change

$$\frac{\partial\left[\alpha\rho_v\left(h_v+\frac{1}{2}\vec{w}_v\vec{w}_v-\frac{P}{\rho_v}\right)\right]}{\partial t}+\nabla\left[\alpha\rho_v\vec{w}_v\left(h_v+\frac{1}{2}\vec{w}_v\vec{w}_v\right)\right]= \\ -P\frac{\partial\alpha}{\partial t}-\vec{\tau}_i\vec{w}_v+\alpha\vec{\tau}_i\left(\vec{w}_v-\vec{w}_l\right)+\alpha\rho_v\vec{g}\vec{w}_v+ \\ \dot{q}_{wv}+\dot{q}_i+\psi\left(h_{\psi,v}+\frac{1}{2}\vec{w}_\psi\vec{w}_\psi\right)+S_{e,v} \tag{2.65}$$

2.1.7 CATHARE Governing Equations

CATHARE uses a six-equation model [27, 5]. The mass, momentum, and energy conservation equations are written for the vapor and liquid phases. The equations are written for one dimensional axial flow. Up to two transport equations can be added for noncondensable gasses. As before, the noncondensable gasses are assumed to be at the same temperature and move with the same velocity as the vapor phase. Thus, only the mass conservation equation is needed for the noncondensable gasses.

Mass Conservation

It is assumed that the phase interface has no thickness or mass. The mass conservation equations for the liquid and vapor phases are shown below. The mass conservation equation for the noncondensable gas field is also provided as Equation 2.68. The interfacial mass transfer is represented in the mass balance equations by Γ.

$$A\frac{\partial\alpha\rho_G}{\partial t}+\frac{\partial A\alpha\rho_G v_G}{\partial z}=A\Gamma \tag{2.66}$$

$$A\frac{\partial(1-\alpha)\,\rho_l}{\partial t}+\frac{\partial A\,(1-\alpha)\,\rho_l v_L}{\partial z}=-A\Gamma \tag{2.67}$$

Noncondensable Gas

$$\frac{\partial}{\partial t}A\alpha\rho_G X_i+\frac{\partial}{\partial z}A\alpha\rho_G X_i v_G=S_i \tag{2.68}$$

$$\Gamma=\frac{\chi/Aq_{wi}-q_{LI}-q_{GI}}{H_V-H_L} \tag{2.69}$$

The TRACE conservation Equations (2.24 and 2.25) are very similar to the mass conservation equations for CATHARE.

Momentum Conservation

The liquid and vapor momentum equations are shown below, as Equation 2.70 and 2.71, respectively. Note that the interfacial tension is neglected, and that both phases are assumed to have the same velocity at the interface.

$$A\frac{\partial(1-\alpha)\,\rho_l v_L}{\partial t} + \frac{\partial A\,(1-\alpha)\,\rho_l v_L^2}{\partial z} + A\,(1-\alpha)\,\frac{\partial P}{\partial z} = \chi\tau_{WL} + A\,[-I + (1-\alpha)\,\rho_l g] + f_L\frac{\partial A}{\partial z} \tag{2.70}$$

$$A\frac{\partial\alpha\rho_G v_G}{\partial t} + \frac{\partial A\alpha\rho_G v_G^2}{\partial z} + A\alpha\frac{\partial P}{\partial z} = -\chi\tau_{WG} + A\,[I + \alpha\rho_G g] + f_G\frac{\partial A}{\partial z} \tag{2.71}$$

The I term in the above equations is the interfacial exchange of momentum. It is calculated as shown in Equation 2.72

$$I = -\tau_1 - \beta\alpha\,(1-\alpha)\,[\alpha\rho_G + (1+\alpha)\,\rho_l]\left[\frac{d_G v_G}{dt} - \frac{d_L v_L}{dt}\right] - p_1\frac{\partial\alpha}{\partial Z} + \Gamma V_i \tag{2.72}$$

For stratified flows, the pressure term (p_1) is:

$$p_1 = \alpha\,(1-\alpha)\,(\rho_l - \rho_g)\,gD_h \tag{2.73}$$

and for non-stratified flows, the pressure term is:

$$p_1 = \frac{\alpha\,(1-\alpha)\,\rho_g\rho_l}{\alpha\rho_l + (1-\alpha)\,\rho_g}\,(v_G - v_L)^2 \tag{2.74}$$

Energy Conservation

As before in the momentum balance equations, the conservation of energy equations shown below also neglect interfacial tension.

$$\begin{aligned} A\frac{\partial}{\partial t}\left[(1-\alpha)\,\rho_l\left(H_L+\frac{v_L^2}{2}\right)\right]+ \\ \frac{\partial}{\partial z}\left[A\,(1-\alpha)\,\rho_l\left(H_L+\frac{v_L^2}{2}\right)\right]-A\,(1-\alpha)\,\frac{\partial P}{\partial t}= \\ A\left[Q_{LI}+(1-\alpha)\,\rho_l v_L g\right]+\chi Q_{WL} \end{aligned} \tag{2.75}$$

$$\begin{aligned} A\frac{\partial}{\partial t}\left[\alpha\rho_G\left(H_G+\frac{v_G^2}{2}\right)\right]+ \\ \frac{\partial}{\partial z}\left[A\alpha\rho_G v_G\left(H_G+\frac{v_G^2}{2}\right)\right]-A\alpha\frac{\partial P}{\partial t}= \\ A\left[Q_{GI}+\alpha\rho_G v_G g\right]+\chi Q_{WG} \end{aligned} \tag{2.76}$$

The Q_{GI} and Q_{LI} terms represent the energy exchanges between the applicable phase (vapor or liquid) and the interface. These terms are defined in the equations below:

$$Q_{GI}=q_{GI}+\Gamma\left(h_V+\frac{1}{2}V_1^2\right) \tag{2.77}$$

$$Q_{LI}=q_{LI}-\Gamma\left(h_L+\frac{1}{2}V_1^2\right) \tag{2.78}$$

Noncondensable State Equations

The state equations for a noncondensable gas mixture are provided below. These equations are used to compute the needed input values for the conservation equations when noncondensable gases are present. Note that the code is limited to 4 different noncondensable gas

types.

$$\rho_i = X_i \rho_G \tag{2.79}$$

$$P_i = \rho_i R_i T_G \tag{2.80}$$

$$\rho_G = \sum_{i=1}^{4} \rho_i + \rho_V \left(T_G, H_V\right) \text{ for } i = 1, 4 \tag{2.81}$$

$$P = \sum_{i=1}^{4} P_i + P_V \tag{2.82}$$

$$H_G = \left(1 - \sum_{i=1}^{4} X_i\right) H_V + \sum_{i=1}^{4} \left\{X_i \left[h_{vs7} + cp \left(T_G - T_{s7}\right)\right]\right\} \tag{2.83}$$

Where H_V is a function of P_V and T_G and:

$$h_{vs7} = H_{V\ sat} \left(7bar\right) \approx 2766430\ J/kg \tag{2.84}$$

$$T_{s7} = T_{sat} \left(7bar\right) \approx 164.93°\text{C} \tag{2.85}$$

2.1.8 Governing Equation Summary

The components of the mass, momentum, and energy balance equations from each of the codes are summarized in Tables 3.2, 2.2, 2.3, 2.4, and 2.5. These tables provide a simple comparison between the code versions.

2.2 Flow Regimes

Single-phase flows can be effectively modeled using governing equations and simple heat transfer correlations. While many reactor systems are designed with primary coolant that does not change phase throughout the coolant cycle, some (such as Boiling Water Reactors) experience phase change in the primary coolant as part of the reactor operation, and other

Table 2.1: Mass Conservation Equation Comparison

Code	Time Rate of Change of Mass	Convective Mass Change	Mass Exchange Rate
RELAP5-3D	$\frac{\partial}{\partial t}\left(\alpha_k \rho_k\right)$	$\frac{1}{A}\frac{\partial}{\partial x}\left(\alpha_k \rho_k v_k A\right)$	Γ_k
RELAP-7	$\frac{\partial \alpha_l \rho_l A}{\partial t}$	$\frac{\partial \alpha_l \rho_l u_l A}{\partial x}$	$-\Gamma A_{\text{int}} A$
TRACE	$\frac{\partial[(1-\alpha_g)\rho_l]}{\partial t}$	$\nabla\cdot\left[\left(1-\alpha_g\right)\rho_l \vec{V}_l\right]$	$-\Gamma_g$
WCOBRA/TRAC-TF2	$\frac{\partial(\alpha_k \rho_k)}{\partial t}$	$\nabla\left[\left(\alpha_k \rho_k\right)\cdot \underline{u}_k\right]$	Γ_k
TRAC-M	$\frac{\partial(\alpha \rho_v)}{\partial t}$	$\nabla\cdot\left(\alpha \rho_v \vec{V}_g\right)$	Γ
ATHLET	$\frac{\partial[(1-\alpha)\rho_l]}{\partial t}$	$\nabla\left[\left(1-\alpha\right)\rho_l \vec{w}_l\right]$	$-\psi$
CATHARE	$\frac{\partial}{\partial t}\left[A\left(1-\alpha\right)\rho_l\right]$	$\frac{\partial}{\partial z}\left[A\left(1-\alpha\right)\rho_l v_L\right]$	$-A\Gamma + S_L$

reactor designs with liquid coolant can experience phase change during accident scenarios. For reactor system design and safety analysis, it is essential that the system code be able to model two-phase flows. Two-phase flow introduces significant complexity to the coolant hydrodynamic model.

Two-phase flows can be categorized into groups based on their appearance and the structure of the flow. Flow regimes are divided up into pre- and post-CHF flow. Pre-CHF flows are typically sub-categorized into vertical flows, horizontal flows, inclined flows. Post-CHF flows are less affected by inclination of the flow [22, 1]. Figures 2.12, 2.13 and 2.14 show the vertical, horizontal, and post-CHF flow regimes [22, 1].

The first vertical flow regime is called dispersed bubble, with small bubbles scattered through the bulk coolant. With increasing void fraction, the bubbles coalesce into larger "slugs", marking the transition to slug flow. The flow structure becomes unstable with increasing flow velocity. The net flow remains upward, but components of the flow travel in both directions. The instability comes from the balance of the gravity and shear forces acting in opposing directions on the thin liquid film of the Taylor bubbles. Slug bubbles are more likely in smaller pipes, while Taylor cap bubbles are more common in larger pipes.

Table 2.2: Momentum Conservation Equation Comparison RELAP and TRACE Codes

Component	RELAP5-3D	RELAP-7	TRACE
Time Rate of Change of Momentum	$\alpha_k \rho_k A \frac{\partial v_k}{\partial t}$	$\frac{\partial \alpha_l \rho_l u_l A}{\partial t}$	$\frac{\partial \left[(1-\alpha_g)\rho_l \vec{V_l}\right]}{\partial t}$
Rate of momentum change from convection	$\frac{1}{2}\alpha_k \rho_k A \frac{\partial v_k^2}{\partial x}$	$\frac{\partial \alpha_l A \left(\rho_l u_l^2 + p_l\right)}{\partial x}$	$\nabla \cdot (1-\alpha_g)\,\rho_l \vec{V_l}\vec{V_l}$
Pressure gradient	$-\alpha_k A \frac{\partial P}{\partial x}$	$p_{\text{int}} A \frac{\partial \alpha_l}{\partial x} + p_l \alpha_l \frac{\partial A}{\partial x}$	$(1-\alpha_g)\,\nabla P$
Momentum change from body forces	$\alpha_k \rho_k B_x A$	$\alpha_l \rho_l \vec{g} \cdot \hat{n}_{axis} A$	$(1-\alpha_g)\,\rho_l \vec{g}$
Wall Drag	$(\alpha_k \rho_k A)\, FW_k \cdot v_k$	$--$	$\vec{f_{wl}}$
Momentum from phase change mass transfer	$\Gamma_k A\,(v_{kI} - v_k)$	$-\Gamma A_{\text{int}} u_{\text{int}} A$	$-\Gamma \vec{V_i}$
Interfacial Drag	$(\alpha_k \rho_k A)\, FI_k \cdot (v_k - v_r)$	$f_l \alpha_l \rho_l \left(u_l - u_w\right)^2 (\pi A)^{\frac{1}{2}} - f_l^{'} \frac{1}{2} \rho_l \left(u_l - u_{\text{int}}\right)^2 A_{\text{int}} A$	$\vec{f_i}$
Virtual Mass Force	$C \alpha_k \alpha_r \rho_m A \left[\frac{\partial (v_k - v_r)}{\partial t} + v_r \frac{\partial v_k}{\partial x} - v_k \frac{\partial v_r}{\partial x}\right]$	$--$	$--$
Velocity Relaxation	$--$	$A\lambda\,(u_g - u_l)$	$--$

The annular mist regime follows with higher temperatures and increased flow rates. The interfacial shear of the high velocity gas on the liquid film dominates over gravity in the annular flow regime [1].

Horizontal flow regimes have slightly different characteristics. There is a bubbly flow regime very similar to that for the vertical flows. Following the bubbly flow regime is the stratified flow regime. The orientation of the flow separates the vapor and liquid phases, which causes the bulk of the coolant to collect at the bottom of the pipe or channel. For stratified flow, the coolant and vapor are effectively separated. With increased velocities, the

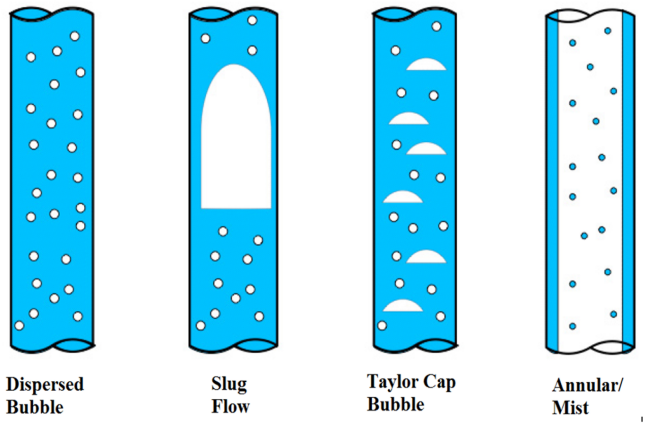

Figure 2.2: Vertical Pre-CHF Flow Regimes [1]

stratified flow becomes wavy, and the interface between the vapor and liquid phases is not smooth and stable. Horizontal plug/slug flows have sections of flow that fill the piping with liquid, and may have bubbles. For fast, hot flows, the annular mist regime is also possible [1]

Post-CHF flow regimes occur after the wall temperature exceeds the CHF temperature and the wall experiences dryout. The post-CHF flow regimes are characterized by the fact that the coolant no longer comes into contact with the wall. In inverted annular flows, there is a core of liquid in the center of the pipe surrounded by an annulus of vapor [1]. In inverted slug flow, large slugs of liquid surrounded by vapor are present. In dispersed flows, droplets are present in a vapor flow with no liquid in contact with the wall. The points of dryout and rewet characterize the start and end of the post-CHF flow regime. Figure 2.14 shows the post-CHF flow regimes and the points of dryout and re-wet.

2.2.1 Flow Regime Maps

The complex flow regimes described above are simplified for modeling in reactor system codes. The transition between flow regimes is particularly difficult to model. It would be computationally prohibitive to model the flow regimes in great detail. Detailed Computational Fluid Dynamics (CFD) codes are typically used to model these two-phase flows

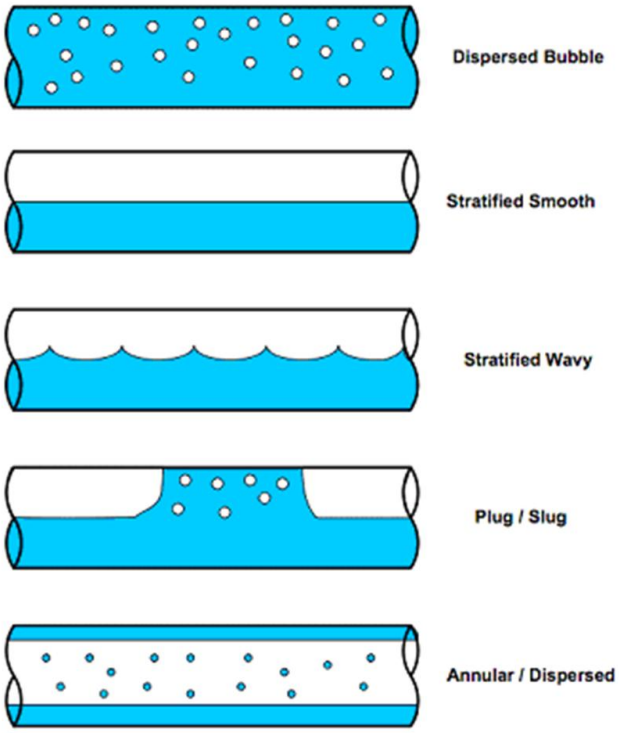

Figure 2.3: Horizontal Flow Regimes [1]

accurately. Instead of detailed and complex models, the system codes use flow regime maps that use parameters such as flow velocity, void fraction, and temperature to determine which flow regime is present, and then the correct closure relationship is selected to match that flow regime. The flow regime maps are important in the determination of the closure relationships and will be discussed later.

RELAP5-3D

The heat transfer coefficient that is used between the phases in the bulk flow of the coolant depends on the flow regime. Therefore, detailed flow regime maps have been developed for use in RELAP5-3D, with different heat transfer correlations for each regime. The vertical and horizontal flow regime maps for RELAP5 are shown in Figure 2.5 and Figure 2.6, respectively.

The horizontal flow regime map is used for volumes that have an inclination between 0

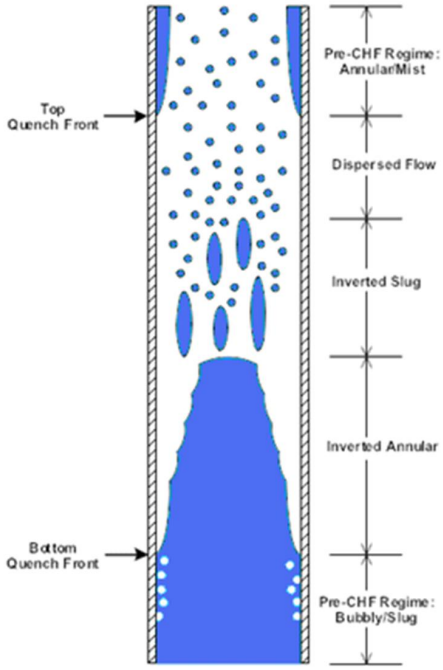

Figure 2.4: Inverted flow regimes for post-CHF [1]

and 30 degrees. The vertical flow regime map is used for volumes with angles between 60 and 90 degrees. For volume inclination angles between 30 and 60 degrees, a linear interpolation is used [2]. Although different maps are used, it will be seen that the closure relationships are not always modified based on flow orientation. For example, interfacial heat transfer for flow regimes with the same name uses the same correlation regardless of flow orientation [13]. The flow orientation does have an effect on the interfacial drag for some flow regimes [13].

The specific vertical flow regime is determined using mixture velocity (v_m), void fraction (α_g) and vapor superheat above saturation ($T_g - T^s$). If the flow velocity is slow enough, it is considered to be vertically stratified, regardless of void fraction or superheat [2]. At the Taylor bubble rise velocity (v_{Tb}), the flow regimes are considered separate. Equation 2.86 shows the calculation for the Taylor bubble rise velocity [2].

$$v_{Tb} = 0.35 \left[\frac{g D_h \left(\rho_l - \rho g \right)}{\rho_l} \right]^{\frac{1}{2}} \tag{2.86}$$

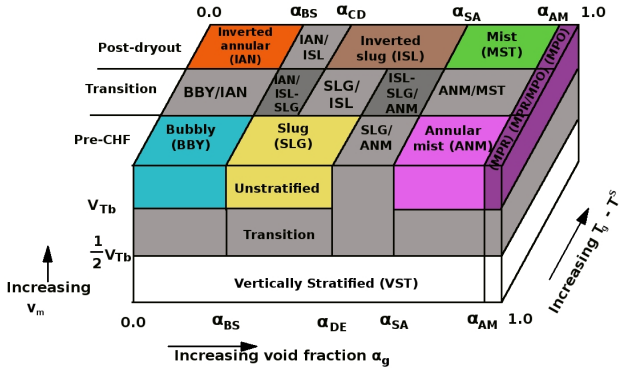

Figure 2.5: RELAP5 Vertical Flow Regime Map [2]

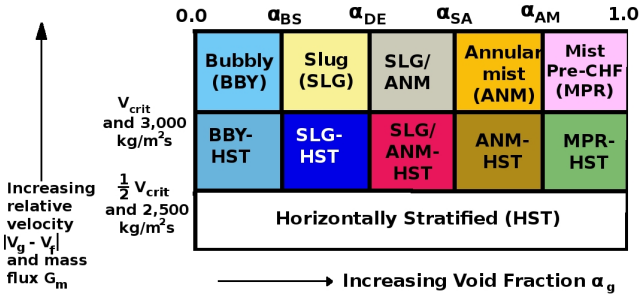

Figure 2.6: RELAP5 Horizontal Flow Regime Map [2]

The transition from vertically stratified flow to a unique flow regime begins as the velocity is increased to $\frac{1}{2}v_{Tb}$. Interpolation techniques are used to compute the heat transfer in the transition region between the vertically stratified flow and the more complex flow regimes. The heat transfer coefficient in the transition region from $\frac{1}{2}v_{Tb}$ and v_{Tb} is computed by interpolation. The interpolation algorithm selects the maximum of three linear factors. The three linear factors are determined from the void fraction, mixture velocity and superheated temperature [2].

The void fraction that indicates the start of the bubbly-to-slug transition (α_{BS}) is com-

puted as shown in Equation 2.87.

$$\alpha_{BS} = \begin{cases} \alpha^*_{BS} & \text{for } G_m \leq 2,000 kg/m^2 s \\ \alpha^*_{BS} + \frac{\left(0.5 - \alpha^*_{BS}\right)}{1{,}000} \left(G_m - 2,000\right) & \text{for } 2,000 < G_m < 3,000 kg/m^2 s \\ \alpha_{BS} = 0.5 & \text{for } G_m \geq 3,000 kg/m^2 s \end{cases} \tag{2.87}$$

Where α^*_{BS} and G_m are defined:

$$\alpha^*_{BS} = \max\left\{0.25 \min\left[1, (0.045 D^*)^8\right], 10^{-3}\right\} \tag{2.88}$$

$$G_m = \alpha_g \rho_g |v_g| + \alpha_f \rho_l |v_f| \tag{2.89}$$

$$\text{and } D^* = D\left[\frac{g\left(\rho_l - \rho_g\right)}{\sigma}\right]^{\frac{1}{2}} \tag{2.90}$$

The void fraction that indicates the end of the bubbly-to-slug transition and the start of the inverted slug regime (α_{CD}) is computed as shown in Equation 2.91.

$$\alpha_{CD} = \alpha_{BS} + 0.2 \tag{2.91}$$

The void fraction marking the switch from inverted slug flow to mist flow or annular mist flow is α_{SA} and is defined as shown in Equation 2.92.

$$\alpha_{SA} = \max\ \left[\alpha^{min}_{AM},\ \min\ \left(\alpha^f_{crit}, \alpha^e_{crit}, \alpha^{max}_{BS}\right)\right] \tag{2.92}$$

Where the additional vapor fractions in Equation 2.92 are defined:

$$\alpha_{AM}^{min} = \begin{cases} 0.5 & \text{pipes} \\ 0.8 & \text{bundles} \end{cases} \tag{2.93}$$

$$\alpha_{crit}^{e} = \min \left\{ \frac{3.2}{v_g} \left[\frac{g\sigma \left(\rho_l - \rho_g\right)}{\rho_g^2} \right]^{\frac{1}{4}}, 1.0 \right\} \tag{2.94}$$

$$\alpha_{crit}^{f} = 0.75 \tag{2.95}$$

$$\alpha_{BS}^{max} = 0.9 \tag{2.96}$$

The last void fractions shown in Figure 2.5 define the boundary between slug flow and slug-to-annular mist flow (α_{DE}) and the transition to pre- and post-CHF mist flows (α_{AM}) are defined below:

$$\alpha_{DE} = \max \left(\alpha_{BS}, \alpha_{SA} - 0.05\right) \tag{2.97}$$

$$\alpha_{AM} = 0.9999 \tag{2.98}$$

Figure 2.5 shows a transition region between the pre-CHF and post-dryout regimes. For the transition region between these regimes, the interfacial heat transfer coefficient is computed from a cubic spline interpolation between the superheated and subcooled regimes. The transition region is defined by the temperature of the coolant. The interpolation scheme is used if the liquid temperature is between 1 degree K subcooled and 1 degree K superheated [2].

Horizontal flows are divided into flow regimes using characteristic parameters (void fraction and velocity) in much the same way that was done for the vertical flow regimes. As with the vertical flow regimes, a characteristic velocity can be used to define the transition between horizontally stratified flow and the remaining flow regimes. This characteristic

velocity, v_{crit} is defined in equation 2.99 [2].

$$\frac{1}{2}\left[\frac{(\rho_l - \rho_g)\, g\alpha_g A}{\rho_g D \sin\theta}\right]^{\frac{1}{2}} (1 - \cos\theta) \tag{2.99}$$

For horizontal flows, the transition between bubbly and slug flows (α_{BS}) is defined as shown in Equation 2.100.

$$\alpha_{BS} = \begin{cases} 0.25 & \text{for } G_m \leq 2,000 kg/m^2 s \\ 0.25 + 0.00025\,(G_m - 2,000) & \text{for } 2,000 < G_m < 3,000 kg/m^2 s \\ 0.5 & \text{for } G_m \geq 3,000 kg/m^2 s \end{cases} \tag{2.100}$$

The remaining divisions between flow regimes are marked by the void fractions α_{DE}, α_{SA} and α_{AM}. The values of those fractions are defined below:

$$\alpha_{DE} = 0.75 \tag{2.101}$$

$$\alpha_{SA} = 0.8 \tag{2.102}$$

$$\alpha_{AM} = 0.9999 \tag{2.103}$$

In addition to the vertical, horizontal, and post-CHF flow maps, RELAP5-3D also has a high mixing map (for pumps and compressors) and an ECC mixer map. These specialized maps will not be discussed in detail.

TRACE

The interfacial heat transfer models consider four pre-Critical Heat Flux flow regimes as shown in Figure 2.12. The bubbly flow regimes (dispersed bubble, slug flow, and Taylor cap bubble) are referred to collectively as the "bubbly/slug" flow regime [1].

The TRACE pre-CHF flow regime map is shown in Figure 2.7. The differences from the

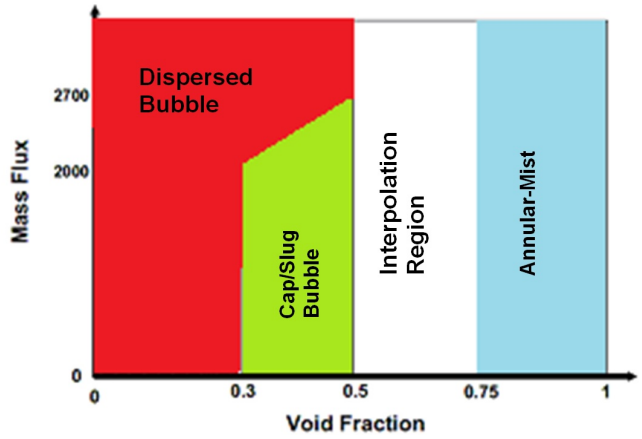

Figure 2.7: TRACE Pre-CHF flow regime - interfacial heat transfer [1]

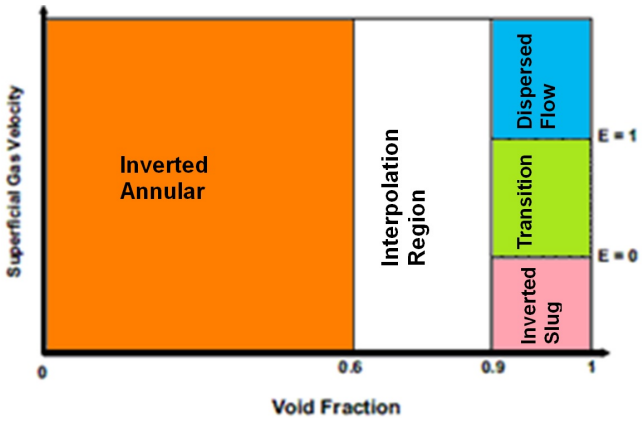

Figure 2.8: TRACE Post-CHF flow regime map [1]

RELAP5-3D flow regime map that are immediately apparent are that there is no vertically stratified flow regime, and also no dependence on temperature. Instead of temperature dependence, a separate flow regime map is used for the post-CHF flow regimes. The post-CHF regime is shown in Figure 2.8. The TRACE code does not have models for vertically stratified flows [1].

The flow regime is determined based on void fraction and mass flux as shown in Figure 2.7. The dispersed bubble flow regime is present for void fractions less than 0.3 for mass fluxes less than 2000 kg/m^2s. For greater mass fluxes, the larger Taylor cap or slug bubbles get broken up into smaller bubbles consistent with dispersed bubble flows. For high enough mass fluxes (2700 kg/m^2s), the dispersed bubble extends to the transition region between

the bubbly/slug flow regimes and the annular/mist flow regime. This profile is defined mathematically in Equation 2.104.

$$\alpha_{DB} = \begin{cases} 0.3 & \text{for } G \leq 2000\,(kg/m^2 s) \\ 0.3 + 0.2\left(\frac{G-2000}{2700-2000}\right) & \text{for } 2000 < G < 2700\,(kg/m^2 s) \\ 0.5 & \text{for } G \geq 2700\,(kg/m^2 s) \end{cases} \tag{2.104}$$

The remaining flow regimes are defined by very simple void fraction limits. The interpolation region between the bubbly/slug flow and the annular-mist flow begins at a void fraction of 0.5. The annular mist regime begins at a void fraction of 0.75 and continues to a void fraction of 1.0 [1].

The representative post-CHF heat transfer regimes are shown in Figure 2.14. The post-CHF region is defined by the bottom and top quench front seen in Figure 2.14. Outside of this region, the normal pre-CHF closure relationships are used. If the computational volume is partially quenched, the results of the closure relationships are interpolated between the pre- and post-CHF values [1]. The post-CHF flow regimes are characterized as shown in the flow map in Figure 2.8. Note that the flow regimes are characterized by void fraction and entrainment fraction (governed by the supercritical velocity). The inverted annular regime exists for void fractions from 0.0 to 0.6. The interpolation region exists from void fraction 0.6 up to a void fraction of 0.9. Above the void fraction of 0.9 and below a void fraction of 1.0, the droplets are considered to be entrained liquid. The remainder of the fluid is considered to be inverted slugs. There are three separate regimes for void fractions above 0.9 - inverted slug, dispersed flow, and a transition region between them. The transition region begins where the entrained fraction is zero, and ends when the entrained fraction is

1.0. The entrained liquid fraction is computed as shown in the equations below [1].

$$j_{g,crit} = 0.6 \left[\frac{sigma^{0.316} \left(g\Delta\rho\right)^{0.228}}{\rho_g^{0.456}\mu_g^{0.0879}} \right] \tag{2.105}$$

$$G_d = 2.16x10^{-4} \left[\left(\frac{j_g}{j_{g,crit}} \right)^3 - 1 \right] N_{\mu g}^{0.236} \Delta\rho j_g \tag{2.106}$$

$$\alpha_d \approx \frac{G_d}{\rho_l \cdot \max\left(0.01, V_l\right)} \tag{2.107}$$

$$E = \frac{\alpha_d}{(1-\alpha)} \tag{2.108}$$

There is no separate flow map in the TRACE code for horizontal flows. Volumes that are oriented horizontally use the same closure models for the bubbly, slug, and annular mist regimes as were used for the vertical volumes. Special models are included in order to capture the flow stratification in horizontal volumes [1]. These models capture the effects of stratification on wall drag, interfacial drag, and interfacial heat transfer. Although horizontal flows use the same flow regime map as the vertical flows, this is not always a correct assumption. Slow flows in horizontal or inclined pipes can become stratified as gravity causes the phases to separate.

WCOBRA/TRAC-TF2

The pre-CHF flow regimes that are recognized by the WCOBRA-TRAC code are shown the flow regime map in Figure 2.9.

The pre-CHF flow regime map is very similar to that already shown for the TRACE code (Figure 2.7). The only exception is in the approach for the transition between the bubbly flow and the slug flow. The WCOBRA-TRAC code models the entire region between void fractions of 0.3 and 0.5 and mass flux values of 2000 and 2700 kg/m^2s as the transition region, where TRACE defines a boundary that changes linearly with increasing void fraction. The WCOBRA-TRAC approach will use interpolation in the transition region, rather than having

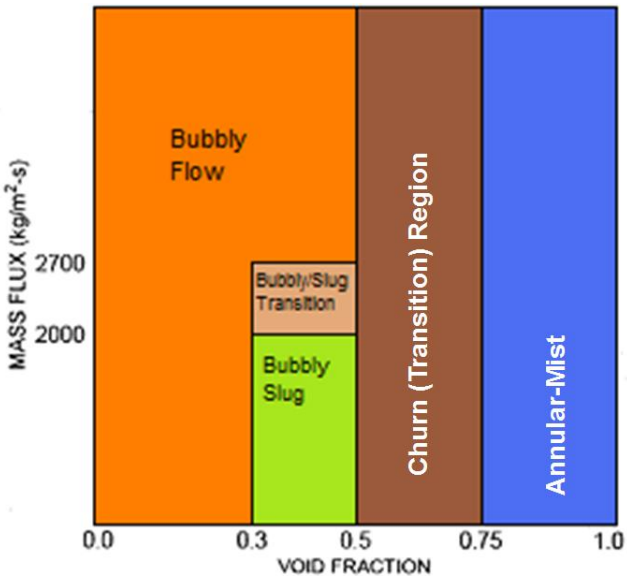

Figure 2.9: WCOBRA-TRAC Pre-CHF flow regime map [3]

a sharp border between the two regimes [3]. In all other respects, the characterization of the pre-CHF flow regimes in WCOBRA-TRAC are very similar to those used in the TRACE code.

The WCOBRA/TRAC post-CHF flow regimes are referred to as "hot wall" flows, and model heat transfer for flow regimes that do not have a wetted wall. The closure relations for hot wall flows are used to model the blowdown and reflood phases of a large LOCA in a nuclear reactor system. Any time a momentum cell has a heated surface (provided by a heat structure) with a temperature greater than the CHF temperature, the hot wall relations are used. The flow regime map is not provided in the publicly-available manuals [3], but the regimes that are defined are: Subcooled inverted annular, Inverted liquid slug, Dispersed droplet, Falling film and Top deluge.

Comparing the list above with the regimes depicted in Figure 2.8, it is clear that the post-CHF flow regimes in WCOBRA/TRAC are more specialized than those in the TRACE code, even if the details are not documented in publicly available sources.

TRAC-M

The flow regime map for the TRAC-M code is identical to the map already seen for the WCOBRA/TRAC system code (Figure 2.9), and is applied in much the same way [4]. The post-CHF flow regime in TRAC-M is called the reflood flow-regime model. As with the post-CHF flow in WCOBRA/TRAC, the post-CHF flow regimes in TRAC-M capture the heat transfer behavior during the blowdown and reflood phase of a reactor after a LOCA. The reflood model is divided into the familiar post-CHF regimes. Moving downstream from the point of CHF these regimes are: Transition boiling, Smooth inverted annular flow, Rough-wavy inverted annular flow, Agitated inverted annular flow, Dispersed flow, and Highly dispersed flow.

These regimes are depicted in Figure 2.10. Note the similarity to the regimes shown in Figure 2.14. Figure 2.10 shows the axial locations (Z) of the transition between flow regimes. The capillary number (Ca) is computed as shown in the figure, and is used in the calculation of the location of the transition points. Note also that a few of the transitions are dependent upon void fraction (α).

ATHLET

As with the other system codes, ATHLET divides two-phase flows into specific flow regimes (flow patterns). For vertical and inclined channels, the flow pattern has two regions: dispersed and non-dispersed flow [26]. The prediction of the onset of liquid entrainment defines the transition between the regions. ATHLET uses the Taitel et al. formulation [28], which is formulated form the assumption that annular-dispersed flow cannot exist unless the gas velocity in the core is high enough to cause liquid entrainment. If the velocity is not high enough, the droplets will coalesce, and the resulting flow regime will be churn or slug flow [26]. The minimum gas velocity required to suspend a drop is calculated as shown in Equation

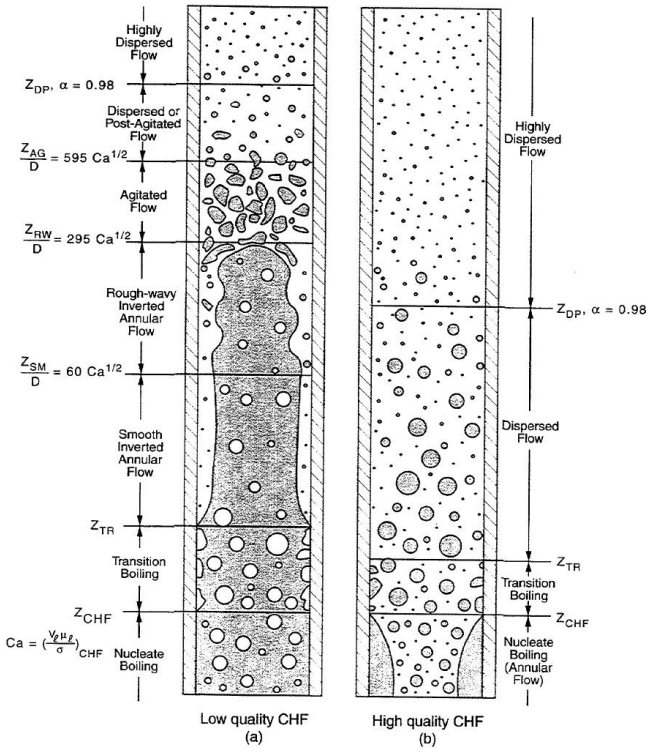

Figure 2.10: TRAC-M post-CHF flow regime map [4]

2.109.

$$w_{V,e} = \left[\left(\frac{4}{3}\frac{We}{C_{D,i}}\right)^{\frac{1}{4}} + 1.6\cos\theta\right] \cdot \left(\frac{\sigma\Delta\rho g}{\rho_v^2}\right)^{\frac{1}{4}} \tag{2.109}$$

The recommended values for the Weber number (We) and drag coefficient ($C_{D,i}$) are 30 and 0.44, respectively [28]. Bundle geometries use a simpler correlation:

$$w_{V,e} = 0.25\sqrt{\frac{\rho_l}{\rho_v}} \tag{2.110}$$

The fraction of dispersed liquid (E_d) is computed as the ratio of the volume of dispersed liquid to the total liquid volume, and is used to describe dispersed flows. The fraction of dispersed liquid is computed from an S-shape correlation described in reference [29] and

shown as Equation 2.111.

$$E_d = 1 - e^{\left(K_e \frac{j^* - w_{V,e}}{w_{V,e}}\right)} \tag{2.111}$$

Where j^* is the larger of the phase superficial velocities and K_e is a geometry dependent constant. For pipes, use a geometry constant (K_e) of 0.5.

With these equations, the simplified vertical flow map is defined as a function of the largest phase superficial velocity (j^*). The regimes are:

- $j^* < w_{V,e}$ - non-dispersed flow
- $j^* = w_{V,e}$ - onset of entrainment
- $j^* > w_{V,e}$ - annular-dispersed flow with increasing entrained liquid fraction

The horizontal flow regimes defined in ATHLET are stratified, wavy, slug, and a transition from non-dispersed to dispersed flows. The prediction of the transition between stratified smooth and stratified wavy is defined by the minimum gas velocity necessary to generate waves [26]. The equation is shown below.

$$w_{V,w} = \frac{2}{\sqrt{s}} \left[g \cos\theta \frac{\mu_L}{w_l} \frac{(\rho_l - \rho_V)}{\rho_l \rho_V} \right]^{1/2} \tag{2.112}$$

The onset of slug flow transition is developed from the basis of the classic Kelvin-Helmholtz instability. The transition region is defined as before, using the minimum gas/-vapor velocity for slug flow [26]. The equation for the minimum gas velocity is shown below.

$$w_{V,s} = \left(1 - \frac{h_{CL}}{D_h}\right) \left[\frac{\pi}{4} \alpha g \cos\theta \frac{D_h}{\sqrt{1 - \left(2\frac{h_{cl}}{D_h} - 1\right)^2}} \frac{\rho_l - \rho_V}{\rho_V} \right]^{\frac{1}{2}} \tag{2.113}$$

The transition between the slug and stratified flow regimes is a function of the fraction of non-stratified liquid (E_w). The calculation of E_w is dependent on flow velocities as shown below [26].

$$E_w = \begin{cases} 0.0 & \text{for } w_{max} < w_{r,s} \\ \frac{w_{max} - w_{r,s}}{w_{r,s}} & \text{for } w_{r,s} < w_{max} < 2.0\ w_{r,s} \\ 1.0 & \text{for } w_{max} > 2.0\ w_{r,s} \end{cases} \tag{2.114}$$

The relative velocity between the vapor and liquid ($w_{r,s}$) is:

$$w_{r,s} = w_{V,s} \pm w_{min} \tag{2.115}$$

Where w_{max} and w_{min} are the largest and smallest absolute value of the phase velocities, respectively. The $\pm$ in Equation 2.115 depends upon co-current (+) and counter-current (-) flow [26].

The transition between dispersed and non-dispersed flow is modeled using the parameter E_d, which is the fraction of dispersed liquid, defined as the volume of dispersed liquid divided by the total liquid volume (see below).

$$E_d = \frac{V_{L,disp}}{(V_{L,nd} + V_{L,disp})} \tag{2.116}$$

The onset of liquid entrainment is determined by the velocity of the vapor/gas that causes entrainment ($w_{V,e}$), which is computed as follows:

$$w_{V,e} = \max\ \left[0.5 \sqrt{\frac{(\rho_l - \rho_V)\, g \alpha A}{\rho_g D}}, 0.6 \sqrt{\frac{\rho_l}{\rho_V}} \right] \tag{2.117}$$

When the gas/vapor velocity exceeds $w_{V,e}$, liquid entrainment begins. The fraction of dispersed liquid is computed from Equation 2.111. The mapping of the horizontal flow regimes in ATHLET is therefore:

- $w_{max} < w_{r,s}$ - Stratified Flow
- $w_{r,s} \leq w_{max} \leq 2\ w_{r,s}$ - Wavy flow - transitioning between stratified smooth and slug flow ($0 < E_w < 1$)
- $2\ w_{r,s} < w_{max}$ - Slug flow ($E_w = 1$)
- $w_{V,e} \leq w_{max}$ - Transition from non-dispersed flow to dispersed flow with increasing entrained liquid fraction ($E_d > 0.0$)

CATHARE

The pre-CHF flow regimes in the CATHARE code are bubbly (nucleate boiling) or annular (forced convective evaporation). The pre-CHF flow regimes are depicted graphically in Figure 2.11 [5]. The criteria for determining the exact flow regime on the flow map are not described in the available literature, and cannot be covered here. However, the map does show what regimes are included in the code. Only two flow regime transitions are explicitly written into the CATHARE closure relationships. The first transition is between stratified flow and non-stratified flow (shown in Figure 2.11). The criteria for this transition are based on the Kelvin-Helmholtz instability threshold and the relative effects of bubble sedimentation and bubble turbulent mixing. The second transition is between annular and droplet flows [27, 5].

The post-CHF flow regimes in CATHARE are: inverted annular (vapor films and liquid core) and dispersed flow (slugs and/or drops of liquid) [5].

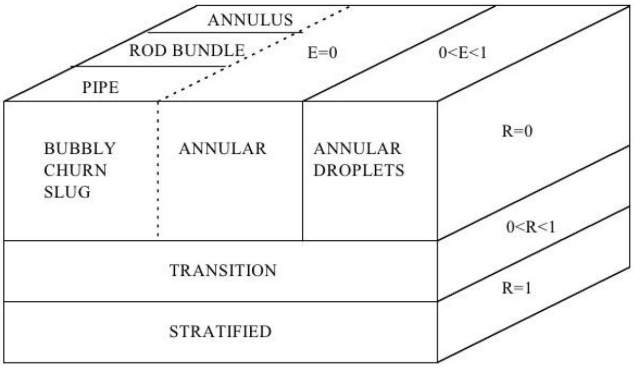

Figure 2.11: CATHARE pre-CHF flow regime map [5]

2.3 Numerical Solution

The system of equations that result from the conservation equations and closure relationships must be solved numerically. The solution methods can be compared by methods of discretization and by the matrix solver that is implemented. The numerical solution methods influence the performance of the codes in terms of code speed, as well as code time step requirements. Different solution schemes place different restrictions on the solutions.

One of these restrictions results from the Courant limit. The Courant stability limit is based on the time that it takes for parcels of fluid or pressure waves to travel completely through a control volume. The calculational timestep must be less than the Courant limit. In practice, the pressure wave propagation is frequently less critical to the evaluation, since that level of detail is usually not required [1].

2.3.1 Discretization and Time Step

The conservation equations and closure models involve many differential equations. The numerical solution schemes require that these equations be discretized. The time step size is important in determining the runtime for the system code. The timestep size can be limited by the numerical solution method. The following sections will discuss these considerations for the system codes.

RELAP5-3D

Code speed in RELAP5-3D is improved by limiting use of implicit numeric evaluation to terms important to sonic wave propagation and phenomena with small time constants (e.g. velocity in the mass and energy transport terms, pressure gradient in the momentum equations, interface mass and momentum exchange terms) [22].

Additional computing speed improvement is achieved by selecting time-level evaluations so that resulting implicit terms are linear in the new time variables. Taylor series expansions about the old-time values are developed to retain nonlinearities and obtain a formulation that is linear in the new time variables. The linear formulation eliminates the need to iteratively solve systems of nonlinear equations [22].

RELAP5-3D has a nearly-implicit option that allows violation of the Courant limit. In general, this numeric scheme is suitable for steady-state calculations and quasi-steady transients. This scheme is based on a fractional step (multiple step) method. The equations are split into fractional steps that are based upon physical phenomena. The nearly-implicit scheme has two steps. The first step solves all seven conservation equations, treating the interface exchange process, pressure propagation process and momentum convection process implicitly. The finite-difference versions of the conservation equations used in the nearly-implicit solution method are exactly the same as the expanded equations solved in the semi-implicit scheme, except that the convective terms are evaluated implicitly (in linearized form) instead of in an explicit donored fashion (as in the semi-implicit scheme). The second step solves the unexpanded form of the mass and energy equations using the final junction velocities and interface exchange terms resulting from the first step. The interface heat and mass exchanges are computed using the partial solution from the first step [22].

The difference equations are built on a staggered mesh, where scalar properties (such as pressure, specific internal energies, and void fraction) are defined at cell centers and vector quantities (such as velocities) are defined on cell boundaries [22].

TRACE

Two options are available for numerical solution in TRACE. The first is called the Stability-Enhancing Two-Step (SETS) method, which the code uses by default. The second method (available as a user option) is a semi-implicit method similar to that used by the RELAP5-3D code. The advantage of the SETS method is that it effectively eliminates the Courant stability limit. The disadvantage of the SETS method is that it results in relatively higher numerical diffusion. The semi-implicit technique has less numerical diffusion, but the Courant limit is more of an issue [1].

The semi-implicit method relaxes the effect of the Courant limit restrictions by evaluating the terms that are involved in pressure wave propagation at the new time level. This means that new-time values in the pressure gradient term are needed in the momentum equation. The velocities involved in the flux of mass and energy must also be evaluated at the new-time. The mass, momentum, and energy conservation equations are thus re-written with new-time variables. This makes it possible for information about a pressure disturbance in any cell available to any other cell during the same time step. Since the pressure wave information is available at every point during each timestep, the sound speed is removed as part of the Courant stability calculation, leaving only the fluid velocity as part of the Courant stability limit. This means that fluid parcels must not cross an entire volume during a single timestep. This version of the Courant limit is frequently called the material Courant limit [1]. Two independent variables are selected to complete the problem definition. For simplicity, the pressure and temperature are chosen. Pressure is selected because small errors in the pressure solution will have even smaller error in density. The temperature is chosen since it simplifies two-phase calculations that assume the vapor/gas phase is a mixture of different gases at the same temperature. Density and internal energy are functions of pressure and temperature. The combination of the discretized flow equations and the equations of state results in a coupled set of nonlinear equations. TRACE uses an iterative method to get a

solution to these equations [1]. The force terms can be made more stable if the fully implicit equations are linearized. This is done by assuming small changes in the new-time velocity from the old-time velocity and substituting these terms into the wall friction expression and the interfacial drag expression. This results in more stable solution behavior [1].

The SETS method was developed with the goal of eliminating the material Courant stability limit with minor changes to the semi-implicit method. This method is documented in detail in Reference [1]. Recall that the semi-implicit method effectively propagates information about sound waves. In the SETS method, a correction step was devised to propagate information for continuity waves. Consider a single-phase mass equation. For each time step the semi-implicit method is used to establish the new time velocity field. A correction step is then used to get a final value of the new time density. This density is dependent on new-time velocities, but it is not a fully-implicit calculation, since all the new-time velocities are known quantities. The density change information in any computational cell is propagated to all other cells within the same time step, and a correction step is devised for each of the mass, momentum, and energy equations. Mass and energy equations do the semi-implicit step first, then the corrector step. The momentum (motion) stabilizer equation is evaluated before the semi-implicit equations. Computational time is reduced by not computing temperatures and pressures that are fully consistent with densities and energies obtained from solving stabilizer mass and energy equations. The values for temperature and pressure that are used are those obtained during the semi-implicit equation step.

The momentum equation solution is identical to the semi-implicit method, but stabilizer velocities are used for momentum transport. For the solution to the mass and energy equations, the void fraction and new-time thermodynamic variables are intermediate results. Final new-time values are set by the stabilizer mass and energy equations, which are solved after the mass and energy equations. Final new-time values are only computed for void fraction, macroscopic densities and macroscopic energies. The thermodynamic equation of state is not used after the stabilizer mass and energy equations are solved. When basic

thermodynamic variables are needed to evaluate viscosity or heat transfer coefficients, the values from the previous semi-implicit step are used to save computational time [1].

The SETS method is not unconditionally stable. The heat transfer and friction coefficients are still evaluated at the old time, and some problems can result in bounded instabilities [1].

Similar to RELAP, a staggered mesh is used for 1D components, where velocities are defined at mesh-cell interfaces and pressure, gas volume fraction, temperatures, internal energy, and density are defined at mesh-cell centers. Scalar field equations (mass and energy) apply to a mesh cell, while velocity component motion equations apply to the interface between mesh cells in the three velocity-component directions [1].

WCOBRA-TRAC / TRAC-M

The numerical solution routines used in the WCOBRA-TRAC code were largely imported from the TRAC-M code. The numerical solution routines used in the TRAC-M code were largely implemented in the TRACE code [3]. It is therefore unnecessary to describe the WCOBRA-TRAC or TRAC-M methods, since they were already described in the TRACE section (2.3.1).

ATHLET

The In ATHLET, a finite-volume approach is used to bound the conservation equations for solution. The mass and energy equations are solved within control volumes, while the momentum equations solved over junctions between control volume centers. Thus, pressures and temperatures are solved at cell volume centers, and velocities are solved at volume junctions. The mixed momentum flux terms from the 5-equation model described in section 2.1.6 are discretized using a first-order upwind scheme. In order to allow large timesteps, the ATHLET code uses Euler solutions at the new time to support an extrapolation algorithm. The extrapolation technique also helps control the discretization errors introduced by the

solution discretization in time [26].

CATHARE

CATHARE discretizes all the terms in the six-equation model and the closure relationships fully implicitly in 1D (e.g. pipes) and 0D (boundary condition) components and semi-implicitly in 3D (vessel) components. The discretization includes mass exchange between phases, as well as the pressure and convection terms. The non-linear equations that result are solved using iterative Newton solver methods. The CATHARE code supports multiple processors [5].

2.3.2 Matrix Solution

RELAP5-3D

In RELAP5-3D, the equations are formed into a linear time-advancement matrix that is solved by direct inversion using a border-profile lower upper (BPLU) solver [22]. The BPLU solver is used to efficiently solve sparse linear systems of the form AX = B. It is designed to take advantage of pipelines, vector hardware, and shared-memory parallel architecture to run fast. BPLU is most efficient solving systems that correspond to networks, such as pipes, but it is efficient on any system that can be permuted into border-banded form. BPLU is an efficient direct LU factorization scheme that minimizes both fill-in and wasteful operations with zero. The sparse-matrix solver can also be used based on user-input.

The system of RELAP5-3D governing equations and the assumptions in their development do not result in a well-posed problem. This is resolved by selective implicit evaluation of spatial gradient terms at the new time, donor formulations for the mass and energy flux terms, and the use of donor-like formulation for momentum flux terms (donor-like because momentum flux formulation consists of a centered formulation for spatial velocity gradient plus a numerical viscosity term) [22]. The RELAP5-3D code is limited to first order accu-

racy, and although the code offers 3D capabilities, the number of 3D components is limited by the input model format.

TRACE

The solution of the system of equations is made by direct solution for the velocity terms as linear functions of pressure in the TRACE system code. The velocity equations are substituted into the mass and energy equations, and the system is solved using Newton iteration to get pressures, temperatures, void fraction and mass fraction of noncondensable gas. TRACE uses a finite volume solution of discretized, volume-averaged conservation equations with closure relations. Direct Gaussian elimination of the 5X5 linear system is used for 1D components [1]. The 3D components in TRACE use the Capacitance Matrix Method [1].

Well-posedness in the TRACE code relies on the introduction of minor modifications to field equations by the numerical solution procedures [1]. Due in part to standard models for interfacial drag and reasonable finite-difference nodalizations, the problem solved is numerically well-posed.

WCOBRA-TRAC TRAC-M

As with the numerical solution and discretization, the TRACE code has adopted the methods used in TRAC-M and WCOBRA-TRAC. The details of the WCOBRA-TRAC and TRAC-M solution methods are the same as those presented in section 2.3.2 [3].

ATHLET

A Forward-Euler, Backward-Euler (FEBE) technique is used to perform the time integration of the thermo-fluid dynamics. It solves the general non-linear system of differential equations of first order that results from the conservation equations [26]. The system is split into two

parts. The first part is integrated explicitly, and the second implicitly. Generally, the fully implicit option is used. The linear-implicit Euler system requires calculation of the Jacobian matrix. Generally, the Jacobian matrix is sparse. A block sparse matrix solver is used to efficiently compute the Jacobian matrix, as well as the linear system of equations that results. The sparse matrix solver is called FTRIX, and is a separate package from ATHLET. FEBE is also a separate package from ATHLET. The codes are coupled together by a programming interface.

CATHARE

CATHARE has a first-order finite volume, finite-difference scheme with staggered mesh and donor cells. It uses a Newton-Raphson iterative method with fully implicit discretization for 0D and 1D modules. The 3D module is semi-implicit. CATHARE has a well-posed, hyperbolic system of equations [30].

2.3.3 Code solution Summary

The significant code solution strategies are summarized in Table 2.6. In all cases, more detailed information about the information presented in the table is available in the applicable code section.

2.4 Significant Code Assumptions

System codes are forced to make significant assumptions to simplify the solution schemes and make solutions possible. The first major assumption is used by all of the codes; the assumption that the component-based approach is adequate. Each code models plant hardware and equipment as self-contained components of the reactor coolant loop system. These components are nodalized into physical volumes. The fluid conditions are averaged within these volumes, and the averaged values are used in the conservation equations. It is a sig-

nificant assumption that reactor system components can be modeled accurately using these methods. A related assumption made by all the codes is that the coolant properties are constant throughout the control volumes. This has the effect of making the volume average pressure (or temperature, or other scalar property) the pressure at the center of the volume. For very large volumes or very fast transients, this may not be a valid assumption. It may also be invalidated if the volume has more than one outlet or inlet junction, which would allow fluid flow to or from multiple sources, resulting in differences in pressure, flow, or temperature within a single volume.

Another assumption common to all the system codes presented here (with the exception of RELAP-7) is that the pressures in the two-phases (vapor and liquid) are equal, and the interfacial pressure is assumed to be equal to the vapor/liquid pressure as well. This simplifies the solution of the momentum conservation equations, but does introduce the possibility of inaccuracies during transient analyses where phase change or flow changes are occurring rapidly. This assumption is not generally used for stratified flows [22, 1, 26]. In addition, the interface temperature between the phases is assumed to be equal to the saturation temperature for these system codes. This reasonable assumption simplifies the calculation.

All the system codes considered here assume that the noncondensable gas and dissolved solute move with the vapor and liquid as appropriate, with minimal interactions with the working fluid. The noncondensable gas field is assumed to be in thermal equilibrium with steam. It is also assumed that Dalton's law applies, so that the total pressure = Partial Pressure of vapor/steam + Partial Pressure of noncondensable gas.

None of the codes allow for noncondensable gas to go into solution with the coolant. When noncondensable gases are included in the codes, they are only included as mixtures with the vapor phase. In actual operation, some percentage of the noncondensable gases can dissolve into solution in much the same way that carbon dioxide is in solution in soft drinks. Just as with soft drink containers, the gas thus dissolved in the reactor coolant can come

out of solution rapidly if the pressure suddenly drops. This can cause gas bubbles to appear to transport around the reactor system with pressure pulses.

Fluid convected from one volume to another is assumed by these codes to be homogeneously mixed, and therefore has the same properties as the average properties of the source volume. This tends to cause numerical diffusion, which smears out the gradient of the fluid properties within the flow passage being modeled. This can also result in errors in mass and energy flux calculations when there is substantial phase separation in the upwind volume [2].

The RELAP, TRAC-M, WCOBRA-TRAC, and TRACE codes use a quasi-steady assumption for the heat transfer coupling between the wall and the fluid. They also use the assumption for the closure relations for interfacial and wall-to-fluid heat transfer and drag. This assumption requires detailed knowledge of the local fluid parameters and ignores the time dependencies, so the time rate of change in the closure relationships is infinite, which drives the time constants to zero. This approach is reasonably simple and generally applicable to a wide range of problems [3, 4, 1, 2].

Abrupt area changes in transient two-phase flows in RELAP assume that the flow process is quasi-steady. Thus, the transient inertia, mass, and energy storage are neglected, and the flow process can be satisfied by the upstream and downstream conditions at discrete times during the transient [22]. This same assumption is made in the TRACE and TRAC-based codes. Abrupt area changes also require the code, the user, or both to provide loss coefficients to accurately capture the effects irreversible losses due to abrupt area changes. The abrupt expansion model in TRACE assumes that the pressure and velocity profiles are uniform at the cell junctions above and below the interface. This simplifies the calculation of the pressure drop across the expansion using a control-volume analysis and the Bernoulli equation [1].

When zirconium cladding interacts with steam at a sufficiently high temperature, an exothermic oxidation reaction can occur. The metal-water reaction model in RELAP is used to model the heat addition from this reaction. The RELAP reaction model assumes that there is always enough steam for the reaction to continue. The model does not include the

capability to reduce the reaction rate due to insufficient steam. The code does account for the available cladding material, and reduction or elimination of the cladding as a result of the reaction will limit the reaction [22].

The TRACE and TRAC codes include similar models for the heat generated by the zirc-water reaction. It is unclear from the literature if lack of steam will limit the reaction rate, but based on the model details presented in the manuals, it seems likely that the same assumption holds, and sufficient steam to continue the reaction is assumed to be available [1]. ATHLET is different, and includes the capability to reduce or stop the reaction due to lack of steam [26].

TRAC-M, WCOBRA-TRAC, and TRACE also assume that the volumetric flow from a cell center to the cell edge is a constant value [4, 3, 1]. This assumption permits simple calculation of the velocity at the center of the cell based on the velocity at the cell edge. Recall that the codes calculate vector quantities (like velocity) at cell edges, so values for the velocity at a cell center must be computed using other methods. If a large variation in fluid void fraction within a mesh cell is present, it can result in a conservation error in the momentum-flux due in part to the assumption of constant volumetric flow [1]. The assumption that the average macroscopic density at the cell edge is equivalent to that at the cell center is an additional part of the error in momentum conservation for analysis problems with rapidly changing void fractions.

Since the TRACE code uses a 6-equation, two fluid model, the droplet velocities for the drag and interfacial heat transfer calculations must be inferred. TRACE assumes that the droplet velocity is approximately the same as the vapor velocity in the annular/mist flow regime. This simplifies the calculations, but may not be accurate, since the droplets will behave differently from a vapor flow [1]. This is similar to the methods and assumptions used in TRAC-M and WCOBRA-TRAC.

Choked or critical flow occurs at the location of a pipe break or in sections of flow area reduction within the plant. The mass flow through the choked region is limited and will not

increase if the downstream pressure is decreased. This maximum flow is computed by the codes using choked flow models [3, 4, 1, 2]. Since choked flow often occurs during a pipe rupture, the choked flow models must include two-phase effects. The RELAP5, TRAC-M, WCOBRA-TRAC, and TRACE codes assume that the liquid and vapor within the choked region are in thermal equilibrium [3, 4, 1, 2]. This is a reasonable assumption, since the flow does not spend much time in the choked region, so the effect of heat transfer between the phases will be minimal.

The field equations in all the system codes were derived assuming that viscous shear stresses within a given phase are negligible [3, 4, 1, 2]. Due to this assumption, the codes do not include the viscous effects, and should not be used for situations where the viscous stresses would be the same or larger than the wall or interfacial shear stresses. Explicit turbulence modeling is not coupled to the conservation equations for any of the codes (although turbulence effects can be accounted for with specialized engineering models for specific situations).

The major assumptions are summarized for the codes in Table 2.7.

2.5 Closure Relations

The conservation equations discussed in section 2 of Reference [12] are often simplified by averaging over volume and time. The closure relations compensate for information that is lost during the averaging process, in addition to making the conservation equation set solvable. There are many closure relationships available for each flow regime. The vertical flow regimes are shown in Figure 2.12. Figure 2.13 shows the horizontal flow regimes. The vertical post-CHF flow regimes are depicted in Figure 2.14. The flow regimes are discussed in greater detail in Reference [12].

The closure relationship that is selected for a particular flow condition or situation can affect the analysis results in significant ways. Many of the differences between the codes result from the selection and application of the closure relationships. The closure relationships

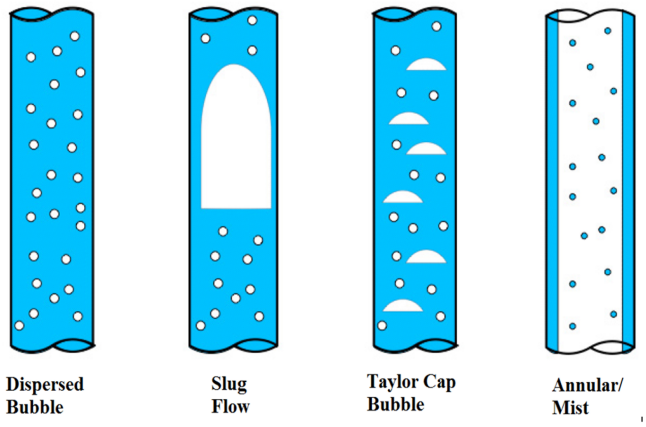

Figure 2.12: Vertical Pre-CHF Flow Regimes [1]

determine the key parameters that are required for solution of the conservation equations, and can affect the solution methods. Some closure relationships require re-meshing of regions in the model. This re-meshing can change the solution time, as well as the accuracy and stability of the solution. Closure relationships are critical to obtaining a solution, but they can also affect solution methods, techniques, and stability. In conjunction with numerical stability concerns, some closure relationships can improve computational speed. In many cases, the availability of closure models does not allow for selection based on speed, but for those cases where one model is decidedly faster than another, the user should be aware of the consequences of the model selection.

The following sections discuss details of selected closure relations used in the compared system codes. The selected closure relationships illustrate some of the significant differences between the codes without providing a complete description of all the relationships for every system code. A complete characterization of the closure relations for even a single system code would require much more explanation than is possible here. Complete explanations of the closure relationships are available in the user manual for each system code.

The mass and energy governing equations balance the exchange of mass between the phases. The energy equation accounts for temperature changes as heat transfers from one phase to another. The closure relations compute the necessary details to solve the balance

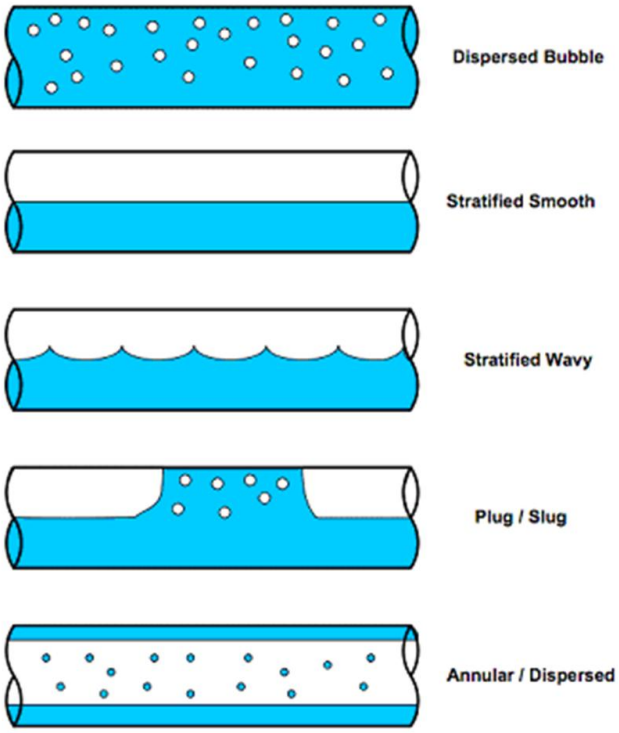

Figure 2.13: Horizontal Flow Regimes [1]

equations. Closure relationships compute heat transfer rates between phases, heat transfer coefficients between phases and the walls, the viscous shear in the flow, mass exchange among fields at the phase boundaries, momentum exchange at the phase interfaces, drag forces at the solid boundaries, turbulence terms in the continuous fields, droplet entrainment and de-entrainment, and other information. The point of Critical Heat Flux (CHF) is a closure relationship that is used to distinguish between flow regimes that have liquid in contact with the wall and those that are experiencing dryout, and there is little or no liquid contact with the wall.

2.5.1 Interfacial Drag

Interfacial drag models have been selected and implemented for the flow regimes discussed previously. The complexity of the individual models and the number of regimes limits what can be covered in this document. The bubbly flow regime has been selected to illustrate the

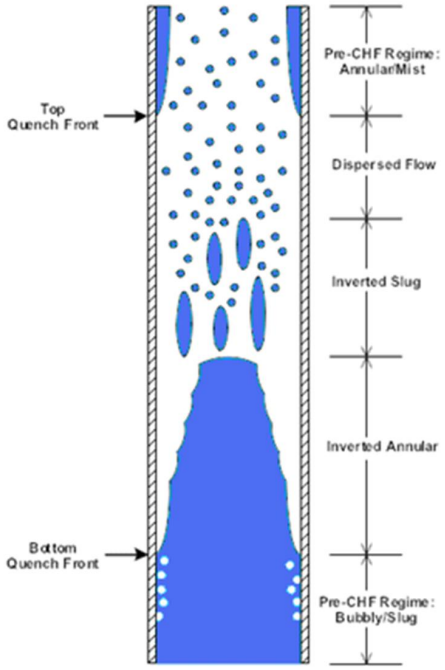

Figure 2.14: Inverted flow regimes for post-CHF [1]

application of interfacial drag in the system codes discussed here. Each of the system code models is considered in turn to provide adequate comparison of their capabilities.

RELAP5-3D: Bubbly Flow

Both the bubbly and the droplet flow regimes are considered to be dispersed flows. The interfacial drag is affected by the inclination angle of the flow. For vertical bubbly flows, the drift flux model is used. For non-vertical bubbly flow and all of the droplet flow regimes, the drag coefficient model is used.

Horizontal and Mist Flows Dispersed bubbles or droplets are assumed to be spherical particles with a Nukiyama-Tanasawa distribution [31]. The probability (p^*)of particles with a nondimensional diameter d^* is defined in Equation 2.118.

$$p^* = 4d^{*2}e^{-2d^*} \tag{2.118}$$

The nondimensional diameter is computed as shown below:

$$d^* = \frac{d}{d'} \tag{2.119}$$

Where d' represents the most probable particle diameter. The average particle diameter can be computed as:

$$d_o = 1.5d' \tag{2.120}$$

Which leads to the derivation of the surface area per unit volume:

$$a_{gf} = \frac{6\overline{\alpha}}{d'} - \frac{\int d^{*2} p^* dd^*}{\int d^{*3} p^* dd^*} = \frac{2.4\overline{\alpha}}{d'} \tag{2.121}$$

In the above formulas, $\overline{\alpha}$ is equivalent to α_g if in a bubbly flow regime, and α_f for a mist (droplet) flow. If Equation 2.120 is solved for d' and substituted into the right-hand side of Equation 2.121, the interfacial surface area per unit volume can be obtained from the average diameter (d_o) as shown in Equation 2.122.

$$a_{gf} = \frac{3.6\overline{\alpha}}{d_o} \tag{2.122}$$

Some simplifying assumptions on the probable particle diameter are used to simplify the calculation of the interfacial area. Equation 2.122 defines the interfacial area in terms of the average particle diameter, which is defined in terms of the "most probable" particle diameter (d'). In the RELAP5-3D code it is assumed that the average particle diameter (d_o) can also be defined in terms of the maximum particle diameter as $d_o = {}^1/_2 d_{max}$. The maximum particle diameter is dependent on the critical Weber number. The critical Weber number is computed as shown in Equation 2.123.

$$We = \frac{d_{max}\rho_c \left(v_g - v_f\right)^2}{\sigma} \tag{2.123}$$

The values for We are assumed to be $We = 10.0$ for bubbly flow, $We = 3.0$ for mist-pre-CHF flow, and $We = 12.0$ for mist and mist-post-CHF flows. Based on these assumptions, Equation 2.123 can be recast to solve for d_{max}, which can then be used to solve for the interfacial area per unit volume.

The drag coefficient for non-vertical bubbly and all droplet flows is computed from the correlation developed by Ishii and Chawla [32]. The drag coefficient thus developed is:

$$C_{D,i} = \frac{24\left(1.0 + 0.1Re_p^{0.75}\right)}{Re_p} \tag{2.124}$$

The particle Reynolds number Re_p is:

$$Re_p = \frac{|v_g - v_f| d_o \rho_c}{\mu_m} \tag{2.125}$$

The continuous phase density (ρ_c) is shown in Equations 2.123 and 2.125 and is assumed to be ρ_l for bubbles, and ρ_g for droplets. The mixture viscosity (μ_m) is also assumed to be the viscosity of the continuous phase and is computed for mist pre-CHF as shown below:

$$\mu_m = \begin{cases} \frac{\mu_f}{\alpha_f} \text{ for bubbles} \\ \frac{\mu_g}{(\alpha_g)^{2.5}} \text{ for droplets} \end{cases} \tag{2.126}$$

For mist and mist post-CHF droplets, it is assumed that $\mu_m = \mu_g$.

Vertical Bubbly Flow Recall that the same interfacial drag correlations are used for horizontal and vertical droplet flows. For bubbly flows, a drift flux model is used in the computation of the interfacial drag. The drift flux model used in RELAP is determined by geometry and flow conditions. Seven correlations are used for various flow geometries and velocities. The correlations are listed below, with references [29]: EPRI [33] updated in [34] and [35], Griffith [36], Churn-turbulent bubbly flow [37], Katoka-Ishii [38], and Zuber-Findlay [39] and [40].

The correlation used is selected based on flow geometry, mass flow rate, and direction; the geometries considered in the code are: Rod Bundles, Narrow Rectangular Channels, Small pipes (Diameter $<$ 0.018 m), Intermediate pipes (0.018 m $<$ D $\leq$ 0.08 m), and Large pipes (D $>$ 0.08 m).

The flows are divided into upflow and downflow and range from 1500 kg/m^2sec downflow to 100 kg/m^2sec upflow. Flow rages outside this range use the correlation defined for the maximum in that flow direction. Transitions between the defined mass flow rates are generated by linear interpolation. More details are provided in the RELAP manuals [22] [2].

TRACE

The interfacial drag force per unit volume in TRACE is computed by:

$$F_i^{'''} = C_{D,i} V_r |V_r| \tag{2.127}$$

The interfacial drag coefficient ($C_{D,i}$) is computed based on flow regime. The flow regimes are divided into three classes as described in the Flow Regime Section of [12]. The pre-CHF flow regimes are dispersed bubble, cap/slug bubble, and annular-mist. There are also interfacial drag models for stratified flows.

The models used in TRACE for interfacial drag in the pre-CHF flow regimes are used for both vertical and horizontal geometries. This is different from the RELAP5 code, which uses unique models for vertical bubbly flows (2.5.1). For the special case of stratified flows, TRACE uses stratified flow models. TRACE has models for bubbly flow regimes with pipe or rod bundle geometries. For pipe geometry, the code considers two sub-groups of the bubbly/slug region. They are: dispersed bubbly flow and slug or Taylor cap bubbly flow. The dispersed bubbly flow is characterized by relatively small bubbles that may be spherical or distorted. The slug of Taylor cap bubbly flow consists of larger bubbles that are either slugs (in smaller diameter pipes) or Taylor cap bubbles (large diameter pipes).

The only type of dispersed bubbly flow that is modeled is churn-turbulent flow. Wallis [31] describes the regime as something of a transition region between the "ideal bubbly flow" and slug flow, where large bubbles fill the tube. The flow pattern is agitated and unsteady. The Ishii correlation was selected for the churn-turbulent regime.

The interfacial drag coefficient must be computed to properly account for the interfacial drag force and to compute the relative velocities of the phases. Equation 2.128 is used to compute the interfacial drag coefficient.

$$C_{D,i} = \frac{\alpha\left(1-\alpha\right)^3 g\Delta\rho}{\overline{v}_{gj}^2}\cdot P_s \tag{2.128}$$

The interfacial drag is dependent on two additional terms: the drift flux velocity ($\overline{v}_{gj}$) and the profile slip factor (P_s). The drift flux velocity is given in Equation 2.129. The profile slip factor is calculated as shown in Equation 2.130.

$$\overline{v}_{gj} = \sqrt{2}\left(\frac{\sigma g\Delta\rho}{\rho_l^2}\right)^{1/4} \tag{2.129}$$

$$P_s = \frac{\left(\frac{1-C_0\langle\alpha\rangle}{1-\langle\alpha\rangle}\overline{V}_g - C_0\overline{V}_l\right)^2}{V_r^2} \tag{2.130}$$

The distribution parameter (C_0) seen in the profile slip factor represents the cross-sectional area averaged gas and liquid velocities resulting from the radial distribution of the void and velocity. The calculation of the distribution parameter is defined as shown in Equation 2.131. The development of the distribution parameter is discussed in detail in Reference [6]. An example plot showing the vapor velocity vs. total volumetric flow for a fully-developed two-phase flow regime of steam and water is shown in Figure 2.15. Note that the data points are clustered around a straight line. The linearity of the data is improved when the drift velocity is either constant or small enough to be neglected. For a given flow

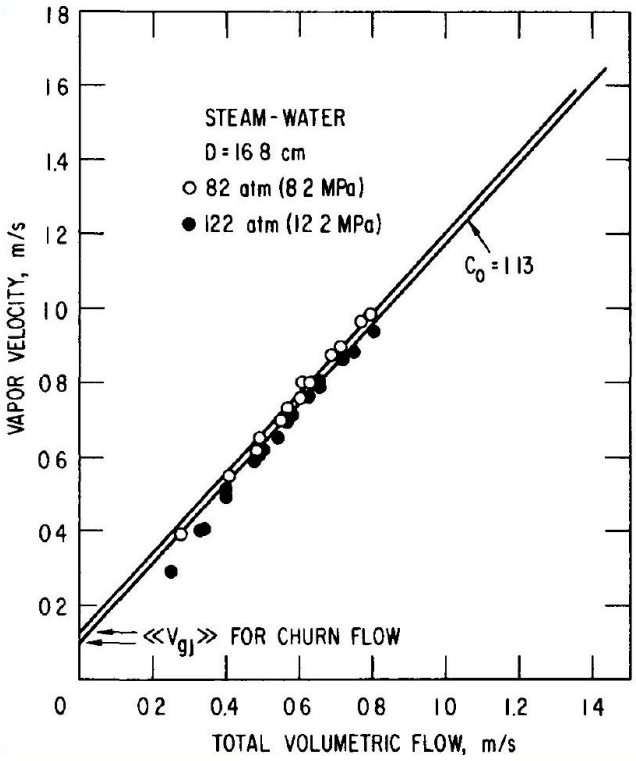

Figure 2.15: Vapor Velocity vs. Total Volumetric flow [6]

regime, the vapor velocity may be plotted as a function of the total volumetric flow, and the distribution parameter (C_0) may be obtained from the slope of the line (see Figure 2.15). Additionally, the intercept of the line with the mean velocity axis is the weighted mean local drift velocity.

The distribution parameter is dependent on pressure, channel geometry, and flow rate, but the maximum distribution parameter has been obtained from experimental results by Nikuradse [6]. The maximum value is found using a single-phase flow and varies slightly with Reynolds number, but is 1.2 for a wide range of flows in round pipe. Thus, as void fraction approaches zero, and the density ratio approaches zero, the distribution factor should approach 1.2. Similarly, as the void fraction (and density ratio) approaches unity, the distribution parameter should also become unity. Equation 2.131 shows the equation used in the TRACE code and developed in Reference [6] that meets these requirements for round pipe.

Rectangular channels use 1.35 and 0.35 in place of 1.2 and 0.2 in Equation 2.131 [6].

$$C_0 = 1.2 - 0.2\sqrt{\frac{\rho_g}{\rho_L}} \tag{2.131}$$

The code limits the churn-turbulent drift flux velocity from Equation 2.129 to be less than that for the slug flow regime to prevent unrealistic flow regimes in small diameter pipes. The remaining TRACE flow regimes (slug, annular mist, etc.) use different correlations to define the distribution parameter and drift flux velocity. Flow geometry can also affect the value of the distribution parameter. For example, in rod bundles, TRACE uses a value of 1.0, which agrees more closely with available data. The TRACE manual [1] describes these other models in greater detail.

The distribution parameter and drift flux velocity defined above can be used to compute an interfacial drag coefficient (see Equation 2.128. The interfacial drag coefficient is critical in determining the rate of bubble break up due to interfacial shear forces and relative phase velocities. All flow regimes use the interfacial drag calculation shown in Equation 2.128, but the drift velocity and distribution parameter vary depending on flow regime and flow geometry.

The interfacial drag coefficient is used primarily for closure of the momentum equations. Accurate representation of the velocities of each phase requires understanding of the forces between them. Without the interfacial drag coefficient, the velocity of the liquid and vapor phases would, by necessity, be assumed to be equivalent. In addition, the amount of interfacial drag can delay the onset of "larger bubble" regimes due to shear forces breaking up the bubbles.

WCOBRA/TRAC-TF2

The interfacial drag force in WCOBRA/TRAC is computed in much the same way as was used in TRACE. The interfacial drag force per unit volume (M_i) is computed as shown

below:

$$M_i = C_{D,i} \cdot V_r \cdot |V_r| \tag{2.132}$$

The interfacial drag coefficient ($C_{D,i}$) in Equation 2.132 is defined as:

$$C_{D,i} = \frac{3}{4} \frac{C_{Db} \cdot \alpha \rho_l}{D_b} \cdot P_s \tag{2.133}$$

The interfacial drag coefficient is the same as what appears in the WCOBRA/TRAC 1D momentum equations in Reference [12]. This coefficient is required to close the momentum equation. In order to solve for this value, the bubble diameter (D_b) and bubble drag coefficient (C_{Db}) must be known. As with the TRACE code, the values of these parameters are dependent on the flow regime. This section will describe the derivation of the interfacial drag for bubbly flow. The derivation of the profile slip factor (P_s) shown in Equation 2.132 is also shown.

The bubble diameter is computed as described by Ishii [41] and shown in Equation 2.134 is stated by Ishii to be an approximate arithmetic average of the minimum and maximum bubble diameters in the flow.

$$D_b = 2 \cdot \sqrt{\frac{\sigma}{g\left(\rho_l - \rho_g\right)}} \tag{2.134}$$

The bubble drag coefficient is defined based on the bubble Reynolds number (Re_b), which is shown below

$$Re_b = \frac{D_b V_r \rho_l}{\mu_l} \tag{2.135}$$

The bubble drag coefficient is then determined:

$$C_{Db} = \begin{cases} 240 & Re_b \leq 0.1031 \\ \frac{240.0}{Re_b}\left(1.0 + 0.15 Re_b^{0.687}\right) & 0.1031 < Re_b < 989.0 \\ 0.44 & Re_b \geq 989.0 \end{cases} \tag{2.136}$$

The profile factor (P_s) is designed to account for the redistribution of the bubbles in the flow channel due to the velocity profile. Higher flow velocities are concentrated in the center of the channel. The bubbles tend to migrate to the higher-velocity regions. The profile factor attempts to compensate for the increased void fraction in the central region of the flow and the corresponding increase in slip between the phases. This factor originated in reference [41], and is computed as shown below.

$$P_s = \frac{\left(C_l V_g - C_0 V_l\right)^2}{V_r^2} \tag{2.137}$$

Where the distribution parameters (C_0 and C_l) are given (note the similarity to the TRACE equations):

$$C_0 = 1.2 + 0.2\sqrt{\frac{\rho_l}{\rho_g}} \tag{2.138}$$

$$C_l = \frac{1.0 - C_0 \alpha}{1.0 - \alpha} \tag{2.139}$$

Reference [6] provides more details on the development of the distribution coefficient (C_0). The slug flow uses a different bubble diameter calculation, but the rest of the equations shown here provide the basis for the interfacial drag in the slug flow as well.

TRAC-M

As with the TRACE and WCOBRA/TRAC codes, the interfacial drag coefficient ($C_{D,i}$) is required in order to close the momentum equations in TRAC-M. As before, the value of this coefficient is dependent on flow regime. The equation used to determine the drag coefficient is identical to that used for the WCOBRA/TRAC code (Equation 2.132. If bubbly slug flow develops in an upper plenum, the interfacial drag coefficient is redefined based on the correlation developed by Wilson [42]. This model is implemented in the vessel (3D) components. Details of this model are available in reference [21].

The definition of the bubble diameter (D_b) is similar to that shown in Equation 2.134, but an additional term, XS is included in the equation below.

$$D_b = 2\sqrt{\frac{\sigma}{g\left(\rho_l - \rho_g\right)}}\left(1 - XS\right) + min\left(40\sqrt{\frac{\sigma}{g\left(\rho_l - \rho_g\right)}}, 0.9D_h\right) \cdot XS \tag{2.140}$$

where XS is defined as:

$$XS = \begin{cases} 0.0 & \text{bubbly flow} \\ \frac{2700-G}{2700-2000} \cdot \frac{\alpha-0.3}{0.5-0.3} & \text{bubbly slug transition} \\ \frac{\alpha-0.3}{0.5-0.3} & \text{bubbly slug flow} \end{cases} \tag{2.141}$$

Note that for simple bubbly flow, equation 2.140 reduces to the same equation used in WCOBRA/TRAC (2.134). In addition to the above definitions, the bubble diameter must be constrained as shown below:

$$0.0001 \text{ m} < D_b < min\left(40\sqrt{\frac{\sigma}{g\left(\rho_l - \rho_g\right)}}, 0.9D_h\right) \tag{2.142}$$

The profile slip factor (P_s) is computed as shown previously (Equation 2.137).

It has been shown that the models developed here are very similar to those used in

the WCOBRA/TRAC code. This is to be expected as TRAC is the basis for the WCOBRA/TRAC code. The details of the TRAC-M models, as well as further discussion of the interfacial drag for the remaining flow regimes, are provided in [21].

ATHLET

The equation of motion derived from the momentum and continuity equations for two-phase flow is used to balance inertia, interfacial shear, wall friction, gravitation and pressure forces acting on the phases. This balance can be used to derive the steady-state interfacial shear force. Assuming that local variations of the phase momentum flows are negligible and that the pressure of both phases is the same for every location in the flow, the following equation can be derived:

$$\frac{C_{D,i}}{\alpha\left(1-\alpha\right)}\left(w_v - w_l\right)\left|w_v - w_l\right| = -\frac{C_{w,V}}{\alpha}w_v|w_v| + \frac{C_{w,L}}{1-\alpha}w_l|w_l| + g\left(\rho_L - \rho_V\right)\sin\theta \tag{2.143}$$

The local drift flux velocity is computed from the flooding-based drift flux model documented in reference [43] and shown below:

$$w_{V,j} = C_0\left(\frac{3}{4}\right)^2 w_{0L}\frac{-\frac{1}{2} + \sqrt{\frac{1}{4} + B^2}}{B^2} \tag{2.144}$$

Where the B term is defined:

$$B = \frac{C_0\alpha\left(\frac{3}{4}\right)^2 w_{0L}}{\left(1 - C_0\alpha\right)w_{0V}} \tag{2.145}$$

In the equations above, the limiting superficial liquid (w_{0L}) and vapor (w_{0V}) velocity are defined as:

$$w_{0L} = \left(gD \frac{\rho_L - \rho_V}{\rho_L} \right)^{\frac{1}{2}} \tag{2.146}$$

$$w_{0V} = \left(gD \frac{\rho_L - \rho_V}{\rho_V} \right)^{\frac{1}{2}} \tag{2.147}$$

The ATHLET code defines the interfacial drag as a function of the drift flux parameters as shown below [26]:

$$\tau_i \frac{Perim_i}{A} = C_{D,i} w_r |w_r| = \alpha (1-\alpha) \frac{g \Delta \rho}{\left(\frac{w_{V,j}}{1-\alpha} \right)^2} w_r |w_r| \tag{2.148}$$

Where the cross sectional average relative velocity (w_r) is calculated using the regime-dependent phase distribution parameter C_0.

$$w_r = \frac{1 - \alpha C_0}{1 - \alpha} w_v - C_0 w_l \tag{2.149}$$

The phase distribution parameter (C_0) is computed for vertical ($sin\theta \geq 0.2$) flow in cylindrical pipes by

$$C_0 = \min \ (C_{01}, C_{02}, C_{03}) \tag{2.150}$$

Where $C_{01},\ C_{02}$, and C_{03} are defined as:

$$C_{01} = 1 + \left(0.2 - 0.2\sqrt{\frac{\rho_V}{\rho_L}}\right)\left(1 - e^{-18\alpha}\right) \tag{2.151}$$

$$C_{02} = 1 + \frac{(1-\alpha)\,(1-E_d)}{\alpha + \sqrt{\frac{1+150(1-\alpha)}{\sqrt{\alpha}}\frac{\rho_V}{\rho_L}}} \tag{2.152}$$

$$C_{03} = \frac{w_{V0}}{\alpha w_{V0} + \sqrt{\alpha}\,(1-\alpha)\,\frac{9}{16}w_{L0}} \tag{2.153}$$

Determination of the fraction of dispersed liquid (E_d) is covered in detail in the references [26]. This term is essentially the volume of the dispersed liquid divided by the total liquid volume (both dispersed and non-dispersed). An S-shape correlation is used to compute the dispersed liquid fraction.

The distribution parameter for horizontal flow is computed in a similar manner, as shown below:

$$C_0 = \min\ (C_{01}, C_{02}) \tag{2.154}$$

$$C_{01} = 1 + \left(0.5 - 0.5\sqrt{\frac{\rho_V}{\rho_L}}\right)\left(1 - e^{-18\alpha}\right) \tag{2.155}$$

$$C_{02} = 1 + \frac{(1-\alpha)\,(1-E_d)}{\alpha + \sqrt{\frac{1+75(1-\alpha)}{\sqrt{\alpha}}\frac{\rho_V}{\rho_L}}} \tag{2.156}$$

The details of the calculation of the distribution parameter for the other flow regimes are provided in reference [26].

CATHARE

The CATHARE code uses a drift-flux model to compute the interfacial drag on the bubbles in bubbly flow. The drift flux model can be translated in terms of interfacial friction

correlations. A general expression of the drift velocity model is shown in the equations below:

$$V_g = C_0 J + V_{g,j} \tag{2.157}$$

$$V_{g,j} = C_m \left[g \Delta \rho \mathcal{L}_m / \rho_{mdl} \right]^{1/2} \tag{2.158}$$

Where C_m and $\mathcal{L}_m$ are a model constant and a model length scale. The C_0 term is a distribution factor for the position of the vapor bubbles in the flow. In vertical flows, buoyancy and interfacial friction are dominant. The CATHARE momentum balance equations [12] can be reduced to the interfacial shear for vertical flow:

$$\tau_i = \alpha \left(1 - \alpha\right) \Delta \rho g \tag{2.159}$$

From the drift flux model shown in Equations 2.157 and 2.158 and Equation 2.159, the buoyancy term can be eliminated, and the interfacial shear for horizontal (non-buoyant) flows is obtained:

$$\tau_i = \alpha \left(1 - \alpha\right) \frac{1}{C_m^2} \frac{\rho_m}{\mathcal{L}_m} \left(1 - C_0 \alpha\right)^2 \left[v_v - \frac{C_0 \left(1 - \alpha\right)}{1 - C_0 \alpha} v_l \right]^2 \tag{2.160}$$

The $\mathcal{L}_m$ and C_m terms are dependent on flow configuration. The CATHARE code has three possible configurations: rod bundles, pipes, and annuli. This discussion will be limited to pipe flows. Further details on the development of the models are available in reference [27].

For bubbly pipe flow, the drift velocity ($V_{g,j}$) is:

$$V_{g,j} = \left[\frac{g \Delta \rho \mathcal{L}_m}{K_L \rho_L + K_G \rho_G} \right]^{1/2} \tag{2.161}$$

Where the K_L and K_G terms are obtained from fits to available data. Details of these parameters were not discussed in the available literature [27],[44],[30],[5]. The model length

scale ($\mathcal{L}_m$) is:

$$\mathcal{L}_m = \left(\frac{1}{D^2} + \frac{1}{f^2(\alpha)\,\sigma/g\Delta\rho} \right)^{-0.5} \tag{2.162}$$

Equation 2.162 can be substituted into Equation 2.158 to solve for C_m. Similarly, if the mixture superficial velocity (J) and vapor velocity (V_g) are known, the distribution parameter (C_0) can be calculated from Equations 2.161 and 2.157.

2.5.2 Interfacial Heat Transfer

Heat transfer coefficients are needed to close the mass and energy balances. The heat transferred between the liquid and vapor phases, from the wall to the liquid, and from the wall to the vapor is needed for closure of the energy balance equations. The correlations are dependent on the vapor/gas or fluid temperatures relative to saturation. The flow regime is determined by the characteristics of the flow, including void fraction, fluid velocity, and superheated margin.

Interfacial heat transfer models are used to model the exchange of heat and mass between phases. The interfacial closure model that is selected is dependent on the flow regime. Interfacial heat transfer is not particularly dependent on the geometry of the flow, since it is only concerned with the transfer between phases. There are many flow regimes modeled by each of the system codes discussed herein. The specific details of the models used by each code are provided in the respective manuals. Some additional details of the correlations used in each of the codes are provided below.

RELAP5-3D

The RELAP5-3D code divides the interfacial heat transfer into four categories for each flow regime based on working fluid temperature. Each regime has correlations for superheated liquid, superheated vapor, subcooled liquid and subcooled vapor. In some cases, the correlations

are re-used (e.g. bubbly subcooled vapor uses the same correlation as bubbly superheated vapor). This amounts to 27 correlations for interfacial heat transfer in RELAP5-3D. The correlations are summarized in Table 2.8.

The bubbly superheated vapor (SHV) is an empirically based formula that is fundamentally a very large heat transfer coefficient to drive the vapor temperature down to saturation conditions. The bubbly subcooled vapor heat transfer uses the same correlation as the bubbly superheated vapor. In slug flow, the special model for the heat transfer between the Taylor bubbles and subcooled liquid coolant does not have a literature reference in the RELAP manuals, but the coefficients used in the equation fall between those known from turbulent and laminar correlations. Since the flow around Taylor bubbles is not perfectly laminar, but also not likely to be turbulent, this correlation is plausible, but could still be significantly in error. The heat transfer between the subcooled vapor Taylor bubbles and the liquid uses the heat transfer coefficient from the bubbly SHV regime and the void fraction and interfacial area from the slug SHL.

The large HTC model for Taylor bubbles with superheated liquid is an ad hoc correlation that is designed to provide a large heat transfer coefficient that will bring the vapor temperature to saturation quickly. The Brown correlation [49] is used for the droplet to vapor heat transfer for subcooled liquid conditions in the annular mist regime. This correlation is based on experimental data for plunging heated spheres into baths at uniform temperature. This model does not address the increase in droplet size due to condensation, and it models the droplet surface temperature as a constant. The convective heat transfer coefficient to the droplets is actually a conduction heat transfer model based on the thermal conductivity of water at 150 ^oF. The Theofanous correlation [50] used for the film portion of the annular mist subcooled liquid heat transfer was developed using data from vapor absorption by a turbulent, thin falling liquid film in quiescent air. This is clearly not the exact conditions of annular flow, where the vapor core will not be “quiescent”, and the liquid film may not be turbulent.

These and other concerns call into question the use of Theofanous for annular film heat conduction and the code should be assessed against experiment results. Heat transfer between the droplets and the superheated liquid in the annular mist regime is computed from a large value for the heat transfer coefficient coupled with a function that increases quadratically. Again, this is to quickly return the temperatures to saturation. The heat transfer between the liquid core and the vapor annulus in inverted annular flow with superheated vapor is from an ad hoc correlation. This correlation needs to be compared to experimental data for evaluation.

In the horizontal stratified regime with subcooled liquid conditions, the Nusselt number is based on the Dittus-Boelter correlation. Contrary to common practice, the code does not use the phasic hydraulic diameter when computing the Reynolds number that is used in the correlation. Additionally, the Dittus-Boelter correlation is valid for single-phase flow filling ducts - it has not been evaluated explicitly for partially-filled flows. More comparison to experimental results is needed to validate the use of this correlation for horizontally stratified flows. Vertically stratified regimes are computed by a combination of the horizontally stratified heat transfer correlation and the applicable flow regime.

For the remaining entries in Table 2.8, indication of large Nusselt number or heat transfer coefficient shows where large values were selected for these terms in order to drive the conditions toward saturation. In many cases, this is appropriate, since the flow conditions are unstable. The ad hoc indications should all be evaluated against experimental data for accuracy.

TRACE

The TRACE code does not characterize the interfacial heat transfer correlations based on fluid temperature in the way that is done in the RELAP code. Instead, a standard set of correlations is implemented, and modifications are made to account for alternate coolant temperatures (i.e. subcooled boiling). Otherwise, as with RELAP, correlations are used to

capture the interfacial heat transfer for each flow regime considered by the TRACE code. Table 2.9 summarizes the correlations used for each regime.

The liquid-side interfacial heat transfer for bubbly flow correlation is modified to account for near-wall condensation when in subcooled boiling. The model was suggested by Lahey and Moody [55]. Heat transfer in the transition region between bubbly/slug and the annular mist flow is computed by interpolation between those regimes. TRACE includes a flashing model for conditions where the liquid is superheated with respect to the saturation temperature. This model is very simple, and assumes a high heat transfer coefficient to bring the liquid temperature closer to saturation as quickly as possible. The flashing model is flow-regime independent. In TRACE, stratified flow is only assumed for horizontal or inclined pipes. The same Nusselt number correlations are used for stratified flows as those used for the liquid film in annular flow, but the Reynolds number is computed using the liquid-phase hydraulic diameter. The Kuhn-Schrock-Peterson [56] empirical correlation (for falling films) is used as a lower bound for the heat transfer.

Inverted annular flow is the reverse of annular flow; it is a vertical flow regime with a core of liquid water within an annulus of vapor (see Figure 2.14). The inverted annular flow uses a constant value for the liquid-to-interface Nusselt number based on results of the Fung [57] experiments and FLECHT-SEASET [58] simulations. The vapor-to-interface uses the vapor film thickness as the characteristic length in the laminar heat transfer coefficient calculation. The vapor film thickness is computed from the void fraction based on geometric formulae for a tube or rod bundle. The vapor-to-liquid and flashing modes of heat transfer are not considered to be important for the inverted annular film boiling regime, but are included in the code for completeness. The vapor-to-liquid sensible heat transfer uses the same heat transfer coefficient that was computed for the vapor-to-interface heat transfer. The flashing model simply uses a large value for the heat transfer coefficient to keep the liquid temperatures close to saturation.

Inverted slug flow is made up of dispersed droplets and larger liquid fragments. The

entrainment fraction is used to distinguish between these two forms. The fraction of liquid considered to be in dispersed droplets is given by the entrainment fraction; the rest of the liquid is considered to be the inverted slugs. A linear weighting scheme based on the entrainment fraction is used to compute the interfacial heat transfer.

The model of Renksizbulut and Yuen is used for the vapor side heat transfer to the drops in the dispersed flow regime. This model is very similar to the Ranz-Marshall [51] correlation, but it includes a "blowing factor" to account for the added effect of mass transfer. As for the inverted annular regime, the sensible heat for the vapor to liquid uses the heat transfer coefficient for the vapor to interface. The TRACE code interpolates between the inverted annular regime and the dispersed flow regime to allow for a smooth transition between the two.

WCOBRA-TRAC

The summary of the interfacial heat transfer correlations in the WCOBRA-TRAC code is provided in Table 2.10. Note that while there is a droplet field included in the evaluation of the 3D component in the WCOBRA-TRAC code, the 1D constitutive models (described here) do not have a separate field for the droplets. Thus, the droplets and continuous liquid are considered only insofar as the applicable correlations are weighted together within the code.

The bubbly slug regime in the WCOBRA-TRAC code covers bubbly flows, bubbly-slug transition, and bubbly-slug flows. For low void fractions, slugs do not form, and bubbly flow dominates. For higher void fractions (between 30 and 50%), slugs and bubbles coexist for low mass flows (less than 2000 $^{kg}/_{m^2 \cdot s}$). Slugs do not form for flows greater than 2700 $^{kg}/_{m^2 \cdot s}$. The Chen and Mayinger correlation is used for the liquid side heat transfer during condensation. Chen and Mayinger conducted experiments that injected bubbles of saturated vapor into slow downward flows of subcooled liquid. A modified Whittaker correlation [64] for solid spheres plunged into a bath is used as the lower boundary for the Nusselt #. The

vapor-side heat transfer coefficient is a large constant value for the bubbly slug regime to bring the vapor temperature back to saturation. Subcooled boiling is assumed to only occur during bubbly flow, and the Lahey and Moody mechanistic model is used to compute the heat transfer coefficient that is added to that of the bubbly flow using a weighting factor.

The Churn flow regime is actually the transition between the bubbly-slug and annular mist regimes. The heat transfer coefficients are interpolated between these other regimes using a weighting factor that is computed based on the void fraction. The inverted annular liquid-side heat transfer coefficient is computed by the correlation by Forslund and Rohsenow [62] modified as suggested by Yuen and Chen [65].

The constant values that are assumed for heat transfer from the vapor to the coolant in the inverted slug regime are dependent upon which part of the liquid is involved and the temperatures. The model for liquid side heat transfer for the dispersed flow regime is not provided in the publicly available manuals. The heat transfer coefficient to a superheated liquid from the vapor is a constant value. For subcooled liquid droplets, the HTC is computed using the correlation by Andersen [61].

Only the liquid-side heat transfer calculations are specified for horizontally stratified flows. The work by Linehan [63] suggested a constant Stanton number criterion that is used to compute the heat transfer coefficient. The vapor-side heat transfer is the same value that would be determined by the flow regime map without stratification. If the flow is not fully stratified, as with other codes, the heat transfer factors are interpolated between the fully stratified value and the applicable value from the regime map.

TRAC-M

The summary of the interfacial heat transfer correlations in the TRAC-M code is provided in Table 2.11.

Similar to the WCOBRA-TRAC code, the bubbly slug regime in the TRAC-M code covers bubbly flows, bubbly-slug transition, and bubbly-slug flows. For Reynolds numbers

greater than 10^4, the Nusselt number is calculated from the Chen and Mayinger correlation with the Reynolds number set to 10^4, and is based only on the Prandtl number. The Chen and Mayinger correlation is used for the liquid side heat transfer for the mid-range Reynolds numbers, and the Whittaker correlation [64] is used as a lower bound on the Nusselt number for low Reynolds numbers. This methodology is very similar to that used in the WCOBRA-TRAC code. The same methods applied to the WCOBRA-TRAC code for subcooled boiling are again used in TRAC-M. The liquid-side heat transfer to the entrained droplets in the annular mist regime is a transient conduction formulation developed by Pasamehmetoglu and Nelson [67], and the annular film heat transfer is computed from the Stanton number using a relationship by Bankoff. The inverted annular liquid-side heat transfer coefficient is computed from the correlation by Hsu and Graham, though the coefficients have been changed slightly. The reference provided in the TRAC-M manual for this correlation does not seem to be correct. The inverted annular interfacial heat transfer is included as part of the reflood model in TRAC-M. The reflood modeling is discussed further in section 2.5.5. The horizontally stratified models are identical to those used in WCOBRA-TRAC.

The available documentation for the other codes considered in this report (CATHARE, ATHLET) did not clearly provide explanations of the interfacial heat transfer correlations used.

2.5.3 Wall-To-Fluid Heat Transfer

Heat transfer between the wall and the fluid is dependent on several factors. The flow channel geometry is of particular importance to the wall to fluid heat transfer. If the wall is a tube bundle, the heat transfer correlation will be very different from that used for walls that are parallel plates. Another important parameter in the determination of a wall to fluid heat transfer coefficient is the fluid flow regime. Bubbly flows have much more coolant in contact with the wall than post-CHF regimes, and the velocity and volume of actual coolant is much different from the annular or slug regimes. This section will discuss the wall to fluid heat

transfer models for each of the system codes. Full details of all the models included in the individual code manuals.

Table 2.12 outlines the details of the implementation of wall heat transfer for the various codes. The heat transfer models are characterized by three parameters: the number of specific geometries that are considered by the code, the number of models (correlations) that the code has implemented, and the number of modes of heat transfer that are considered.

The number of geometry types for each code was evaluated by counting the geometry configurations with code-specific correlations. For example, if no specific correlation exists in the code for modeling heated parallel plates, that geometry is not included in the count, even though the code may be capable of modeling heated parallel plates using two rectangular heat structures. RELAP5-3D has implemented specific models for six geometry types by specific options in the input for the heat structure models. The geometry types are pipes, parallel plates, rod bundles, swirl tubes, horizontal plate, and aluminum-walled annuli. TRACE has specific correlations for only four geometries; rods, plates, cylinders, and tube bundles. The remaining codes have only three specific geometries; rods, plates, and cylinders.

The number of heat transfer models is essentially a count of the number of heat transfer correlations that are used to model the various geometry configurations for each heat transfer mode. For example, the TRACE code models single-phase flow for tube geometries using three correlations for laminar forced convection, turbulent forced convection, and natural convection. These count as three of the models used in the TRACE code. Similar methods are used for the remaining codes.

The codes differentiate between heat transfer modes based on void fraction, wall temperatures, and other working fluid conditions. These heat transfer modes are: single phase flow, nucleate boiling, transition boiling, condensation, natural circulation, etc.

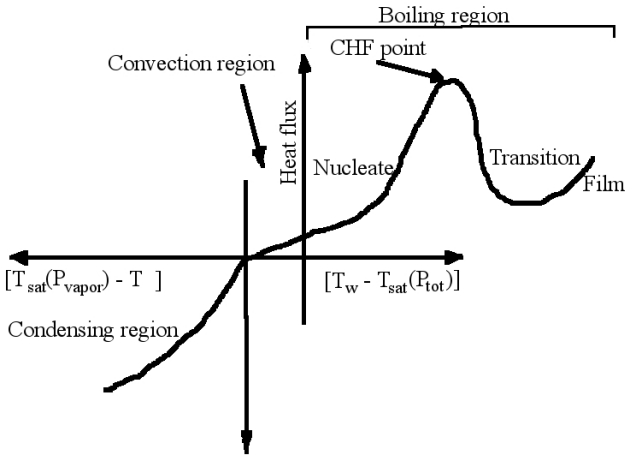

Figure 2.16: Boiling Curve

2.5.4 Critical Heat Flux Closure Models

The CHF closure models are important for the determination of flow regimes. The CHF point is defined as the maximum heat flux on the boiling curve shown in Figure 2.16. The CHF point marks the transition between wetted-wall heat transfer regimes like nucleate boiling, and the post-CHF regimes like transient or film boiling.

RELAP5-3D

The calculation of the CHF point in RELAP is used to determine the heat transfer regime that should be used (either pre- or post-CHF). The PG-CHF correlation in the RELAP5-3D code is a newly implemented set of CHF correlations that were developed by the Nuclear Research Institute Rez in the Czech Republic [68],[69]. The correlations are based on data in the Czech Republic data bank from 173 different sets of tube data, 23 sets of annular data, and 153 sets of rod bundle data. There are four formulations of the correlations. These are: basic, flux, geometry, and power. The ratio that results from the first three forms is the departure from nucleate boiling ratio (DNBR), which is 1.0 when the CHF point is reached. The basic formulation uses the local equilibrium quality and the local heat flux. The flux method uses the local heat flux and the heated length, which includes the axial

power peaking. The geometry form computes the CHF based on local equilibrium quality and the heated length, again including axial peaking. The power formulation utilizes a heat balance method and can be used to compute the Critical Power Ratio (CPR). These closure relations are used to determine the onset of CHF.

Once CHF is reached, the RELAP code uses the Chen transition boiling model [70] to compute the heat transfer from the wall to the coolant during the transition boiling regime. The fractional wall wetted area represents the amount of liquid present at any instant at a particular section of the heated tube. It is also dependent on the probability of this liquid contacting the hot wall. This term is empirically correlated as part of the Chen model.

TRACE

The Critical Heat Flux (CHF) model in TRACE serves much the same purpose as the model used in the RELAP5 code. The temperature of the CHF point is important in the determination of the start of the transition boiling region. However, unlike the RELAP code, the CHF point (see Figure 2.17) is also used to provide an upper bound on the transition boiling region heat transfer. The default model to determine the point of CHF is the 1995 AECL-IPPE look-up table. This table is based on an extensive CHF database obtained in tubes with a vertical upflow of a steam water mixture. The correlation provides a value for critical heat flux as a function of local conditions. A correction factor is used to improve the accuracy when applied to rod bundles. The minimum film boiling temperature (Tmin, Figure 2.17, also known as the Leidenfrost point) provides a lower bound for the transition boiling heat flux. The minimum film boiling temperature represents the point where the heat transfer regime switches from transition boiling to film boiling. In TRACE, the minimum film boiling temperature is computed using the Groeneveld-Stewart correlation [71]. These two points are used in the TRACE code to define the transition boiling heat transfer regime. The heat transfer based on wall superheat is determined by interpolation between these two points. The heat flux in the transition region is computed using an interpolation approach

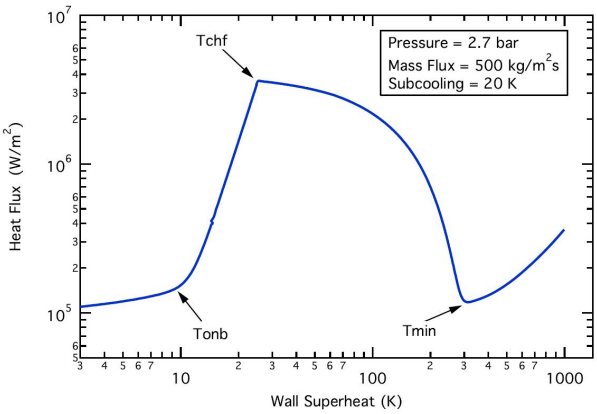

Figure 2.17: TRACE Heat Flux vs. Wall Superheat

suggested by Bjornard and Griffith [72].

WCOBRA-TRAC

The CHF is predicted in WCOBRA-TRAC using the Biasi [73] correlation, though some modifications are made to account for low flows and higher void fractions. The CHF value is used in the Chen nucleate boiling heat transfer correlation to compute the critical heat flux temperature, using iterative techniques. The Biasi correlation was developed from test data for tubes that were as small as 0.12 inches in diameter, up to 1.47 inches. The length of tube was up to 20 ft. As with TRACE, the transition boiling regime is bounded by the CHF point and the minimum film boiling point. The minimum film boiling temperature is used to mark the beginning of the film boiling regime and the end of transition boiling. It is assumed that the minimum film boiling temperature is the wall temperature that results in an instantaneous contact temperature equal to the homogeneous nucleation temperature after contact effects and surface thermal properties are taken into account. The homogeneous nucleation temperature is computed from a third-order polynomial curve fit to the Fauske data [74].

TRAC-M

As in the TRACE code, TRAC uses the CHF temperature as the lower limit of the transition boiling region, and the minimum film boiling temperature (Tmin) to determine the upper limit. As for WCOBRA-TRAC, the modified Biasi correlation is used to determine the CHF value. The minimum film boiling temperature is computed using the homogenous nucleation temperature method that was described for the WCOBRA-TRAC code.

ATHLET

Multiple CHF correlations are available in the ATHLET code. Two options exist for selection of the CHF correlation that is used. The user can set the code to pick the minimum of the results of the first four correlations. Otherwise, the user can pick a single correlation for use. The available correlations are listed below:

1. Westinghouse-W-3 [75]
2. Transient Hench-Levy [76]
3. Israel-Casterline-Matzner [77]
4. Biasi [73]
5. Zuber-Griffith [78, 79]
6. Gidropress [80]
7. Osmachkin [81, 82]
8. Mirshak [83]
9. Doroschuk/Konkov [84]

ATHLET calculates the minimum film boiling temperature using the Groeneveld-Stewart correlation [85]. The upper temperature boundary for rewetting after film boiling is called the rewetting temperature (T_{REW}), and is computed from Groeneveld [85]. The return to nucleate boiling temperature that indicates a return to nucleate boiling at the end of the rewetting process is (T_{RNB}). ATHLET uses a simpler method to determine if the flow is in transition boiling. The transition boiling region after departure from nucleate boiling (temperature is increasing) is used if the wall temperature is greater than the fluid temperature and the critical heat flux temperature (T_{CHF}), but less than $T_{CHF} + 10K$. After a departure from film boiling (temperature is decreasing), the transition boiling region is used when the wall temperature is between the return to nucleate boiling temperature (T_{RNB}) and the rewetting temperature (T_{REW}) [26]. The minimum film boiling temperature in ATHLET is used to determine when the flow regime changes from transition boiling to the post-CHF regimes. A user-input parameter determines how the heat transfer during transition boiling is calculated. Both methods interpolate between the pre-CHF regime (nucleate boiling) heat transfer coefficient and the film boiling heat transfer coefficient. The first option selects a cosine shape interpolation based on the time since the onset of transition boiling. The user selects the upper bound for interpolation by defining the time that transition boiling is expected to continue (the manuals suggest 0.5 seconds). This implies that after 0.5 seconds (or the time designated by the user), the interpolation will select the film boiling coefficient regardless of other flow conditions. The second option performs the cosine interpolation based on the wall temperature. The lower bound for the interpolation is the temperature at CHF determined as described previously. The upper bound is 10 K higher than the CHF temperature. Again, this suggests that once the CHF temperature is exceeded by 10 degrees, the film boiling heat transfer coefficient is used.

CATHARE

The model of transition boiling in CATHARE relies on the adequate prediction of the CHF point. The table proposed by Groeneveld [86] is used to compute CHF based on pressure, quality and mass velocity. Correction factors are applied for rod bundles. The transition boiling heat flux is derived from a parabolic interpolation between the CHF temperature and the minimum temperature that is identical to the method used in the TRACE code. The minimum temperature is based on the Groeneveld-Stewart correlation [85]. In the post-CHF flows, three heat transfer mechanisms are considered: radiation heat transfer from the surface to the vapor and liquid, convective heat transfer from the wall to the vapor, and convective heat transfer from the vapor to the liquid interface. These three mechanisms are modeled individually to capture the heat transfer to the post-CHF (dryout) flow regimes.

2.5.5 Reflood Modeling

Reflood conditions occur in the third phase of a Loss of Coolant Accident (LOCA) when the Emergency Core Cooling (ECC) system is activated. The ECC system injects coolant into the reactor vessel in an attempt to keep the reactor core covered. Under these conditions, the reactor is generally at low pressure and high temperature. The emergency flow is also generally at low pressure, and the high temperatures inside the vessel can result in the coolant flashing to steam before reaching the water in the vessel. The steam will eventually condense on the vessel wall and the fuel rods. The point at which a liquid film exists on the heated surfaces is called the quench front. In the vicinity of the quench front, many different heat transfer regimes are possible. In the region above the front, axial conduction dominates the heat transfer in the fuel rods or vessel wall. Heat is transferred from the non-quenched regions to those that have a liquid layer through the metal itself. Below the quench front, heat is transferred to the film via nucleate boiling. The models must adapt as the water level in the core begins to rise and the quench front moves. System codes typically include

special models to more effectively capture the conditions during reflood.

RELAP5-3D

The RELAP5-3D code includes user options to activate the reflood model. This model includes rezoning of the wall mesh and axial conduction. The rezoning capability allows the code to add nodes in the axial direction to minimize the effect of temperature gradients across the quench front. If the temperatures between two rows of nodes are too high, the code can divide the distance in half and add another row of nodes between. This process is repeated until the number of axial nodes reaches the maximum specified by the user. In a similar manner, the additional nodes can be removed when they are no longer needed. This capability is reserved for the reflood model. The reflood models can be activated based on a trip number or at a low pressure condition with high void fraction. The modifications to the interfacial drag, interfacial heat transfer, and wall heat transfer models are all used when reflood is active.

The modifications to the interfacial heat transfer model change the calculation of interfacial area and the logic that determines if the wall is wet or dry. The droplet diameter was reduced for the wet wall interfacial area calculation, and the Weber number for the dry wall was also reduced. The modifications to the logic selection of wet or dry walls forces the code to use the wet wall interfacial values close to the quench front.

The modifications to the interfacial heat transfer model were also made to the interfacial drag models. Additionally, the modified Bestion correlation [87] was implemented for the interfacial drag in vertical bubbly-slug flow at low pressure. This correlation replaces the EPRI correlation for non-reflood conditions at low pressures. Higher pressures still use the EPRI correlation, even during reflood.

The heat transfer coefficients for transition and film boiling are both changed when the reflood option is activated. At the bottom quench front, a modified Weisman correlation [88] replaces the Chen correlation [70] for transition boiling heat transfer to the liquid. The

transition boiling heat transfer coefficient to the vapor is the same that was used for non-reflood conditions, but it is ramped to zero using the void fraction. Thus, the heat transfer will be zero when the void fraction is zero.

The film boiling heat transfer coefficient to the liquid at the bottom quench front uses the maximum of a film coefficient, the modified Forslund-Rohsenow [62] and the normal Bromley correlation [89] (the same as is used in non-reflood conditions). The film coefficient is made up of an empirical length-dependent expression and a modified Bromley correlation coefficient. A radiation heat transfer to the droplets [90] is added to the final film boiling coefficient. The film boiling heat flux to vapor uses the same model as was used for the non-reflood condition.

The heat transfer calculations for both transition and film boiling at the top quench front are the same as those used at the bottom, with the exception of the characteristic dimensions used in the calculations. Instead of using the distance to the bottom quench front, these calculations use the distance to the top quench front. Also, the top quench front calculations are only used for rod bundle geometries.

The CHF model is also changed for a reflood condition. A modified Zuber correlation [91] replaces the default Groeneveld Table Lookup [86] for low mass flux values.

TRACE

The motion of the quench front during reflood conditions can result in significant temperature differences in the axial direction. In order to better capture the impact of these gradients, TRACE has the capability to add transitory nodes to the model. This re-meshing helps to minimize the impact of a large temperature jump across the quench front. The nodes are added whenever the temperature difference between two rows of "permanent" nodes is greater than a regime-dependent value. This technique is similar to that described for the RELAP5-3D code. Unlike RELAP5-3D, there are no special models for heat transfer or drag during reflood. The interfacial and wall heat transfer during reflood use the same models as

for non-reflood conditions.

WCOBRA-TRAC

There are no specific heat transfer or interfacial drag correlations for the reflood condition in WCOBRA-TRAC. Instead, there are specific correlations for the droplet entrainment in vessel (3D) components. These correlations are based on either a bottom-up or a top-down quenching scenario. The droplet sizes are also approximated as part of the entrainment calculations. These sizes are used in the normal correlations for interfacial and wall heat transfer, as well as interfacial drag. No special models have been implemented in WCOBRA-TRAC for 1D reflood.

TRAC-M

The overall reflood interfacial heat transfer is during reflood is computed by a weighted average of the bubbly, inverted annular, and dispersed flow heat transfer. This is a purely mathematical model, and does not involve actual flow physics, but it does provide a smooth transition between dominant regimes. The interfacial heat transfer for bubbly flow during reflood is identical to that used for non-reflood conditions, described in section 2.5.2. The only change from the previous methods is to the flashing model. The new liquid-side flashing model is based on the kinetic theory of evaporation from liquid surfaces, and is based on the work of Hsu and Graham [66].

The liquid-side heat transfer for inverted annular flow in reflood for subcooled flows is computed using the subcooled heat transfer correlations for the given flow regime. If the liquid is superheated, then the liquid-side flashing model used for the bubbly flow regime is again used, with a modified evaporation coefficient to adjust for the change in flow regime. The vapor-side heat transfer and liquid to gas sensible heat transfer use fixed heat transfer coefficients that are sufficiently large to prevent large excursions from saturated conditions.

The dispersed flow liquid-side heat transfer is very similar to that for the inverted annular

flow. For subcooled conditions, the standard subcooled model for the given flow regime is used. For superheated liquid, the modified Hsu and Graham model is again used, this time identical to the inverted annular model, including the use of the same evaporation coefficient. The vapor-side heat transfer is defined as a single small value for homogenous void fractions greater than 1 and small (< 0.05) droplet fractions. If the volume has a void fraction less than 0.98, a post-agitated dispersed-flow regime is indicated, and a different model based on the void fractions at the flow regime transitions between smooth, rough-wavy, dispersed and highly dispersed flows is used. For highly dispersed flows, a modified form of Unal's model for vapor generation [66] is used.

The liquid to gas heat transfer is modeled as a weighted sum of the heat transfer coefficient for the droplet field and the film field. The interpolation and weighting factor were developed specifically for TRAC. The heat transfer coefficient for the droplet field is based on the Ryskin model [53]. The film field heat transfer comes from Bankoff's annular-mist flow model [60].

ATHLET

A quench front model is included in ATHLET to capture the steep gradients in temperature that occur along the fuel rods and core internals during reflood conditions. The axial heat conduction in the vicinity of the quench front is considered by the models as well as the pre-cooling of the dry rod surface near the quench front. The code is capable of calculating both the upper and lower quench front positions using analytical correlations.

The user defines a quench region for a hot rod and one for an average rod. The upper and lower quench front position is determined for each region. The lower quench front velocity is determined using the Semeria-Martinet correlation [92]. The Upper quench front velocity correlation is from Yamanouchi [93]. The cladding temperature in the un-rewetted region is assumed to be the same as the temperature of that wall section when the quench front entered the control volume. This temperature directly affects the quench front movement. The model assumes that axial conduction will force the wall temperature to be below the

Leidenfrost temperature, although the actual wall temperature may be higher. This allows the re-wetting front to continue to move to the next control volume around the next rod segment, even if the surface temperature of the rod exceeds the Leidenfrost point. However, if the code detects a rise in wall temperatures above the Leidenfrost point at a location that has already been re-wetted, the quench front will jump back instantly to a wall location that is below the Leidenfrost temperature. If the wall temperature in the next volume exceeds a pre-defined limit, the quench front velocity will be reduced to result in a more gradual approach to the high temperature zone. The Leidenfrost temperature is computed using the Schröder-Richter analytical method, which was presented at the GRS in 1992. The heat transfer mode selection logic forces the heat transfer model to be in film boiling if it is between the upper and lower quench fronts. Outside that region, condensation, nucleate boiling, and transition boiling regimes are used. The volume that contains the quench front computes the heat transfer coefficient as a weighted average of the wetted and non-wetted parts of the volume.

CATHARE

The vapor-to-interface superheating during reflooding in CATHARE is computed using a classical laminar forced convection heat transfer model. As the reactor vessel refills during reflood, the quench front moves up through the reactor. The model for heat transfer from the dry walls immediately above the quench front is enhanced, due to the droplets that are ejected from bursting bubbles at the liquid interface entering the thermal boundary layer at the wall. The enhanced heat transfer as computed by Juhel [94] is implemented in CATHARE. Instead of interpolation, CATHARE uses an empirical correlation developed by Clement and Regnier [95]. These details of the reflood model in CATHARE have been obtained from [27].

2.5.6 Wall to Wall Radiation

This modeling capability allows for the calculation of heat transfer directly between heated or cooled surfaces without coolant exchange between them. This is an important feature in several of the Small Modular Reactor and advanced reactor designs being considered for development. These designs rely on passive cooling systems that include heat transfer from the reactor vessel to pipes lining the walls of the containment building. Cool water flowing through these pipes is intended to aid in the removal of decay heat during an accident. Without a model for radiation heat transfer between these pipes and the vessel wall, it will not be possible for these codes to accurately account for the heat lost in this way. Several accident scenarios involving traditional PWR and BWR designs can also benefit from these models. These scenarios involve severe accidents with significant loss of coolant and core dryout, reflood situations, as well as severe accidents that require analysis of the reactor containment.

RELAP5-3D

The RELAP5-3D radiation enclosure model is used for wall-to-wall radiation modeling. The model assumes that the fluid in the enclosure neither emits nor absorbs radiant thermal energy. This is not entirely the case, as water between two radiating surfaces would, in fact, absorb some of the energy in the exchange. The radiation model also assumes that the reflectance from a surface is not dependent on direction or frequency of the incident radiation. It also assumes that temperature, reflectance, and radiosity (emitted energy flux plus reflected energy flux) are constant for each of the surfaces. View factors for the calculation must be provided by the user. The radiation enclosure term is not implicit in surface temperature. This can cause solution instabilities for thin surfaces and large timesteps unless convection dominates radiation.

TRACE

Radiation heat transfer between surfaces in TRACE is modeled using either a CHAN (BWR fuel bundles) or a RADENC (radiation enclosure) component. Shumway developed the actual model [96]. These models include rod-to-rod and rod-to wall radiation interfacial heat transfer as well as wall-to-fluid. The enclosure model is automatically used for CHAN components. It is a user option for other heat structures.

WCOBRA-TRAC

The publicly available WCOBRA-TRAC manuals do not provide details about the radiation heat transfer models implemented.

TRAC-M

The FOTRAN 90 version of the TRAC-M code does not include the radiation enclosure models used to analyze wall-to-wall heat transfer.

ATHLET

The radiation model assumes that all the emissive surfaces are gray and all bodies are treated as infinitely long cylinders. Flow regimes with high void fractions are the only ones that use radiative heat transfer models. View factors for RBMK core channels are built into the code, but other geometries can be used if correct view factors are provided.

CATHARE

The available literature for the CATHARE code [27] does not provide any details about a wall-to-wall radiation model.

2.6 Experiment Validation

Code validation is essential for understanding the capabilities and weaknesses of system codes. Validation is necessary to establish model credibility with regulatory agencies and to help users determine the correct code to use for a particular analysis. Code validation can be grouped into three parts.

2.6.1 Validation Against Phenomenological Cases

These are basic problems with exact solutions. Simple examples would be calculating the pressure drop along the length of a pipe, or the change in pressure due to elevation head. These cases can be used to assess code performance for very specific, analyses. When new models or capabilities are added to the code, this part of the validation process will check to be sure that the newly added or improved model is functioning as desired. There are no specific tests or experiments that have been designed to perform this part of the validation, since by nature, the problems are simple and can be solved mathematically outside of the system code.

2.6.2 Validation Against Separate Effects Tests (SETs)

These tests are more complicated, and are generally used to test code performance against thermal-hydraulic experiment results for a particular component or geometry. The experiments are relatively simple, and address one or very few specific phenomena that are to be checked in the code. An example would be a single coolant channel with a heating element that is forced to the CHF regime. The code to be validated would model the same conditions, and parameters such as pressure, flow rate, void fraction, and onset of CHF would be compared to the test results. Some examples of SETs that have been conducted and used for validation of the codes considered here are the Marviken tests, Edward's pipe, FLECHT-SEASET, MOBY DICK, and TAPIOCA.

The Marviken test consisted of a pressure vessel with a discharge pipe. There was a test nozzle at the end of the discharge pipe and a rupture disk at the end of the test nozzle. The vessel contains gratings that reduce vortex generation. The nozzle and rupture disks could be exchanged to test different conditions. The tests were conducted by filling the pressure vessel with water and heating it. When the desired internal pressures and temperature distributions were obtained, the rupture disk was broken, and the resulting flow was directed to a discharge tank. The nozzle was expected to choke, and the test was allowed to continue until a predetermined time or until vapor was detected in the discharge pipe. The Edward's Pipe experiment was very similar to the Marviken test in that it was a pipe filled with water, pressurized and heated. In this case however, no nozzle was used. Void fraction was measured in two places within the pipe, and pressure and temperature were measured in seven places. Blowdown forces along the length of the pipe were also measured.

The Full-Length Emergency Cooling Heat Transfer Separate Effects and Systems Effects Tests (FLECHT-SEASET) were conducted in a vessel that contained an array of electrically heated rods. The rods were arranged as a full-length 17 x 17 bundle, representative of a Westinghouse PWR. This experiment has been used to test reflooding models in system codes. The pressure and cladding temperature test conditions were established, and the experiment was commenced when the injection flow began. The experiment measured steam superheat and void fraction along the bundle length. The test results can be compared to the reflood models in the system codes, and in some cases, used to set modeling coefficients to improve the results.

The MOBY DICK tests were designed to test steady-state two-phase choked flow in a vertical divergent nozzle at low pressure. The test fluid was a mixture of water and nitrogen. The test consisted of a pump, preheater, nitrogen injection system, test section and a condenser. Flow was initiated through the loop, and the pressure in the condenser was brought close to atmospheric pressure. The nitrogen was injected nearly one meter upstream of the test section. The test monitored temperatures, void fractions, and pressures at the

inlet and throughout the test section. The data is used to compare to the two-phase choked flow models in the system codes. Flashing was also observed downstream of the divergent nozzle during the experiments.

The TAPIOCA test was a blowdown test consisting of a pipe that was 2.6 m long and 0.324 m in inner diameter. It had break locations at the side, top, bottom, and in the middle. The break sizes varied from 2 to 35 mm. The test was brought to temperature, and then one of the break locations would be opened, and the resulting temperature and pressure pulses were recorded to be compared to computational results.

2.6.3 Validation Against Integral Effects Tests (IETs)

This class of experiments validate the entire code model in a comprehensive way; making sure that all the components work together and achieve good results. Since these tests are composed of entire systems of components, they tend to be more expensive. The cost has reduced the available test data for use in validation work. The aspects of the code that are validated are the outcome from relatively simple problems such as pump shutdown or inadvertent valve closures to very severe plant accidents such as primary coolant loop breaks and loss of coolant accidents. Experiments are often designed to use non-nuclear heat sources, but some experiments have been conducted using specially-designed reactors with operational nuclear cores. Data from actual reactor accidents has also been used for validation work. In this light, accidents such as Fukushima, Three-Mile Island and Chernobyl are all very important for code validation work. Some of the purpose-built experiments used for IET validation are: LOFT, Semiscale, LOBI, and ROSA.

The LOFT facility had a nuclear core and an intact loop with a steam generator, pressurizer and pump scaled from a full-size PWR. A second "broken" loop was included that had a fast-opening valve that discharged into a surge tank. The facility allowed testing of loss of pump flow, loss of secondary cooling, reactor over-power conditions, as well as loss of coolant accidents via the loop blowdown system. The experiment was well-instrumented, and the

wide range of tests provided substantial data for use in code validation. A potential problem with the LOFT facility is the possibility of excessive core bypass, lack of measurements in certain areas, and some compromises in the scaling methodology [97]. The Semiscale facility is a non-nuclear facility that was scaled to LOFT using the same proportions and rules that were used when scaling a PWR to LOFT. The overall semiscale test was very similar to the LOFT experiment. The results of the semiscale tests were used to confirm the LOFT results and provide additional validation data. The semiscale facility could also run a transient from the start of blowdown through reflood, which was a distinct advantage over larger test facilities.

The LOBI facility is a full-power high-pressure system that is a scale model of a PWR. It was originally developed to perform large break LOCA tests, and then was extended to include other tests as well as small-break LOCAs. The experiment was fully instrumented to measure pressure, temperature, void fraction, and other characteristic system parameters. Like LOFT, there are two system loops, one that is intact, the other "broken" with quick acting valves to allow for rapid blowdown. Each loop has a coolant circulation pump and a steam generator. The core is simulated by an electrically heated 8 x 8 square-matrix rod bundle. The primary system operates at normal PWR conditions. The secondary system contains a condenser, cooler, main feedwater pump and auxiliary system.

The Rig-of-Safety (ROSA) test program was conducted to investigate small-break LOCAs and operational transients in a Westinghouse PWR. The facility had two equal-volume loops. The core simulator has 16 heater rod assemblies with rods arranged in a 7 x7 square grid. There are an additional 8 semi-crescent rod assemblies. As with the other IETs, the data from this test has been used to validate code results for system-wide performance during accidents.

The details of the validation for each of the codes in this evaluation are provided in each of the system code manuals. An evaluation of the Integral Effects Tests for applicability to model specific plant conditions is contained in Reference [97]. Similar information for the

SETs is provided in References [98, 99]. An assessment of the robustness of the validation of each system code can be obtained by comparing the tests selected for the validation of particular models against the reports assessing the applicability of the test to the regime in question.

2.6.4 Validation Applications

Code improvements and additions of new code models require rigorous testing to verify that the changes had the desired effect and did not reduce the applicability of the code. This testing can be conducted using analytical solutions to known problems, or experimental data as described in the previous sections. The principal phenomena involved in the code additions must be identified. The available experimental results must then be evaluated and matched up with the phenomena to be tested. If the additional code model improves the calculation of the interfacial area between bubbles and liquid, it would not be practical to use tests that involved only single-phase flow. In general, the selection of appropriate test data is complicated. References [97] and [100] outline the process of experiment selection. The United States Nuclear Regulatory Commission has established additional guidelines for the nuclear industry for appropriate selection of experimental data to be used in code validation [101].

In addition to appropriate selection of experimental results based upon the phenomena tested, collected data must also be evaluated. Inaccuracies in the methods of collecting the data, and uncertainties in the equipment used can result in poor comparisons to the model. The developer must understand the limitations of the data before making detailed comparisons, and include the information in the selection process.

Reference [100] provides a description of the process for code validation against experimental data. Once a test is selected, a model is developed in the code to be tested. Accuracy to the experiment facility is important, as differences can result in inaccurate conclusions. The information provided in the test documentation is used to set parameters in the model

such as valve open and close times, pump trips, heater setpoints, etc. The model is run, and the results are compared to the experiment. Differences in the computed results to the experimental results can be caused by many factors, including errors in the experiment data collection, errors, or omissions in the documentation of the experiment parameters, modeling errors, etc. In cases where the experiment data does not include sufficient information (for example, exact timing of pressurizer heater startup), other collected data can be used to infer the needed information (change in the system pressure is indicative of the heater condition).

When the model and experiment results are in the best possible agreement, an assessment must be made of the quality of the code model. Reference [100] suggests qualifications of "Excellent", "Reasonable", "Minimal" and "Insufficient" Agreement with the data.

Excellent agreement applies when the code shows no deficiencies when modeling a given behavior. Major and minor phenomena are captured, along with trends being correctly predicted. Major phenomena are those which influence key parameters such as fuel cladding temperature, pressure, mass flow rate, etc. The calculated results agree closely with the data, and most of the calculated results lie within the uncertainty of the data. This qualification suggests that no changes are necessary to the code or modeling technique.

Reasonable agreement implies that the code has minor deficiencies. The code predicts the data acceptably, predicting the major trends and phenomena well. Calculation results occasionally lie outside the uncertainty bands for the data. While the results are acceptable for use, the code models and experiment data should be reviewed to see if improvements can be made.

Minimal agreement suggests that the code has significant deficiencies. The code predictions are only conditionally acceptable, meaning that selected regions of the data may be in good agreement, but not the entire experiment range. Some of the major trends and/or phenomena are not predicted correctly. Some of the calculated results may be well outside the experiment uncertainty band. If the calculated results are used in similar applications,

incorrect conclusions might be reached. Before the code can be used with confidence in similar applications, selected models must be reviewed and modified to improve agreement.

Insufficient agreement indicates that the code has major deficiencies. Trends are not captured, major and minor phenomena are completely missed, and most calculated values lie outside the uncertainty band of the data. Warnings should be issued to users and the models should be reviewed, modified, and reassessed before they can be used with confidence.

Recent developments in validation techniques allow for better comparisons to experimental results by comparing to multiple sets of data using Bayesian data analysis techniques. For some modeling cases (such as interfacial drag models), several experimental data sets may apply. Statistical comparisons of multiple data sets using Bayesian methods allows the various uncertainties and different ranges of results in each data set to be included. Data from several experiments can be consolidated and combined with data from other experiments, maintaining the uncertainty from each experiment/data set. The collected set of data can then be used for validation of the calculation results. The result is better code validation over a wider range of data, and a more complete understanding of the applicability and accuracy of the code models. More details of these techniques are presented in References [102] and [103].

2.7 Code Limitations

This discussion addresses significant modeling deficiencies in each of the codes, and helps in the selection of appropriate codes for use in particular analyses.

A significant limitation of all the system codes presented is the lack of verification of the models that would be needed in analyses of the next-generation of nuclear plants, particularly gas-cooled, graphite-moderated plants. The gas coolant can be modeled by the codes using settings in the input models or user-supplied data about the gas properties, but the verification and validation experiments for these codes do not provide validation of the gas-flow models. It is unclear how the codes will perform when modeling a gas-cooled reactor.

Although the capabilities are included in the codes, and the governing equations and heat transfer models do not differ significantly from the models and closure relationships used for the vapor phase, these models have not been checked against experimental data and results to verify accuracy. The governing equations used for the liquid-cooled system should be sufficient to model a gas-only system, assuming that the correct gas properties are used. The closure relations will vary significantly for a gas-only system, and these relations should be investigated, implemented in the codes, and then verified and validated.

One of the gas-cooled reactor designs uses graphite pebbles to contain the fuel. These pebbles are spheres that will be placed into a large vessel, and the gas coolant will flow around them. RELAP5-3D includes a model for spherical heat structures (useful to modeling pebbles in pebble-bed reactors), but the correlations included in the code are not valid for spherical geometries. It should also be noted that none of the codes considered here have the capability to model the complex flow path of the gas coolant through the bed of pebbles. These are very distinct limitations to the current system codes.

Another recent reactor design is for a Small Modular Reactor (SMR). These reactors have been designed to provide a flexible cost-effective alternative to large generation plants. These low-power (300 MWe) reactors are designed with all of the system components within a single containment vessel. Their small size allows them to be constructed off-site, shipped to the desired location, and set up at the plant. Several of the current designs consider using multiple SMRs at a single location to generate large amounts of electricity while capitalizing on the economics of a single plant location. Various SMR designs have been developed that employ diverse coolant types, such as: water, gas, liquid metal, or molten-salt.

Since SMRs are compact and must contain all the standard reactor components within a single vessel that can be shipped to a location, changes are sometimes made in the design that may challenge the capability of system code models. Various steam generator designs have been utilized in SMRs, including helical and once through straight tube designs. Helical heat exchangers create more crossflow over the tubes than axial flow. Additionally, centripetal

forces on the steam and coolant can have an effect on the performance of the steam generator. Since crossflow solutions depend on robust 3D modeling, mixing and void drift models must be efficiently employed in 3D system codes. The current system codes may be able to model the performance of these unique steam generators if empirical results or correct user-defined adjustment coefficients are used. The drawback to using empirical results or user-defined coefficients is that the models must be subjected to additional validation and checks to verify their performance against actual experimental results of the new generator designs. Data from experimental results must be adequate to satisfy regulatory requirements. Results of experiments with stratified flow, natural circulation, sub-cooled liquid entrainment, and even large pool behavior must be verified and used to validate code models. Another shortfall in the use of user-defined coefficients is that the accuracy of the result will be heavily dependent on the capability and care that the user is able to bring to the analysis.

The models for SMRs that will use non-water coolant will also need to be evaluated for accuracy. The code validation already described showed no specific validation against metallic or molten salt coolants in the open literature. As with the steam generators, existing models might be sufficient for modeling the hydrodynamics of the alternative coolants if the characteristic parameters of each coolant are included in the calculations. Nonetheless, additional validation efforts would be beneficial to evaluate the code performance with alternative coolants.

TRACE is not fully assessed for BWR stability calculations, or for modeling situations in which transfer of momentum plays an important role at a localized level [1]. The fluid dynamics in a pipe branch or plenum are not modeled in detail, nor are flows in which the radial velocity profile across the pipe is not flat. It is also not appropriate for transients in which there are large changing asymmetries in the reactor-core power, unless PARCS is used for 3D spatial kinetics. In TRACE, neutronics are evaluated on a core-wide basis by a point-kinetics model by default.

The hydrodynamic models in TRACE are not suited to evaluate situations where the

viscous stresses are the same or larger than the wall and/or interfacial shear stresses. It is also important to note that neither the TRAC-based codes (TRACE, TRAC-M, WCOBRA-TRAC) nor RELAP can model recirculation flows in a large open region, even with a fine-mesh size. Buoyancy driven flows through the reactor coolant system (natural circulation) can be modeled, but recirculation in large volumes, such as spent fuel pools, is not accurately computed. TRACE does not capture the stress/strain effect of temperature gradients in structures. Thermal expansion is not modeled explicitly.

Flow-induced forces on piping are not modeled by any of the system codes. Forces on piping components such as "elbows" or "tees" are not computed by the codes. Some pressure effects, such as water hammer, can be computed, but the forces on the piping resulting from these pressure pulses are not computed in these cases.

RELAP requires an additional coupled code (SCDAP) to model structural effects in the solid materials. This type of result can be used to support more detailed calculations.

Viscous heating terms within the fluid are ignored in TRACE. In addition, some of the approximations made in the development of the models make it difficult to predict certain phenomena. The wall and interface heat flux approximations result in poor analytical performance for phenomena like steam bubble collapse that blocks natural circulation, or capturing the details of steam condensation at the water surface.

None of the system codes considered are fully implicit. The codes have made inroads by using enhancements to the standard solution schemes, interpolation techniques, and inner-iterations to solve part of the problem implicitly while leaving the rest to explicit solution methods. The limitations of the Courant limit have been reduced or eliminated in many cases. As long as limitations on the timesteps remain, through Courant stability issues or explicit solution schemes, users of the codes will have to be cautious when executing analyses of complex designs to prevent convergence problems.

CATHARE and ATHLET share many of the limitations that are present in the other codes. For simplicity, they will not be detailed here.

Table 2.3: Momentum Conservation Equation Comparison TRAC, ATHLET and CATHARE Codes

Component	WCOBRA/ TRAC-TF2	TRAC-M	ATHLET	CATHARE
Time Rate of Change of Momentum	$\frac{\partial \underline{u}_l}{\partial t}$	$\frac{\partial \vec{V}_g}{\partial t}$	$\frac{\partial[(1-\alpha)\rho_l \vec{w}_l]}{\partial t}$	$A\frac{\partial(1-\alpha)\rho_l v_L}{\partial t}$
Rate of momentum change from convection	$\underline{u}_l \cdot \nabla \underline{u}_l$	$\vec{V}_g \cdot \nabla \vec{V}_g$	$\nabla\left[(1-\alpha)\,\rho_l \vec{w}_l \vec{w}_l\right]$	$\frac{\partial A(1-\alpha)\rho_l v_L^2}{\partial z}$
Pressure gradient	$-\frac{1}{\rho_l} \cdot \nabla P$	$-\frac{1}{\rho_v}\nabla P$	$\nabla\left[(1-\alpha)\,P\right]$	$A\,(1-\alpha)\,\frac{\partial P}{\partial z}$
Momentum change from body forces	$-\underline{g} \cdot \cos(\theta)$	$\vec{g}$	$-\,(1-\alpha)\,\rho_l \vec{g} +$ $\alpha\,(1-\alpha)\,(\rho_l - \rho_v)$ $\vec{g} D_h \nabla\alpha + S_{i,l}$	$A\,(1-\alpha)\,\rho_l g$
Wall Drag	$-\frac{C_{wl}}{\alpha_l \rho_l} \cdot \lvert\underline{u}_l\rvert \cdot \underline{u}_l$	$-\frac{C_{wv}}{\alpha\rho_v}\vec{V}_g\lvert\vec{V}_g\rvert$	$-\,(1-\alpha)\,\vec{f}_w$	$\chi\tau_{WL}$
Momentum from phase change mass transfer	$\frac{\Gamma^-}{\alpha_l \rho_l} \cdot \left(\underline{u}_l - \underline{u}_g\right)$	$-\frac{\Gamma^+}{\alpha\rho_v}\left(\vec{V}_g - \vec{V}_l\right)$	$-\psi\vec{w}_\Gamma$	ΓV_i
Interfacial Drag	$-\frac{C_{D,i}}{\alpha_l \rho_l} \cdot \lvert\underline{u}_l - \underline{u}_g\rvert \cdot \left(\underline{u}_l - \underline{u}_g\right)$	$-\frac{C_{D,i}}{\alpha\rho_v}\lvert\vec{V}_g - \vec{V}_l\rvert\left(\vec{V}_g - \vec{V}_l\right)$	$\vec{\tau}_i$	$A\tau_1 + f_L\frac{\partial A}{\partial z}$
Virtual Mass Force	$--$	$--$	$\alpha\,(1-\alpha)\,\rho_m$ $\left(\frac{\partial \vec{w}_R}{\partial t} + \nabla\vec{w}_R\right)$	$A\beta\alpha\,(1-\alpha)$ $\left[\alpha\rho_G + (1+\alpha)\,\rho_l\right]$ $\left[\frac{d_G v_G}{dt} - \frac{d_L v_L}{dt}\right]$
Velocity Relaxation	$--$	$--$	$--$	$--$

Table 2.4: Energy Conservation Equation Comparison RELAP5-3D, RELAP-7, and TRACE Codes

Component	RELAP5-3D	RELAP-7	TRACE
Rate of Energy Change	$\frac{\partial}{\partial t}\left(\alpha_k \rho_k U_k\right)$	$\frac{\partial \alpha_l \rho_l E_l A}{\partial t}$	$\frac{\partial\left[(1-\alpha_g)\rho_l\left(e_l+V_l^2/2\right)\right]}{\partial t}$
Mass crossing boundary	$\frac{1}{A}\frac{\partial}{\partial x}\left(\alpha_k \rho_k U_k v_k A\right)$	$\frac{\partial \alpha_l u_l A(\rho_l E_l + p_l)}{\partial x}$	$\nabla\cdot\begin{bmatrix}(1-\alpha_g)\,\rho_l \\ \left(e_l+\frac{P}{\rho_l}+\frac{V_l^2}{2}\right)\vec{V_l}\end{bmatrix}$
Energy Change From Interfacial Boundary Movement	$-P\frac{\partial \alpha_k}{\partial t}$	$--$	$--$
Flow Work Energy Change	$-\frac{P}{A}\frac{\partial}{\partial x}\left(\alpha_k v_k A\right)$	$p_{\text{int}} u_{\text{int}} A \frac{\partial \alpha_l}{\partial x}$	$--$
Heat transfer from wall	Q_{wk}	$\alpha_l h_{lw}\left(T_w - T_l\right)$ $\left[4\pi A + \left(\frac{\partial A}{\partial x}\right)^2\right]^{\frac{1}{2}}$	q_{wl}
Heat transfer from the interface	Q_{ik}	$A_{\text{int}} h_{Tl}\left(T_{\text{int}} - T_l\right) A$	q_{il}
Phase change in bulk fluid	$\Gamma_{ig} h_k^*$	$\Gamma A_{\text{int}}\left(\frac{p_{\text{int}}}{\rho_{\text{int}}} - H_{l\ \text{int}}\right) A$	$-\Gamma h_l^{'}$
Phase change at wall	$\Gamma_w h_k^{'}$	$--$	$--$
Energy lost to gravity, wall drag, etc.	$DISS_k$	$\alpha_l \rho_l u_l \vec{g}\cdot \hat{n}_{axis} A$	$\left(1-\alpha_g\right)\rho_l \vec{g}\cdot\vec{V_l} +$ $\left(\vec{f_i}+\vec{f_{wl}}\right)\cdot\vec{V_l}$
Direct fluid heating	$--$	$--$	q_{dl}
Pressure/Velocity relaxation	$--$	P: $-\overline{p}_{\text{int}} A\mu\left(p_l - p_g\right)$ V: $\overline{u}_{\text{int}} A\lambda\left(u_g - u_l\right)$	$--$

Table 2.5: Energy Conservation Equation Comparison TRAC, ATHLET and CATHARE Codes

Component	WCOBRA/TRAC-TF2	ATHLET	CATHARE
Rate of Energy Change	$\frac{\partial(\alpha_g\rho_g e_g+\alpha_l\rho_l e_l)}{\partial t}$	$\frac{\partial\left[(1-\alpha)\rho_l\left(h_l+\frac{1}{2}\vec{w}_l\vec{w}_l-\frac{P}{\rho_l}\right)\right]}{\partial t}$	$A\frac{\partial}{\partial t}\left[\begin{array}{c}(1-\alpha)\,\rho_l\cdot\\ \left(H_L+\frac{v_L^2}{2}\right)\end{array}\right]$
Mass crossing boundary	$\nabla\left(\alpha_g\rho_l e_l\right)\cdot\underline{u}_g+$ $\nabla\left(\alpha_l\rho_l e_l\right)\cdot\underline{u}_l$	$\nabla\left[\begin{array}{c}(1-\alpha)\,\rho_l\vec{w}_l\cdot\\ \left(h_l+\frac{1}{2}\vec{w}_l\vec{w}_l\right)\end{array}\right]$	$\frac{\partial}{\partial z}\left[\begin{array}{c}A\,(1-\alpha)\,\rho_l\cdot\\ \left(H_L+\frac{v_L^2}{2}\right)\end{array}\right]$
Energy Change From Interfacial Boundary Movement	$--$	$-P\frac{\partial(1-\alpha)}{\partial t}$	$-A\,(1-\alpha)\,\frac{\partial P}{\partial t}$
Flow Work Energy Change	$-P\cdot\left[\begin{array}{c}\nabla\alpha_g\cdot\underline{u}_g+\\ \nabla\alpha_l\cdot\underline{u}_l\end{array}\right]$	$--$	$--$
Heat transfer from wall	$q_{wg}+q_{wl}$	$\dot{q}_{wl}$	χQ_{WL}
Heat transfer from the interface	$--$	$\dot{q}_i$	AQ_{LI}
Phase change in bulk fluid	$--$	$\psi\left(h_{\psi,l}+\frac{1}{2}\vec{w}_\psi\vec{w}_\psi\right)$	$--$
Phase change at wall	$--$	$--$	$--$
Energy lost to gravity, wall drag, etc.	$--$	$\vec{\tau}_i\vec{w}_l+$ $(1-\alpha)\,\vec{\tau}_i\,(\vec{w}_v-\vec{w}_l)+$ $(1-\alpha)\,\rho_l\vec{g}\vec{w}_l$	$A\,(1-\alpha)\,\rho_l v_L g$
Direct fluid heating	$q_{dg}+q_{dl}$	$--$	$--$
Pressure/Velocity relaxation	$--$	$--$	$--$

Table 2.6: Summary of Code Numerical Solution Details

	Solution Method	Time Step Limit	Linear Equation Solver	Accuracy
RELAP5-3D	Semi- or nearly-implicit	Courant limited, except for nearly implicit	Direct inversion by BPLU	First order
RELAP-7	Explicit	Courant & Stability-limited	JFNK Nonlinear	Second order
TRACE	SETS or semi-implicit	Courant limited, except for SETS method	Gauss elimination	First order
WCOBRA-TRAC	Semi-implicit	Courant limited	Gauss elimination	First order
TRAC-M	SETS (1D)	Courant (3D)	Gauss elimination	First order
ATHLET	Explicit (forward) Implicit (backward)	Limited by estimated error	Forward-Euler, Backward-Euler	Second order
CATHARE	1D: Fully-implicit 3D: semi-implicit	Courant (3D)	Newton-Raphson	First order

Table 2.7: Summary of Code Assumptions

	RELAP5-3D	RELAP-7	TRACE	WCOBRA-TRAC	TRAC-M	ATHLET	CATHARE
Component Approach	✓	✓	✓	✓	✓	✓	✓
Constant properties within control volume	✓	✓	✓	✓	✓	✓	✓
Liquid and vapor at same pressure	✓		✓	✓	✓	✓	✓
Minimal interaction with noncon-densables	✓	✓	✓	✓	✓	✓	✓
Homogeneous fluid mixture within volumes	✓		✓	✓	✓	✓	✓
Quasi-Steady Heat Transfer Coupling	✓		✓	✓	✓		
Quasi-Steady Abrupt area change flow	✓		✓	✓	✓		
Constant Volumetric flow from cell center to edge			✓	✓	✓		
Droplet velocity same as vapor velocity	✓		✓	✓	✓	✓	✓
Viscous shear within a phase is negligible	✓		✓	✓	✓	✓	✓

Table 2.8: RELAP5-3D Interfacial Heat Transfer Models

Regime		Subcooled Liquid	Subcooled Vapor	Superheated Liquid	Superheated Vapor
Bubbly		Modified [45] Unal [46] and Lahey	Bby SHV	Max of Plesset-Zwick [47] or Lee-Ryley [48]	Empirically based
Slug	Small Bubble	Bby SCL	Slug SHV	Bby SHL	Bby SHV
	Taylor Bubble	Special Model	h_{ig} from Bby SHV	Large HTC	Modified Lee-Ryley
Annular	Droplets	Brown [49]	Large HTC	Quadratic Function	Lee-Ryley
Mist	Film	Theofanous [50]		Large Nu	Dittus-Boelter
Inverted	Bubbles	Bby SCL	Inverted Ann. SHV	Bby SHL	Bby SHG
Annular	Core	Dittus-Boelter		Large HTC	Ad hoc
Inverted Slug		Brown	Inv. Slug SHV	Large Nu	Ad Hoc and modified Lee-Ryley
Dispersed		Brown	Bby SHV	Large Nu	Modified Lee-Ryley
Horizontal Stratified		Dittus-Boelter	Hrz. Stratified SHV	Large Nu	Dittus-Boelter and large Nu
Vertical Stratified		Vert. stratified SHL	Vert. stratified SHV	Stratified HTC and non-stratified condition	Vert. stratified SHL with vapor properties

Table 2.9: TRACE Interfacial Heat Transfer Models

Regime	Liquid Side	Vapor Side
Bubbly	Ranz-Marshall [51]	Large Constant HTC
Cap Bubble/Slug	Ranz-Marshall [51]	Bubbly
Annular Mist - Annular Film	Laminar - Kuhn Turbulent - Gnielinski	Max of Dittus-Boelter and 4.0
Annular Mist - Entrained Droplets	Kronig and Brink [52]	Ryskin [53]
Inverted Annular	Constant	Thin film laminar convection
Inverted Slug	Dispersed	Dispersed
Dispersed	Kronig and Brink [52]	Renksizbulut and Yuen [54]

Table 2.10: WCOBRA-TRAC Interfacial Heat Transfer Models

Regime	Liquid Side	Vapor Side
Bubbly Slug	Chen and Mayinger [59]	Large Constant HTC
Churn	Interpolation	Interpolation
Annular Mist - Annular Film	Bankoff [60]	Bankoff
Annular Mist - Entrained Droplets	Andersen [61]	Ryskin [53]
Inverted Annular	Modified Forslund and Rohsenow [62]	Large HTC
Inverted Slug	Inverted Annular	Constant
Dispersed	Unavail.	Constant or Andersen
Horizontal Stratified	Linehan et. al. [63]	No Change

Table 2.11: TRAC-M Interfacial Heat Transfer Models

Regime	Liquid Side	Vapor Side
Bubbly Slug	Chen and Mayinger [59]	Large Constant HTC
Churn	Interpolation	Interpolation
Annular Mist - Annular Film	Bankoff [60]	Bankoff
Annular Mist - Entrained Droplets	Transient Conduction	Ryskin [53]
Inverted Annular	Modified Hsu and Graham [66]	Large HTC
Dispersed	Inverted Annular	Small Constant
Horizontal Stratified	Linehan et. al. [63]	No Change

Table 2.12: Wall to Fluid Heat Transfer Model Comparison

Code	Number of Geometry Types	Number of Heat Transfer Models	Number of Heat Transfer Modes
RELAP5-3D	6	31	12
TRACE	4	20	11
WCOBRA/ TRAC	3	10	8
TRAC-M	3	13	8
ATHLET	3	14	12
CATHARE	3	8	6

CHAPTER 3

Mass, Momentum, and Energy Conservation Equations for Six Fields

3.1 Exact Integral Two-Phase Balance Equations

Specific conservation equations for mass, momentum, and energy can be developed from a general balance equation for a mass intensive property. These conservation equations can be written for a particular phase as well as at the interface between phases.

3.1.1 Phase-Specific General Conservation Equation

Equation 3.1 shows the general integral balance that serves as the starting location of the development of the differential balance equation. The integral balance uses the fluid density (ρ_k), the efflux ($\mathbb{J}_k$), and the body source (ϕ_k) of any quantity (ψ_k), defined for a unit mass.

$$\frac{d}{dt}\int_{V_k} \rho_k \psi_k \, dV = -\oint_{A_k} \vec{n}_k \cdot \mathbb{J}_k \, dA + \int_{V_k} \rho_k \phi_k \, dV \tag{3.1}$$

In words, Equation 3.1 shows that the time rate of change of $\rho_k \psi_k$ in the volume V_m is equal to the influx through the surface that bounds the volume plus the material source. The subscript k indicates the applicable phase.

The differential form of the balance equation can be derived using the Reynolds Transport theorem (Equation 3.2) and Green's theorem (Equation 3.3).

$$\frac{d}{dt}\int_{V_k} F_k \, dV = \int_{V_k} \frac{\partial F_k}{\partial t} \, dV + \oint_{A_k} F_k \vec{v}_k \cdot \vec{n} \, dA \tag{3.2}$$

$$\int_V \nabla\cdot F_k \, dV = \oint_A \vec{n}\cdot F_k \, dA \tag{3.3}$$

By applying the Reynold's Transport Equation (3.2) to Equation 3.1, and then Green's theorem (Equation 3.3) to the result we obtain:

$$\int_{V_k} \frac{\partial \rho_k \psi_k}{\partial t} + \nabla\cdot\left(\vec{v}_k \rho_k \psi_k\right) \, dV = \int_{V_k} -\nabla\mathbb{J}_k + \rho_k \phi_k \, dV \tag{3.4}$$

Recognizing that the left and right sides of Equation 3.4 are integrated over the same volume, the integrals can be eliminated, yielding the familiar local instantaneous differential transport equation:

$$\frac{\partial \rho_k \psi_k}{\partial t} + \nabla\cdot\left(\vec{v}_k \rho_k \psi_k\right) = -\nabla\cdot\mathbb{J}_k + \rho_k \phi_k \tag{3.5}$$

The first term in Equation 3.5 is the time rate of change of the quantity per unit volume. Recall that the ψ term is a property per unit mass. Multiplying that term by the density changes the term to a per unit volume basis. The second term on the left-hand side is the rate of convection per unit volume. The terms on the right side of the equation are for the surface flux and the volume source.

3.1.2 Interface Jump Conditions

A generalized balance equation can also be written for the interface between the phases. The interfacial region is characterized by the contact surface between the phases, which has an area A_i. We then assume that the interfacial region is a volume that has a thickness δ, with δ_1 and δ_2 on each side of the contact surface (where $\delta = \delta_1 + \delta_2$). A second surface, orthogonal to the contact surface, traces the perimeter of A_i and is designated Σ_i. The surface Σ_i has a width of δ. The intersection between Σ_i and A_i is a line, C_i. The thickness

δ is assumed to be sufficiently small in comparison to the area A_i so as to make the areas of the outside of the interfacial region (at δ_1 and δ_2) equivalent to A_i ($A_1 = A_2 = A_i$). In addition, the outward normal vectors from phase 1 and phase 2 are assumed to be equal and opposite. The outward normal vector of Σ_i (which is tangential to the interface) is $\vec{N}$. Using the above terminology, the general balance equation for the interfacial volume is:

$$\begin{aligned}\frac{d}{dt}\int_{V_i}\rho\psi\,dV &= \sum_{k=1}^{2}\int_{A_k}\vec{n}_k\cdot\left[\left(\vec{v}_k-\vec{v}_i\right)\rho_k\psi_k+\mathbb{J}_k\right]\,dA \\ &-\int_{C_i}\int_{-\delta_2}^{\delta_1}\vec{N}\cdot\left[\left(\vec{v}-\vec{v}_i\right)\rho\psi+\mathbb{J}\right]\,d\delta\,dC+\int_{V_i}\rho\phi\,dV\end{aligned} \tag{3.6}$$

The first and second terms on the right side of the equation account for the fluxes from surfaces A_1, A_2 (the summation term) and surface Σ_i (the double-integral). It is desirable to simplify the expression by reducing the volume integrals to surface integrals. This can be accomplished by the introduction of several surface properties.

We will define a surface mean particle velocity ($\vec{v}_s$) as:

$$\rho_s\vec{v}_s\delta \equiv \int_{-\delta_2}^{\delta_1}\rho\vec{v}\,d\delta \tag{3.7}$$

The mean density per unit surface area (ρ_a) will also be used in the simplification. The mean density per unit surface area and the mean density on the surface (ρ_s) are defined as:

$$\rho_a = \rho_s\delta \equiv \int_{-\delta_2}^{\delta_1}\rho\,d\delta \tag{3.8}$$

Weighted averages of the mass intensive property, ψ and the body source term ϕ are given by:

$$\rho_a \psi_s \equiv \int_{-\delta_2}^{\delta_1} \rho\psi \, d\delta \tag{3.9}$$

$$\rho_a \phi_s \equiv \int_{-\delta_2}^{\delta_1} \rho\phi \, d\delta \tag{3.10}$$

The velocity of the interfacial surface, $\vec{v}_i$ can be split into the tangential and normal components:

$$\vec{v}_i = \vec{v}_{ti} + \vec{v}_{ni} \tag{3.11}$$

The tangential component is given by the average tangential particle velocity ($\vec{v}_{ti} = \vec{v}_{ts}$). If the interface position is given by the function $f(\vec{x}, t) = 0$, then the normal component of the interfacial surface velocity is the surface displacement velocity:

$$\vec{v}_{ni} = \vec{v}_i \cdot \vec{n} = -\frac{\frac{\partial f}{\partial t}}{|\nabla f|} \tag{3.12}$$

The unit vector $\vec{N}$ is normal to the Σ_i surface, and tangent to the interfacial surface (A_i), so:

$$\vec{N} \cdot \vec{v}_i = \vec{N} \cdot \vec{v}_s \tag{3.13}$$

Combining Equations 3.7 and 3.13 gives:

$$\int_{-\delta_2}^{\delta_1} \rho\vec{N} \cdot (\vec{v}_i - \vec{v}) \; d\delta = 0 \tag{3.14}$$

$$\int_{-\delta_2}^{\delta_1} \rho\psi\vec{N} \cdot (\vec{v}_i - \vec{v}) \; d\delta = \int_{-\delta_2}^{\delta_1} \rho\vec{N} \cdot (\vec{v}_s - \vec{v}) \; d\delta \tag{3.15}$$

An average line efflux along the line C_i is now defined as:

$$\mathbb{J}_a \equiv \int_{-\delta_2}^{\delta_1} \left[\mathbb{J} - (\vec{v}_s - \vec{v})\,\rho\psi\right]\,d\delta \tag{3.16}$$

The definitions above can be applied to Equation 3.6 to yield the simpler expression without volume integrals:

$$\begin{aligned}\frac{d}{dt}\int_{A_i}\rho_a\psi_s\,dA = \sum_{k=1}^{2}\int_{A_k}\vec{n}_k\cdot\left[(\vec{v}_k - \vec{v}_i)\,\rho_k\psi_k + \mathbb{J}_k\right]\,dA \\ -\int_{C_i}\vec{N}\cdot\mathbb{J}_a\,dC + \int_{A_i}\rho_a\phi_s\,dA\end{aligned} \tag{3.17}$$

The expression above is primarily in terms of surface integrals. It may be further simplified if the derivative in the first term can be moved inside the integral and if the integral in terms of the line C_i can be converted to a surface integral. These goals are achieved using the surface transport theorem and Green's theorem. Once the integrals have all been converted to surface integrals, they can be eliminated. The resulting expression for generalized interfacial balance is [104, 11]:

$$\begin{aligned}\frac{d_s}{dt}(\psi_a) + \psi_a\nabla_s\cdot\vec{v}_i = \sum_{k=1}^{2}\left[\rho_k\psi_k\vec{n}_k\cdot(\vec{v}_k - \vec{v}_i) + \vec{n}_k\cdot\mathbb{J}_k\right] \\ -A^{\alpha\beta}g_{ln}\left(t_\alpha^n\mathbb{J}_a^{l_*}\right)_{,\beta} + \phi_a\end{aligned} \tag{3.18}$$

3.2 Averaging

Equation 3.5 is the local instant formulation of the balance equation in terms of a single field k. In order to write an equation in terms of a single field within a two-phase mixture, several changes are required. The functions that define the conditions for each field are assumed to be continuously differentiable everywhere within the region occupied by that phase, except

in the interfacial regions. The parameters in the balance equation must also be averaged in time, weighted by the void fraction or by mass.

We begin with a two state density functions. These are functions that return a one or a zero depending on the conditions at a given time and location in the flow. The function M_k returns a 1 for a point occupied by phase k (where k is 1 or 2), and a zero when near the interface. The function M_s returns a 1 for a point occupied by the interface, and a zero for a point in phase k.

The time-average of M_k is essentially the local void fraction of phase k, which is represented by α_k :

$$\alpha_k = \overline{M}_k \tag{3.19}$$

The term P_k will be used to represent the instant, local physical or flow variables of each phase. If we use the phase density function (M_k) as a weighting function for the average of P_k, we can define a phase average:

$$\overline{\overline{P}}_k \equiv \frac{\overline{M_k P_k}}{\overline{M_k}} = \frac{\overline{P_k}}{\alpha_k} \tag{3.20}$$

Note that the M_k term in the numerator of the expression can be removed, since we are assuming that this average is conducted within a single phase, so the state density function will return a 1. We have also substituted the time average of M_k in the denominator with the void fraction, α_k.

Rearranging the expression gives a relationship between the simple time-average and the phase average:

$$\overline{P}_k = \alpha_k \overline{\overline{P}}_k \tag{3.21}$$

Using similar reasoning as for the density function weighted average, we can define a density-weighted average as:

$$\widehat{\psi}_k = \frac{\overline{\overline{\rho_k \psi_k}}}{\overline{\overline{\rho_k}}} \tag{3.22}$$

The time average of ∇F is defined in [104] as:

$$\overline{\nabla F} = \nabla \overline{F}\left(\vec{x}_o, t_o\right) + \frac{1}{\Delta t}\sum_j \frac{1}{v_{ni}}\left(\vec{n}^+ F^+ + \vec{n}^- F^-\right) \tag{3.23}$$

Where the $^+$ and $^-$ superscripts indicate opposite sides of the interface, and F can be a scalar, a vector, or a tensor. The ∇ can be a divergence or a gradient operator, depending on F.

Another averaging definition from [104] is:

$$\begin{aligned}\overline{\left(\frac{\partial \rho_k \psi_k}{\partial t}\right)} + \overline{\nabla\cdot\left(\rho_k \psi_k \vec{v}_k\right)} = \frac{\partial \alpha_k \overline{\overline{\rho_k}}\widehat{\psi}_k}{\partial t} + \nabla\cdot\left(\alpha_k \overline{\overline{\rho_k}}\widehat{\psi}_k \widehat{\vec{v}}_k\right) + \\ \nabla\cdot\left(\alpha_k \mathbb{J}_k^T\right) + \frac{1}{\Delta t}\sum_j\left[\frac{1}{v_{ni}}\vec{n}_k\cdot\rho_k\left(\vec{v}_k - \vec{v}_i\right)\psi_k\right]\end{aligned} \tag{3.24}$$

The expressions above can be applied to Equation 3.5 to produce a generalized time averaged balance equation. Equation 3.5 can be re-cast as the balance of a quantity in a unit volume (as opposed to the balance of a quantity on a surface).

$$B_v = \frac{\partial \rho_k \psi_k}{\partial t} + \nabla\cdot\left(\vec{v}_k \rho_k \psi_k\right) + \nabla\cdot\mathbb{J}_k - \rho_k \phi_k = 0 \tag{3.25}$$

Similarly, the general interfacial balance equation (3.18) can be expressed as the balance

of a quantity on a surface.

$$B_s = \frac{1}{\delta}\left\{\frac{d_s}{dt}\left(\psi_a\right) + \psi_a \nabla_s \cdot \vec{v}_i - \sum_{k=1}^{2}\left[\rho_k \psi_k \vec{n}_k \cdot \left(\vec{v}_k - \vec{v}_i\right) + \vec{n}_k \cdot \mathbb{J}_k\right] + A^{\alpha\beta} g_{ln}\left(t_\alpha^n \mathbb{J}_a^{l_*}\right)_{,\beta} - \phi_a\right\} = 0 \tag{3.26}$$

Note that Equation 3.18 has been divided by the interface thickness (δ), which results in an expression that is the balance of ψ per unit volume of the region.

Equation 3.26 can be rearranged and averaged to give the interfacial transfer condition:

$$\overline{B_s} = \frac{1}{\Delta t}\sum_j \frac{1}{v_{ni}}\left\{\frac{d_s}{dt}\left(\psi_a\right) + \psi_a \nabla_s \cdot \vec{v}_i - \phi_a + A^{\alpha\beta} g_{ln}\left(t_\alpha^n \mathbb{J}_a^{l_*}\right)_{,\beta} - \sum_{k=1}^{2}\left[\rho_k \psi_k \vec{n}_k \cdot \left(\vec{v}_k - \vec{v}_i\right) + \vec{n}_k \cdot \mathbb{J}_k\right]\right\} = 0 \tag{3.27}$$

An average form of Equation 3.25 can be found by averaging each term in the equation, and then simplifying by substitution of the appropriate equations. Equation 3.24 can be substituted in for the averaged first two terms of Equation 3.25. Equations 3.23 and 3.20 are then applied to the averaged third term. Finally, the fourth term is averaged, and Equation 3.20 is again used to simplify the expression, followed by Equation 3.22. When the averaging is complete, the volume balance is (3.28):

Note that Equation 3.5 has been written in terms of a single phase k. In order to write an equation in terms of a single phase within a two-phase mixture, several changes are required. The functions that define the conditions for each phase are assumed to be continuously differentiable everywhere within the region occupied by that phase, except in the interfacial regions. The balance equation must also be averaged in time (weighted average by the void fraction - denoted as $\overline{\overline{X}}$) or a time average weighted by mass (denoted as $\widehat{X}$). In addition, a local void fraction term (α_k) must be included. The details of the two-phase derivation are beyond the scope of this article, but are presented in greater detail in [104]. The averaged

balance equation for a phase k is presented below:

$$\frac{\partial \alpha_k \overline{\overline{\rho_k}} \widehat{\psi_k}}{\partial t} + \nabla \cdot \left(\alpha_k \overline{\overline{\rho_k}} \widehat{\psi_k} \widehat{\vec{v_k}} \right) + \nabla \cdot \left[\alpha_k \left(\overline{\overline{\mathbb{J}_k}} + \mathbb{J}_k^T \right) \right] - \alpha_k \overline{\overline{\rho_k}} \widehat{\phi_k} + \frac{1}{\Delta t} \sum_j \left\{ \frac{1}{v_{ni}} \left[\vec{n}_k \cdot \rho_k \left(\vec{v}_k - \vec{v}_i \right) \psi_k + \vec{n}_k \cdot \mathbb{J}_k \right] \right\} = 0 \tag{3.28}$$

Where the summation in Equation 3.28 is made over j interfaces in a two-phase flow. We can simplify it by making the substitution:

$$I_k = -\frac{1}{\Delta t} \sum_j \left\{ \frac{1}{v_{ni}} \vec{n}_k \cdot \left[\rho_k \left(\vec{v}_k - \vec{v}_i \right) \psi_k + \mathbb{J}_k \right] \right\} \tag{3.29}$$

The balance equation for the k^{th} phase is therefore:

$$\frac{\partial \alpha_k \overline{\overline{\rho_k}} \widehat{\psi_k}}{\partial t} + \nabla \cdot \left(\alpha_k \overline{\overline{\rho_k}} \widehat{\psi_k} \widehat{\vec{v_k}} \right) = -\nabla \cdot \left[\alpha_k \left(\overline{\overline{\mathbb{J}_k}} + \mathbb{J}_k^T \right) \right] + \alpha_k \overline{\overline{\rho_k}} \widehat{\phi_k} + I_k \tag{3.30}$$

Equation 3.30 represents a temporally or statistically averaged 3D model for k fields. A set of three conservation equations (mass, momentum, and energy) can be constructed for each field using this model. However, the averaged fields are not independent of each other. The liquid fields can vaporize and transfer to the vapor phase. The droplet fields can coalesce back into the continuous liquid field, or break up into smaller droplets. These interactions appear as source terms in the conservation equations.

Equation 3.30 can now be written as the conservation of mass, momentum, and energy by specifying the terms ψ, $\mathbb{J}$, and ϕ as shown in Table 3.1.

Table 3.1: Balance Equation Parameters for Mass, Momentum, and Energy

Property	ψ_k	$\mathbb{J}_k$	ϕ_k
Mass	1	0	0
Momentum	$\vec{v}$	$-\mathbb{T} = p_k\mathbb{I} - \mathfrak{T}_k$	$\vec{g}_k$
Energy	$u_k + \frac{v_k^2}{2}$	$\vec{q}_k - \mathbb{T}\cdot\vec{v}_k$	$\frac{\dot{q}_k}{\rho_k} + \vec{g}_k\cdot\vec{v}_k$

3.2.1 Mass Conservation Equation

By applying the values for mass conservation in Table 3.1 to Equation 3.30, the generalized mass conservation equation can be written as:

$$\frac{\partial \alpha_k \overline{\overline{\rho_k}}}{\partial t} + \nabla\cdot\left(\alpha_k \overline{\overline{\rho_k}}\,\widehat{\vec{v}_k}\right) = \Gamma_k \tag{3.31}$$

Where the mass generation source for phase k (Γ_k) is defined as:

$$\Gamma_k \equiv I_k = -\frac{1}{\Delta t}\sum_j \left\{ \frac{1}{v_{ni}}\vec{n}_k\cdot\rho_k\left(\vec{v}_k - \vec{v}_i\right)\right\} \tag{3.32}$$

and is constrained to be:

$$\sum_k \Gamma_k = 0 \tag{3.33}$$

The summation in Equation 3.32 is made over j interfaces in a two-phase flow, making it a generalized equation for two-phase flows with multiple interfaces.

3.2.2 Momentum Conservation Equation

Some additional definitions are needed before developing the momentum balance equation. These additional definitions are shown below:

$$\mathbb{J}_k^T \equiv \overline{\overline{\rho_k \psi_k' \vec{v}_k'}} \tag{3.34}$$

Applying the value for ψ from Table 3.1 to Equation 3.34 yields the following definition for the turbulent flux $\mathfrak{T}_k^T$:

$$\mathfrak{T}_k^T \equiv -\mathbb{J}_k^T = -\overline{\overline{\rho_k \vec{v}_k' \vec{v}_k'}} \tag{3.35}$$

The momentum source from interfacial transfer is then defined as:

$$M_k \equiv I_k = -\frac{1}{\Delta t} \sum_j \left\{ \frac{1}{v_{ni}} \vec{n}_k \cdot \left[\rho_k \left(\vec{v}_k - \vec{v}_i \right) v_k - \mathbb{T}_k \right] \right\} \tag{3.36}$$

The momentum equation can now be written by substituting the appropriate values from Table 3.1 into Equation 3.30:

$$\begin{aligned} \frac{\partial \alpha_k \overline{\overline{\rho_k}} \widehat{\vec{v}_k}}{\partial t} + \nabla \cdot \left(\alpha_k \overline{\overline{\rho_k}} \widehat{\vec{v}_k} \widehat{\vec{v}_k} \right) &= -\nabla \cdot \left[\alpha_k \left(\overline{\overline{p_k \mathbb{I} - \mathfrak{T}_k}} + \mathbb{J}_k^T \right) \right] + \\ &+ \alpha_k \overline{\overline{\rho_k}} \widehat{\vec{g}_k} - \frac{1}{\Delta t} \sum_j \left\{ \frac{1}{v_{ni}} \vec{n}_k \cdot \left[\rho_k \left(\vec{v}_k - \vec{v}_i \right) v_k - \mathbb{T}_k \right] \right\} \end{aligned} \tag{3.37}$$

Substituting Equations 3.35 and 3.36 into Equation 3.37 and re-arranging, the general

momentum balance equation is obtained.

$$\frac{\partial \alpha_k \overline{\overline{\rho_k}} \widehat{\vec{v}_k}}{\partial t} + \nabla\cdot\left(\alpha_k \overline{\overline{\rho_k}} \widehat{\vec{v}_k} \widehat{\vec{v}_k}\right) = -\nabla\left(\alpha_k \overline{\overline{p_k}}\right) + \nabla\cdot\left[\alpha_k\left(\overline{\overline{\mathfrak{T}_k}} + \mathfrak{T}_k^T\right)\right] + \alpha_k \overline{\overline{\rho_k}} \widehat{\vec{g}}_k + M_k \tag{3.38}$$

Where M_k is the k^{th} phase momentum source resulting from the interfacial transfer and $\mathfrak{T}_k^T$ is the turbulent stress tensor.

3.2.3 Energy Conservation Equation

The generalized energy conservation equation is obtained by substituting the appropriate values from Table 3.1 into Equation 3.30 to obtain Equation 3.39.

$$\frac{\partial \alpha_k \overline{\overline{\rho_k}} \widehat{\left(u_k + \frac{v_k^2}{2}\right)}}{\partial t} + \nabla\cdot\left(\alpha_k \overline{\overline{\rho_k}} \widehat{\left(u_k + \frac{v_k^2}{2}\right)} \widehat{\vec{v}_k}\right) = -\nabla\cdot\left[\alpha_k\left(\overline{\overline{\vec{q}_k - \mathbb{T}_k\cdot\vec{v}_k}} + \mathbb{J}_k^T\right)\right] + \alpha_k \overline{\overline{\rho_k}} \widehat{\left(\vec{g}\cdot\vec{v}_k + \frac{\dot{q}_k}{\rho_k}\right)} + E_k \tag{3.39}$$

Where E_k is the total energy gain in phase k through the interfaces and is defined:

$$E_k \equiv I_k = -\frac{1}{\Delta t}\sum_j \left\{\frac{1}{v_{ni}}\vec{n}\cdot\left[\rho_k\left(\vec{v}_k - \vec{v}_i\right)\left(u_k + \frac{v_k^2}{2}\right) + \vec{q}_k - \mathfrak{T}_k\cdot\vec{v}_k\right]\right\} \tag{3.40}$$

Some further simplification of Equation 3.39 is possible with the following additional terms and definitions:

The mean turbulent heat flux q_k^T:

$$\vec{q}_k^T = \mathbb{J}_k^T - \overline{\overline{\mathbb{T}_k\cdot\vec{v}_k'}} \tag{3.41}$$

The instantaneous velocity as the sum of the mass-weighted average velocity value and

the velocity fluctuating component:

$$\vec{v}_k = \widehat{\vec{v}}_k + \vec{v}'_k \tag{3.42}$$

Re-examining the internal and kinetic energy terms from Equation 3.39, and using Equation 3.42:

$$\widehat{u_k + \frac{v_k^2}{2}} = \widehat{u}_k + \frac{1}{2}\left(\widehat{\vec{v}}_k + \widehat{\vec{v}'}_k\right)^2 = \widehat{u}_k + \frac{1}{2}\left(\widehat{\vec{v}_k^2} + \widehat{\left(\vec{v}'_k\right)^2}\right) + \widehat{\vec{v}}_k\widehat{\vec{v}'}_k \tag{3.43}$$

The mass weighted average velocity from Equation 3.43 can be written:

$$\widehat{\vec{v}'}_k = \frac{\overline{\overline{\rho_k \vec{v}'_k}}}{\overline{\overline{\rho_k}}} \tag{3.44}$$

Recognizing that the phase average of the product of the density and the velocity fluctuation is zero ($\overline{\overline{\rho_k \vec{v}'_k}} = 0$), Equation 3.43 can be simplified:

$$\widehat{u}_k + \frac{1}{2}\widehat{\left(\vec{v}'_k\right)^2} + \frac{1}{2}\widehat{(\vec{v}_k)^2} \tag{3.45}$$

We define the apparent internal energy $\widehat{e}_k$ as:

$$\widehat{e}_k \equiv \widehat{u}_k + \frac{1}{2}\widehat{\left(\vec{v}'_k\right)^2} \tag{3.46}$$

A similar method to that used to develop the apparent internal energy can be used to simplify the turbulent energy effects.

$$\begin{aligned}\overline{\overline{\vec{q}_k - \mathbb{T}_k \cdot \vec{v}_k}} + \mathbb{J}_k^T = \overline{\overline{\vec{q}_k - \mathbb{T}_k \cdot \left(\widehat{\vec{v}}_k + \vec{v}'_k\right)}} + \mathbb{J}_k^T = \\ \overline{\overline{\vec{q}_k - \mathbb{T}_k \cdot \widehat{\vec{v}}_k - \mathbb{T}_k \cdot \vec{v}'_k}} + \mathbb{J}_k^T\end{aligned} \tag{3.47}$$

Applying Equation 3.41 to Equation 3.47:

$$\overline{\overline{\vec{q}_k - \mathbb{T}_k \cdot \widehat{\vec{v}}_k - \mathbb{T}_k \cdot \vec{v}_k'}} + \mathbb{J}_k^T = \overline{\overline{\vec{q}_k - \mathbb{T}_k \cdot \widehat{\vec{v}}_k}} + \vec{q}_k^T \tag{3.48}$$

Substituting Equations 3.46 and 3.48 into Equation 3.39 and recognizing that the internal heating ($\dot{q}$) in two-phase flows can be neglected, the general energy balance equation is obtained:

$$\begin{aligned} &\frac{\partial}{\partial t}\left[\alpha_k \overline{\overline{\rho_k}}\left(\widehat{e}_k + \frac{\widehat{v}_k^2}{2}\right)\right] + \nabla\cdot\left[\alpha_k \overline{\overline{\rho_k}}\left(\widehat{e}_k + \frac{\widehat{v}_k^2}{2}\right)\widehat{\vec{v}}_k\right] = \\ &-\nabla\cdot\left[\alpha_k\left(\overline{\overline{\vec{q}_k}} + \vec{q}_k^T\right)\right] + \nabla\cdot\left(\alpha_k \overline{\overline{\mathbb{T}_k}}\cdot\widehat{\vec{v}}_k\right) + \alpha_k \overline{\overline{\rho_k}}\widehat{\vec{g}}\cdot\widehat{\vec{v}}_k + E_k \end{aligned} \tag{3.49}$$

Equation 3.49 is the total energy equation, including both mechanical and thermal effects. The mechanical energy equation can be determined by taking the dot product of the momentum equation with the velocity. When this is subtracted from the total energy equation, the result is the internal energy equation:

$$\begin{aligned} \frac{\partial}{\partial t}\left(\alpha_k \overline{\overline{\rho_k}}\widehat{e}_k\right) + \nabla\cdot\left(\alpha_k \overline{\overline{\rho_k}}\widehat{e}_k\widehat{\vec{v}}_k\right) &= -\nabla\cdot\left(\alpha_k \overline{\overline{\vec{q}_k}}\right) \\ -\nabla\cdot\left\{\alpha_k\left(\vec{q}_k^T + \mathfrak{T}_k^T\cdot\widehat{\vec{v}}_k\right)\right\} - \alpha_k \overline{\overline{p}}_k\nabla\cdot\widehat{\vec{v}}_k + &\\ \alpha_k\left(\overline{\overline{\mathfrak{T}}}_k + \mathfrak{T}_k^T\right) : \nabla\widehat{\vec{v}}_k + \Lambda_k & \end{aligned} \tag{3.50}$$

Where:

$$\mathfrak{T}_k : \nabla\vec{v}_k \equiv (\mathfrak{T}_k\cdot\nabla)\cdot\vec{v}_k = \nabla\cdot(\mathfrak{T}_k\cdot\vec{v}_k) - \vec{v}_k\cdot(\nabla\cdot\mathfrak{T}_k) \tag{3.51}$$

$$\Lambda_k \equiv \frac{\widehat{\vec{v}}_k^{\,2}}{2}\Gamma_k - M_k\cdot\widehat{\vec{v}}_k + E_k \tag{3.52}$$

for a symmetrical stress tensor $\mathfrak{T}$.

Recall that the energy conservation equation presented above (3.50) does not include the mechanical energy portion of the energy balance. The formulation as presented is simpler

than if the mechanical energy were included. Although not included in the energy balance explicitly, the turbulent energy from mean motion and the turbulent kinetic energy are accounted for, as long as the models for the appropriate turbulent terms that appear in the momentum formulation are included [105].

Equations 3.31, 3.38, and 3.50 represent a two-fluid three-dimensional model based on temporal or statistical averaging. The complete model uses the mass, momentum, and energy equations written for each phase. The averaged fields of one phase are not independent of the other phase, so interaction terms appear as source terms in the field equations. Considering this, the conservation equations are written for each field in the next section. The additional terms to account for inter-field relationships of the six proposed fields are included.

3.3 Six-Field Conservation Equations

The preceding sections provided the derivation of a generalized conservation equation for a general property of phase (or field) k. The complete set of conservation equations in mass, momentum, and energy will now be shown for each of the six proposed fields, beginning with mass conservation.

3.3.1 Mass Continuity

The mass conservation equation (3.31) is repeated here as:

$$\frac{\partial \alpha_k \rho_k}{\partial t} + \nabla \cdot (\alpha_k \rho_k \vec{v}_k) = \Gamma_k \tag{3.53}$$

Note that the averaging notation in Equation 3.31 has been omitted from Equation 3.53 for simplicity - the variables are still averaged in space and time as before.

We now focus on the mass exchange between fields. The two-field model formulation used in most system codes includes a single interface for the transfer of mass and energy

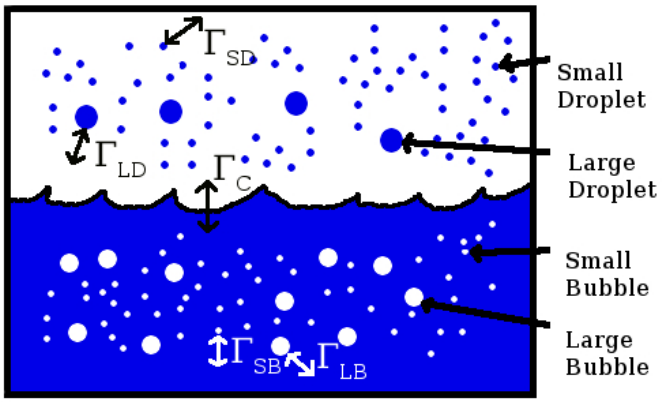

Figure 3.1: Phasic interaction examples

between the phases/fields. Figure 3.1 provides a graphical depiction of the mass transfer between the proposed fields in an arbitrary volume.

The figure shows mass exchange due to phase exchange between the continuous vapor and the large (Γ_{LD}) and small (Γ_{SD}) droplets, as well as between the continuous liquid and the large and small bubbles (Γ_{LB}, Γ_{SBu}) and the continuous liquid to the continuous vapor (Γ_C). The mass exchange due to phase change can be in the form of evaporation (vapor generation) or condensation. Note from Equation 3.33 that the vapor mass generation is equal in magnitude, but opposite in sign from the liquid mass generation. This means that if the term is assumed to represent vapor generation and the solution gives a value of vapor generation that is negative, the sign reversal indicates that in fact it was condensation, not vapor generation. For simplicity, references to mass exchange will be in terms of vapor generation, though in practical use, the same expression can also model condensation, with a simple sign reversal.

Thus, there are five interfaces between the fields where phase change will result in mass exchange between the phases. The total vapor generation from all liquid fields is represented by Γ_g. It is assumed that the total vapor generation can be partitioned into mass transfer at the vapor/liquid interface (Γ_{ig}), and that in the thermal boundary layer near the walls (Γ_w) [22].

The net heat and mass transfer across the phase interface is assumed to be zero; this is

because the interface is assumed to have no volume. Thus, all the energy or mass leaving one phase must cross the interface into the other phase. This simplifying assumption allows for the energy and mass equations to balance across the interface. The equation for mass exchange per unit volume at the interface due to phase change is shown as Equation 3.54.

$$\Gamma_{ig} = -\frac{H_{ig}\left(T^s - T_g\right) + H_{if}\left(T^s - T_f\right)}{h_g^* - h_f^*} \tag{3.54}$$

where:

$$h_g^* = \frac{1}{2}\left[\left(h_g^s + h_g\right) + \Upsilon\left(h_g^s - h_g\right)\right] \tag{3.55}$$

$$h_f^* = \frac{1}{2}\left[\left(h_f^s + h_f\right) - \Upsilon\left(h_f^s - h_f\right)\right] \tag{3.56}$$

The vapor generation per unit volume at a superheated wall is computed using the total heat flux from the wall to the fluid. Equation 3.57 shows this calculation.

$$\Gamma_w = \frac{q_w^{''} A_w}{V\left(h_g^{'} - h_f^{'}\right)} \frac{h_f - h_{cr}}{\left(h_f^s - h_{cr}\right)\left(1 + \epsilon_p\right)} \tag{3.57}$$

where:

$$h_g^{'} = \frac{1}{2}\left[\left(h_g^s + h_g\right) + \epsilon\left(h_g^s - h_g\right)\right] \tag{3.58}$$

$$h_f^{'} = \frac{1}{2}\left[\left(h_f^s + h_f\right) - \epsilon\left(h_f^s - h_f\right)\right] \tag{3.59}$$

We now define some additional terms:

η=Fraction of vapor generation from both large and small droplet fields

η_{LD}=Fraction of total vapor generation from large droplets

η_{SD}=Fraction of total vapor generation from small droplets

$\Gamma_L = (1-\eta)\,\Gamma$ = Vapor generation rate from continuous liquid

$\Gamma_{LD} = \eta_{LD}\Gamma$ = Vapor generation rate from large droplets

$\Gamma_{SD} = \eta_{SD}\Gamma$ = Vapor generation rate from small droplets

The fraction of vapor generation coming from the entrained liquid can now be determined as shown in Equation 3.60.

$$\eta = \min\left[\frac{\alpha_{LD}+\alpha_{SD}}{1-\alpha_g}, \left(1.0 - \frac{q'''_w}{\Gamma_g h_{fg}}\right)\right] \tag{3.60}$$

The two terms within the minimum function in Equation 3.60 are used to compute the fraction of the total liquid volume that is small or large droplets, or the fraction of the heating from the wall that is going to the droplet fields (as opposed to the continuous liquid field). This fraction represents the fraction of the vapor that is generated by the droplet fields.

We can further expand the definition to include the fraction of the vapor from the large droplets alone:

$$\eta_{LD} = \frac{\alpha_{LD}}{\alpha_{LD}+\alpha_{SD}}\eta \tag{3.61}$$

Which indicates that the vapor generation from the large droplet field will be:

$$\Gamma_{LD} = \eta_{LD}\Gamma_g \tag{3.62}$$

Similarly, the fraction of vapor generated from the small droplet field and the correspond-

ing vapor generation from the small droplet field can be computed as:

$$\eta_{SD} = \frac{\alpha_{SD}}{\alpha_{LD} + \alpha_{SD}} \eta \tag{3.63}$$

$$\Gamma_{SD} = \eta_{SD} \Gamma_g \tag{3.64}$$

In addition to mass transfer from phase changes, mass can be transferred from one field to another by physical mechanisms. This includes large droplets impacting fuel rod spacer grids and breaking up into smaller droplets, droplets being entrained in the vapor from the continuous liquid due to high relative velocities between the phases or vigorous bubble generation due to heating, and other mechanisms.

These physical mechanisms are included in the mass continuity equation in the form of source terms. Specific closure models are needed to provide the values of these terms in system analyses.

Based on the above considerations, mass conservation equations can be developed for each of the considered fields. Equation 3.65 shows the mass conservation for the continuous liquid. Note the two additional terms for the small and large droplet fields. It is assumed that there is no direct droplet-to-bubble phase transfer, so no terms are included representing that mode.

$$\underbrace{\frac{\partial}{\partial t}\left(\alpha_f \rho_f\right)}_{\text{A}} + \underbrace{\nabla \cdot \left(\alpha_f \rho_f \vec{v}_f\right)}_{\text{B}} = \underbrace{-\Gamma_L}_{\text{C}} - \underbrace{S'''_{LD,E}}_{\text{D}} - \underbrace{S'''_{SD,E}}_{\text{E}} + \underbrace{S'''_{LD,DE}}_{\text{F}} + \underbrace{S'''_{SD,DE}}_{\text{G}} \tag{3.65}$$

A - Rate of change of mass

B - Mass change due to convection

C - Rate of mass transfer from continuous liquid due to phase change

D - Mass lost to large droplet field by entrainment

E - Mass lost to small droplet field by entrainment

F - Mass gained from large droplet field by de-entrainment

G - Mass gained from small droplet field by de-entrainment

The mass conservation for large droplet fields is shown as Equation 3.66. Equation 3.67 shows the same mass conservation equation for small droplets.

$$\frac{\partial}{\partial t}\left(\alpha_{LD}\rho_f\right) + \nabla\cdot\left(\alpha_{LD}\rho_f\vec{v}_{LD}\right) = \underbrace{-\Gamma_{LD}}_{\text{A}} + S'''_{LD,E} - S'''_{LD,DE} - \underbrace{S'''_{LD,SB}}_{\text{B}} - \underbrace{S'''_{LD,FB}}_{\text{C}} + \underbrace{S'''_{SD,C}}_{\text{D}} \tag{3.66}$$

A - Mass lost due to large droplet evaporation

B - Mass lost to small droplet by spacer-breakup

C - Mass lost to small droplet field by flow breakup

D - Mass gained from small droplet field coalescence

$$\frac{\partial}{\partial t}\left(\alpha_{SD}\rho_f\right) + \nabla\cdot\left(\alpha_{SD}\rho_f\vec{v}_{SD}\right) = \underbrace{-\Gamma_{SD}}_{\text{A}} + S'''_{SD,E} + S'''_{LD,SB} + S'''_{LD,FB} - S'''_{SD,DE} - S'''_{SD,C} \tag{3.67}$$

A - Mass lost due to small droplet evaporation

The following three equations were developed following the same pattern used for the liquid phases. Equation 3.68 is the mass balance for the continuous vapor phase. This equation and those following include additional terms for the mass exchange between the

new fields (large and small bubbles).

$$\frac{\partial}{\partial t}\left(\alpha_g \rho_g\right) + \nabla\cdot\left(\alpha_g \rho_g \vec{v}_g\right) = \underbrace{\Gamma_{CV}}_{\text{A}} - \underbrace{S'''_{SBu,E}}_{\text{B}} + \underbrace{S'''_{LB,C}}_{\text{C}} - \underbrace{S'''_{LB,E}}_{\text{D}} + \underbrace{S'''_{LB,DE}}_{\text{E}} + \underbrace{S'''_{SB,DE}}_{\text{F}} \tag{3.68}$$

A - Rate of mass gained by continuous vapor from phase change

B - Rate of mass loss by entrainment of small bubbles

C - Rate of mass gain by coalescence of large bubbles

D - Rate of mass loss by entrainment of large bubbles

E - Rate of mass gain by de-entrainment of large bubbles

F - Rate of mass gain by de-entrainment of small bubbles

Note from equation 3.68 that there is no term for the gain of mass in the continuous vapor field due to the coalescence of small bubbles. This formulation assumes that the small bubbles must first coalesce into large bubbles before they will coalesce to the point of being considered part of the continuous vapor field. Thus, the rate of mass gain by coalescence of small bubbles is not needed. The next two equations (3.69, 3.70) are for mass conservation in the new large bubble and small bubble fields, respectively.

$$\frac{\partial}{\partial t}\left(\alpha_{LB} \rho_g\right) + \nabla\cdot\left(\alpha_{LB} \rho_g \vec{v}_{LB}\right) = \underbrace{\Gamma_{LB}}_{\text{A}} + \underbrace{S'''_{SBu,C}}_{\text{B}} - S'''_{LB,C} + S'''_{LB,E} - S'''_{LB,DE} - \underbrace{S'''_{LB,SB}}_{\text{C}} - \underbrace{S'''_{LB,FB}}_{\text{D}} \tag{3.69}$$

A - Rate of large bubble generation due to evaporation

B - Mass gained by large bubbles by small bubble coalescence

C - Mass lost from large bubble field by spacer grid breakup

D - Mass lost from large bubble field by flow breakup

$$\frac{\partial}{\partial t}\left(\alpha_{SBu}\rho_g\right)+\nabla\cdot\left(\alpha_{SBu}\rho_g\vec{v}_{SBu}\right)=\underbrace{\Gamma_{SBu}}_{\text{A}}+S'''_{SBu,E}-S'''_{SBu,DE}-S'''_{SBu,C}+S'''_{LB,SB}+S'''_{LB,FB} \tag{3.70}$$

A - Rate of small bubble generation due to evaporation

3.3.2 Momentum Continuity

Interactions between phases are not limited to mass exchange. In fact, significant importance should be applied to the exchange of momentum between phases. Any phase interface will involve the exchange of momentum. This momentum transfer is the reason that droplets of water are carried along in a vapor flow. High velocity vapor flows are one of the primary sources of droplets in the vapor field (by way of entrainment).

The general momentum conservation equation (3.38) is repeated here, but the momentum source term M_k has been expanded to show the effect of the interfacial momentum transfer as detailed in [104].

$$\begin{aligned}\frac{\partial\alpha_k\overline{\overline{\rho_k}}\widehat{\vec{v}_k}}{\partial t}+\nabla\cdot\left(\alpha_k\overline{\overline{\rho_k}}\widehat{\vec{v}_k}\widehat{\vec{v}_k}\right)&=-\nabla\left(\alpha_k\overline{\overline{p_k}}\right)+\\ \nabla\cdot\left[\alpha_k\left(\overline{\overline{\mathfrak{T}_k}}+\mathfrak{T}_k^T\right)\right]&+\alpha_k\overline{\overline{\rho_k}}\widehat{\vec{g}}_k+\\ \left[\widehat{\vec{v}_{i,k}}\Gamma_k+\overline{\overline{p_{ki}}}\nabla\alpha_k+M_{ik}-\nabla\alpha_k\cdot\overline{\overline{\mathfrak{T}_{ki}}}\right]&\end{aligned} \tag{3.71}$$

When the convective derivative is applied to the left-hand side of Equation 3.71 and the

equation is re-arranged, the two-phase momentum conservation equation is obtained:

$$\begin{aligned}\alpha_k\overline{\overline{\rho_k}}\frac{D_k\widehat{\vec{v}_k}}{Dt} = -\alpha_k\nabla\overline{\overline{p_k}} + \nabla\cdot\left[\alpha_k\left(\overline{\overline{\mathfrak{T}_k}} + \mathfrak{T}_k^T\right)\right] + \alpha_k\overline{\overline{\rho_k}}\widehat{\vec{g}}_k + \\ \left(\overline{\overline{p_{ki}}} - \overline{\overline{p_k}}\right)\nabla\alpha_k + \left(\widehat{\vec{v}_{i,k}} - \widehat{\vec{v}_k}\right)\Gamma_k + M_{ik} - \nabla\alpha_k\cdot\overline{\overline{\mathfrak{T}_{ki}}}\end{aligned} \tag{3.72}$$

Momentum equations are now derived for each field. With a separate equation for each field, the droplets can have different velocities than the continuous liquid, as well as different velocities from one another. The same is true for the large and small bubble fields. Closure relationships for the physical models are required to solve the momentum equations by providing the details of the mass and momentum exchange between the fields and the drag forces at the walls. The closure models provide information about the turbulence and entrainment for the continuous fields.

The momentum conservation equation for continuous liquid, including the terms for momentum exchange with the additional fields is shown as Equation 3.73. Note the additional terms for momentum exchange due to droplet entrainment/de-entrainment, and that the variables are still averaged as before, though the overbar and hat notations have been re-

moved for simplicity.

$$
\begin{aligned}
&\underbrace{\alpha_f \rho_f \frac{D\vec{v}_f}{Dt}}_{\text{A}} = \underbrace{-\alpha_f \nabla p_f}_{\text{B}} + \underbrace{\nabla\cdot\left[\alpha_f\left(\mathfrak{T}_f + \mathfrak{T}_f^T\right)\right]}_{\text{C}} + \underbrace{\alpha_f \rho_f \vec{g}_f}_{\text{D}} + \\
&\underbrace{\left(p_{fi} - p_f\right)\nabla\alpha_f}_{\text{E}} + \underbrace{\left(\vec{v}_{i,L} - \vec{v}_f\right)\Gamma_L}_{\text{F}} + \underbrace{\left(\vec{v}_{i,LB} - \vec{v}_f\right)\Gamma_{LB}}_{\text{G}} + \\
&\underbrace{\left(\vec{v}_{i,SBu} - \vec{v}_f\right)\Gamma_{SBu}}_{\text{H}} + \underbrace{M_{if}}_{\text{I}} + \underbrace{M_{wf}}_{\text{J}} - \underbrace{\nabla\alpha_f\cdot\mathfrak{T}_{fi,g}}_{\text{K}} - \\
&\underbrace{\nabla\alpha_f\cdot\mathfrak{T}_{fi,SBu}}_{\text{L}} - \underbrace{\nabla\alpha_f\cdot\mathfrak{T}_{fi,LB}}_{\text{M}} - \underbrace{S'''_{LD,E}v_{LD}}_{\text{N}} - \underbrace{S'''_{SD,E}v_{SD}}_{\text{O}} + \\
&\underbrace{S'''_{SD,DE}v_{SD}}_{\text{P}} + \underbrace{S'''_{LD,DE}v_{LD}}_{\text{Q}}
\end{aligned}
\tag{3.73}
$$

Where the equation terms are defined in words:

A - Rate of change of liquid momentum, including convective effects

B - Pressure gradient in continuous liquid

C - Momentum change from average viscous stress and the turbulent stress effects

D - Momentum change from body forces (gravity, pump head)

E - Pressure difference between interface and continuous liquid

F - Momentum change due to phase change across the continuous liquid/vapor interface

G - Momentum change due to phase change across the large bubble/vapor interface

H - Momentum change due to phase change across the small bubble/vapor interface

I - Interfacial drag from pressure imbalance at interface and skin drag from imbalanced shear forces

J - Wall drag from imbalanced shear forces

K - Momentum lost due to average interfacial shear stress at continuous vapor interface

L - Momentum lost due to average interfacial shear stress at small bubble interface

M - Momentum lost due to average interfacial shear stress at large bubble interface

N - Momentum lost due to large droplet entrainment

O - Momentum lost due to small droplet entrainment

P - Momentum gained from small droplet de-entrainment (to continuous liquid field)

Q - Momentum gained from large droplet de-entrainment

Equation 3.74 is for momentum conservation in the small droplet field. In addition to the entrainment and de-entrainment terms from Equation 3.73, Equation 3.74 includes terms for momentum increase due to the breakup of large droplets, from grid spacers or flow effects. Note that the viscous and turbulent stress effects on momentum have been eliminated from the small droplet momentum conservation equation. This is due to the fact that these effects would only affect the fluid within the droplet itself. Interfacial effects between the droplets and the vapor field are captured elsewhere in the balance equation.

$$\begin{aligned}\alpha_{SD}\rho_f\frac{D\vec{v}_{SD}}{Dt} = &-\alpha_{SD}\nabla p_{SD} + \alpha_{SD}\rho_f\vec{g}_{SD} + \left(p_{i,SD} - p_{SD}\right)\nabla\alpha_{SD} + \\ &\left(\vec{v}_{i,SD} - \vec{v}_{SD}\right)\Gamma_{SD} + M_{i,SD} - \nabla\alpha_{SD}\cdot\mathfrak{T}_{SDi,g} + \\ &\underbrace{S'''_{SD,E}v_{SD}}_{\text{A}} + \underbrace{S'''_{LD,SB}v_{LD}}_{\text{B}} + \underbrace{S'''_{LD,FB}v_{LD}}_{\text{C}} - \underbrace{S'''_{SD,DE}v_{SD}}_{\text{D}} - \underbrace{S'''_{SD,C}v_{SD}}_{\text{E}}\end{aligned} \tag{3.74}$$

A - Momentum lost due to small droplet entrainment

B - Momentum increase from spacer breakup of large droplets

C - Momentum increase from flowing breakup of large droplets

D - Momentum lost from small droplet de-entrainment

E - Momentum lost from small droplet coalescence (to large droplets)

The large droplet momentum balance is similar to that for the small droplet balance and is shown in Equation 3.75. The terms of the equation are the same as those in the equations previously presented, but are for large droplets.

$$\begin{aligned}\alpha_{LD}\rho_f\frac{D\vec{v}_{LD}}{Dt} = &-\alpha_{LD}\nabla p_{LD} + \alpha_{LD}\rho_f\vec{g}_{LD} + \left(p_{i,LD} - p_{LD}\right)\nabla\alpha_{LD} + \\ &\left(\vec{v}_{i,LD} - \vec{v}_{LD}\right)\Gamma_{LD} + M_{i,LD} - \nabla\alpha_{LD}\cdot\mathfrak{T}_{LDi,g} + \\ &\underbrace{S'''_{LD,E}v_{LD}}_{\text{A}} - \underbrace{S'''_{LD,SB}v_{LD}}_{\text{B}} - \underbrace{S'''_{LD,FB}v_{LD}}_{\text{C}} - \underbrace{S'''_{LD,DE}v_{LD}}_{\text{D}} + \underbrace{S'''_{SD,C}v_{SD}}_{\text{E}}\end{aligned} \tag{3.75}$$

The momentum balance in the continuous vapor field is given by Equation 3.76. The terms are very similar to those for the continuous liquid equation.

$$\begin{aligned}\alpha_g\rho_g\frac{D\vec{v}_g}{Dt} = &-\alpha_g\nabla p_g + \nabla\cdot\left[\alpha_g\left(\mathfrak{T}_g + \mathfrak{T}_g^T\right)\right] + \alpha_g\rho_g\vec{g}_g + \\ &\left(p_{gi} - p_g\right)\nabla\alpha_g + \left(\vec{v}_{i,g} - \vec{v}_g\right)\Gamma_g + \left(\vec{v}_{i,LD} - \vec{v}_g\right)\Gamma_{LD} + \\ &\left(\vec{v}_{i,SD} - \vec{v}_g\right)\Gamma_{SD} + M_{ig} + M_{wg} - \underbrace{\nabla\alpha_f\cdot\mathfrak{T}_{gi,f}}_{\text{A}} - \underbrace{\nabla\alpha_f\cdot\mathfrak{T}_{gi,SD}}_{\text{B}} - \\ &\underbrace{\nabla\alpha_f\cdot\mathfrak{T}_{gi,LD}}_{\text{C}} + \underbrace{\Gamma_{LD}\left(v_{LD,i} - v_{LD}\right)}_{\text{D}} + \underbrace{\Gamma_{SD}\left(v_{SD,i} - v_{SD}\right)}_{\text{E}}\end{aligned} \tag{3.76}$$

A - Momentum loss due to average interfacial shear stress at continuous liquid interface

B - Momentum loss to interfacial shear at the small droplet interface

C - Momentum loss to interfacial shear at the large droplet interface

D - Momentum increase from large droplet evaporation

E - Momentum increase from small droplet evaporation

The small and large bubble momentum conservation equations are shown in Equations 3.77 and 3.78. The bubbles are also susceptible to entrainment and de-entrainment by coalescence and breakup. The additional terms for these effects are indicated for each equation.

$$\begin{aligned}\alpha_{SBu}\rho_g\frac{D\vec{v}_{SBu}}{Dt} = &-\alpha_{SBu}\nabla p_{SBu} + \alpha_{SBu}\rho_g\vec{g}_{SBu} + \left(p_{i,SBu} - p_{SBu}\right)\nabla\alpha_{SBu} + \\ &\left(\vec{v}_{i,SB} - \vec{v}_{SBu}\right)\Gamma_{SB} + M_{i,SBu} - \nabla\alpha_{SBu}\cdot\mathfrak{T}_{SBi,f} + \\ &\underbrace{S'''_{SB,E}v_{SBu}}_{\text{A}} + \underbrace{S'''_{LB,SB}v_{LB}}_{\text{B}} + \underbrace{S'''_{LB,FB}v_{LB}}_{\text{C}} - \underbrace{S'''_{SB,DE}v_{SBu}}_{\text{D}} - \underbrace{S'''_{SB,C}v_{SBu}}_{\text{E}}\end{aligned} \tag{3.77}$$

A - Momentum change due to small bubble entrainment

B - Momentum increase due to large bubble spacer grid breakup

C - Momentum increase due to large bubble flow-driven breakup

D - Momentum lost to continuous vapor by small bubble de-entrainment

E - Momentum lost to large bubbles by small bubble coalescence

$$\begin{aligned}\alpha_{LB}\rho_g\frac{D\vec{v}_{LB}}{Dt} = &-\alpha_{LB}\nabla p_{LB} + \alpha_{LB}\rho_g\vec{g}_{LB} + \left(p_{i,LB} - p_{LB}\right)\nabla\alpha_{LB} + \\ &\left(\vec{v}_{i,LB} - \vec{v}_{LB}\right)\Gamma_{LB} + M_{i,LB} - \nabla\alpha_{LB}\cdot\mathfrak{T}_{LBi,f} + \\ &\underbrace{S'''_{LB,E}v_{LB}}_{\text{A}} - S'''_{LB,SB}v_{LB} - S'''_{LB,FB}v_{LB} - \underbrace{S'''_{LB,DE}v_{LB}}_{\text{B}} + S'''_{SB,C}v_{SBu}\end{aligned} \tag{3.78}$$

A - Momentum change due to large bubble entrainment

B - Momentum lost to continuous vapor by large bubble de-entrainment

The difference between large and small bubbles (droplets) is somewhat dependent on the flow conditions, but will be computed based on the Sauter Mean Diameter and the Weber number. The governing equations presented in this work have terms to account for the exchange between the two sizes and making it possible for the mass, momentum, and energy

balances to differentiate between the various fields. The actual division between the small and large droplets relies on information available from the closure of the governing equations.

This momentum transfer is the reason that droplets of water are carried along in a vapor flow. High velocity vapor flows are one of the primary sources of droplets in the vapor field (by way of entrainment). The momentum conservation equation for the small droplet field includes terms for entrainment and de-entrainment, as well as terms for momentum increase due to large droplet breakup from either grid spacers or flow effects. The viscous and turbulent stress effects on momentum have been eliminated from the small droplet momentum conservation equation. This is due to the fact that these effects would only affect the fluid within the droplet itself. Interfacial effects between the droplets and the vapor field are captured elsewhere in the balance equation.

The energy balance equation is simplified by defining a virtual enthalpy term. Other system codes that have been modified to include additional fields have simplified the energy balance equations by assuming that the droplets are the same temperature as the continuous liquid [7]. When the droplets and the continuous liquid have the same temperature, the energy balance for the liquid phase can be reduced to a single equation for both droplets and the liquid field. The same is true for the vapor and bubble fields.

The current development of the energy balance equations includes a separate equation for each field and the additional applicable terms for energy exchange between them. Aside from direct droplet entrainment, the only mechanism for energy exchange between the continuous liquid and the droplets is through radiation heat transfer. The droplets and the continuous liquid may not be at the same temperature, but they will be close in temperature; both will be near the saturation temperature for the liquid. Radiation heat transfer between materials of similar temperatures does not play a significant role in the heat exchange between them, so the heat exchange between the droplets and the continuous liquid will be neglected. A similar line of reasoning provides support to an assumption that heat transfer between the large droplet and small droplet fields may also be neglected. The direct heat transfer between

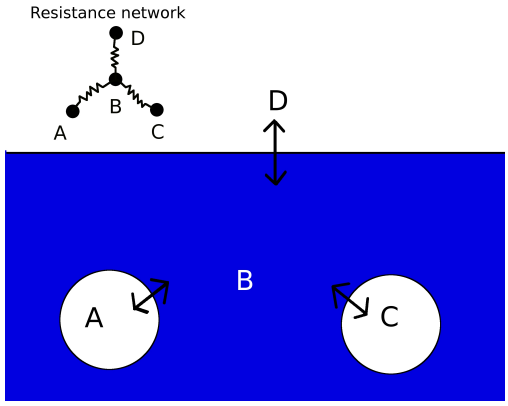

Figure 3.2: Bubble to liquid heat transfer

the continuous vapor and the vapor bubbles, as well as between the large and small bubbles can also be neglected, since the heat transfer between those fields is included in the bubble to continuous liquid and the continuous liquid to vapor (or bubble) heat transfer. The continuous liquid phase becomes the medium for the heat transfer between the bubble fields and between a bubble field and the vapor field. Figure 3.3 shows this exchange graphically.

If we assume that the temperature in Bubble A is greater than the temperature of the coolant (point B), there will be heat transfer from the surface of bubble A to the continuous liquid at B. The heat transfer through the interface between bubble A and the continuous liquid is represented as a resistor in the nodal network shown as an inset to Figure 3.3. As heat is transferred to the liquid, the temperature will rise. If the temperature in the continuous liquid (point B) is higher than the continuous vapor (point D) or a different bubble (point C), the heat may subsequently be transferred to those fields.

The direct heat transfer between the continuous vapor and the vapor bubbles, as well as between the large and small bubbles can also be neglected, since the heat transfer between those fields is included in the bubble to continuous liquid and the continuous liquid to vapor (or bubble) heat transfer. The continuous liquid phase becomes the medium for the heat transfer between the bubble fields and between a bubble field and the vapor field. Figure 3.3 shows this exchange graphically.

If we assume that the temperature in Bubble A is greater than the temperature of the

coolant (point B), there will be heat transfer from the surface of bubble A to the continuous liquid at B. The heat transfer through the interface between bubble A and the continuous liquid is represented as a resistor in the nodal network shown as an inset to Figure 3.3. As heat is transferred to the liquid, the temperature will rise. If the temperature in the continuous liquid (point B) is higher than the continuous vapor (point D) or a different bubble (point C), the heat may subsequently be transferred to those fields.

The remaining heat exchange modes between the fields, and those that must be captured by the conservation equations are: 1) Continuous liquid to/from vapor 2) Continuous liquid to/from droplets by droplet entrainment/de-entrainment 3) Continuous liquid to/from bubbles 4) Continuous vapor to/from droplets 5) Continuous vapor to/from bubbles by bubble entrainment/de-entrainment.

Required source/sink terms have been added to the governing equations to include the effects of entrainment, de-entrainment, bubble breakup and droplet breakup. These terms are dependent to some degree on the flow phenomena and the geometry of the flow. The general governing equations shown here are based on 6 fields before they are adapted to RELAP5-3D.

3.3.3 Energy Continuity

The general energy balance equation is repeated here as Equation 3.79. The balance equation is simplified by defining a virtual enthalpy as in Equation 3.80. In addition, the two-phase interfacial energy transfer is redefined as shown in Equation 3.81 [104]. is obtained.

$$\begin{aligned}\frac{\partial}{\partial t}\left(\alpha_k\overline{\overline{\rho_k}}\widehat{e}_k\right)+\nabla\cdot\left(\alpha_k\overline{\overline{\rho_k}}\widehat{e}_k\widehat{\vec{v}}_k\right)&=-\nabla\cdot\left(\alpha_k\overline{\overline{\vec{q}}}_k\right)\\ -\nabla\cdot\left\{\alpha_k\left(\vec{q}_k^{\,T}+\mathfrak{T}_k^T\cdot\widehat{\vec{v}}_k\right)\right\}-\alpha_k\overline{\overline{p}}_k\nabla\cdot\widehat{\vec{v}}_k+&\\ \alpha_k\left(\overline{\overline{\mathfrak{T}}}_k+\mathfrak{T}_k^T\right):\nabla\widehat{\vec{v}}_k+\Lambda_k&\end{aligned}\tag{3.79}$$

$$\widehat{h_k} = \widehat{e_k} + \frac{\overline{\overline{p_k}}}{\overline{\overline{\rho_k}}} \tag{3.80}$$

$$\begin{aligned}\Lambda_k = \left(\Gamma_k \widehat{h_{ki}} + a_i \overline{\overline{q_{ki}''}}\right) - \overline{\overline{p_{ki}}} \frac{D\alpha_k}{Dt} + M_{ik} \cdot \left(\widehat{\vec{v}_{i,k}} - \widehat{\vec{v}_k}\right) \\ -\nabla\alpha_k \cdot \overline{\overline{\mathfrak{T}_{ki}}} \cdot \left(\widehat{\vec{v}_{i,k}} - \widehat{\vec{v}_k}\right) + W_{ki}^T\end{aligned} \tag{3.81}$$

Substituting 3.80 and 3.81 into 3.79 and re-arranging:

$$\begin{aligned}\frac{\partial}{\partial t}\left(\alpha_k \overline{\overline{\rho_k}} \widehat{h}_k\right) + \nabla \cdot \left(\alpha_k \overline{\overline{\rho_k}} \widehat{h}_k \widehat{\vec{v}}_k\right) = -\nabla \cdot \alpha_k \left(\overline{\overline{\vec{q}}}_k + \vec{q}_k^T\right) \\ + \frac{D_k}{Dt}\left(\alpha_k \overline{\overline{p_k}}\right) - \widehat{\vec{v}}_k \cdot \nabla \cdot \left(\alpha_k \mathfrak{T}_k^T\right) + \alpha_k \overline{\overline{\mathfrak{T}}}_k : \nabla \widehat{\vec{v}}_k + \left(\Gamma_k \widehat{h_{ki}} + a_i \overline{\overline{q_{ki}''}}\right) \\ -\overline{\overline{p_{ki}}} \frac{D\alpha_k}{Dt} + M_{ik} \cdot \left(\widehat{\vec{v}_{i,k}} - \widehat{\vec{v}_k}\right) - \nabla\alpha_k \cdot \overline{\overline{\mathfrak{T}_{ki}}} \cdot \left(\widehat{\vec{v}_{i,k}} - \widehat{\vec{v}_k}\right) + W_{ki}^T\end{aligned} \tag{3.82}$$

Which, by using the convective derivative, can be simplified as:

$$\begin{aligned}\alpha_k \overline{\overline{\rho_k}} \frac{D_k \widehat{h_k}}{Dt} = -\nabla \cdot \alpha_k \left(\overline{\overline{\vec{q}}}_k + \vec{q}_k^T\right) \\ + \alpha_k \frac{D_k \overline{\overline{p_k}}}{Dt} + \Phi_k^T + \Phi_k^\mu + \Gamma_k \left(\widehat{h_{ki}} - \widehat{h_k}\right) + a_i \overline{\overline{q_{ki}''}} + \\ \left(\overline{\overline{p_k}} - \overline{\overline{p_{ki}}}\right) \frac{D_k \overline{\overline{\alpha_k}}}{Dt} + M_{ik} \cdot \left(\widehat{\vec{v}_{i,k}} - \widehat{\vec{v}_k}\right) - \nabla\alpha_k \cdot \overline{\overline{\mathfrak{T}_{ki}}} \cdot \left(\widehat{\vec{v}_{i,k}} - \widehat{\vec{v}_k}\right)\end{aligned} \tag{3.83}$$

Where the turbulent energy source (Φ_k^T) and the viscous dissipation term (Φ_k^μ) are [104]:

$$\Phi_k^T \equiv -\widehat{\vec{v}_k} \cdot \nabla \cdot \left(\alpha_k \mathfrak{T}_k^T\right) + W_{ki}^T \tag{3.84}$$

$$\Phi_k^\mu \equiv \alpha_k \overline{\overline{\mathfrak{T}}}_k : \nabla \widehat{\vec{v}}_k \tag{3.85}$$

Other system codes that have been modified to include additional fields have simplified

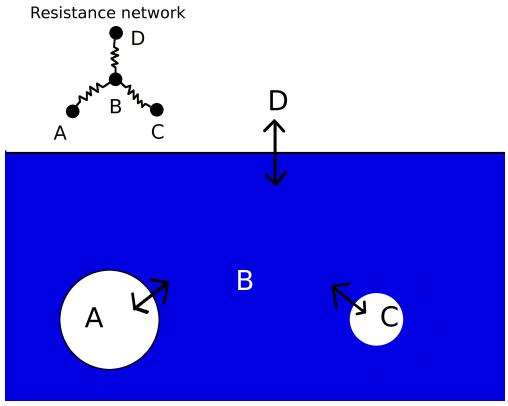

Figure 3.3: Bubble to liquid heat transfer

the energy balance equations by assuming that the droplets are the same temperature as the continuous liquid [7]. When the droplets and the continuous liquid have the same temperature, the energy balance for the liquid phase can be reduced to a single equation for both droplets and the liquid field. The same is true for the vapor and bubble fields.

The current development of the energy balance equations includes a separate equation for each field and the additional applicable terms for energy exchange between them. Aside from direct droplet entrainment, the only mechanism for energy exchange between the continuous liquid and the droplets is through radiation heat transfer. The droplets and the continuous liquid may not be at the same temperature.

The direct heat transfer between the continuous vapor and the vapor bubbles, as well as between the large and small bubbles can be neglected, since the heat transfer between those fields is included in the bubble to continuous liquid and the continuous liquid to vapor (or bubble) heat transfer. The continuous liquid phase becomes the medium for the heat transfer between the bubble fields and between a bubble field and the vapor field. Figure 3.3 shows this exchange graphically.

If we assume that the temperature in Bubble A is greater than the temperature of the coolant (point B), there will be heat transfer from the surface of bubble A to the continuous liquid at B. The heat transfer through the interface between bubble A and the continuous liquid is represented as a resistor in the nodal network shown as an inset to Figure 3.3.

As heat is transferred to the liquid, the temperature will rise. If the temperature in the continuous liquid (point B) is higher than the continuous vapor (point D) or a different (small) bubble (point C), the heat may subsequently be transferred to those fields.

The remaining heat exchange modes between the fields, and those that must be captured by the conservation equations are:

- Continuous liquid to/from vapor
- Continuous liquid to/from droplets by droplet entrainment/de-entrainment
- Continuous liquid to/from bubbles
- Continuous vapor to/from droplets
- Continuous vapor to/from bubbles by bubble entrainment/de-entrainment

Closure relationships will be required to capture the heat transfer between the fields. If appropriate closure relationships cannot be defined, the droplet and liquid temperatures may be assumed to be the same to reduce the required information for the energy balance. Temperatures and pressures of the droplet fields will be close to those of the continuous liquid field. If closure relationships are not available, the assumption of constant temperature will not vary drastically from real conditions. The energy balance for the continuous liquid field is shown as Equation 3.86. Note that the averaging notation has been removed for simplicity;

the terms are still averaged as indicated previously.

$$\underbrace{\alpha_f \rho_f \frac{D_f h_f}{Dt}}_{\text{A}} = \underbrace{-\nabla\cdot \alpha_f \left(\vec{q}_f + \vec{q}_f^{T}\right)}_{\text{B}} \underbrace{+\alpha_f \frac{D_f p_f}{Dt}}_{\text{C}} + \Phi_f^T + \Phi_f^{\mu} +$$

$$\underbrace{\Gamma_{f,i}\left(h_{f,i} - h_f\right)}_{\text{D}} + \underbrace{\Gamma_{f,w}\left(h_{f,w} - h_f\right)}_{\text{E}} + \underbrace{\Gamma_{f,SBu}\left(h_{f,SBu} - h_f\right)}_{\text{F}} +$$

$$\underbrace{\Gamma_{f,LB}\left(h_{f,LB} - h_f\right)}_{\text{G}} + \underbrace{a_i q''_{f,i}}_{\text{H}} + \underbrace{a_{i,SBu} q''_{SBu,i}}_{\text{I}} + \underbrace{a_{i,LB} q''_{LB,i}}_{\text{J}} + \underbrace{a_{w,f} q''_{w,f}}_{\text{K}} + \tag{3.86}$$

$$\underbrace{\left(p_f - p_{f,i}\right)\frac{D_f \alpha_f}{Dt}}_{\text{L}} + \underbrace{M_{i,f}\cdot\left(\vec{v}_{f,i} - \vec{v}_f\right)}_{\text{M}} \underbrace{- \nabla\alpha_f \cdot \mathfrak{T}_{f,i}\cdot\left(\vec{v}_{f,i} - \vec{v}_f\right)}_{\text{N}} -$$

$$S'''_{LD,E} h_f - S'''_{SD,E} h_f + S'''_{LD,DE} h_{LD} + S'''_{SD,DE} h_{SD}$$

Where the terms are defined as:

A - Time rate of change of energy in terms of enthalpy, including convective effects

B - Energy transfer from average conduction and turbulent heat flux

C - Energy from averaged flow work term

D - Energy transfer due to phase change at the continuous vapor interface

E - Energy transfer due to phase change at the wall

F - Energy transfer due to phase change at the small bubble interface

G - Energy transfer due to phase change at the large bubble interface

H - Energy transferred between continuous liquid and continuous vapor fields

I - Energy transferred between continuous liquid and small bubbles

J - Energy transferred between continuous liquid and large bubbles

K - Energy transferred from the wall to the continuous liquid

L - Energy transfer from pressure differences at interface

M - Energy transferred due to interfacial drag between continuous fields

N - Energy transfer from interfacial shear stress

Equation 3.87 is the energy conservation equation for small droplets, while Equation 3.88 is for large droplets.

$$\begin{aligned}\alpha_{SD}\rho_{SD}\frac{D_{SD}h_{SD}}{Dt} = \Gamma_{SD,i}\left(h_{SD,i} - h_{SD}\right) + a_i q''_{SD,i} + \\ \left(p_{SD} - p_{SD,i}\right)\frac{D_{SD}\alpha_{SD}}{Dt} + M_{i,SD}\cdot\left(\vec{v}_{SD,i} - \vec{v}_{SD}\right) - \\ \nabla\alpha_{SD}\cdot\mathfrak{T}_{SD,i}\cdot\left(\vec{v}_{SD,i} - \vec{v}_{SD}\right) - S'''_{LD,C}h_{SD} + S'''_{SD,E}h_f + \\ S'''_{LD,SB}h_{LD} + S'''_{LD,FB}h_{LD} - S'''_{SD,DE}h_{SD}\end{aligned} \tag{3.87}$$

$$\begin{aligned}\alpha_{LD}\rho_{LD}\frac{D_{LD}h_{LD}}{Dt} = \Gamma_{LD,i}\left(h_{LD,i} - h_{LD}\right) + a_i q''_{LD,i} + \\ \left(p_{LD} - p_{LD,i}\right)\frac{D_{LD}\alpha_{LD}}{Dt} + M_{i,LD}\cdot\left(\vec{v}_{LD,i} - \vec{v}_{LD}\right) - \\ \nabla\alpha_{LD}\cdot\mathfrak{T}_{LD,i}\cdot\left(\vec{v}_{LD,i} - \vec{v}_{LD}\right) + S'''_{LD,C}h_{SD} + S'''_{LD,E}h_f - \\ S'''_{LD,SB}h_{LD} - S'''_{LD,FB}h_{LD} - S'''_{LD,DE}h_{LD}\end{aligned} \tag{3.88}$$

Note the presence of the entrainment/de-entrainment source terms in Equation 3.87 and Equation 3.88. These source terms (and similar terms in the equations for energy conservation in the bubble fields) are dependent to some extent on the flow phenomena and the geometry of the flow. Improved model performance will be possible if closure relationships are used that compensate for variations in the flow characteristics. The energy balance for

the continuous vapor field is shown in Equation 3.89.

$$\begin{aligned}\alpha_g\rho_g\frac{D_g h_g}{Dt} = -\nabla\cdot\alpha_g\left(\vec{q}_g + \vec{q}_g^{T}\right) + \alpha_g\frac{D_g p_g}{Dt} + \Phi_g^T + \Phi_g^\mu + \\ \Gamma_{g,i}\left(h_{f,i} - h_f\right) + \Gamma_{g,w}\left(h_{f,w} - h_f\right) + \Gamma_{g,SBu}\left(h_{f,SBu} - h_f\right) + \\ \Gamma_{g,LB}\left(h_{f,LB} - h_f\right) + a_i q_{g,i}^{''} + a_{g,SD}q_{SD,i}^{''} + a_{i,LD}q_{LD,i}^{''} + a_{w,g}q_{w,g}^{''} + \\ \left(p_g - p_{g,i}\right)\frac{D_g\alpha_g}{Dt} + M_{i,g}\cdot\left(\vec{v}_{g,i} - \vec{v}_g\right) - \nabla\alpha_g\cdot\mathfrak{T}_{g,i}\cdot\left(\vec{v}_{g,i} - \vec{v}_g\right) - \\ S_{LB,E}^{'''}h_g - S_{SB,E}^{'''}h_g + S_{LB,DE}^{'''}h_{LB} + S_{SB,DE}^{'''}h_{SBu}\end{aligned} \tag{3.89}$$

The equation below is the energy conservation for small bubbles. Equation 3.91 is the energy conservation equation for large bubbles.

$$\begin{aligned}\alpha_{SBu}\rho_{SBu}\frac{D_{SBu}h_{SBu}}{Dt} = \underbrace{\Gamma_{SBu,i}\left(h_{SBu,i} - h_{SBu}\right)}_{\text{A}} + a_i q_{SBu,i}^{''} + \\ \left(p_{SBu} - p_{SBu,i}\right)\frac{D_{SBu}\alpha_{SBu}}{Dt} + M_{i,SBu}\cdot\left(\vec{v}_{SBu,i} - \vec{v}_{SBu}\right) - \\ \nabla\alpha_{SBu}\cdot\mathfrak{T}_{SBu,i}\cdot\left(\vec{v}_{SBu,i} - \vec{v}_{SBu}\right) - S_{SBu,C}^{'''}h_{SBu} + S_{SBu,E}^{'''}h_g + \\ S_{LB,SB}^{'''}h_{LB} + S_{LB,FB}^{'''}h_{LB} - S_{SBu,DE}^{'''}h_{SBu}\end{aligned} \tag{3.90}$$

A - Phase change from small bubbles to liquid

$$\begin{aligned}\alpha_{LB}\rho_{LB}\frac{D_{LB}h_{LB}}{Dt} = \Gamma_{LB,i}\left(h_{LB,i} - h_{LB}\right) + a_i q_{LB,i}^{''} + \\ \left(p_{LB} - p_{LB,i}\right)\frac{D_{LB}\alpha_{LB}}{Dt} + M_{i,LB}\cdot\left(\vec{v}_{LB,i} - \vec{v}_{LB}\right) - \\ \nabla\alpha_{LB}\cdot\mathfrak{T}_{LB,i}\cdot\left(\vec{v}_{LB,i} - \vec{v}_{LB}\right) + S_{SBu,C}^{'''}h_{SBu} + S_{LB,E}^{'''}h_f - \\ S_{LB,SB}^{'''}h_{LB} - S_{LB,FB}^{'''}h_{LB} - S_{LB,DE}^{'''}h_{LB}\end{aligned} \tag{3.91}$$

3.4 Assumptions for Derivation of 6 Field Governing Equations for RELAP5-3D

The conservation equations derived in Reference [106] and shown in the previous section have been formulated in three dimensions. The current RELAP5-3D six-equation model and new 18-equation model for 6 fields began from Eulerian equations that were similarly formulated [105]. Simplifying assumptions were made to make the model easily solvable. These simplifications will now be applied to the six-field model presented above to generate appropriate governing equations for use in a modified version of RELAP5-3D [22].

The preceding equations have all been formulated in 3D. The vessel component in RELAP5-3D uses governing equations formulated in 3D to solve the flows within that component. The remaining components in RELAP5-3D solve the flow in one dimension only. When the six-field model is applied to the 1D components, the multi-dimensional formulation can be further simplified by reducing it to one dimension. It is true that this reduces the versatility of the code, since flows with significant components in the "y" or "z" directions cannot be represented. However, for flows that can be assumed to exist primarily in one dimension (e.g., those within the pipes of a reactor system), the 1D formulation can significantly simplify the solution and reduce computational time. The six-field model developed herein will not be simplified to 1D at this time, but could easily be simplified for use in 1D components in RELAP5-3D.

The RELAP5-3D momentum equations (3.73 through 3.78) can be simplified by neglecting Reynolds stresses, assuming the phasic pressures are equal, assuming that the interfacial pressure is equal to the phasic pressures (with the exception of stratified flow), interfacial momentum storage is neglected, phasic viscous stresses are neglected.

By examining Equation 3.73, we can get an idea of the effect that these simplifications will have. The Reynolds stresses are represented by $\mathfrak{T}_f^T$ in that equation, so this term can be neglected. The phasic pressures are those for the liquid or vapor phase. Only one of

the pressures appears in Equation 3.73, but the interfacial pressure is also assumed to be equivalent to the phasic pressures, so term "E" in Equation 3.73 can be neglected as well.

The interfacial momentum storage is included in terms "J" through "L" in Equation 3.73, so these terms can also be neglected. The phasic viscous stresses (that are also neglected) are represented by $\mathfrak{T}_f$ in Equation 3.73. These simplifications can be applied to all the momentum conservation equations.

The energy conservation equations in the current RELAP5-3D model have been simplified using similar assumptions to those for the momentum formulation. These assumptions are that the Reynolds heat flux is neglected, the interfacial energy storage is neglected, internal phasic heat transfer is neglected.

Starting with the liquid field energy balance equation (3.86), we see that we can neglect the internal phasic heat transfer q_f as well as the Reynolds (turbulent) heat flux q_f^T. As before, the interfacial pressure is equal to the bulk pressure, so term L in Equation 3.86 can also be eliminated. We again neglect the effects of interfacial shear ($\mathfrak{T}_{f,i}$). The same steps can be used to simplify the remaining energy balance equations.

3.5 RELAP5-3D Six-Field Formulation

Applying all the simplifications from section 3.4, the six-field equation model can be re-formulated to be more consistent with the assumptions for the current RELAP5-3D six-equation model. These simplified equations are presented in the following sections.

3.5.1 Mass Conservation

The continuous liquid mass conservation equation is Equation 3.92. Equations 3.93 and 3.94 are the large and small droplet mass conservation, respectively.

$$\frac{\partial}{\partial t}\left(\alpha_f \rho_f\right) + \nabla\cdot\left(\alpha_f \rho_f \vec{v}_f\right) = -\Gamma_L - S'''_{LD,E} - S'''_{SD,E} + S'''_{LD,DE} + S'''_{SD,DE} \tag{3.92}$$

$$\frac{\partial}{\partial t}\left(\alpha_{LD}\rho_f\right)+\nabla\cdot\left(\alpha_{LD}\rho_f\vec{v}_{LD}\right)=-\Gamma_{LD}+S'''_{LD,E}-S'''_{LD,DE}- S'''_{LD,SB}-S'''_{LD,FB}+S'''_{SD,C} \tag{3.93}$$

$$\frac{\partial}{\partial t}\left(\alpha_{SD}\rho_f\right)+\nabla\cdot\left(\alpha_{SD}\rho_f\vec{v}_{SD}\right)=-\Gamma_{SD}+S'''_{SD,E}+S'''_{LD,SB}+ S'''_{LD,FB}-S'''_{SD,DE}-S'''_{SD,C} \tag{3.94}$$

The simplified continuous vapor (3.95), large bubble (3.96), and small bubble (3.97) mass conservation equations are shown below.

$$\frac{\partial}{\partial t}\left(\alpha_g\rho_g\right)+\nabla\cdot\left(\alpha_g\rho_g\vec{v}_g\right)=\Gamma_g-S'''_{SBu,E}+S'''_{LB,C}-S'''_{LB,E}+ S'''_{SBu,DE}+S'''_{LB,DE} \tag{3.95}$$

$$\frac{\partial}{\partial t}\left(\alpha_{LB}\rho_g\right)+\nabla\cdot\left(\alpha_{LB}\rho_g\vec{v}_{LB}\right)=\Gamma_{LB}+S'''_{SBu,C}-S'''_{LB,C}+ S'''_{LB,E}-S'''_{LB,DE}-S'''_{LB,SB}-S'''_{LB,FB} \tag{3.96}$$

$$\frac{\partial}{\partial t}\left(\alpha_{SBu}\rho_g\right)+\nabla\cdot\left(\alpha_{SBu}\rho_g\vec{v}_{SBu}\right)=\Gamma_{SBu}+S'''_{SBu,E}-S'''_{SBu,DE}- S'''_{SBu,C}+S'''_{LB,SB}+S'''_{LB,FB} \tag{3.97}$$

3.5.2 Momentum Conservation

The simplified conservation equations for the liquid fields (continuous liquid, large and small droplets) are shown in Equations 3.98, 3.99, and 3.100, respectively.

$$\begin{aligned}\alpha_f \rho_f \frac{D\vec{v}_f}{Dt} = -\alpha_f \nabla p_f + \alpha_f \rho_f \vec{g}_f + \left(\vec{v}_{i,L} - \vec{v}_f\right)\Gamma_L + \\ \left(\vec{v}_{i,LB} - \vec{v}_f\right)\Gamma_{LB} + \left(\vec{v}_{i,SBu} - \vec{v}_f\right)\Gamma_{SBu} + M_{if} + M_{wf} - \\ S'''_{LD,E} v_{LD} - S'''_{SD,E} v_{SD} + S'''_{SD,DE} v_{SD} + S'''_{LD,DE} v_{LD}\end{aligned} \tag{3.98}$$

$$\begin{aligned}\alpha_{SD} \rho_f \frac{D\vec{v}_{SD}}{Dt} = -\alpha_{SD} \nabla p_{SD} + \alpha_{SD} \rho_f \vec{g}_{SD} + \\ \left(\vec{v}_{i,SD} - \vec{v}_{SD}\right)\Gamma_{SD} + M_{i,SD} + S'''_{SD,E} v_{SD} + S'''_{LD,SB} v_{LD} + \\ S'''_{LD,FB} v_{LD} - S'''_{SD,DE} v_{SD} - S'''_{SD,C} v_{SD}\end{aligned} \tag{3.99}$$

$$\begin{aligned}\alpha_{LD} \rho_f \frac{D\vec{v}_{LD}}{Dt} = -\alpha_{LD} \nabla p_{LD} + \alpha_{LD} \rho_f \vec{g}_{LD} + \\ \left(\vec{v}_{i,LD} - \vec{v}_{LD}\right)\Gamma_{LD} + M_{i,LD} + S'''_{LD,E} v_{LD} - S'''_{LD,SB} v_{LD} - \\ S'''_{LD,FB} v_{LD} - S'''_{LD,DE} v_{LD} + S'''_{SD,C} v_{SD}\end{aligned} \tag{3.100}$$

The simplified conservation equations for the Vapor fields (continuous vapor, large and small bubbles) are shown in Equations 3.101 through 3.103, respectively.

$$\begin{aligned}\alpha_g \rho_g \frac{D\vec{v}_g}{Dt} = -\alpha_g \nabla p_g + \alpha_g \rho_g \vec{g}_g + \left(\vec{v}_{i,g} - \vec{v}_g\right)\Gamma_g + \\ \left(\vec{v}_{i,LD} - \vec{v}_g\right)\Gamma_{LD} + \left(\vec{v}_{i,SD} - \vec{v}_g\right)\Gamma_{SD} + M_{ig} + M_{wg} + \\ \Gamma_{LD}\left(v_{LD,i} - v_{LD}\right) + \Gamma_{SD}\left(v_{SD,i} - v_{SD}\right)\end{aligned} \tag{3.101}$$

$$\alpha_{SBu}\rho_g\frac{D\vec{v}_{SBu}}{Dt} = -\alpha_{SBu}\nabla p_{SBu} + \alpha_{SBu}\rho_g\vec{g}_{SBu} + \\ \left(\vec{v}_{i,SB} - \vec{v}_{SBu}\right)\Gamma_{SB} + M_{i,SBu} + S'''_{SB,E}v_{SBu} + S'''_{LB,SB}v_{LB} + \\ S'''_{LB,FB}v_{LB} - S'''_{SB,DE}v_{SBu} - S'''_{SB,C}v_{SBu} \tag{3.102}$$

$$\alpha_{LB}\rho_g\frac{D\vec{v}_{LB}}{Dt} = -\alpha_{LB}\nabla p_{LB} + \alpha_{LB}\rho_g\vec{g}_{LB} + \\ \left(\vec{v}_{i,LB} - \vec{v}_{LB}\right)\Gamma_{LB} + M_{i,LB} + S'''_{LB,E}v_{LB} - S'''_{LB,SB}v_{LB} - \\ S'''_{LB,FB}v_{LB} - S'''_{LB,DE}v_{LB} + S'''_{SB,C}v_{SBu} \tag{3.103}$$

3.5.3 Energy Conservation

The following equations represent the complete set of energy balance equations for the six-field model. Equation 3.104 is for continuous liquid; Equation 3.105 is for the small droplet field, and Equation 3.106 is for the large droplets.

$$\alpha_f\rho_f\frac{D_f h_f}{Dt} = \alpha_f\frac{D_f p_f}{Dt} + \Phi_f^T + \Phi_f^\mu + \Gamma_{f,i}\left(h_{f,i} - h_f\right) + \\ \Gamma_{f,w}\left(h_{f,w} - h_f\right) + \Gamma_{f,SBu}\left(h_{f,SBu} - h_f\right) + \Gamma_{f,LB}\left(h_{f,LB} - h_f\right) + \\ a_i q'''_{f,i} + a_{i,SBu}q'''_{SBu,i} + a_{i,LB}q'''_{LB,i} + a_{w,f}q'''_{w,f} + \\ M_{i,f}\cdot\left(\vec{v}_{f,i} - \vec{v}_f\right) - S'''_{LD,E}h_f - S'''_{SD,E}h_f + \\ S'''_{LD,DE}h_{LD} + S'''_{SD,DE}h_{SD} \tag{3.104}$$

$$\alpha_{SD}\rho_{SD}\frac{D_{SD}h_{SD}}{Dt} = \Gamma_{SD,i}\left(h_{SD,i} - h_{SD}\right) + a_i q'''_{SD,i} + \\ M_{i,SD}\cdot\left(\vec{v}_{SD,i} - \vec{v}_{SD}\right) - S'''_{LD,C}h_{SD} + S'''_{SD,E}h_f + \\ S'''_{LD,SB}h_{LD} + S'''_{LD,FB}h_{LD} - S'''_{SD,DE}h_{SD} \tag{3.105}$$

$$\alpha_{LD}\rho_{LD}\frac{D_{LD}h_{LD}}{Dt} = \Gamma_{LD,i}\left(h_{LD,i} - h_{LD}\right) + a_i q'''_{LD,i} + M_{i,LD}\cdot\left(\vec{v}_{LD,i} - \vec{v}_{LD}\right) + S'''_{LD,C}h_{SD} + S'''_{LD,E}h_f - S'''_{LD,SB}h_{LD} - S'''_{LD,FB}h_{LD} - S'''_{LD,DE}h_{LD} \tag{3.106}$$

The energy balance equation for continuous vapor is shown as Equation 3.107. Equation 3.108 is for the small bubble field, and Equation 3.109 is for the large bubbles.

$$\alpha_g\rho_g\frac{D_g h_g}{Dt} = \alpha_g\frac{D_g p_g}{Dt} + \Phi_g^T + \Phi_g^\mu + \Gamma_{g,i}\left(h_{f,i} - h_f\right) + \Gamma_{g,w}\left(h_{f,w} - h_f\right) + \Gamma_{g,SBu}\left(h_{f,SBu} - h_f\right) + \Gamma_{g,LB}\left(h_{f,LB} - h_f\right) + a_i q'''_{g,i} + a_{g,SD}q'''_{SD,i} + a_{i,LD}q'''_{LD,i} + a_{w,g}q'''_{w,g} + M_{i,g}\cdot\left(\vec{v}_{g,i} - \vec{v}_g\right) - S'''_{LB,E}h_g - S'''_{SB,E}h_g + S'''_{LB,DE}h_{LB} + S'''_{SB,DE}h_{SBu} \tag{3.107}$$

$$\alpha_{SBu}\rho_{SBu}\frac{D_{SBu}h_{SBu}}{Dt} = \Gamma_{SBu,i}\left(h_{SBu,i} - h_{SBu}\right) + a_i q'''_{SBu,i} + M_{i,SBu}\cdot\left(\vec{v}_{SBu,i} - \vec{v}_{SBu}\right) - S'''_{SBu,C}h_{SBu} + S'''_{SBu,E}h_g + S'''_{LB,SB}h_{LB} + S'''_{LB,FB}h_{LB} - S'''_{SBu,DE}h_{SBu} \tag{3.108}$$

$$\alpha_{LB}\rho_{LB}\frac{D_{LB}h_{LB}}{Dt} = \Gamma_{LB,i}\left(h_{LB,i} - h_{LB}\right) + a_i q'''_{LB,i} + M_{i,LB}\cdot\left(\vec{v}_{LB,i} - \vec{v}_{LB}\right) + S'''_{SBu,C}h_{SBu} + S'''_{LB,E}h_f - S'''_{LB,SB}h_{LB} - S'''_{LB,FB}h_{LB} - S'''_{LB,DE}h_{LB} \tag{3.109}$$

Note the presence of the entrainment/de-entrainment source terms in Equation 3.105 and Equation 3.106. These source terms (and similar terms in the equations for energy conservation in the bubble fields) are dependent to some extent on the flow phenomena and the geometry of the flow. Improved model performance will be possible if closure relationships

are used that compensate for variations in the flow characteristics.

Tables 3.2, 3.3, and 3.4 were initially shown in Reference [106], but are extended here to provide a comparison of the new 6-field, 18 equation model that has been derived and the current RELAP5-3D and TRACE sets of governing equations.

Table 3.2: Mass Conservation Equation Comparison

Code	6-Field Model (continuous liquid)	RELAP5-3D		TRACE
		1D	3D	
Time Rate of Change of Mass	$\frac{\partial}{\partial t}\left(\alpha_f \rho_f\right)$	$\frac{\partial}{\partial t}\left(\alpha_k \rho_k\right)$	$\frac{\partial}{\partial t}\left(\alpha_k \rho_k\right)$	$\frac{\partial[(1-\alpha_g)\rho_l]}{\partial t}$
Convective Mass Change	$\nabla\cdot\left(\alpha_f \rho_f \vec{v}_f\right)$	$\frac{1}{A}\frac{\partial}{\partial x}\left(\alpha_k \rho_k v_k A\right)$	$\frac{1}{A}\nabla\cdot\left(\alpha_k \rho_k v_k A\right)$	$\nabla\cdot\left[\left(1-\alpha_g\right)\rho_l \vec{V}_l\right]$
Mass Exchange Rate	Γ_L	Γ_k	Γ_k	$-\Gamma_g$
Additional Source Terms (vary by field)	$S'''_{LD,E} - S'''_{SD,E} + S'''_{LD,DE} + S'''_{SD,DE}$	–	–	–

Table 3.3: Momentum Conservation Equation Comparison

Component	6-Field Model (continuous liquid)	RELAP5-3D		TRACE
		1D	3D	
Time Rate of Change of Momentum	$\alpha_f \rho_f \frac{D\vec{v}_f}{Dt}$	$\alpha_k \rho_k A \frac{\partial v_k}{\partial t}$	$\alpha_k \rho_k A \frac{\partial \vec{v}_k}{\partial t}$	$\frac{\partial\left[(1-\alpha_g)\rho_l \vec{V}_l\right]}{\partial t}$
Rate of momentum change from convection		$\frac{1}{2}\alpha_k \rho_k A \frac{\partial v_k^2}{\partial x}$	$\frac{1}{2}\alpha_k \rho_k A \nabla\cdot \vec{v}_k^2$	$\nabla\cdot\left(1-\alpha_g\right)\rho_l \vec{V}_l \vec{V}_l$
Pressure gradient	$-\alpha_f \nabla p_f$	$-\alpha_k A \frac{\partial P}{\partial x}$	$-\alpha_k A \nabla\cdot P$	$\left(1-\alpha_g\right)\nabla P$
Momentum change from body forces	$\alpha_f \rho_f \vec{g}_f$	$\alpha_k \rho_k B_x A$	$\alpha_k \rho_k \vec{B} A$	$\left(1-\alpha_g\right)\rho_l \vec{g}$
Wall Drag	–	$\left(\alpha_k \rho_k A\right) FW_k \cdot v_k$	$\left(\alpha_k \rho_k A\right) FW_k \cdot \vec{v}_k$	$\vec{f}_{wl}$
Momentum from phase change mass transfer	$\left(\vec{v}_{i,L}-\vec{v}_f\right)\Gamma_L +$ $\left(\vec{v}_{i,LB}-\vec{v}_f\right)\Gamma_{LB} +$ $\left(\vec{v}_{i,SBu}-\vec{v}_f\right)\Gamma_{SBu}+$	$\Gamma_k A\left(v_{kI}-v_k\right)$	$\Gamma_k A\left(\vec{v}_{kI}-\vec{v}_k\right)$	$-\Gamma\vec{V}_i$
Interfacial Drag	M_{if}	$\left(\alpha_k \rho_k A\right) FI_k \cdot$ $\left(v_k - v_r\right)$	$\left(\alpha_k \rho_k A\right) FI_k \cdot$ $\left(\vec{v}_k - \vec{v}_r\right)$	$\vec{f}_i$
Virtual Mass Force	–	$C\alpha_k \alpha_r \rho_m A$ $\left[\begin{array}{c} \frac{\partial(v_k - v_r)}{\partial t} + v_r \frac{\partial v_k}{\partial x} \\ -v_k \frac{\partial v_r}{\partial x} \end{array}\right]$	$C\alpha_k \alpha_r \rho_m A$ $\left[\begin{array}{c} \frac{\partial(\vec{v}_k - \vec{v}_r)}{\partial t} + \vec{v}_r \nabla \vec{v}_k \\ -\vec{v}_k \nabla \vec{v}_r \end{array}\right]$	–
Additional Source Terms (vary by field)	$S'''_{LD,E} v_{LD} -$ $S'''_{SD,E} v_{SD} +$ $S'''_{SD,DE} v_{SD} +$ $S'''_{LD,DE} v_{LD}$	–	–	–

Table 3.4: Energy Conservation Equation Comparison

Component	6-Field Model (continuous liquid)	RELAP5-3D		TRACE
		1D	3D	
Rate of Energy Change	$\alpha_f \rho_f \frac{D_f h_f}{Dt}$	$\frac{\partial}{\partial t}\left(\alpha_k \rho_k U_k\right)$	$\frac{\partial}{\partial t}\left(\alpha_k \rho_k U_k\right)$	$\frac{\partial\left[(1-\alpha_g)\rho_l\left(e_l+V_l^2/2\right)\right]}{\partial t}$
Mass crossing boundary		$\frac{1}{A}\frac{\partial}{\partial x}\left(\alpha_k \rho_k U_k v_k A\right)$	$\frac{1}{A}\nabla\cdot\left(\alpha_k \rho_k U_k \vec{v}_k A\right)$	$\nabla\cdot\left[\begin{array}{l}\left(1-\alpha_g\right)\rho_l \\ \left(e_l+\frac{P}{\rho_l}+\frac{V_l^2}{2}\right)\vec{V}_l\end{array}\right]$
Energy Change From Interfacial Boundary Movement	–	$-P\frac{\partial \alpha_k}{\partial t}$	$-P\frac{\partial \alpha_k}{\partial t}$	–
Flow Work Energy Change	$\alpha_f \frac{D_f p_f}{Dt}$	$-\frac{P}{A}\frac{\partial}{\partial x}\left(\alpha_k v_k A\right)$	$-\frac{P}{A}\nabla\cdot\left(\alpha_k \vec{v}_k A\right)$	–
Heat transfer from wall	$a_{w,f} q_{w,f}^{'''}$	Q_{wk}	Q_{wk}	q_{wl}
Heat transfer from the interface	$a_i q_{f,i}^{'''} + a_{i,SBu} q_{SBu,i}^{'''} + a_{i,LB} q_{LB,i}^{'''}$	Q_{ik}	Q_{ik}	q_{il}
Phase change in bulk fluid	$\Gamma_{f,i}\left(h_{f,i}-h_f\right) + \Gamma_{f,SBu}\left(h_{f,SBu}-h_f\right) + \Gamma_{f,LB}\left(h_{f,LB}-h_f\right)$	$\Gamma_{ig} h_k^*$	$\Gamma_{ig} h_k^*$	$-\Gamma h_l^{'}$
Phase change at wall	$\Gamma_{f,w}\left(h_{f,w}-h_f\right)$	$\Gamma_w h_k^{'}$	$\Gamma_w h_k^{'}$	–
Energy lost to gravity, wall drag, etc.	$M_{i,f}\cdot\left(\vec{v}_{f,i}-\vec{v}_f\right)$	$DISS_k$	$DISS_k$	$\left(1-\alpha_g\right)\rho_l \vec{g}\cdot\vec{V}_l + \left(\vec{f}_i+\vec{f_{wl}}\right)\cdot\vec{V}_l$
Additional Source Terms (vary by field)	$S_{LD,E}^{'''} h_f - S_{SD,E}^{'''} h_f + S_{LD,DE}^{'''} h_{LD} + S_{SD,DE}^{'''} h_{SD}$	–	–	–

CHAPTER 4

Mass Equation Closure Models

The closure relationships that are necessary for solution of the mass balance equations in the six-field model presented previously are described in this chapter. They were selected from closure relations that were found in a wide literature search. The selected models meet the following criteria:

1. The closure model must be adaptable to produce a mass generation rate per unit volume, so that it can be consistent with the existing governing equations.

2. The closure model must be applicable to a flow field. Models of individual interactions between droplets or bubbles are not useful, since the system code does not track individual bubbles or droplets.

3. Sufficient information must be available in the literature to allow use of the model.

4.1 Closure Models for Mass Balance of Liquid Phase

The mass balance equations for six fields are shown in Chapter 3. The three liquid phase equations are Equations 3.65, 3.66, and 3.67.

The source terms (S''' - terms) in the mass conservation equations represent the physical phenomena that cause the liquid coolant to change from one field to another. Such mechanisms include breakup on spacer grids and breakup due to shear with the vapor phase. The source terms are determined using multiple correlations and have units of $^{kg}/_{m^3 s}$. It is impossible to solve the six field equations without adequate closure models that solve for the source terms.

The key source terms related to the six-field model in the above equations are:

- $S'''_{LD,E}$ - Large droplet entrainment in vapor from continuous liquid field

- $S'''_{SD,E}$ - Small droplet entrainment in vapor from continuous liquid field
- $S'''_{LD,DE}$ - Large droplet de-entrainment into continuous liquid field
- $S'''_{SD,DE}$ - Small droplet de-entrainment into continuous liquid field
- $S'''_{LD,SB}$ - Breakup of large droplets into small droplets due to spacer grid impact
- $S'''_{LD,FB}$ - Aerodynamic breakup of large droplets into small droplets due to flow effects
- $S'''_{SD,C}$ - Coalescence of small droplets into large droplets

The closure models that will be used to solve for each of these terms are discussed in the following sections.

4.1.1 Droplet Entrainment Terms ($S'''_{LD,E}$, $S'''_{SD,E}$)

Equations 3.65, 3.66, and 3.67 have source terms representing the entrainment and de-entrainment of droplets from/to the continuous liquid field. The entrainment terms are $S'''_{LD,E}$ for large droplet entrainment, and $S'''_{SD,E}$ for small droplet entrainment. Solution of the mass balance for the droplet and continuous liquid fields requires models to account for the large and small droplet entrainment. Two closure relationships will be used to solve for these source terms. The first model computes the overall droplet entrainment rate, including all sizes of droplets. The second model determines the distribution of those droplets into the "large" and "small" fields.

Droplet Entrainment Rate

When considering droplet entrainment, orientation of the flow (horizontal or vertical) is important. In vertical flows, the surface tension of the liquid is the most significant force that must be overcome in order for droplets to be generated and entrained in the vapor/gas phase. If the flow field is horizontal, then gravitational forces must also be overcome, and

should be considered in any models used for that orientation. The entrainment rate for pipes that are inclined between horizontal and vertical will be determined by the angle of inclination. Pipes angled at less than 45 degrees will be considered to be horizontal; those greater than 45 degrees will use the results of the vertical entrainment model.

We consider three flow configurations where entrainment is possible:

1. Upward Annular Flow
2. Reflood Quench Front/Froth Front
3. Horizontal Annular Flow

These will be addressed in the following sections.

Upward Annular Flow In upward annular flows, there is a layer of liquid coating the inside surface of the pipe. A core flow of vapor may be flowing in the same direction as the liquid film or in the opposite direction. The vapor flow may contain droplets that have been entrained. The droplet entrainment rate is a function of: 1. The volume of liquid swept off of the wavelets, 2. The wavelength of the wavelets, 3. Number of waves in the control volume, and 4. The wave velocity through the control volume. The general expression is then [107]:

$$S_E''' = \frac{V_{entr,w}\rho_f N_{w,cv}}{V_{ann}\tau_{w,cv}} \tag{4.1}$$

Equation 4.1 computes the droplet entrainment flux (S_E - $^{kg}/_{m^3 s}$) for a vertical annular flow based on the maximum volume of liquid entrained from a wave crest ($V_{entr,w}$), liquid density, number of waves in a control volume ($N_{w,cv}$), the volume of liquid in the annulus (continuous liquid field) within the control volume (V_{ann}), and the period of entrainment in the control volume ($\tau_{w,cv}$).

The waves within a control volume will grow in amplitude if the normal stresses are greater than the surface tension stress, and as the waves get larger, the tops of the waves

will be drawn along by the vapor/gas flow until the surface tension is overcome, and droplets break off of the wave tops. Using the Kelvin-Helmholtz instability as the primary characteristic length scale for wave geometry calculation and computing the forces acting at the interface and then performing a force balance at the wave crests, several of the terms in equation 4.1 can be defined. We assume that the height of the control volume is equivalent to the wavelength of the waves formed on the annular surface (λ).

$$V_{ann} = \alpha_f \lambda \frac{\pi D_{hy}^2}{4} \tag{4.2}$$

$$\tau_{w,cv} = \frac{\lambda}{\overline{u}_{gc} - \overline{u}_f} \tag{4.3}$$

$$N_{w,cv} = \frac{P_w}{\lambda} \tag{4.4}$$

Where:

- λ - wavelength
- $\overline{u_{gc}}$ - average gas core velocity
- $\overline{u_f}$ - average liquid film velocity
- P_w - wetted perimeter
- α_f - Volume fraction occupied by continuous liquid (liquid film)
- t_{ann} - thickness of liquid annulus
- D_{hy} - Hydraulic diameter of pipe

Substituting 4.2, 4.3, and 4.4 into Eqn. 4.1 gives:

$$S'''_{E,max} = \frac{4 V_{entr,w} \rho_f P_w \left(\overline{u}_{gc} - \overline{u}_f\right)}{D_{hy}^2 \alpha_f \pi \lambda^3} \tag{4.5}$$

Equation 4.5 gives the maximum entrainment mass flux in co-current upward annular flow. The solution of the liquid governing equations requires an average droplet entrainment rate, not a maximum. The predictions of Equation 4.5 have been compared to experimental data. This generated corrections which are applied to 4.5 to yield an expression for the average entrainment mass flux, shown as Equation 4.6 [107].

$$S_E''' = 0.0311 Re_{film}^{1.67} \left(\frac{\rho_f}{\rho_g}\right)^{7/8} N_\mu^3 \frac{4 V_{entr,w} \rho_f P_w \left(\overline{u}_{gc} - \overline{u}_f\right)}{D_{hy}^2 \alpha_f \pi \lambda^3} \tag{4.6}$$

Where the viscosity number N_μ is:

$$N_\mu = \frac{\mu_l}{\left(\rho_f \sigma \sqrt{\frac{\sigma}{g\left(\rho_f - \rho_g\right)}}\right)} \tag{4.7}$$

Note that 4.6 has an added term, N_{wav}, which is the control volume length divided by the wavelength to adjust for the assumption that the control volume length is the same as the wavelength.

Reflood Quench Front Reflood conditions are of particular importance in reactor design and accident analysis. Recovery from severe accidents often involves emergency coolant flows into the core. The coolant in contact with the hot fuel bundles will flash to steam until the rods cool sufficiently to allow the water to begin filling the core. As this happens, the quench front progresses higher in the core. The process of flashing to steam often carries droplets into the vapor flow. These droplets can impact the spacer grids and fuel rods at higher locations in the core, aiding in the cooling process. Detailed modeling of the reflood process, including the droplet entrainment, is important for accurate representation of accident scenarios.

Although detailed tests using prototypic PWR geometries (fuel rod bundles with spacer grids) have been performed (e.g. FLECHT-SEASET [108]), such tests present challenges to fundamental model development due to cross flows and spacer grid effects. The reflood entrainment model that will be used to solve the six-field governing equations is based on

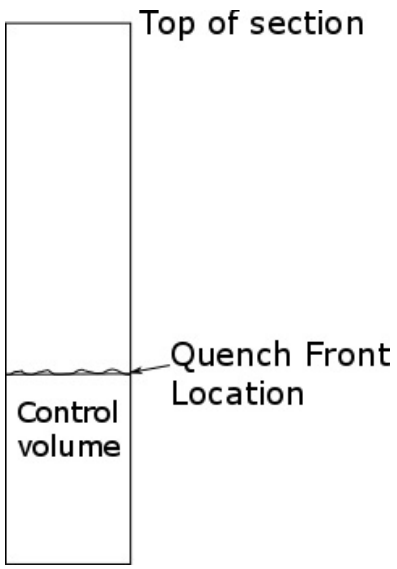

Figure 4.1: Control volume for reflood conditions

data from tests with simple tubular geometries and flows (such as REFLEX [109, 110]).

There is no appreciable film flow up the sides of the tube, which is partially full of water during reflood. The region above the quench front that is characterized by droplets, slugs, and ligaments of water is referred to as the "froth region". This region is the result of vapor generation and other disturbances at the quench front.

We define the control volume for the reflood condition as the volume that includes all the liquid within the tube, extending from the tube inlet to the liquid/vapor interface, as shown in Figure 4.1. Crossflow across the control volume boundary below the quench front is not accounted for in this model. This may be a poor assumption for conditions where cross flow is likely, such as those with a radial power shape, pressure drop, or flow restrictions. In spite of those concerns, this reflood entrainment model provides a good starting point.

A similar method to that used for the annular flow is used to characterize droplet entrainment in the frothy region. Droplet entrainment is assumed to be a function of: the volume of liquid that is swept off of each wave at the interface, the wavelength, the number of waves within the selected control volume, and the velocity of the waves. A control volume analysis on the region that includes the quench front and frothy region results in a source

term for droplet entrainment mass flux at the top of the froth front [107].

$$S_E''' = C_1 \frac{\lambda_{crit} \rho_f P_H \left(U_{vap,crit}^2 + U_{vap,bqf}^2\right)^{1/2}}{V_f} Re_{vap,gen}^{C_2} \tag{4.8}$$

Where the coefficients are:

$C_1 = 1.46 \times 10^{-8}$

$C_2 = 1.83$

and the vapor generation Reynolds number is:

$$Re_{vap,gen} = \frac{\Gamma D_{hy}}{A_F \mu_g} \tag{4.9}$$

Where the D_{hy} is the hydraulic diameter for the control volume in the direction of the quench front motion. The vapor generation rate is represented by Γ, and A_f is the flow area of the pipe.

The characteristic wavelength for droplet formation comes from:

$$\lambda_{crit} = \frac{2\pi\sigma g}{\rho_g U_{vap,crit}^2} \tag{4.10}$$

Horizontal Flow Horizontal annular flows are similar to vertical flows, but the pipe is oriented horizontally. The gravitational effects of the orientation generally result in slightly thicker liquid films toward the bottom of the pipe. Entrainment in horizontal flows is also different from vertical flows due to gravitational effects, which cause droplet concentration to increase in the lower portion of a horizontal flow field. The model presented here is summarized from [111].

Changes in the gas flow rate have a larger effect on entrainment than changes in the liquid flow rate. In addition, entrainment tends to decrease for high total liquid mass flow at intermediate gas velocities.

The average rate of droplet atomization can be given as:

$$S_E''' = \frac{k_A' U_G^2 \left(\rho_g \rho_f\right)^{1/2} \left(W_{LF} - W_{LFC}\right)}{P \sigma t_{film}} \tag{4.11}$$

Where W_{LF} is the mass flow rate of the liquid film. W_{LFC} is the critical film flow per unit length. For film flows above the critical flow, droplet entrainment may occur. The film flow shown in Equation 4.11 is available as an average value for each control volume in the calculation. This loses some fidelity in the calculation, since the gravitational effects are lost by the averaging. If system codes are developed that can preserve the variation in flow around the pipe circumference, this equation can be easily modified as suggested in [111] to recapture these effects. For cases where the actual film flow is less than the critical film flow (resulting in a negative numerator in Equation 4.11), there will be no droplet entrainment.

The annular film thickness can be computed from a knowledge of the volume ratio of the film and the hydraulic diameter of the pipe as shown in Equation 4.12.

$$t_{film} = \frac{4 D_{hy} \left(1 - \sqrt{1 - \alpha_{film}}\right)}{8} \tag{4.12}$$

Liquids with low viscosity experience the initiation of entrainment when waves appear in the liquid layer. This is similar to the mechanism for droplet entrainment in vertical flows, where droplets break off of the tops of the waves [111]. The critical flow per unit length can be obtained using equations derived from vertical flow tests. The critical Reynolds number is related to the critical flow per unit length as [111]:

$$Re_{LFC} = \frac{4 \xi_c}{\mu_L} \tag{4.13}$$

Where the critical Reynolds number can be computed using:

$$Re_{LFC} = 7.30\left(\log_{10}\omega\right)^3 + 44.2\left(\log_{10}\omega\right)^2 - 263\left(\log_{10}\omega\right) + 439 \tag{4.14}$$

$$\omega = \frac{\mu_L}{\mu_g}\sqrt{\frac{\rho_g}{\rho_f}} \tag{4.15}$$

The critical flow per unit length (around the pipe circumference) is:

$$\xi_c = \frac{W_{LFC}}{\pi D} \tag{4.16}$$

Air and water at standard conditions have $\omega \approx 1.861$ and $Re_{LFC} \approx 370$. Equation 4.14 is valid for ω between 1.8 and 28.

Small Droplet Fraction

The models for droplet entrainment rate in horizontal and vertical flows were provided in the previous sections, but those models make no distinction between the large and small droplet fields. A model that provides the volume ratio of small droplets must be used in conjunction with the entrainment models to effectively differentiate between $S'''_{LD,E}$ and $S'''_{SD,E}$ for the governing equations. The small droplet volume ratio can be multiplied by the source term for droplet generation to obtain the source term for "small" droplets. The remainder of the droplets will be assumed to be "large".

Vertical Flows The Sauter mean diameter is the diameter of a drop that has the same volume to surface area ratio as the entire droplet distribution. This is a convenient characteristic to use when developing the volume ratio of small droplets. The Sauter mean diameter is defined as [7]:

$$D_{SM} = D_{3,2} = \frac{\sum_{i=1}^{NG} \frac{n_i}{n_T \Delta D} D_i^3 \Delta D}{\sum_{i=1}^{NG} \frac{n_i}{n_T \Delta D} D_i^2 \Delta D} = \frac{\sum_{i=1}^{NG} n_i D_i^3}{\sum_{i=1}^{NG} n_i D_i^2} = \frac{6V_d}{A_d} \tag{4.17}$$

Where n_T represents the total number of groups, and NG is the number of groups of the similar-sized droplets. The droplet size distribution was established using a volume fraction oversize (volume fraction of droplets having a diameter larger than D). The volume fraction oversize is represented by Δ. The rate of change of Δ can be computed using Equations 4.18 and 4.19 [7].

$$\frac{d\Delta}{dy} = -\frac{0.884}{\sqrt{\pi}} e^{-0.781\nu^2} \tag{4.18}$$

$$\nu = \ln\left(\frac{2.13 D_t}{D_{max} - D_t}\right) \tag{4.19}$$

The mean droplet size is determined using the volume median droplet diameter (where 50% of the droplets are larger than the median diameter). The ratio of max drop size to the volume median droplet diameter is [112]:

$$\frac{D_{max}}{D_{vm}} = 3.13 \tag{4.20}$$

The ratio of the Sauter mean diameter to the volume median droplet diameter is [7]:

$$\frac{D_{SM}}{D_{vm}} = 0.8 \tag{4.21}$$

Equations 4.18, 4.19, and 4.20 can be used in to evaluate and tabulate the volume fraction and area fraction of drops having diameters between an arbitrary diameter, D_o and D_{vm} [113].

Volume fractions were obtained by integrating 4.18 and 4.19. For different D/D_{vm} ratios, volume fractions of small droplets generated by entrainment were evaluated. If the diameter used for D in the ratio is the Sauter mean diameter, the volume ratio of small droplets is 34 percent [113].

The Sauter mean diameter can be computed from known parameters, so the volume

median droplet diameter D_{vm} can be calculated using 4.21.

If D represents the diameter of the smallest drop in the large drop field, then it is also an upper limit on the range of diameters for the small droplet field. This diameter limit is computed using the Weber number criteria that will be developed for droplet breakup in section 4.1.2.

Relative drop velocities can be determined using a simple force balance for a single drop. The effects of the drag force are computed as [7]:

$$\tau = 0.375 \frac{C_d}{\frac{D}{2}} \frac{\rho_g}{\rho_d} |U_d| \tag{4.22}$$

where:

$$C_d = \frac{24}{Re} \left[1.0 + 0.1 \left(Re\right)\right]^{0.75} \tag{4.23}$$

and the Reynolds number is:

$$Re = \frac{\rho_g U_d D}{\mu_g} \tag{4.24}$$

In the above equations, U_d is the relative drop velocity, and ρ_g and μ_g are the vapor density and viscosity, respectively. The ρ_d term in Equation 4.22 is the liquid density of the droplet.

Then, a force balance can be used to compute the relative velocity:

$$g = \tau U_d \tag{4.25}$$

Note that g is the gravitational acceleration.

Equations 4.22 to 4.25 are solved iteratively, by guessing a droplet velocity and solving through until the velocity in Equation 4.25 matches the initial guess.

The Weber numbers of the drops with diameters measured during the Rod Bundle Heat

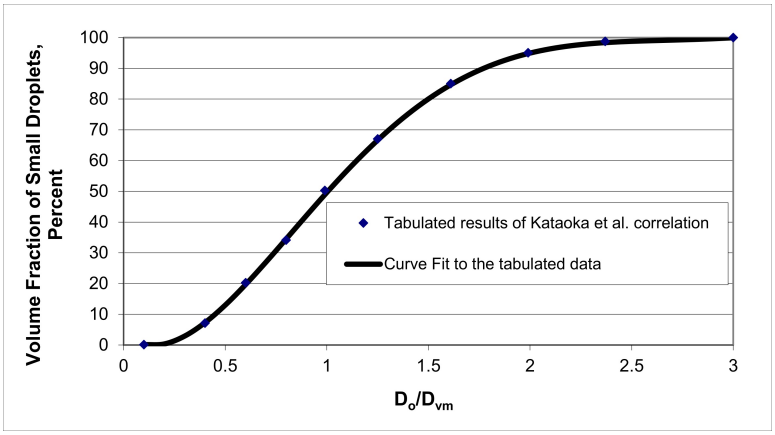

Figure 4.2: Volume fractions for small droplet field vs. D_o/D_{vm} [7]

Transfer (RBHT [114]) tests are calculated based on the relative drop velocity computed as described above. The COBRA-TF criteria for droplet size indicates that droplets with weber numbers smaller than 150.0 are considered to be part of the "large" droplet field [115]. The droplet diameter corresponding to a Weber of 150 from evaluation of the RBHT results is 0.00221 ft (0.0674 cm) [7]. Therefore, the upper diameter for small droplets using the COBRA-TF criteria is 0.00221 ft, which can be used in D/D_{vm}.

Figure 4.2 summarizes the volume fractions for the small droplet field with different D_o/D_{vm} ratios, where in this case, D_o represents the smallest diameter of a large group droplet. The Sauter mean diameter can be used in Equation 4.21 to obtain D_{vm}. Then, using the upper diameter for small droplets (0.00221 ft), the volume fraction of small droplets can be found from Figure 4.2.

Horizontal Entrainment Distribution The gravitational term in Equation 4.25 indicates that the droplets are assumed to be flowing upwards in this scenario, and the gravitational force acts to slow the droplets. In horizontal flow, the gravitational force does not apply in this way. The velocity vector in horizontal flows does not act in the same direction as the gravitational direction. The drag force multiplied by the droplet velocity in a horizontal flow does not balance the gravitational force. In part due to these differences, the distribution of large and small droplets entrained into horizontal flows requires a different

model.

Data for droplet size in horizontal entrainment conditions is sparse, so the droplet size distribution for vertical flows described in the previous section will be applied to horizontal flows as well.

Discussion of Droplet Entrainment

The preceding sections provide necessary closure models for the droplet entrainment terms in Equations 3.65, 3.66, and 3.67. The entrainment terms are $S'''_{LD,E}$ and $S'''_{SD,E}$, which are for large and small droplet entrainment, respectively.

The closure models solve for these terms depending on the orientation and flow conditions. For the vertical annular and froth regions, the entrainment rate is determined as shown in 4.1.1, then the distribution of those droplets into the "small" and "large" droplet fields is determined as described in 4.1.1. For horizontal annular flow, the entrained droplets are all assumed to be part of the small bubble field.

4.1.2 Droplet Breakup Terms ($S'''_{LD,FB}$, $S'''_{LD,SB}$)

The mass balance equations for the droplet fields include terms to account for the breakup of the droplets due to effects from the vapor flow or spacer grid impact. Large droplet flow breakup is represented in the governing equations by $S'''_{LD,FB}$. Two types of flow breakup are possible, bag-type and shear (stripping) breakup.

In addition to breakup due to flow effects, large droplets that impact spacer grids can be broken up into smaller droplets. This type of breakup is represented in the governing equations by the source term $S'''_{LD,SB}$, which can be computed using methods described in [7].

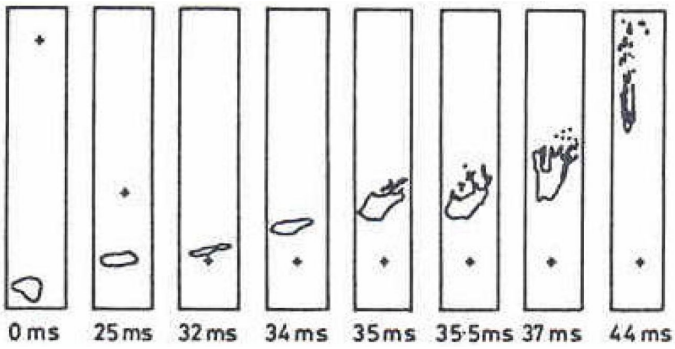

Figure 4.3: Bag-Type Breakup [8]

Bag-Type Breakup

Bag-type breakup occurs when the large droplets deform into a bag shape. The small droplets then break out of the center of the bag shape, as shown in Figure 4.3. The critical Weber number for bag-type breakup is 12 [7]. The Weber number is calculated:

$$We = \frac{\rho_f \left(U_v - U_d\right)^2 D_o}{\sigma} \tag{4.26}$$

If the Weber number is larger than 12, then bag-breakup can occur. The time that is required for bag breakup to occur can be used to determine the droplet generation rate. The time required for breakup is determined by Equation 4.27 [7], using the liquid and vapor densities, the initial droplet diameter (D_o), and the initial vapor velocity (relative to the droplet - u_{ro}).

$$t_{brk} = 6.5 \frac{D_o}{u_{ro}} \sqrt{\frac{\rho_f}{\rho_g}} \tag{4.27}$$

The model will compute the Weber number for the large droplet field within a volume. If it is greater than 12.0, then droplet breakup can occur. The rate of droplet generation is

then:

$$S'''_{LD,BB} = \frac{\rho_f \alpha_{LD}}{t_{brk}} \tag{4.28}$$

The ratio of the diameter of the largest drop generated by bag breakup to the diameter of the original large drop (a_{fr}) is 0.2 [7]. The limit log normal distribution combined with that ratio gives a formula for the Sauter mean diameter of the droplets resulting from the breakup.

$$D_{SM,bagtype} = \frac{1}{3} a_{fr} D_o \tag{4.29}$$

Once the Sauter mean diameter is known, a volume ratio of the large drops remaining after breakup and the generated small drops can be used to give the ratio of large drop mass to small drop mass. [7].

$$\frac{m_{small}}{m_{large}} = \frac{\frac{\pi}{6}\left(D_{SM,bagtype}\right)^3}{\frac{\pi}{6}\left(D_o\right)^3} = \frac{\left(\frac{1}{3} a_{fr} D_o\right)^3}{\left(D_o\right)^3} = \left(\frac{1}{3} a_{fr}\right)^3 \tag{4.30}$$

And, since $a_{fr} \approx 0.2$ [7]:

$$\frac{m_{small}}{m_{large}} \approx 0.0003 \tag{4.31}$$

Stripping Breakup

Stripping, or shear breakup is characterized by the fact that the large droplets do not maintain their shape as they break up. Shear breakup occurs in flows with high vapor velocities. The high velocities stretch the large droplets into extremely distorted and elongated shapes, which then shear off into smaller droplets. The critical Weber number for this type of breakup

is 50.0 [7]. If the Weber number for the large drop exceeds 50, then stripping breakup occurs. The time required for droplet breakup is used to determine the rate at which breakup occurs. The time for break up is:

$$t_{StripBU} = \frac{D_o}{u_{ro}}\sqrt{\frac{\rho_f}{\rho_g}} \tag{4.32}$$

The same method is used for calculating the stripping breakup rate as was used for the bag-type breakup.

$$S'''_{LD,StB} = \frac{\rho_f \alpha_{LD}}{t_{StripBU}} \tag{4.33}$$

The value of a_{fr} for stripping breakup is 0.1 [7]. The Sauter mean diameter can be found as for bag-type breakup, using a_{fr} and the upper limited log normal distribution. Using the same forms as shown in Equations 4.29 and 4.30 but replacing *bagtype* with *strippingtype*, and setting $a_{fr} \approx 0.1$ for the stripping type of breakup, we can show:

$$\frac{m_{small}}{m_{large}} \approx 0.000037 \tag{4.34}$$

The bag-type breakup and stripping type breakup sources can be applied based on the computed Weber number to give the source term for total aerodynamic breakup of large droplets $\left(S'''_{LD,FB}\right)$.

There is a sharp discontinuity in the source term for droplet breakup where the model switches from Bag-Type to Stripping breakup. This change occurs at a Weber number of 50, and is shown in Figure 4.4. As seen in the figure, the jump between the types of breakup is very large. This suggests another potential area of research. Additional studies may be able to reduce the size of the jump.

The numerical solution methods used for solving the system of governing equations do

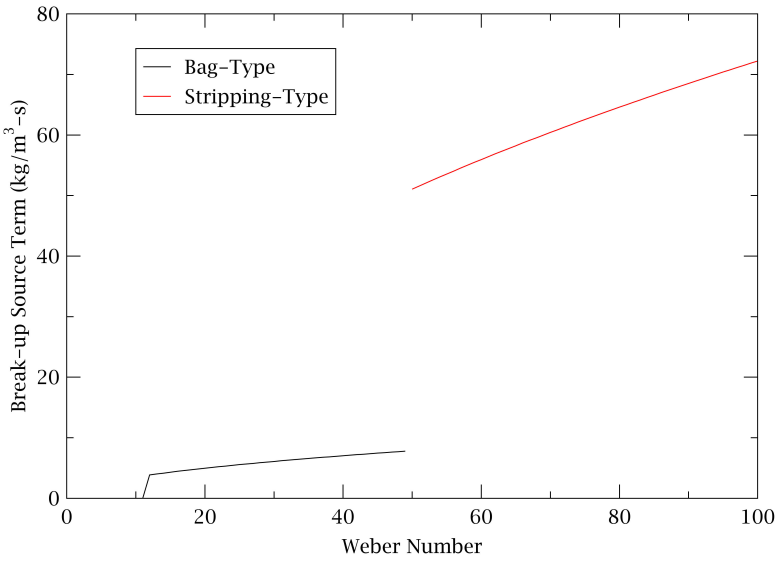

Figure 4.4: Flow Breakup Source Terms

not work well across sharp discontinuities. Instabilities resulting from the discontinuity can cause the calculation to fail. A sigmoid function that ranges from 0.0 to 1.0 will be used to smooth the transition between the bag-type and stripping-type source terms. The sigmoid function that will be used to smooth the step change is shown in Equation 4.35.

$$\epsilon = \frac{1}{1 + e^{-(x-x0)/\phi}} \tag{4.35}$$

The terms in Equation 4.35 are:

- ϵ = Smoothing multiplier for the two breakup functions
- x = Independent value from the functions - in this case, the Weber number
- $x0$ = Point at which the discontinuity occurs - 50 in this case
- ϕ = Range over which the functions will be smoothed - 2 in this case

The sigmoid function is a multiplier to the bag-type and stripping breakup source func-

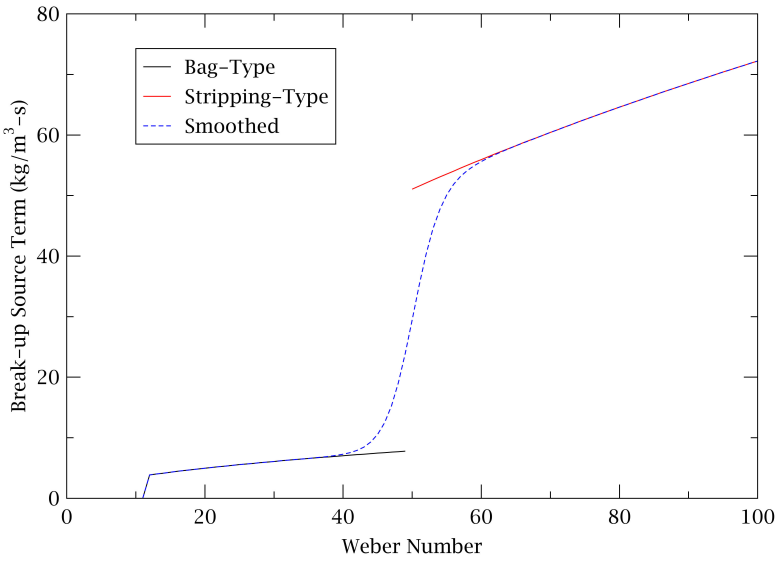

Figure 4.5: Flow Breakup Source Terms

tions as shown in Equation 4.36.

$$S_{flow-breakup} = (1-\epsilon)\, f_1 + \epsilon f_2 \tag{4.36}$$

Where f_1 is Equation 4.28 and f_2 is Equation 4.33. The resulting smoothed function is plotted with the discontinuous functions in Figure 4.5

Spacer Grid Impact

When large droplets impact against a spacer grid, the drop can be split into two large droplets, or it may split into a single large droplet and many small droplets [7]. If the impact is sufficiently forceful, the droplet may be completely shattered, producing only small droplets. The amount of small droplets that are generated by spacer grid breakup is related to the size of the impacting drop and the fraction of incident drops that contact the grid. The mass of small drops generated after breakup is a function of the entrained drop

flow rate and grid blockage area [7]:

$$m_{DB} = \eta_e \left(\frac{A_g}{A_c} \right) m_E \tag{4.37}$$

Where η_e is the grid efficiency factor, which relates to the portion of the drop that is shattered into microdroplets. The area of the grid is represented by A_g, and the channel area is A_c. The mass of droplets entering the grid is m_E, and the mass of small droplets resulting from grid impact is m_{DB}. FEBA and FLECHT-SEASET experiments have shown that η_e can be taken as 0.6 [7]. The same grid efficiency is used for the large droplet breakup as well as the further breakup of small droplets.

The source term for small droplets can be generated by dividing Equation 4.37 by the volume of large droplets within the control volume.

$$S'''_{SpcrBrkup} = \frac{\eta_e A_g m_E}{A_c \alpha_{LD} V_{cell}} \tag{4.38}$$

The Weber number is again used to determine the size of the drops resulting from the impact. The Weber number and Sauter mean diameter of the small droplets can be calculated using the following equations [7].

$$We_D = \frac{\rho_f V_{D_I}^2 D_I}{\sigma} \tag{4.39}$$

$$D_I = \frac{6\alpha_{lrgdrp}}{A_{i,d}} \tag{4.40}$$

$$\frac{D_{SM}}{D_I} = 6.167 We_D^{-0.53} \tag{4.41}$$

Where D_I is the diameter of the drop impacting the spacer grid, and D_{SM} is the Sauter mean diameter of the "small" droplets, based on experimental results. The interfacial area concentration is the ratio of the total droplet interfacial area and the total cell volume ($A_{i,d}$). The droplet volume fraction is represented by α_{lrgdrp}. If the Weber number is small enough, the size of the fragmented "small" drops will be on the same order as the impacting drop. When that happens, no shattering occurs, and the "shattered" drops remain in the large droplet field.

The data produced by the FLECHT-SEASET tests indicate that for Weber numbers lesser than 150, the "broken" drops are large enough to remain in the large drop field [7]. For larger Weber numbers, more of the impacting drop will be broken into small droplets. If the Weber number is greater than 250, the impacting drop is completely shattered, and only small droplets are produced. The fraction of small drops generated by the spacer grid impact can be computed using equation 4.42.

$$\epsilon = \frac{We - 150}{250 - 150} \tag{4.42}$$

When the small droplet fraction is multiplied by the spacer breakup rate as shown in Equation 4.38, the source term for the small droplet field is produced.

$$S'''_{SD,SBu} = \frac{\eta_e A_g m_E}{A_c \alpha_{LD} V_{cell}} \epsilon \tag{4.43}$$

The large droplet field source term is obtained by multiplying 4.38 by $(1 - \epsilon)$.

$$S'''_{LD,SBu} = \frac{\eta_e A_g m_E}{A_c \alpha_{LD} V_{cell}} (1 - \epsilon) \tag{4.44}$$

4.1.3 Droplet Coalescence Term ($S'''_{SD,C}$)

Suitable droplet coalescence models could not be located in the literature. Models of the detailed mechanics of interactions between two droplets were found [116], but could not be applied to the present study, since they could not be converted into a rate of coalescence within a droplet field. Additional models of the distribution of droplets in a flow field [117] were evaluated, but could not be adapted to the needed application of field exchange.

Until more suitable models are made available, droplet coalescence will be modeled using the same techniques that are used for bubble coalescence, which is described in section 4.2.3 of this article.

4.1.4 Droplet De-Entrainment Terms ($S'''_{LD,DE}$, $S'''_{SD,DE}$)

Once droplets are entrained in the vapor flow, they can rejoin the continuous liquid phase by de-entrainment processes. In Equations 3.65, 3.66, and 3.67, the droplet de-entrainment is represented by the terms $S'''_{LD,DE}$ and $S'''_{SD,DE}$, which are for large and small droplets, respectively. As with the droplet entrainment models, the mechanisms for de-entrainment vary based on flow orientation, either vertical or horizontal. The following sections discuss the de-entrainment models for these orientations.

Vertical Annular Flow De-Entrainment

The vertical annular flow regime is characterized by a liquid film coating the walls of the flow path, with a vapor core. One example of this flow regime occurs during reflood conditions, where the upper region of the fuel rods is (relatively) cool, meaning that it can be coated with a liquid film. The point at which the flow regime transitions to vertical annular flow often has a "froth front" where the coolant surface resembles that of a pot of boiling water.

Droplets that are entrained at the froth front can be de-entrained when they impinge on the film layer further up in the annular flow regime due to turbulence in the flow. The de-entrainment rate for vertical film flow is [115]:

$$S_{DE} = \frac{k_\sigma \Delta C P_w \Delta X}{V_{cell}} \tag{4.45}$$

Where:

$$\Delta C = \frac{\alpha_{totdrp}\rho_f}{\alpha_{totdrp} + \alpha_v} \tag{4.46}$$

$$k_\sigma = \max\left(3.0491 \times 10^{12}\sigma^{5.3054}, 12.491\sigma^{0.8968}\right) \tag{4.47}$$

Where the cell height is ΔX, cell volume is V_{cell}, k_σ is a mass transfer coefficient, and ΔC is the droplet concentration gradient in the channel.

No significant difference in droplet deposition rate is expected due to droplet size. Thus, for vertical annular flows, the source terms $S_{LD,DE}$ and $S_{SD,DE}$ are both computed by equation 4.45.

Horizontal Flow De-Entrainment

Droplet concentration is not uniform in horizontal droplet flows. Gravity acts on the droplets entrained in the flow, increasing the density of droplets in the lower portion of the pipe cross section. The local rate of deposition is [111]:

$$R_D = k_D\left(\frac{C_W}{C_B}\right)C_B = k_D\frac{C_W}{C_B}\left(\frac{W_{LE}}{SQ_G}\right) \tag{4.48}$$

In the above equation, C_W is the droplet concentration near the wall, C_B is the bulk droplet concentration, and k_D is the local droplet deposition velocity. For purposes of this calculation, droplet concentration is the mass of droplets per unit volume.

The ratio of the droplet concentration at the wall to the bulk concentration is defined as:

$$\frac{C_W}{C_B} = \frac{\exp\left(-yu_T/\zeta\right)}{\left(2/\pi\right)\int_0^{\pi}\left[\exp\left(-yu_T/\zeta\right)\right]\left(\sin\theta\right)\,d\theta} \tag{4.49}$$

Where θ is the angular position within the pipe measured from the bottom of the pipe. The droplet terminal velocity (u_T) in Equation 4.49 is dependent on the droplet diameter, and is computed by Equation 4.50.

$$u_T = \frac{d^{1.6} g\left(\rho_f - \rho_g\right)}{13.9\rho_g^{0.4}\mu_g^{0.6}} \tag{4.50}$$

In equation 4.50, d is the droplet diameter, g is the acceleration due to gravity, ρ is the density of the (L)-Liquid or (G)-Gas/Vapor, μ_g is the vapor viscosity, and U_G is the vapor velocity.

In Equation 4.49, y is the vertical position within a horizontal pipe. It is computed from the pipe radius and the angle as shown in Equation 4.51.

$$y = R\left(1 - \cos\theta_{int}\right) \tag{4.51}$$

Where θ_{int} is the angle measured from the bottom of the pipe to the point where the water/vapor interface contacts the pipe.

The turbulent diffusivity of the drops (ζ) in Equation 4.49 is computed using the following equation:

$$\zeta = -\left(D/2\right)v^*\varsigma \tag{4.52}$$

In the above equation, D is the diameter of the pipe. The empirical coefficient ς is dependent

on the pipe diameter, and has been found to range between 0.04 and 0.08 [111]. The friction velocity (v^*) is:

$$v^* = U_G \left(f_i/2\right)^{0.5} \tag{4.53}$$

where:

$$f_i = \left[1 + \left(61F^{0.5}\right)^2\right]^{0.5} \left[0.046 \left(\frac{4W_G}{\pi D \mu_g}\right)^{0.2}\right] \tag{4.54}$$

$$F = \frac{\mu_L \rho_g^{0.5} \gamma \left(Re_{LF}\right)}{\mu_g \rho_f^{0.5} Re_G^{0.9}} \tag{4.55}$$

$$\gamma = \left[\left(0.5 Re_{LF}^{0.5}\right)^3 + \left(0.028 Re_{LF}^{0.9}\right)^3\right]^{1/3} \tag{4.56}$$

$$Re_{LF} = \frac{4W_{LF}}{\pi D \mu_L} \tag{4.57}$$

C_W, C_B, and k_D from equation 4.48 vary around the circumference of the pipe. We can average these values around the circumference as shown in Equation 4.58.

$$\left\langle k_D \frac{C_W}{C_B} \right\rangle = \frac{1}{\pi} \int_0^{\pi} k_{D\theta} \left(\frac{C_W}{C_B}\right) d\theta \tag{4.58}$$

Substituting 4.58 into 4.48 gives the average deposition rate around the pipe per unit area:

$$\langle R_D \rangle = \left\langle k_D \frac{C_W}{C_B} \right\rangle \frac{W_{LE}}{SQ_G} \tag{4.59}$$

To convert equation 4.59 into the correct form for use in the governing equations, it must be divided by the length of the control volume.

$$S'''_{HrzSD,DE} = k_D \frac{C_W}{C_B} \frac{W_{LE}}{SQ_G L_{cell}} \tag{4.60}$$

Where the averaging notation has been removed for simplicity.

4.2 Closure Models for Mass Balance Closure of Vapor Phase

The development of the mass balance equations for the six-field model are documented in Chapter 3. The three equations for the vapor phase are Equations 3.68 (Continuous Vapor), 3.69 (Large Bubble), and 3.70 (Small Bubble).

The source terms in the mass conservation equations represent the physical phenomena that cause the vapor in the flow to change from one field to another. Such mechanisms include breakup from impact with spacer grids and breakup due to shear with the liquid phase. The source terms are determined using multiple correlations. It is impossible to solve the six field equations for the vapor phase without adequate closure models that solve for the source terms.

The key source terms related to the six-field model in the above equations are:

- $S'''_{LB,E}$ - Large bubble entrainment in vapor from continuous vapor field
- $S'''_{SBu,E}$ - Small bubble entrainment in vapor from continuous vapor field
- $S'''_{LB,DE}$ - Large bubble de-entrainment into continuous vapor field
- $S'''_{SBu,DE}$ - Small bubble de-entrainment into continuous vapor field
- $S'''_{LB,SB}$ - Breakup of large bubbles into small bubbles due to spacer grid impact
- $S'''_{LB,FB}$ - Aerodynamic breakup of large bubbles into small bubbles due to flow effects
- $S'''_{SBu,C}$ - Coalescence of small bubbles into large bubbles

The closure models that will be used to solve for each of these terms are discussed in the following sections.

4.2.1 Bubble Entrainment Terms ($S'''_{LB,E}$, $S'''_{SBu,E)}$

The bubble entrainment terms in Equations 3.68, 3.69, and 3.70 are $S_{LB,E}$, and $S_{SBu,E}$ (large and small bubbles, respectively). Bubble entrainment occurs when slugs or waves of coolant reconnect with the continuous liquid field, bringing vapor bubbles with them. An exhaustive literature search has not encountered any usable models for a bubble entrainment rate for use in the six field model. The lack of a usable model for bubble entrainment offers two possibilities for resolution. Either the entrainment of bubbles can be neglected, or a potentially less applicable model can be used. Until suitable bubble entrainment models are developed, it is recommended that the droplet entrainment model (see Section 4.1.1) be implemented as a bubble entrainment model. Although this model is not designed to reflect bubble entrainment, it will allow testing of the impact of the bubble entrainment phenomenon.

4.2.2 Bubble Breakup Terms ($S'''_{LB,FB}$, $S'''_{LB,SB}$)

Bubbles can be broken up by flow effects and spacer grid impacts, in much the same way that droplets are broken up.

Spacer grid breakup of large bubbles is represented by source terms in the governing equations (3.69 and 3.70). Bubbles resulting from spacer breakup may all be small bubbles, or may have a large bubble and some small bubbles.

Governing Equations 3.69 and 3.70 include a term for breakup of large bubbles due to aerodynamic effects - $S'''_{LB,FB}$. There are three primary modes for aerodynamic bubble breakup. These are:

- Turbulent impact
- Shear off
- Surface instability

Breakup by turbulent impact occurs when turbulent liquid eddies of sufficient size impact a bubble and cause it to break into smaller bubbles. Bubble shear off refers to a cap bubble that develops a "skirt" from which small bubbles are sheared off. Breakup by surface instability is caused when the bubble grows to sufficient size that surface tension is no longer able to hold it together, and it breaks into smaller bubbles.

The flow breakup equations presented here were originally developed to determine the rate of change in area concentration for the bubble fields. Interfacial area concentration is the interfacial area per unit mixture volume ($^{m^2}/_{m^3}$ or m^{-1}), which means that as originally developed, the equations presented here have units of $^{1}/_{ms}$.

The source terms for the governing equations (see Equations 3.68, 3.69, 3.70) are in units of $^{kg}/_{m^3 s}$, so the area concentration equation should be adjusted to provide the correct units.

The area concentration is effectively:

$$\text{Area Concentration} = \frac{A_{tot}}{V_{tot}} \tag{4.1}$$

In order for the area concentration shown above to be used in the governing equations, it must be modified to have units of $^{kg}/_{m^3}$. Since we assume that the large and small bubble fields are of different but uniform size, we can compute the number of bubbles in a given field by dividing the total area by the area of a single bubble.

$$N_{bub} = \frac{A_{tot}}{A_{bub}} \tag{4.2}$$

The total volume occupied by bubbles can be computed using the number of bubbles and the volume of a single bubble:

$$V_{bub,tot} = N_{bub} \times V_{bub} \tag{4.3}$$

With a known total bubble volume and the density of the bubbles, the mass of the

bubbles may be computed. By substituting Equation 4.2 into Equation 4.3, we get:

$$V_{bub,tot} = A_{tot} \times \frac{V_{bub}}{A_{bub}} \tag{4.4}$$

The area and volume of a single bubble can be computed by assuming the bubble is of spherical shape and using the bubble radius (r_{bub}).

$$V_{bub} = \frac{4}{3}\pi r^3 \tag{4.5}$$

$$A_{bub} = 4\pi r^2 \tag{4.6}$$

Substituting Equations 4.5 and 4.6 into Equation 4.4, we obtain:

$$V_{bub,tot} = A_{tot} \times \frac{r_{bub}}{3} \tag{4.7}$$

Equation 4.7 shows that if the equations for rate of change of area concentration are multiplied by $\rho_{bub} r_{bub}/3$, the correct units for use in the governing equations ($kg/m^3 s$) are obtained. This has been done for the bubble breakup equations presented in the following sections.

Turbulent Impact

Turbulent impact results when sufficiently large turbulent eddies impact a bubble and cause it to break up into two smaller bubbles. The turbulent eddy must be large enough to start the breakup, but not so large that it just pushes the bubbles around.

This model assumes that eddies up to 50% of the bubble size will not be large enough to cause bubble disintegration. The model was developed more completely in [9], and is summarized here. Breakup criteria depend on the eddy energy and the bubble surface tension. A critical Weber number based on the balance of these two effects is:

$$We_{c,TI} = \frac{\rho_f \overline{u}_{tc}^2 D_b}{\sigma} \tag{4.8}$$

For air bubbles in water, the critical Weber number ranges between 2.3 and 8.0 [118]. The critical eddy velocity for bubble breakup is $\overline{u}_{tc}$ in Equation 4.8. It can be computed using Equation 4.9.

$$\overline{u}_{tc}^2 = 2.0\left(\chi D_b\right)^{2/3} \tag{4.9}$$

Where χ is the turbulent kinetic energy dissipation rate per unit of mixture mass, and D_b is the bubble diameter.

If the Weber number of the flow is greater than that computed using Equation 4.8, then bubble breakup by turbulent impact is possible. The flow Weber number is:

$$We = \frac{\rho_f \overline{u}_t^2 D_b}{\sigma} \tag{4.10}$$

Where u_t is the average turbulent eddy velocity.

Small Group Bubble Breakup Breakup of bubbles within the small bubble group can be computed as shown in Equation 4.11 [9].

$$S'''_{SBu,SBu,TI} = 0.12 C_{TI,SBu}\chi^{1/3}\left(1-\alpha_t\right)\frac{A_{i,SBu}^{5/3}}{\alpha_{SBu}^{2/3}} \times \exp\left(-\frac{We_{c,TI,SBu}}{We_{SBu}}\right) \times \sqrt{1-\frac{We_{c,TI,SBu}}{We_{SBu}}}\frac{\rho_g r_{SBu}}{3} \tag{4.11}$$

The adjustable coefficient (C_{TI}) for turbulent impact of small bubbles is 0.03. The critical weber number for turbulent breakup of small bubbles is ($We_{c,TI,SBu}$) is 6.5 [118]. In order for breakup to occur, We_{SBu} must be greater than $We_{c,TI,SBu}$. Equation 4.10 is used to compute We_{SBu}, which has $u_{t,SBu}$ and $D_{sm,SBu}$ in place of u_t and D_b.

Small bubbles breaking up into smaller bubbles does not affect the overall volume fraction

of small bubbles, but it does affect the average size of the small bubbles. Tracking the breakup of small bubbles makes it possible to follow the changing average diameter of the small bubble field.

Large Group Bubble Breakup The breakup of bubbles in the large bubble group is more complicated, since there can be multiple bubbles resulting from the breakup which may be large enough to still be in the large group, or they may be small enough to be considered small bubbles. This model assumes that the bubble breaks up into two "daughter" bubbles. A generation rate of small bubbles from the large bubble turbulent breakup can be obtained [9]:

$$S'''_{LB,SBu,TI} \approx 2.71 C_{TI,LB} \alpha_{LB} (1-\alpha_t) \frac{\chi^{1/3} G^{2/3} \left(R_c^*\right)^{5/3} \left[1-\left(R_c^*\right)^{5/3}\right]}{R_{m,LB}^{7/3}} \times \exp\left(-\frac{We_{c,TI,LB}}{We_{LB}}\right) \sqrt{1-\frac{We_{c,TI,LB}}{We_{LB}}} \frac{\rho_g r_{LB}}{3} \tag{4.12}$$

Where G is the narrow dimension of the flow channel that was used in the development of the correlation. In the case of more typical pipe flows, the value of G will be set to the pipe radius. The dimensionless radius of curvature for a cap bubble is R_c^*, which is computed as [9]:

$$R_c^* = \frac{R_c}{R_{m,LB}} \tag{4.13}$$

Where the radius of a bubble on the boundary between the small and large bubble groups is R_c, and the maximum radius of a large group bubble is $R_{m,LB}$.

A generation rate for large bubbles resulting from the turbulent breakup of a large bubble

is:

$$S'''_{LB,LB,TI} \approx 1.4 C_{TI,LB} \alpha_{LB} \frac{\chi^{1/3} G}{R_{m,LB}^{8/3}} (1-\alpha_t)(1-2R_c^*) \times \exp\left(-\frac{We_{c,TI,LB}}{We_{LB}}\right) \sqrt{1-\frac{We_{c,TI,LB}}{We_{LB}}} \frac{\rho_g r_{LB}}{3} \tag{4.14}$$

Where the adjustable coefficient (C_{TI}) for the large bubble turbulent impact breakup is 0.02, and the critical Weber number is 7.0.

As for the small bubbles breaking up into smaller bubbles, this model enables the code to track the changing average size of the large bubble field.

Shear Breakup

Shear breakup occurs when smaller bubbles are sheared off of the rim around the base of a cap bubble. The viscous interaction between the liquid flow and the bubble surface acts against surface tension and generates a "skirt" at the rim of the large bubble. This skirt is a thin layer of vapor. If the interacting forces are strong enough, bubbles can be sheared off of this vapor layer.

The model summarized herein comes from [9]. It assumes that the skirt is straight and perpendicular to the cap bubble base. It is also assumes that the bubbles that shear off of the skirt have a diameter that is equivalent to the skirt thickness, and that bubbles in the small bubble group do not experience shear breakup. Figure 4.6 shows bubble shear breakup.

The maximum diameter of the stable small bubbles that shear off with the liquid can be estimated as:

$$d_{s,max} = \left(\frac{We_c \sigma}{2\rho_f}\right)^{3/5} \chi^{-2/5} \propto \left(\frac{\sigma}{\rho_f}\right)^{3/5} G^{2/5} v_{rb}^{-6/5} \tag{4.15}$$

where We_c is the critical Weber number for bubble breakup, and v_{rb} is the relative velocity

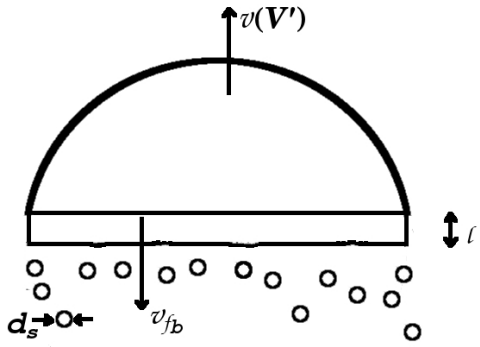

Figure 4.6: Small bubbles shearing off the rim of a large (cap) bubble

of a cap bubble with respect to the liquid around the bubble base.

Equation 4.15 represents a theoretical upper limit for small bubble size based on a critical Weber number for bubble breakup. Using a best fit to the experimental data from [118], Equation 4.16 for the small bubble diameter is obtained [9]. This expression accounts for fluid property effects that are not represented in the theoretical upper bubble limit.

$$d_s = C_d \left(\frac{\sigma}{\rho_f}\right)^{3/5} G^{2/5} v_{rb}^{-6/5} \tag{4.16}$$

where C_d is an empirical constant that is 4.8 based on air/water experimental results.

It is assumed that the bubbles that shear off of the larger bubble are all of the same size [9]. If the large bubbles have a Weber number greater than the critical Weber number for shear-off ($We_{c,SO}$ - see Equation 4.18), and if the large bubble volume is bounded by $V_{SO,c}$ (the smallest bubble that can experience bubble shear-off) and $V_{m,LB}$ (the largest volume for a bubble in the large bubble group), the source term for small bubbles generated is:

$$S_{LB,SB,SO} = 64.51 C_{SO} C_d^2 \frac{\alpha_{LB} v_{rb}}{G R_{m,LB}} \left[1 - \left(\frac{We_{c,SO}}{We_{m,LB}}\right)^3\right] \frac{\rho_g r_{SBu}}{3} \tag{4.17}$$

The shear off coefficient (C_{SO}) is determined based on experimental results to be 3.8×10^{-5} [118]. The critical Weber number for bubble shear off ($We_{SO,c}$) is 4500 [118].

The critical Weber numbers for shear off breakup and maximum large group bubbles are:

$$We_{c,SO} = \frac{2\rho_f v_{rb}^2 R_{SO,c}}{\sigma} \tag{4.18}$$

$$We_{m,LB} = \frac{2\rho_f v_{rb}^2 R_{m,LB}}{\sigma} \tag{4.19}$$

where bubbles with a Weber number larger than $We_{c,SO}$ get sheared off.

Instability Breakup

Surface instability is caused when the bubble grows to sufficient size that the surface tension is no longer strong enough to hold the bubble together, and it breaks up [9]. The mechanisms that result in bubbles of sufficient size for this type of breakup are coalescence or wake entrainment. Bubbles in the small group that experience coalescence interactions are not likely to exceed the critical volume where instability will result in bubble breakup.

Bubbles in the "large" group are therefore assumed to be the primary source of instability breakup. This occurs when two large cap bubbles coalesce together by wake entrainment or random collision, and then immediately break up due to surface instability. Thus, no net change in the large group volume occurs.

The total rate of breakup from surface instability, including wake entrainment (WE) and random collisions (RC), is [9]:

$$\begin{aligned} S'''_{LB,SBu,SI} \approx 1.25\alpha_2^2 \left(\frac{\sigma}{g\left(\rho_f - \rho_g\right)}\right)^{-1} \Bigg\{ C_{RC}^{(2)} \frac{\chi^{1/3}}{W^2} \left(\frac{\sigma}{g\left(\rho_f - \rho_g\right)}\right)^{7/6} \times \\ \left[1 - \exp\left(-C_{RC2}\alpha_2^{1/2}\right)\right] + 2.3 \times 10^{-4} C_{WE}^{(2)} \sqrt{C_{D2} g G} \Bigg\} \frac{\rho_g r_{LB}}{3} \end{aligned} \tag{4.20}$$

The relationship between the size of the eddies and the distance between bubbles is captured by the C_{RC2} coefficient which has been found to be 3.0 in water and air experiments [118]. The other experimental coefficients in the above equation are [118]: $C_{RC}^{(2)} = 0.005$ and

$C_{WE}^{(2)} = 0.005$. These three coefficients account for the various effects of the flow on the random collision and wake entrainment processes that cause large bubbles to coalesce into larger bubbles that are then subject to breakup by instability. Thus, these coalescence terms are important in the calculation of instability breakup.

Flow conditions will determine which of the three methods of flow breakup is appropriate for the calculation. To a significant degree, the Weber number can be used to determine if turbulent impact, shear breakup, or instability breakup is the more likely condition. Once the probable type of breakup is determined, the appropriate model for the source term will be used in the solution of the six-field equations. For flows in a transition region between the known models, interpolation between the source terms for each breakup type will be made based on the Weber number.

Spacer Grid Impact

The term for spacer grid breakup of large bubbles is $S'''_{LB,SB}$ in the governing Equations (3.69 and 3.70). The model for droplet breakup by spacer grid impact (Section 4.1.2) will be used to model the breakup of bubbles by the spacer grids. The Weber number used for the droplet breakup criteria is 150. This number may need to be adjusted in the future if suitable data becomes available for comparison. It is expected that differences in viscosity and surface tension for the bubbles will have an impact on the breakup model. Models specific for bubble breakup will need to take these characteristics into account.

4.2.3 Bubble Coalescence Term ($S'''_{SBu,C}$)

Bubble coalescence is represented in Equations 3.69 and 3.70 by $S'''_{SBu,C}$. Bubbles coalesce by two principal mechanisms:

1. Random collisions

2. Wake entrainment

Random collisions occur when turbulent eddies of roughly the same size as the bubbles cause the bubbles to impact with enough force to coalesce. Collisions between multiple bubbles are assumed to be infrequent events, so collisions will be assumed between two bubbles only [9].

Wake entrainment occurs when one bubble follows in the wake of another bubble. The bubble in the wake accelerates and coalesces with the leading bubble. The trailing bubble must be equal to or smaller in volume than the leading bubble for wake entrainment to occur [9].

Random Collision Coalescence

Random collisions can occur between two bubbles that are both in the small bubble group, between a small bubble and a large bubble, or two bubbles in the large bubble group. In each of these cases, the liquid turbulence is considered to be the driving force causing the collisions. In real flows, the bubbles move randomly and may move away from each other and not collide. Once they do collide, it is still possible that they will not coalesce if the eddies are not strong enough. Terms are included in the models presented here to account for these uncertainties.

Coalescence of Small Group Bubbles When small group bubbles collide, there are two possible outcomes. The resulting bubble may be small enough to still be part of the small bubble group, or the bubble may be large enough that it is now in the large bubble group. The source term for the first case, where the resulting bubble is still part of the small bubble group is shown below [9]. Although the bubble remains in the "small" bubble field, it is still important to track the increase in these bubbles, since it will have an impact on the average diameter of the small bubbles. Increasing average diameter of the small bubble field will result in more large bubbles being generated by coalescence mechanisms, since the starting

bubbles will be larger.

$$S'''_{SBu,SBu_{RC}} = -0.17C^{(1)}_{RC}\frac{\chi^{1/3}\alpha^{1/3}_{SBu}a^{5/3}_{i,SBu}}{\alpha^{1/3}_{SBu,max}\left(\alpha^{1/3}_{SBu,max}-\alpha^{1/3}_{SBu}\right)}\times \left[1-\exp\left(-C_{RC1}\frac{\alpha^{1/3}_{SBu,max}\alpha^{1/3}_{SBu}}{\alpha^{1/3}_{SBu,max}-\alpha^{1/3}_{SBu}}\right)\right]\frac{\rho_g r_{SBu}}{3} \tag{4.21}$$

where $C^{(1)}_{RC}$ is an empirical coefficient that has been found to be 0.005 by experiment, and C_{RC1} is 3.0.

The source term for the large bubbles that result from collision of two small bubbles is [9]:

$$S'''_{SB,LB_{RC}} \approx 0.68C^{(1)}_{RC}\chi^{1/3}\frac{\alpha^2_{SBu}a^{2/3}_{i1}}{\alpha^{2/3}_{SBu,max}G}\left[1-\exp\left(-C_{RC1}\frac{\alpha^{1/3}_{SBu,max}\alpha^{1/3}_{SBu}}{\alpha^{1/3}_{SBu,max}-\alpha^{1/3}_{SBu}}\right)\right]\times \left[1+0.7G^{7/6}\left(\frac{a_{i,SBu}}{\alpha_{SBu}}\right)^{1/2}\left(\frac{\sigma}{g\left(\rho_f-\rho_g\right)}\right)^{-1/3}\right]\left(1-\frac{2}{3}D^*_{cl}\right)\frac{\rho_g r_{SBu}}{3} \tag{4.22}$$

where:

$$D^*_{cl} = \frac{D_c}{D_{SBu}} \tag{4.23}$$

$$D_c = \left(\frac{6V_c}{\pi}\right)^{1/3} \tag{4.24}$$

$$D_{SBu} = \frac{6\alpha_{SBu}}{a_{i,SBu}} \tag{4.25}$$

Coalescence of a Small Bubble and a Large Bubble The volume of the bubbles in the small group is much less than that of the bubbles in the large group. It is assumed that when a small group bubble coalesces with a large group bubble, the resulting bubble will not exceed the maximum bubble stability volume, and it will remain stable after the collision.

The transfer equation representing the net inter-group mass transport to the large group is [9]:

$$S'''_{SBuLB,RC} = 13.6 C_{SBuLB,RC} \chi^{1/3} \frac{\alpha_{SBu}^{5/3} \alpha_{LB}^2}{R_{m,LB}^{2/3} G} \left(1 + \frac{10.3G}{R_{m,LB}}\right) \times \left[1 - \exp\left(-C_{RC1} \frac{\alpha_{SBu,max}^{1/3} \alpha_{SBu}^{1/3}}{\alpha_{SBu,max}^{1/3} - \alpha_{SBu}^{1/3}}\right)\right] \frac{\rho_g r_{SBu}}{3} \tag{4.26}$$

Coalescence of Large Group Bubbles If two large bubbles coalesce, the resulting bubble may be larger than the maximum bubble size. When that happens, the resulting bubble will break up almost immediately due to surface instability effects, which was discussed in section 4.2.2.

If the resulting bubble is still small enough to be stable, then it will remain part of the large bubble group. The rate of mass generation can be computed as [9]:

$$S'''_{LB,LB,RC} = -13.6 C_{RC}^{(2)} \frac{\alpha_{LB}^2 \chi^{1/3}}{W^2 G} R_{m,LB}^{4/3} \times \left(1 - 2.0 \left(R_c^*\right)^2 + \frac{9.0G}{R_{m,LB}}\right) \times \left[1 - \exp\left(-C_{RC2} \alpha_2^{1/2}\right)\right] \frac{\rho_g r_{LB}}{3} \tag{4.27}$$

Wake Entrainment

Bubbles from either bubble group (large or small) can be in the lead position for wake entrainment to occur. Since the trailing bubble must be smaller than the lead bubble to be contained within the wake region, if the lead bubble is from the small bubble group, the trailing bubble may not be from the large bubble group [9].

Small Bubble Leading If a small bubble is in the lead position, the resulting bubble (after coalescence) may remain in the small bubble group, or it may be large enough to join the large bubble group.

If the resulting bubble remains in the small bubble group, then the mass rate of change for the small bubble field due to wake entrainment is [9]:

$$S'''_{SB,SB_{WE}} = -0.27 C^{(1)}_{WE} u_{r,SBu} C^{1/3}_{D,SBu} a^2_{i,SBu} \frac{\rho_g r_{SBu}}{3} \tag{4.28}$$

Where the wake entrainment coefficient ($C^{(1)}_{WE}$) is 0.002, $u_{r,SBu}$ is the relative velocity of the leading small group bubble, and $C_{D,SBu}$ is the drag coefficient for the leading small bubble [9]. While this interaction does not outwardly change the total amount of small bubble volume within a control volume, tracking these interactions allows us to increase the average diameter of the small bubble field. Once the average diameter of the field of small bubbles increases to sufficient size, they will begin to transition to the large bubble field. Thus, Equation 4.28 captures an important part of the small bubble interactions.

If the resulting bubble is large enough to be in the large bubble group, the source term for the large group bubbles from wake entrainment is:

$$\begin{aligned} S'''_{SB,LB_{WE}} = 1.08 C^{(11,2)}_{WE} u_{r1} C^{1/3}_{D,SBu} \frac{\alpha_{SBu} a_{i,SBu}}{G} \left(1 - \frac{2}{3} D^*_{c,SBu}\right) \times \\ \left[1 + 0.7 G^{7/6} \left(\frac{a_{i,SBu}}{\alpha_{SBu}}\right)^{1/2} \left(\frac{\sigma}{g\left(\rho_f - \rho_g\right)}\right)^{-1/3}\right] \frac{\rho_g r_{SBu}}{3} \end{aligned} \tag{4.29}$$

Where the coefficient for two small group bubbles combining to make a large group bubble ($C^{(11,2)}_{WE}$) is 0.002 [9].

Large Bubble Leading When a large bubble is in the lead position, the trailing bubble may be either a large bubble or a small bubble. In the same way as for random collisions, the resulting bubble may be stable, and remain in the large bubble group, or it may become unstable, and break up by surface instability, as discussed in section 4.2.2.

The net contribution to the large bubble field for entrainment of a small bubble is [9]:

$$S'''_{SB,LB_{WE}} = 26.1 C_{WE}^{(12,2)} \alpha_{SBu} \alpha_{LB} \sqrt{\frac{g C_{D,LB}}{G}} \frac{1}{R_{m,LB}} \times \left(1 + 4.31 \frac{G}{R_{m,LB}}\right) \frac{\rho_g r_{LB}}{3} \tag{4.30}$$

The mass rate of change for entrainment of a large bubble following a large bubble is:

$$S'''_{LB,LB_{WE}} = -15.9 C_{WE}^{(2)} \frac{\alpha_{LB}^2}{R_{m,LB}^2} \sqrt{g C_{D,LB} G} \left(1 + 0.51 R_c^*\right) \frac{\rho_g r_{SBu}}{3} \tag{4.31}$$

4.2.4 Bubble De-Entrainment Terms ($S'''_{LB,DE}$, $S'''_{SBu,DE}$)

Bubble de-entrainment occurs when the bubbles entrained in the continuous liquid encounter and rejoin the continuous vapor phase. Thus, they leave the bubble field and rejoin the continuous vapor field. De-entrainment is represented in Equations 3.68, 3.69, and 3.70 by $S'''_{LB,DE}$ and $S'''_{SBu,DE}$. The mechanism of this interaction is simple, but a literature search has not encountered any usable models of a bubble de-entrainment rate that is applicable on an average basis to a field of bubbles. Individual bubble models are plentiful, but not easily applied to the six-field model.

As was done for the bubble entrainment model discussed previously, the droplet de-entrainment model (see Section 4.1.4) will be implemented for bubble de-entrainment. Consideration will be made to reverse the effect of gravity, since the bubbles will experience a buoyant force that counteracts the gravitational pull that accelerates the droplet de-entrainment. This model may be replaced as more applicable models are developed.

4.3 Mass Closure Validation

The six-field model utilizes the two-field RELAP5-3D code as a developmental starting point. The mass conservation of the two-field code is validated as part of the developmental assessment. The details of the experiments and data that are used for validation are discussed in [100]. The same experiments and procedures are applicable to the six-field model validation,

so this section will only discuss the validations of the additional components of the mass conservation that make up the six-field model. Validation of the proposed six-field model should include comparisons of key model parameters to available experimental data.

4.3.1 Metrics of Interest for Validation

The proposed six-field model introduces a significant number of new parameters. Some of the metrics that will be used to validate the model are listed below.

- Droplet or bubble size
- Rate of bubble or droplet entrainment
- Rate of bubble or droplet de-entrainment
- Rate of phase change at bubble or droplet interface
- Rate of bubble generation at the wall
- Velocity of bubble or droplet field

Two major categories of experiments can be used in the validation effort. Separate effects tests may be used to validate single parts of the model, such as those listed as metrics of interest above. Integral effects tests are used to validate the model as a whole. The following sections will discuss the types of tests recommended for the six-field model validation in greater detail.

Separate Effects Tests

A separate effects test that might be used to validate the droplet or bubble size would provide sufficient data to compute the size of the bubble or droplet for comparison to the values obtained in the model. A potential experiment would be one with a tank of water and bubblers located at the bottom of the tank. By changing the rate of the air entering the

tank or the size of the nozzles, the size of the bubbles could be varied. A model of the tank could be developed for the six-field code and the results compared for validation purposes. A similar technique could be used with a spray nozzle and droplets.

For entrainment/de-entrainment validation, an experiment with stratified flow within a channel could be used. By varying the velocity of the air/vapor in the channel, droplets could be entrained. High-speed video could be used to measure the rate of entrainment or de-entrainment of the droplets or bubbles. In addition, the size of the droplets and bubbles could be measured for comparisons to the calculation.

The rate of phase change at the interface of the bubble with the liquid or the droplet with the vapor field would also need to be measured based on high speed video of an experiment. A suitable experiment may include subcooled or superheated water sprayed into a steam chamber, and video recording of the resulting droplets to monitor the rate that the size of the droplets changes. The mass crossing the boundary could then be computed based on the change in droplet size.

A similar experiment could be conducted to determine the rate of change for vapor bubbles. In a bubble experiment, the superheated or subcooled vapor would be injected into the bottom of a tank of water. As the bubbles rise to the surface of the tank, the reduction in pressure at the shallower water depth would result in an increase in the size of the bubble. This effect would have to be subtracted out from the size measurement of the bubbles for calculating the amount of mass crossing the phase boundary.

Many experiments have been conducted to show the rate off bubble growth at a wall, both with and without forced flow near the wall surface. Those experiments would be suitable for comparison to the computed rate of bubble generation at the wall from the six-field model. These experiments would also provide heat transfer rates at a range of wall superheat conditions.

Experiments that use high-speed video or rapid-fire still photos to track bubbles in a two-phase flow field would provide the data necessary to validate the calculated bubble or

droplet velocities from the model. These experiments often use software to compute the bubble velocity from one frame to the next based on detailed knowledge of the distance the bubble travels. The distance is measured by use of a uniform grid placed behind the flow field.

Integral Effects Tests

Two cases each from the FLECHT-SEASET and the RBHT rod bundle reflood tests are recommended for comparison against the proposed model described in the previous chapters. The FLECHT-SEASET and RBHT tests included vertical rod bundles. Both tests included spacer grids, and data was collected for the rod temperatures, quench front locations, liquid mass stored in the bundle and liquid and steam temperatures. This data can be used in the comparison to the results computed by the modified and un-modified RELAP code. The parameters measured in these tests (quench front location, liquid, and steam temperatures) are a function of many facets of the hydrodynamic model, and thus test the overall performance of the six-field model, rather than a specific aspect. These experiments will be described in greater detail below.

The RBHT experiments are of longer duration than the FLECHT-SEASET experiments. This allows more time for the dispersed flow film boiling conditions to be established. The RELAP model of the RBHT experiments consists of a single channel. The heated rods were modeled with a single cylindrical heat structure, the unheated rods were similarly modeled, and the housing was modeled with a third heat structure.

The heated rods are made up the following layers: a boron nitride insulator, Monel K-500 heating element, an additional layer of boron nitride, and clad with inconel 600. The unheated rods are a cylinder of inconel 600 material. The heat structures are sized to have a cross sectional area and wetted/heated perimeter consistent with the total area of the rods in the experiment.

The analysis was performed using a model of a single channel that represents the 161

heater rods, 16 unheated rods, and the housing from the FLECHT-SEASET tests. The model is similar to that used for the RBHT tests, in that three heat structures are used to model the heated rods, unheated rods, and housing from the FLECHT-SEASET tests.

The heater rods have 4 layers. As before, there is a boron nitride insulation layer, the heating element layer made of Monel K-500, another insulation layer of boron nitride, and finally a cladding layer of stainless steel 316. Unheated rods are simple cylinders of stainless steel 316.

Note that the RBHT and FLECHT-SEASET tests are already included in the developmental assessment of the RELAP and TRACE codes.

4.3.2 Experimental Validation Discussion

The validation of the six-field model will involve development of input models for the system code (RELAP) that reflect the separate effects test or integral effects test that is being used for the comparison. The input model will be run using both the two-field and six-field versions of RELAP, and the computed results compared to the experimental data. Where necessary, input or models can then be modified to improve the performance of the code.

4.4 Mass Closure Model Discussion

This chapter has presented closure relationships that can be used to determine the source terms added to the mass governing equations for the six-field model. These mechanistic models attempt to quantify the amount of mass that is crossing from one field to another. It is possible that these models will intersect for some situations, resulting in discontinuities or conflicting transfer rates. It is important that calculational distance is maintained between the models.

In the cases of droplet entrainment and de-entrainment, the correlations presented in this chapter are applicable to different pipe orientations (horizontal or vertical), and different flow

conditions (reflood or annular). Since the correlations are so case-specific, the code can easily be adapted to use the correct correlation for the particular case. Where the pipe orientation is ambiguous (such as for pipes angled at 45 degrees), an interpolation between the vertical and horizontal correlations will be used. This is the same method currently used by many system codes.

The breakup of droplets by the bag-type or stripping process is defined by specific Weber number boundaries. Bag type breakup occurs only for Weber numbers greater than 12, and stripping breakup is for Weber numbers greater than 50. These limits can be used as boundaries for application of the correlations presented in this chapter. This same idea is applicable to the bubble breakup mechanisms. As was stated in Section 4.2.2, the Weber number can be used to differentiate between the bubble breakup models.

Bubble coalescence by random collision or wake entrainment could conceivably occur at the same time in the same flow. The mass exchange that results is assumed to be additive for the two mechanisms. In order for interactions to occur between large and small bubbles, both fields must be present in a flow. Thus, if there are no small bubbles in the flow, the models for large bubbles coalescing with small bubbles will not be activated.

CHAPTER 5

Momentum and Energy Closure Models

The closure relationships that are necessary for solution of the six-field model momentum and energy balance equations documented in Reference [106] are presented in this document. The closure models that will be used for the energy conservation equations will be discussed first, and then the closure for momentum equations will be described.

5.1 Energy Conservation Equations

The energy balance equations for six fields that are documented in Chapter 3 are not repeated here. The energy balance equation for the continuous liquid field is Equation 3.104. Equation 3.105 is the energy conservation equation for small droplets. Equation 3.106 is for large droplets.

The energy balance equation for continuous vapor is shown as Equation 3.107. Equation 3.108 is for the small bubble field, and Equation 3.109 is for the large bubbles. Thermal energy is transferred to and from the coolant fields in two primary ways. The first is between the fields themselves; energy can be transferred between fields by mass exchange, and directly across the field interfaces. The second method of energy transfer to/from the coolant is by interaction with the solid surfaces that contain the coolant, such as pipe walls. The first section in this chapter will discuss the transfer between coolant phases; a discussion of the "wall" heat transfer will follow.

5.1.1 Interfacial Energy Transfer

The energy balance equations for each field use heat transfer coefficients to model the exchange of heat between the fields across the interfacial boundaries. These interactions are complex, and depend on relative velocities between the fields and interfacial surface areas. This section will outline the proposed closure models that will allow computation of the

interfacial areas and heat transfer coefficients.

Energy transfer between fields is carried out by direct contact between the phases as well as the physical exchange of mass between them. The terms in the energy equations representing the energy exchange that results from mass transfer will be solved for as part of the mass governing equations. These terms include the source terms that define physical exchange between fields (e.g. $S'''_{LB,E}$ [119]). The terms that are needed to account for the energy conduction across field boundaries must still be resolved. These are the heat flux at field interfaces (e.g. small bubble interface - $q''_{SBu,i}$) and area concentration at field interfaces (a_i, k).

The heat flux at the field interfaces can be computed when the heat transfer coefficient at the interface is known. This term will vary depending on the flow regime and configuration. In addition, the system pressure and flow rate also affect the heat transfer. The following sections will describe the selected closure models for the more common flow regimes.

Bubbly Flow

The bubbly flow regime has large and/or small bubbles flowing in the continuous liquid field. In this section, the interfacial heat transfer between the bubble fields (large and small) and the continuous liquid field will be described. The bubbly flow conditions can be classified into four groups:

1. Bubbly flow with superheated liquid
2. Bubbly flow with subcooled liquid
3. Bubbly flow with superheated vapor/gas
4. Bubbly flow with subcooled vapor/gas

Bubbly Superheated Liquid Bubbly flow with the liquid temperature greater than the saturation temperature is considered bubbly superheated liquid. The closure model for heat

transfer for this flow condition selects the larger of a heat transfer coefficient from either Plesset-Zwick or a modified Lee-Ryley as shown in Equation 5.1 [2]. These correlations will be applied to both the large and the small bubble fields. Where diameters are needed, the Sauter mean diameters for each bubble field will be used in place of the average bubble diameter that is required by the correlations, and in the calculation of the interfacial area per unit volume.

$$H_{if} = \left\{ \max \left[\begin{array}{ll} -\frac{k_f}{d_b}\frac{12}{\pi}\Delta T_{sf}\frac{\rho_f C_{pf}}{\rho_g h_{fg}}\beta & \text{Plesset-Zwick} \\ \frac{k_f}{d_b}\left(2.0 + 0.74 Re_b^{0.5}\right) & \text{modified Lee-Ryley} \end{array} \right] + 0.4|v_f|\rho_f C_{pf} F_1 \right\} (a_{gf} F_2 F_3) \tag{5.1}$$

where

$$\Delta T_{sf} = T^{sat} - T_f \tag{5.2}$$

$$Re_b = \frac{(1-\alpha_{bub})\,\rho_f v_{fg} d_b}{\mu_f} \tag{5.3}$$

$$\beta = 1.0 \text{ for bubbly flow} \tag{5.4}$$

$$F_1 = \frac{min\,(0.001, \alpha_{bub})}{\alpha_{bub}} \tag{5.5}$$

$$F_2 = \frac{min\,(0.25, \alpha_{bub})}{\alpha_{bub}} \tag{5.6}$$

$$F_3 = \begin{cases} 1.0 & \Delta T_{sf} \le -1.0 \\ \max\left[0.0, F_4\left(1 + \Delta T_{sf}\right) - \Delta T_{sf}\right] & -1 < \Delta T_{sf} < 0.0 \\ \max\left(0.0, F_4\right) & \Delta T_{sf} \ge 0.0 \end{cases} \tag{5.7}$$

$$F_4 = \min\left[10^{-5}, \alpha_g\left(1 - X_n\right)\right]\left(10^5\right) \tag{5.8}$$

Since the liquid coolant is at a higher temperature than saturation, the bubbles will grow as the liquid changes phase. When the heat transfer coefficient is known, the rate of increase

in bubble volume ($\dot{V}$) can be computed, as well as the mass transfer to the bubble field ($\Gamma_{i,Bub}$), and the heat flux across the bubble/liquid interface ($q_{i,SB}$).

Bubbly Subcooled Liquid Bubbly subcooled liquid is a condition where the liquid temperature is less than the saturation temperature. In this case, the bubbles will shrink as the vapor within the bubble cools and condenses from contact with the liquid. The heat transfer across the bubble interfaces for the six-field governing equation solution is computed using a modified correlation by Unal and Lahey [46, 45, 120] represented in Equation 5.9.

$$H_{if} = \frac{F_3 F_5 h_{fg} \rho_g \rho_f \alpha_{bub}}{\rho_f - \rho_g} \tag{5.9}$$

where F_3 is the same as was used for bubbly superheated liquid, and the following additional terms are needed:

$$F_5 = \begin{cases} 0.075 \frac{1}{Ks} & \alpha_{bub} \geq 0.25 \\ 1.8 \phi C \exp\left(-45 \alpha_{bub}\right) + 0.075 \frac{1}{Ks} & \alpha_{bub} < 0.25 \end{cases} \tag{5.10}$$

$$C = \begin{cases} 65.0 - 5.69 \times 10^{-5} \left(P - 1.0 \times 10^5\right) \frac{1}{Ks} & P \leq \text{1.1272E6 Pa} \\ \frac{2.5 \times 10^9}{P^{1.418}} \frac{1}{Ks} & P > \text{1.1272E6 Pa} \end{cases} \tag{5.11}$$

$$\phi = \begin{cases} 1.0 & |v_f| \leq 0.61 \text{ m/s} \\ \left(1.639344 |v_f|\right)^{0.47} & |v_f| > 0.61 \text{ m/s} \end{cases} \tag{5.12}$$

When the flow regime includes large or small bubble fields, the Sauter mean diameter of each bubble field can be used to compute the interfacial area concentration and the heat flux across the interface between the vapor of the bubble and the continuous liquid field.

Bubbly Superheated Vapor/Gas or Subcooled Vapor/Gas Bubbly superheated vapor is a condition where the vapor within the bubbles is at a temperature greater than the saturation temperature. Bubbly flow with subcooled vapor is the opposite, where the vapor temperature is below the saturation temperature. Both these conditions are relatively unstable.

The two-phase mixture is more stable when the vapor is at saturated conditions. To limit the instability, a large (in magnitude) interfacial heat transfer coefficient is selected for bubbly superheated vapor or subcooled vapor conditions in order to drive the vapor temperature to saturation. The large assumed heat transfer coefficient can be used to compute the interfacial heat flux for either the large or small bubble field. Equation 5.13 is used for these conditions.

$$H_{ig} = h_{ig} F_6 F_7 a_{gf} \tag{5.13}$$

where

$$h_{ig} = 10^4 \ {}^{W}/_{m^2 K} \tag{5.14}$$

$$F_6 = [1 + \eta\,(100 + 25\eta)] \tag{5.15}$$

$$\eta = |\max\,(-2, \Delta T_{sg})| \tag{5.16}$$

$$\Delta T_{sg} = T^{sat} - T_g \tag{5.17}$$

$$F_7 = \frac{\max\,(\alpha_g, 10^{-5})}{\max\,(\alpha_g, 10^{-9})} \tag{5.18}$$

Slug Flow

Slug flows consist primarily of large Taylor bubbles interspersed with liquid slugs. Smaller bubbles are sometimes included within the liquid slug. The addition of two bubble fields

makes it possible to define these bubbles separately for purposes of heat transfer. The interfacial heat transfer for slug flow consists of the heat transferred between the large Taylor bubbles and the surrounding liquid and the heat transfer between the small bubbles and the liquid.

System codes that are limited to two fields are forced to sum these two heat transfer effects to obtain the total heat transfer between the liquid and the vapor fields. With the additional fields included in the more detailed governing equations (Chapter 3 and [106]), the components of the heat transfer can be separated. The Taylor bubbles are included as part of the "large" bubble field, and the other bubbles will be considered "small". The separation between large and small bubble fields for slug flow may vary from that used in the bubbly flow regime described in Section 5.1.1. The actual separation between large and small bubble fields may be determined based on flow conditions [119].

Slug Superheated Liquid This condition is similar to that of bubbly superheated liquid. The temperature of the water exceeds the saturation temperature, and thus the water will be transitioning to vapor until the system reaches equilibrium. Consequently, the model implemented by Equation 5.19 simply assigns a large value to the interfacial heat transfer coefficient between the Taylor bubbles and the liquid coolant.

$$H_{if,Tb} = 3.0 \times 10^6 \, (W/m^2K) \, a_{gf,Tb} \alpha_{Tb} \tag{5.19}$$

where the volumetric interfacial area ($a_{gf,Tb}$) for a Taylor bubble is [2]:

$$a_{gf,Tb} = \frac{4.5}{D} 2.0 \tag{5.20}$$

The Taylor bubble void fraction (α_{Tb}) is simply the void fraction of the "large" bubble field, which is calculated as part of the solution to the six-field governing equations. The Sauter mean diameter for the large bubble field can be used in the calculation of the area of

the Taylor bubbles shown in Equation 5.20. Once these values are known, the heat transfer coefficient can be computed, and the rate of increase in bubble volume and the heat flux across the bubble/liquid interface can also be found.

The small bubbles that may be present between the large Taylor bubbles utilize the heat transfer calculations for bubbly superheated liquid (Section 5.1.1), though in a modified form to reduce the contribution of the bubbly heat transfer to the total heat transfer within the volume. The parameters that are modified are shown below:

$$F_9 = \exp\left[-8\left(\frac{\alpha_g - \alpha_{BS}}{\alpha_{SA} - \alpha_{BS}}\right)\right] \tag{5.21}$$

$$v_{fg} = (v_g - v_f)\, F_9^2 \tag{5.22}$$

$$\beta = F_9 \tag{5.23}$$

Slug Subcooled Liquid Slug subcooled liquid is slug flow with liquid temperature below the saturation temperature. The selected closure relationship uses a volumetric heat transfer coefficient for the Taylor bubbles in subcooled flow that is dependent on the Reynolds and Prandtl numbers. The correlation has been adjusted to use coefficients that are between the values typically used for laminar and turbulent flows. This model was selected since the flow passing the Taylor bubble is relatively thin and will most likely not be fully laminar, but also will not have the full set of turbulent effects. Equation 5.24 shows the relationship for heat transfer to and from the Taylor bubbles in subcooled liquid flow.

$$H_{if,Tb} = 1.18942 Re_f^{0.5} Pr_f^{0.5} \frac{k}{D} a_{gf,Tb} \alpha Tb \tag{5.24}$$

where

$$Pr_f = \frac{C_{pf}\mu_f}{k_f} \tag{5.25}$$

$$Re_f = \frac{\rho_f D \times \min\left(|v_f - v_g|, 0.8\text{m/s}\right)}{\mu_f} \tag{5.26}$$

The small bubbles present between the large Taylor bubbles use the same models as for bubbly subcooled liquid (Section 5.1.1).

Slug Superheated Vapor The heat transfer between the Taylor bubbles and the liquid coolant comes from a modified form of the Lee-Ryley equation [48] that was used for the bubbly flow. The coefficients for this implementation have been increased from the original version, and the dependence on the Prandtl number has been removed as shown in 5.27. The Lee-Ryley equation was developed for laminar flow heat transfer to a sphere, suggesting that this model may not be perfectly suited for Taylor bubbles, which are not necessarily spherical in shape. However, given the limitations of the six-field model for determining the correct geometry of a Taylor bubble, it is a necessary approximation [2].

$$H_{ig,Tb} = \left(2.2 + 0.82 Re_g^{0.5}\right) \frac{k_g}{D} a_{gf,Tb} \alpha_{Tb} \tag{5.27}$$

where

$$Re_g = \frac{\rho_g |v_f - v_g| D}{\mu_g} \tag{5.28}$$

The heat transfer for the small bubbles is computed as:

$$H_{ig,bub} = h_{ig} F_6 \alpha_{bub} a_{gf,bub} \tag{5.29}$$

Where h_{ig} and F_6 are the same as the bubbly superheated vapor flow regime (see Equation 5.13).

Slug Subcooled Vapor The subcooled vapor heat transfer for the Taylor bubbles is set to a large value to bring the temperatures of the vapor and the coolant back to equilibrium

at the saturation value, as shown below:

$$H_{ig,Tb} = h_{ig} F_6 \alpha_{Tb} a_{gf,Tb} \tag{5.30}$$

Where h_{ig} is $10^4 W/m^2 K$, and F_6 is the same as for bubbly superheated vapor in Equation 5.15.

The same equations are used for the small bubbles, though the interfacial area will be different for the small bubbles than for the large bubbles.

Annular Mist

Annular mist flow consists of a liquid film in contact with the inside of the pipe and droplets in the vapor core flowing within the center of the pipe. We will treat the annulus as the "continuous liquid" field, and the droplets will become the "small" and "large" droplet fields. As with the bubble fields, the same correlations can be used for both "small" and "large" droplets, but the interfacial areas will be different, and the two fields will be kept separate within the calculation.

This section will focus on the heat transfer between the two droplet fields, the annulus, and the vapor field. The energy governing equations have terms for both heat transfer between the droplets and the vapor, as well as the energy that is lost from one droplet field to the other as droplets break up or coalesce. These energy exchanges can be modeled by the source terms that have been calculated as part of the mass governing equations [119] and the enthalpy of the liquid.

For simplicity, the heat transfer when the annulus and both droplet fields are at the same temperature (superheated, subcooled, etc.) will be discussed in the following sections. In practice, the temperatures in these three fields may be different, and the droplets may actually be experiencing a different temperature condition than the annulus. The six-field model will track the temperatures of the three fields independently, and the models discussed

in the following sections will be applied to the fields depending on the condition (superheated or subcooled) as appropriate.

Annular Mist Superheated Liquid The heat transfer between the annulus (the continuous liquid field in the six-field formulation) and the vapor core uses a large value for the heat transfer that serves to bring the temperatures back to saturation quickly. This heat transfer coefficient is $3.0 \times 10^6 \frac{W}{Km^2}$, which can be seen in Equation 5.31. This large heat transfer coefficient is multiplied by a factor that reduces the heat transfer coefficient as the flow regime nears a slower, stratified flow condition [2].

$$H_{if,ann} = 3.0 \times 10^6 a_{gf,ann} F_{10} \tag{5.31}$$

where

$$F_{10} = \min\left(1.0 + |\lambda|^{1/2} + 0.05|\lambda|, 6\right) \tag{5.32}$$

$$\lambda = \begin{cases} \frac{v_g}{v_{crit}} & \text{horizontal flow} \\ \frac{\alpha_g v_g}{v_{crit}} & \text{vertical flow} \end{cases} \tag{5.33}$$

$$v_g = \max\left(|v_g - v_f|, 10^{-15}\text{m/s}\right) \tag{5.34}$$

$$v_{crit} = \begin{cases} \max \left\{ \begin{array}{c} 0.5 \left[\frac{\left(\rho_f - \rho_g\right) g \alpha_g A_{pipe}}{\rho_g D \sin\theta} \right]^{1/2} (1 - \cos\theta), \\ |v_g - v_f| 10^{-15}, \\ 10^{-30} \text{m/s} \end{array} \right\} & \text{horiz.} \\ 3.2 \frac{\left[\sigma g \left(\rho_f - \rho_g\right)\right]^{1/4}}{\rho_g^{1/2}} & \text{vert.} \end{cases} \tag{5.35}$$

$$\sigma = \max\left(\sigma, 10^{-7} \text{N/m}\right) \tag{5.36}$$

The interfacial area of the annulus is computed using the same equations developed for the mass conservation equations [119], which relied on a knowledge of the size of the pipe and the volume of liquid in the annulus itself.

The heat transfer to the superheated droplets is based on the thermal conductivity of the liquid in the droplet, the droplet diameter, the droplet area concentration, and a scaling factor that grows quadratically as the liquid temperature increases above the saturation temperature. This helps to drive the superheated liquid to saturation temperatures. The same model is used for both large and small droplet fields and is shown below.

$$H_{if,drp} = \frac{k_f}{d_d} F_{12} F_{13} a_{gf,drp} \tag{5.37}$$

where

$$F_{13} = 2.0 + 7.0 \times \min\left[1.0 + \frac{C_{pf} \max\left(0, \Delta T_{sf}\right)}{h_{fg}}, 8.0\right] \tag{5.38}$$

$$F_{12} = 1 + \xi\left(250 + 50\xi\right) \tag{5.39}$$

$$\xi = \max\left(0, -\Delta T_{sf}\right) \tag{5.40}$$

Annular Mist Subcooled Liquid The heat transfer for a subcooled annulus to the vapor is modeled by a modified Theofanous equation [50] shown in Equation 5.41 that uses the same factor ($F10$) from Equation 5.32 to reduce the heat transfer as the flow regime transitions to stratified flow.

$$H_{if,ann} = 10^{-3}\rho_f C_{pf}|v_f|a_{gf,ann}F_{10} \tag{5.41}$$

The heat transfer between the vapor and entrained droplets is computed by a modified Brown correlation [49] shown as Equation 5.42 that is very similar to that used for the superheated droplets.

$$H_{if,drp} = \frac{k_f}{d_d}F_{13}a_{gf,drp} \tag{5.42}$$

where $a_{gf,drp}$, F_{13}, and d_d are the same as annular mist superheated liquid (see Equation 5.37).

Annular Mist Superheated Vapor/Gas The heat transfer between the vapor and the annular film for the superheated vapor condition is based on the Dittus-Boelter correlation.

$$H_{ig,ann} = \frac{k_g}{D}0.023Re_g^{0.8}a_{gf,ann}F_{10} \tag{5.43}$$

where F_{10} (Equation 5.32) is the same as annular mist with superheated liquid.

The heat transfer to the droplets is derived from the Lee and Ryley correlation, with the Reynolds number coefficient changed from 0.74 to 0.5 [2] as shown in Equation 5.44.

$$H_{ig,drp} = \frac{k_g}{d_d}\left(2.0 + 0.5Re_d^{0.5}\right)a_{gf,drp} \tag{5.44}$$

where

$$Re_d = \frac{\alpha_{droplet}^{2.5} \rho_g \hat{v}_{fg} d_d}{\mu_g} \tag{5.45}$$

Annular Mist Subcooled Vapor/Gas The heat transfer to the annular film uses terms from the bubbly superheated vapor and the annular mist superheated liquid heat transfer correlations (5.46).

$$H_{ig,ann} = h_{ig} a_{gf,ann} F_{10} F_6 \tag{5.46}$$

where h_{ig} and F_6 are from bubbly superheated vapor and F_{10} comes from annular mist superheated liquid (Equation 5.32).

The droplet heat transfer is similar, and uses

$$H_{ig,drp} = h_{ig} a_{gf,drp} F_6 \tag{5.47}$$

where $a_{gf,drp}$ comes from annular mist superheated liquid/vapor (see Equation 5.37).

Inverted Annular

Inverted annular flows are vertical flows that consist of a large slug of water in the core of the flow field, with an annular region of vapor. The central slug of water is not in direct contact with the walls of the pipe. Bubbles may also exist within the central slug of liquid. The interfacial heat transfer for this regime will consist of the heat transfer between the vapor annulus and the central liquid slug, and the interaction between the bubbles and the liquid core. The liquid core and vapor annulus will be treated as the continuous liquid and the continuous vapor fields, respectively.

Inverted Annular Superheated Liquid The interaction between the bubbles and the liquid core is very similar to that for bubbly superheated liquid flow. The heat transfer is computed using Equation 5.1, with changes to the following terms:

$$v_{fg} = (v_g - v_f)\, F_{16}^2 \tag{5.48}$$

$$\beta = F_{16} \tag{5.49}$$

where

$$F_{16} = 1.0 - \exp\left[\frac{-8\,(\alpha_{BS} - \alpha_{IAN})}{\alpha_{BS}}\right] \min\left(\frac{\alpha_g}{0.05}, 0.999999\right) \tag{5.50}$$

$$\alpha_{IAN} = \begin{cases} \alpha_{ann} & \text{Void fraction in annulus for inverted annular regime} \\ \alpha_{BS} & \text{Void fraction limit for transition to inverted slug regime} \end{cases} \tag{5.51}$$

As has been done before, the heat transfer between the liquid core and the vapor annulus is computed using a large value for the heat transfer coefficient, as shown in Equation 5.52. The selection of a large value for the heat transfer coefficient brings the liquid and vapor into a more stable equilibrium quickly.

$$H_{if,ann} = 3 \times 10^6 a_{gf,ann} \tag{5.52}$$

where

$$a_{gf,ann} = \frac{4}{D} F_{15}\,(2.5) \tag{5.53}$$

and

$$F_{15} = (1 - \alpha_B)^{1/2} \tag{5.54}$$

Inverted Annular Subcooled Liquid The heat transfer between the bubbles and the liquid core is computed in the same manner described in Section 5.1.1.

The heat transfer between the liquid core and the vapor annulus is computed using another correlation (Equation 5.55) based on the Dittus-Boelter relationship.

$$H_{if,ann} = \frac{k_f}{D} 0.023 Re_{IAN}^{0.8} a_{gf,ann} F_3 \tag{5.55}$$

where

$$Re_{IAN} = \frac{(1.0 - \alpha_{IAN})\, \rho_f |v_f - v_g| D}{\mu_f} \tag{5.56}$$

where α_{IAN} is computed as in Equation 5.51 and F_3 is as was shown for bubbly superheated liquid (Equation 5.7)

Inverted Annular Superheated or Subcooled Vapor The heat transfer between the bubbles and the liquid core when the bubbles consist of superheated vapor is computed using a very similar equation shown as Equation 5.57 to that used for bubbly flow with superheated vapor described in Section 5.1.1.

$$H_{ig,bub} = h_{ig} F_6 a_{gf,bub} \tag{5.57}$$

where h_{ig} and F_6 come from the bubbly superheated vapor heat transfer calculation (Equations 5.13 and 5.15).

The heat transferred between the inner liquid core and the surrounding vapor annulus is

computed as:

$$H_{ig,ann} = \frac{k_g}{D} F_{19} a'_{gf,ann} \tag{5.58}$$

where:

$$F_{19} = 25 - \Delta T_{sg} \left(0.20 - 0.10 \Delta T_{sg}\right) \tag{5.59}$$

$$a'_{gf,ann} = \frac{a_{gf,ann}}{0.5 \max\left(1.0 - F_{15}, 0.04\right)} \tag{5.60}$$

and F_{15} (5.54) and $a_{gf,ann}$ (5.53) come from the calculations of inverted annular superheated liquid heat transfer.

Inverted Slug Flow

Inverted slug flow consists of large "droplets" or "slugs" of water in a vapor field. The large droplets of water can contain bubbles, though the bubbles will not be considered by the six-field model, since the governing equations were not developed for bubbles within a "droplet" field [106].

The large slugs of water will be part of the large droplet field for this regime, the remaining droplets will be considered part of the small droplet field, and the vapor will be considered the continuous vapor field.

Inverted Slug Superheated Liquid The heat transfer from the liquid "slugs" to the vapor annulus similar to the calculations for the annular mist superheated liquid regime and is shown here in Equation 5.61. In this flow regime, the slugs are modeled as very large droplets, and make up part of the large droplet field.

$$H_{if,ann} = \frac{k_f}{D} F_{12} F_{13} a_{gf,ann} \tag{5.61}$$

where F_{13} is computed as it was for annular mist superheated liquid in Equation 5.38 and F_{12} is computed in Equation 5.39 and D is the pipe diameter.

The heat transfer between the droplets and the vapor field is very similar to that for the liquid "slug" model and is also intended to drive the liquid temperature to saturation. This is due to the instability of two-phase conditions with superheated liquid.

The only differences between the equations are the effective diameters and the interfacial area concentrations, which may be computed from the geometry determined by the solution of the six-field mass equations. The heat transfer is modeled as shown in the equation below.

$$H_{if,drp} = \frac{k_f}{d_d} F_{12} F_{13} a_{gf,drp} \tag{5.62}$$

where d_d is the characteristic (small) droplet diameter and F_{12} and F_{13} are computed as in Equations 5.39 and 5.38.

Inverted Slug Subcooled Liquid The interfacial heat transfer for the large slugs of water and the small droplets in subcooled liquid flows is very similar to the superheated liquid condition. The F_{12} term is omitted, but the remaining terms are the same. The heat transfer between the vapor and the large slugs is:

$$H_{if,ann} = \frac{k_f}{D} F_{13} a_{gf,ann} \tag{5.63}$$

and to the small droplets:

$$H_{if,drp} = \frac{k_f}{d_d} F_{13} a_{gf,drp} \tag{5.64}$$

Inverted Slug Superheated or Subcooled Vapor/Gas The heat transfer correlation selected to model the exchange between the liquid slugs and the vapor for a superheated

vapor condition is shown as Equation 5.65.

$$H_{ig,ann} = \frac{k_g}{D}\frac{F_{19}}{F_{22}}a_{gf,ann} \tag{5.65}$$

where F_{19} is the same as what was used for inverted annular superheated vapor and

$$F_{22} = \max\left\{0.02, \min\left[\frac{\alpha_g}{4}\left(1-\frac{\alpha_g}{4}\right), 0.2\right]\right\} \tag{5.66}$$

The interactions between the vapor and the droplets are modeled using a modified version of Lee-Ryley [48, 2] which is shown below.

$$H_{ig,drp} = \frac{k_g}{d_d}\left(2.0 + 0.5Re_{drp}^{0.5}\right)a_{gf,drp} \tag{5.67}$$

where

$$Re_{drp} = \frac{\rho_g v_{fg} d_d}{\mu_g} \tag{5.68}$$

Dispersed Flow

Dispersed flow has droplets or mist in a vapor field. Large and small droplet fields will both be present for this flow regime. Recall that inverted slug flow also uses large droplets. The selection of the heat transfer correlation to use is dependent upon the flow regime. If the system code determines that the flow regime is dispersed flow, then those heat transfer correlations will be used for the "large" droplets in the flow field. If the flow regime is inverted slug, then those correlations will be used. This prevents discontinuities and instabilities from developing in the code solution.

In the dispersed flow regime model, the droplets will be considered to be spherical in shape. The heat transfer is modeled between the droplets and the vapor phase, and will differ for the large and small droplet fields only in the interfacial area and relative velocities.

Dispersed Superheated Liquid The interaction between the vapor and the droplets for superheated liquid is modeled using an expression (5.69) that increases quadratically as $|\Delta T_{sf}|$ increases.

$$H_{if} = \frac{k_f}{d_d} F_{12} F_{13} F_{23} a_{gf} \tag{5.69}$$

Note that F_{12} and F_{13} are the same as for annular mist superheated liquid (see Equations 5.39 and 5.38). F_{12} serves to increase the heat transfer as the liquid temperature diverges from the saturation temperature. The addition of the F_{23} term aids in numerical stability for high void fraction flows.

$$F_{23} = \begin{cases} \frac{\alpha_{drp}}{\max\left(\alpha_f, 10^{-10}\right)} & \text{for pre-CHF} \\ \frac{\alpha_{drp}}{\max\left(\alpha_f, 10^{-12}\right)} & \text{for post-CHF} \end{cases} \tag{5.70}$$

where α_{drp} is the volume fraction of the droplet field being considered. Note that the various diameters and thermal conductivities are field-dependent for this model. Although the large and small droplet fields will use the same equation for heat transfer calculations, they will use field-specific information, such as droplet diameters and thermal conductivities.

Dispersed Subcooled Liquid The subcooled liquid dispersed flow is more stable than the superheated liquid condition, so the F_{12} term, which helps to drive the liquid temperature to saturation, is not necessary. Removing the F_{12} term produces an equation (5.71) for heat transfer to and from subcooled liquid droplets.

$$H_{if} = \frac{k_f}{d_d} F_{13} F_{23} a_{gf} \tag{5.71}$$

where F_{13} and F_{23} are computed as shown in Equations 5.38 and 5.70. This model is based on that of Brown [49], which was also used for annular mist subcooled liquid.

Dispersed Superheated Vapor/Gas The Lee-Ryley model is again modified for use as a heat transfer correlation for dispersed flow with superheated vapor. The dependence on the Prandtl number is eliminated and coefficient on the Reynolds number has been modified as shown in Equation 5.72.

$$H_{ig} = \frac{k_g}{d_d}\left(2.0 + 0.5Re_{drp}^{0.5}\right)F_{24}a_{gf} \tag{5.72}$$

where the droplet Reynolds number (Re_{drp}) is dependent on the vapor conditions and the relative velocity between the droplet field and the vapor field.

$$Re_{drp} = \frac{\left(1-\alpha_{drp}\right)^{2.5}\rho_g v_{fg} d_d}{\mu_g} \tag{5.73}$$

$$F_{24} = \max\left[0.0, F_{26}\left(F_{25}-1\right)+1\right] \tag{5.74}$$

$$F_{25} = 10^5 \min\left(\alpha_f, 10^{-5}\right) \tag{5.75}$$

$$F_{26} = 1.0 - 5.0 \times \min\left[0.2, \max\left(0.0, \Delta T_{sg}\right)\right] \tag{5.76}$$

Dispersed Subcooled Vapor/Gas The heat transfer for dispersed subcooled vapor is selected to push the vapor temperature back to saturation temperature. As such, the Nusselt number has been selected to be large. This is shown in Equation 5.77.

$$H_{ig} = h_{ig}F_6F_{24}a_{gf} \tag{5.77}$$

where h_{ig} and F_6 are both from the bubbly superheated vapor heat transfer calculation in Section 5.1.1 and F_{24} is computed as in Equation 5.74.

5.1.2 Wall to Fluid Energy Transfer

To model heat transfer from the wall to the coolant requires consideration of the flow regime (single-phase liquid, bubbly, slug, etc.) *and* the geometry of the flow path. Heat transfer

to coolant flowing between the surfaces of parallel plates will be different from heat transfer from the surfaces of rods in a bundle or the inside of a heated tube. As with interfacial heat transfer, there are some terms in the energy balance equations that are related to wall heat transfer. These terms are listed below.

- Heat flux from the wall to the continuous liquid or vapor ($q_{w,k}$)
- Area concentration at wall (a_w)
- Vapor generation at the wall for each bubble field (Γ)

The "solid" parts of the model (pipe walls, plates, heated rods) in a system code are often modeled by a separate component that can model heat conduction as well as heat generation. These components also define the geometry of the surface. Models are often included in system codes that represent the heat transfer between the coolant and each of these geometries. Selection of a particular geometry (e.g. heated rod bundle with parallel flow) is, in effect, selecting a set of heat transfer correlations.

The previous sections described the calculation of interfacial heat transfer coefficients to close the energy balance equations. In addition to heat transfer coefficients at the wall, balancing the energy equations also requires information about the rate of bubble generation at the wall. Vapor generation will occur at the wall surface whenever the liquid temperature at the surface exceeds saturation. In order for the generated vapor to remain in the coolant, the bulk liquid temperature must be approximately the saturation temperature.

Heat transfer to the coolant is dependent on geometry of the heated surface. The principle geometries considered here are:

- Pipe Geometry
- Parallel Plates
- Bundle with in-line Rods and parallel flow

The wall heat transfer will be primarily to the continuous vapor or continuous liquid fields. Thus, the existing models in two-field system codes will be sufficient to compute the heat transfer from the walls to the coolant and provide the heat transfer rate information to the governing equations.

However, additional closure models are still needed for the solution to the energy balance equations. The vapor that is generated within the liquid at the heated surface will form into bubbles. Depending on the coolant flow rate and the rate of heat transfer, the bubbles will vary in size. The size of the generated bubbles must be included in the closure models so that they can be added to the correct field - large or small bubbles.

This section will describe the models for vapor generation and bubble size at time of wall separation (bubble lift-off size). Once the bubbles have entered the bulk coolant flow, they will be modeled as part of the appropriate bubble field and the interfacial heat transfer previously discussed will take over.

Vertical Flows

The rate of vapor generation and the velocity of the coolant flow are the two significant factors that affect bubble size in convective flow. For low vapor generation rates, the bubble regime can be considered "laminar". In laminar regimes, the size of the generated bubbles is relatively constant, and does not depend heavily on flow rate. The bubbles rise at the same rate, and the bubble departure frequency increases with increasing vapor generation rate [121].

A "turbulent" regime results from increased vapor generation rates, and is characterized by larger bubble diameters and a potential for bubble interactions with the preceding bubble. The departure diameter of the bubbles increases as the vapor generation rate increases. In spite of this, the bubble departure frequency remains constant with respect to vapor generation rate. Bubble sizes are not uniform in the turbulent regime. Subcooled boiling conditions generally produce laminar or turbulent bubble regimes [121].

The lift-off diameter for bubbles in vertical flows can be calculated:

$$D_{lo,vert} = \frac{v_f}{u_r\sqrt{C_1}} \frac{4\sqrt{22/3}b^2}{\pi} \frac{Ja_e^2}{Pr_f} \tag{5.78}$$

where

$$C_1 = 3.877G_s^{1/2}\left(Re_b^{-2} + 0.014G_s^2\right)^{1/4} \tag{5.79}$$

$$G_s = \left|\frac{du_r}{dx}\right| \frac{r_b}{u_r} \tag{5.80}$$

$$Re_b = \frac{2r_b u_r}{v_r} \tag{5.81}$$

$$Ja_e = \frac{\rho_f C_{pf} \Delta T_e}{\rho_g i_{fg}} \tag{5.82}$$

$$\Delta T_e = S\left(T_w - T_{sat}\right) \tag{5.83}$$

$$Pr_f = \frac{C_{pf}\mu}{k} \tag{5.84}$$

$$r_b = \frac{2b}{\sqrt{\pi}} Ja\sqrt{\alpha_{diff,f}t} \tag{5.85}$$

$$Ja = \frac{\rho_f C_{pf}\left(T_w - T_{sat}\right)}{\rho_g i_{fg}} \alpha_{diff,f} = \frac{k_f}{\rho_f c_p} b = 1.73 \text{ (Empirical constant)} \tag{5.86}$$

In this model, the rate of bubble generation is not dependent directly on the heat flux or the heat transfer coefficient, but is dependent on the wall superheat. This assumes that the boundary layer adjacent to the wall is at the wall temperature. The bubble Reynolds number (Re_b) introduces the fluid velocity into the model. Therefore, this model includes both factors that significantly affect the bubble size.

The diameter of the generated bubbles is used to categorize the generated bubble as part of the large or small droplet field.

Horizontal Flows

The size of bubbles in convective horizontal flows are also affected by the vapor generation rate and the flow rate. The model for bubble size at departure must be adapted to account for the change in orientation [122].

The horizontal model is similar to models used for pool boiling, but the forces from the convective flows are included. The lift-off diameter can be computed by computing the buoyancy and growth forces. These forces must balance at bubble lift-off:

$$F_b + F_{du} = 0 \tag{5.87}$$

Where the buoyancy force is:

$$F_b = \frac{4}{3}\pi r_b^3 \left(\rho_l - \rho_v\right) g \tag{5.88}$$

The growth force is:

$$F_{du} = -\rho_l \pi r_b^2 \left(\frac{3}{2} C_s \dot{r}_b^2 + a\ddot{r}_b\right) \tag{5.89}$$

where C_s is an empirical constant that was originally used in pool boiling. The same value is used for convective boiling as for pool boiling, thus $C_s = {}^{20}/_{3}$. The overdot ($\dot{}$) indicates differentiation with respect to time.

Substituting the above terms into equation 5.87:

$$\frac{4}{3}\pi r_b^3 \left(\rho_l - \rho_v\right) = \rho_l \pi r_b^2 \left(\frac{3}{2} C_s \dot{r}_b^2 + a\ddot{r}_b\right) \tag{5.90}$$

The bubble radius (r_b) is computed using the vertical flow equation (5.85). Equation 5.90 can be rearranged and solved for the bubble diameter at lift off by using Equation 5.85.

The resulting lift off diameter is:

$$D_{lo,hrz} = 2\left[\frac{12\rho_l\left(\frac{3}{2}C_s+1\right)}{\left(\rho_l-\rho_v\right)g}\right]^{1/3}\left(\frac{\alpha_{diff,f}}{\pi}\right)^{2/3}\left(Ja\cdot b\right)^{4/3} \tag{5.91}$$

5.2 Momentum Conservation Equation Closure

The momentum balance equations for six fields are documented in Chapter 3 and are shown in expanded form (including the virtual mass terms) here. The momentum balance equation for the continuous liquid field is Equation 5.92.

$$\begin{aligned}
\alpha_f\rho_f A\frac{\partial\vec{v}_f}{\partial t}+\frac{1}{2}\alpha_f\rho_f A\nabla\vec{v}_f^{\,2} = -\alpha_f A\nabla p+\alpha_f\rho_f\vec{g}A- \\
\left(\alpha_f\rho_f A\right)FWF\cdot v_f+\Gamma_L A\left(v_{i,L}-v_L\right)+\Gamma_{LB}A\left(v_{i,LB}-v_L\right)+ \\
\Gamma_{SBu}A\left(v_{i,SBu}-v_L\right)-\left(\alpha_f\rho_f A\right)FIF_L\cdot\left(v_L-v_g\right)- \\
\left(\alpha_f\rho_f A\right)FIF_{LB}\cdot\left(v_L-v_{LB}\right)-\left(\alpha_f\rho_f A\right)FIF_{SBu}\cdot\left(v_L-v_{SBu}\right)- \\
C\alpha_f\alpha_g\rho_m A\left[\frac{\partial(v_L-v_g)}{\partial t}+v_g\nabla\vec{v}_L-v_L\nabla\vec{v}_g\right]- \\
C\alpha_f\alpha_g\rho_m A\left[\frac{\partial(v_L-v_{LB})}{\partial t}+v_{LB}\nabla\vec{v}_L-v_L\nabla\vec{v}_{LB}\right]- \\
C\alpha_f\alpha_g\rho_m A\left[\frac{\partial(v_L-v_{SBu})}{\partial t}+v_{SBu}\nabla\vec{v}_L-v_L\nabla\vec{v}_{SBu}\right]- \\
S'''_{LD,E}v_{LD}-S'''_{SD,E}v_{SD}+S'''_{SD,DE}v_{SD}+S'''_{LD,DE}v_{LD}
\end{aligned} \tag{5.92}$$

Equation 5.93 is the momentum conservation equation for small droplets. Equation 5.94

is for large droplets.

$$\begin{aligned}\alpha_{SD}\rho_f A\frac{\partial \vec{v}_{SD}}{\partial t}+\frac{1}{2}\alpha_{SD}\rho_f A\nabla\vec{v}_{SD}^2=-\alpha_{SD}A\nabla p+\alpha_{SD}\rho_f\vec{g}A+\\ \Gamma_{SD}A\left(\vec{v}_{i,SD}-\vec{v}_{SD}\right)-\left(\alpha_{SD}\rho_f A\right)FIF_{SB}\cdot\left(v_{SD}-v_g\right)-\\ C\alpha_{SD}\alpha_g\rho_m A\left[\frac{\partial(v_{SD}-v_g)}{\partial t}+v_g\nabla\vec{v}_{SD}-v_{SD}\nabla\vec{v}_g\right]-\\ S_{SD,E}^{'''}v_{SD}+S_{LD,SB}^{'''}v_{LD}+S_{LD,FB}^{'''}v_{LD}-\\ S_{SD,DE}^{'''}v_{SD}-S_{SD,C}^{'''}v_{SD}\end{aligned}\tag{5.93}$$

$$\begin{aligned}\alpha_{LD}\rho_f A\frac{\partial \vec{v}_{LD}}{\partial t}+\frac{1}{2}\alpha_{LD}\rho_f A\nabla\vec{v}_{LD}^2=-\alpha_{LD}A\nabla p+\alpha_{LD}\rho_f\vec{g}A+\\ \Gamma_{LD}A\left(\vec{v}_{i,LD}-\vec{v}_{LD}\right)-\left(\alpha_{LD}\rho_f A\right)FIF_{LB}\cdot\left(v_{LD}-v_g\right)-\\ C\alpha_{LD}\alpha_g\rho_m A\left[\frac{\partial(v_{LD}-v_g)}{\partial t}+v_g\nabla\vec{v}_{LD}-v_{LD}\nabla\vec{v}_g\right]+\\ S_{LD,E}^{'''}v_{LD}-S_{LD,SB}^{'''}v_{LD}-S_{LD,FB}^{'''}v_{LD}-S_{LD,DE}^{'''}v_{LD}+S_{SD,C}^{'''}v_{SD}\end{aligned}\tag{5.94}$$

The momentum balance for the continuous vapor field is in Equation 5.95.

$$\begin{aligned}\alpha_g\rho_g A\frac{\partial \vec{v}_g}{\partial t}+\frac{1}{2}\alpha_g\rho_g A\nabla\vec{v}_g^2=-\alpha_g A\nabla p+\alpha_g\rho_g\vec{g}A-\\ \left(\alpha_g\rho_g A\right)FWF\cdot v_g+\Gamma_g A\left(v_{i,g}-v_g\right)+\Gamma_{LD}A\left(v_{i,LD}-v_g\right)+\\ \Gamma_{SD}A\left(v_{i,SD}-v_g\right)-\left(\alpha_g\rho_g A\right)FIF_g\cdot\left(v_g-v_f\right)-\\ \left(\alpha_g\rho_g A\right)FIF_{LD}\cdot\left(v_g-v_{LD}\right)-\left(\alpha_g\rho_g A\right)FIF_{SD}\cdot\left(v_g-v_{SD}\right)-\\ C\alpha_f\alpha_g\rho_m A\left[\frac{\partial(v_g-v_L)}{\partial t}+v_L\nabla\vec{v}_g-v_g\nabla\vec{v}_L\right]-\\ C\alpha_f\alpha_g\rho_m A\left[\frac{\partial(v_g-v_{LD})}{\partial t}+v_{LD}\nabla\vec{v}_g-v_g\nabla\vec{v}_{LD}\right]-\\ C\alpha_f\alpha_g\rho_m A\left[\frac{\partial(v_g-v_{SD})}{\partial t}+v_{SD}\nabla\vec{v}_g-v_g\nabla\vec{v}_{SD}\right]-\\ S_{LB,E}^{'''}v_{LB}-S_{SBu,E}^{'''}v_{SBu}+S_{SBu,DE}^{'''}v_{SBu}+S_{LBu,DE}^{'''}v_{LB}\end{aligned}\tag{5.95}$$

Equation 5.96 is the momentum conservation equation for small bubbles. Equation 5.97

is for large bubbles.

$$\begin{aligned}\alpha_{SB}\rho_g A\frac{\partial \vec{v}_{SB}}{\partial t}+\frac{1}{2}\alpha_{SB}\rho_g A\nabla\vec{v}_{SB}^{2}=-\alpha_{SB}A\nabla p+\alpha_{SB}\rho_g\vec{g}A+\\ \Gamma_{SB}A\left(\vec{v}_{i,SB}-\vec{v}_{SB}\right)-\left(\alpha_{SB}\rho_g A\right)FIF_{SB}\cdot\left(v_{SB}-v_L\right)-\\ C\alpha_{SB}\alpha_{SB}\rho_m A\left[\frac{\partial(v_{SB}-v_L)}{\partial t}+v_L\nabla\vec{v}_{SB}-v_{SB}\nabla\vec{v}_L\right]+\\ S_{SB,E}^{'''}v_{SBu}+S_{LB,SB}^{'''}v_{LB}+S_{LB,FB}^{'''}v_{LB}-\\ S_{SB,DE}^{'''}v_{SBu}-S_{SB,C}^{'''}v_{SBu}\end{aligned} \tag{5.96}$$

$$\begin{aligned}\alpha_{LB}\rho_g A\frac{\partial \vec{v}_{LB}}{\partial t}+\frac{1}{2}\alpha_{LB}\rho_g A\nabla\vec{v}_{LB}^{2}=-\alpha_{LB}A\nabla p+\alpha_{LB}\rho_g\vec{g}A+\\ \Gamma_{LB}A\left(\vec{v}_{i,LB}-\vec{v}_{LB}\right)-\left(\alpha_{LB}\rho_g A\right)FIF_{LB}\cdot\left(v_{LB}-v_L\right)-\\ C\alpha_{LB}\alpha_{LB}\rho_m A\left[\frac{\partial(v_{LB}-v_L)}{\partial t}+v_L\nabla\vec{v}_{LB}-v_{LB}\nabla\vec{v}_L\right]+\\ S_{LB,E}^{'''}v_{LB}-S_{LB,SB}^{'''}v_{LB}-S_{LB,FB}^{'''}v_{LB}-S_{LB,DE}^{'''}v_{LB}+S_{SB,C}^{'''}v_{SBu}\end{aligned} \tag{5.97}$$

The momentum balance equations rely on several of the closure relationships that have already been developed to compute the exchange of momentum due to the breakup of large droplets into small droplets, momentum transfer resulting from phase change, and other mass and energy transfer mechanisms.

In addition to the momentum that is transferred due to mass and energy exchanges, momentum can be transferred due to frictional drag of the coolant against the walls and at the phase interfaces between fields.

The additional terms in the momentum governing equations that are not solved for as part of another closure relationship or governing equation are the interfacial and wall drag terms (FIG, FWG, FIF, FWF). The following sections will outline the closure models that will produce these terms so that the governing equations may be solved.

5.2.1 Interfacial Drag

Two methods are used for the calculation of interfacial drag that will be useful in solving for the required terms. The method selected depends on flow regime and geometry. The first is the drift flux model, which is used for bubbly and slug flows that are oriented vertically. The second method is a drag coefficient model, which is used for all the "other" flow regimes.

Both methods require information about the geometry of the interface between the fields and the volume fraction of each field. Using this information, parameters are calculated that can be used to provide the interfacial frictional loss terms from the momentum balance equations.

The drift flux method has been developed for use in a six-field implementation. The model is summarized by the following equations:

$$F_i = C_i |v_R| v_R \tag{5.98}$$

$$C_i = \frac{\alpha_m \alpha_k^3 (\rho_f - \rho_g) g \sin(\phi_j)}{|v_{gj}| v_{gj}} \tag{5.99}$$

$$v_R = C_k v_k - C_0 v_m \tag{5.100}$$

$$C_k = \frac{1 - C_0 \alpha_k}{\alpha_m} \tag{5.101}$$

$$\tag{5.102}$$

Where the subscripts k and m indicate the two interacting fields, g is the gravitational acceleration, ϕ_j is the inclination angle of the junction, and v_{gj} is the vapor drift velocity. The vapor drift velocity and the profile slip distribution coefficient (C_0) are determined from the geometry and flow regime.

A drag coefficient model has been developed for six fields. It is represented by the

following equations:

$$F_i = C_i|v_R|v_R \tag{5.103}$$

$$C_i = \frac{1}{8}\rho_c S_F a_{gf} C_D \tag{5.104}$$

$$v_R = v_1 - v2 \tag{5.105}$$

$$\tag{5.106}$$

Where ρ_c is the density of the continuous phase (vapor for droplet flows, liquid for bubble flows), and C_D is the drag coefficient.

Both of these methods of drag computation require as input geometry- and flow-specific parameters. The detailed information that is available in the six-field model is valuable in these models. For instance, the average size of the droplets in the large droplet field is a known value in the six-field model, so statistical approximations are not necessary to calculate interfacial drag, as they are in system codes based on two fields, such as RELAP5-3D [2]. The following sections will outline how the drag relationships are to be computed for the various flow regimes that will be encountered in reactor system modeling.

Bubbly Flow

The six-field formulation has two fields representing large and small bubbles. As with the interfacial heat transfer, the bubbly flow field may consist of both large and small bubbles. The size determination is based on flow characteristics [119]. The correlations presented in this section can be used for both "small" and "large" bubbles, by use of a correct average diameter for each field.

Recall that for the bubbly flow regime, the orientation of the flow dictates which of the interfacial drag formulations will be used. Horizontal flows use the drag coefficient method, while vertical flows use the drift flux method. The drag coefficient method will be discussed first.

The drag coefficient is [32]:

$$C_D = \frac{24\left(1 + 0.1Re_p^{0.75}\right)}{Re_p} \tag{5.107}$$

where the particle Reynolds number is defined as:

$$Re_p = \frac{\rho_f |v_{SB} - v_f| d_o}{\mu_m} \tag{5.108}$$

where d_o is the average small bubble diameter, which can be obtained from the Sauter mean diameter of the small bubble field. The mixture viscosity (μ_m) is defined as:

$$\mu_m = \frac{\mu_f}{\alpha_f} \tag{5.109}$$

For vertical bubbly flows, the drift flux method is used. The distribution coefficient (C_0) is computed using the EPRI correlation [33]:

$$C_0 = \frac{L}{K_0 + (1 - K_0)\left(\alpha_{SB}\right)^r} \tag{5.110}$$

The terms in Equation 5.110 are:

$$L_n = \begin{cases} 1 - \exp\left(-\alpha_{SB} C_p\right) & \text{if } \alpha_{SB} C_p < 170 \\ 1 & \text{otherwise} \end{cases} \tag{5.111}$$

$$L_d = \begin{cases} 1 - \exp\left(-C_p\right) & \text{if } C_p < 170 \\ 1 & \text{otherwise} \end{cases} \tag{5.112}$$

$$L = \frac{L_n}{L_d} \tag{5.113}$$

$$C_p = \left| \frac{4 P_{crit}^2}{P\left(P_{crit} - P\right)} \right| \tag{5.114}$$

$$K_0 = B_1 + \left(1 - B_1\right) \left(\frac{\rho_g}{\rho_f}\right)^{1/4} \tag{5.115}$$

$$B_1 = \min\left(0.8, A_1\right) \tag{5.116}$$

$$A_1 = \frac{1}{1 + \exp\left\{\max\left[-85, \min\left(85, -\frac{Re}{60{,}000}\right)\right]\right\}} \tag{5.117}$$

$$Re = \begin{cases} Re_{SB} & \text{if } Re_{SB} > Re_f \text{ or } Re_{SB} < 0.0 \\ Re_f & \text{otherwise} \end{cases} \tag{5.118}$$

$$Re_f = \frac{\rho_f j_f D_h}{\mu_f} \tag{5.119}$$

$$Re_{SB} = \frac{\rho_g j_{SB} D_{SB}}{\mu_g} \tag{5.120}$$

$$j_f = \alpha_f v_f \tag{5.121}$$

$$j_{SB} = \alpha_{SB} v_{SB} \tag{5.122}$$

The vapor drift velocity is also needed to complete the drift flux method. The drift

velocity is defined in the EPRI correlation as:

$$v_{gj} = 1.41 \left[\frac{(\rho_f - \rho_g)\, \sigma g}{\rho_f^2} \right]^{1/4} C_1 C_2 C_3 C_4 \tag{5.123}$$

with the following definitions for the terms in Equation 5.123.

$$C_1 = \begin{cases} (1 - \alpha_{SB})^{B_1} & \text{if } Re_{SB} \geq 0 \\ (1 - \alpha_{SB})^{0.5} & \text{if } Re_{SB} < 0 \end{cases} \tag{5.124}$$

$$C_2 = \begin{cases} 1 & \text{if } \frac{\rho_f}{\rho_g} \geq 18,\ C_6 \geq 85 \\ \frac{1}{1 - \exp(-C_6)} & \text{if } \frac{\rho_f}{\rho_g} \geq 18,\ C_5 < 1,\ C_6 < 85 \\ 0.4757 \left\{ \ln \left[\max \left(1.00001, \frac{\rho_f}{\rho_g} \right) \right] \right\}^{0.7} & \text{if } \frac{\rho_f}{\rho_g} < 18 \end{cases} \tag{5.125}$$

$$C_5 = \left[150 \left(\frac{\rho_g}{\rho_f} \right) \right]^{1/2} \tag{5.126}$$

$$C_6 = \frac{C_5}{1 - C_5} \tag{5.127}$$

$$C_4 = \begin{cases} 1 & \text{if } C_7 \geq 1 \\ \frac{1}{1 - \exp(-C_8)} & \text{if } C_7 < 1 \end{cases} \tag{5.128}$$

$$C_7 = \left(\frac{D_2}{D} \right)^{0.6} \tag{5.129}$$

$$C_8 = \frac{C_7}{1 - C_7} \tag{5.130}$$

$$D_2 = 0.09144 \text{ m (normalizing diameter)} \tag{5.131}$$

The C_3 term listed in Equation 5.123 is dependent on the direction of the vapor and liquid

flow. If the flow is in an upward direction (both bubbles and liquid), C_3 is:

$$C_3 = \max\left[0.50, 2\exp\left(-\frac{|Re_f|}{300,000}\right)\right] \tag{5.132}$$

For the downflow condition (both bubbles and liquid), C_3 is:

$$C_3 = \min\left[10, 2\left(\frac{C_{10}}{2}\right)^{B_2}\right] \tag{5.133}$$

with additional terms:

$$B_2 = \frac{1}{\left(1 + 0.05\left|\frac{Re_f}{350,000}\right|\right)^{0.4}} \tag{5.134}$$

$$\begin{aligned} C_{10} = 2\exp\left[\left(\frac{|Re_f|}{350,000}\right)^{0.4}\right] - 1.7\,|Re_f|^{0.035} \times \\ \exp\left[\frac{-|Re_f|}{60,000}\left(\frac{D_1}{D}\right)^2\right] + 0.26\left(\frac{D_1}{D}\right)^{.1}|Re_f|^{0.001} \end{aligned} \tag{5.135}$$

$$D_1 = 0.0381 \text{ m (normalizing diameter)} \tag{5.136}$$

Slug Flow

Recall that slug flow consists of large Taylor bubbles in a liquid flow, possibly with smaller bubbles interspersed between the large ones. The Taylor bubbles in slug flow will be part of the large bubble field, while any small bubbles will be in the small bubble field. The large bubbles will use the drag correlations from this section, while the small bubbles will use the correlations from the bubbly flow section 5.2.1.

In much the same way that the small bubble flow drag models were modified based on

orientation, the large bubble models are also modified. Taylor bubbles in a horizontally oriented flow will use the drag coefficient method; vertical flows use the drift flux method. The drag coefficient method will be discussed first, followed by the drift flux method.

The interfacial area per unit volume (based on the size of the control volume) will be computed from the size information for the large bubbles that is calculated as part of the six-field solution. The Sauter mean diameter can be used as an average diameter for the large bubbles. This diameter can then be used to compute the surface area of the bubble for use in computing the interfacial area per unit volume.

The void fraction of the large bubbles is known through the solution of the six-field governing equations. The drag coefficient for large bubbles is computed [32]:

$$C_D = 10.9 \frac{D^{'}}{D} \left(1 - \alpha_b\right)^3 \tag{5.137}$$

where $D^{'}$ is the diameter of the large bubble, and D is the pipe diameter.

Vertical flows use the drift flux model, which requires a distribution parameter and a drift velocity correlated to large bubbles. The selected correlation was developed by Zuber and Findlay in [39] and [40]. The needed terms are given as:

$$C_0 = 1.2 \tag{5.138}$$

$$v_{gj} = 0.35 \left[\frac{\left(\rho_f - \rho_g\right) g D}{\rho_f}\right]^{1/2} \tag{5.139}$$

Small Droplets (Dispersed Droplet, Mist)

The drag coefficient method is used for both vertical and horizontal droplet flows. The model used is the same as that for horizontal small bubble flows. The drag coefficient equation 5.107 is repeated here for clarity.

$$C_D = \frac{24\left(1 + 0.1 Re_p^{0.75}\right)}{Re_p} \tag{5.140}$$

Note that the particle Reynolds number will vary somewhat from what was used before to account for the change from bubbles to droplets as shown below:

$$Re_p = \frac{\rho_g |v_{SB} - v_L| d_o}{\mu_m} \tag{5.141}$$

The mixture viscosity used in Equation 5.141 depends on the coolant condition, and is:

$$\mu_m = \begin{cases} \frac{\mu_g}{(\alpha_g)^{2.5}} & \text{Pre-CHF drops} \\ \mu_g & \text{Post-CHF drops} \end{cases} \tag{5.142}$$

Continuous Field Interactions

The interactions between the continuous liquid and continuous vapor fields by definition do not involve droplets or bubbles. The flow regimes that result in significant interactions of this type are annular, inverted annular flow, horizontally stratified flow, and vertically stratified flow.

Where droplets or bubbles are entrained in the continuous vapor or liquid fields, the appropriate models will be applied based on the correlations presented in the preceding sections. The drag interactions between the continuous fields will be modeled based on the flow regime. In these cases, the interfacial area can generally be computed from geometry of the flow and a knowledge of the volume fraction taken by each field.

System codes already include models for the interfacial drag between the continuous liquid and vapor fields. The models already included with the system code will be used to model the wall drag effects.

5.2.2 Wall Drag

The new fields in the six-field model are for bubbles and droplets. Bubbles and droplets have little to no interaction with the walls containing the flow. System codes already include

models for the wall drag on the continuous liquid and vapor fields. The models already included with the system code will be used to model the wall drag effects.

5.3 Momentum and Energy Closure Validation

The two-field version of the RELAP5-3D code is able to model several two-phase flow regimes [22], including bubbly, slug, and droplet flows. The heat transfer and interfacial drag conditions vary depending on flow regime, and the existing two-field code is able to select appropriate correlations for the flow conditions.

5.3.1 Metrics of Interest for Validation

Some of the metrics of interest for the momentum and energy closure models are listed below.

- Interfacial area
- Relative velocity between the liquid and vapor phase
- Heat transfer coefficient between liquid and vapor fields

Separate and integral effects tests can also be used in the validation effort of the momentum and energy closure models. As with the mass closure models, the two-field model validation is documented in detail in [100]. Since the correlations for the two-field code already included the effects from droplet and bubble fields, the same validation cases and procedures documented in [100] will be used for the six-field code.

CHAPTER 6

Solving the Six-Field System of Equations

6.1 Numerically Convenient Governing Equations

The six fields that are to be modeled are numbered in order of increased "fracturing" for ease in notation. The fields are numbered as shown in Table 6.1.

Table 6.1: Fields Corresponding to Indicies

Index	Description
1	Continuous liquid
2	Large droplet
3	Small droplet
4	Continuous vapor
5	Large bubble
6	Small bubble

The detailed governing equations that balance the mass, momentum, and energy exchange between each of the fields are provided in this section. This section will also show the development of these equations into a form that will be solvable using typical numerical schemes.

6.1.1 Primary Variables

The primary dependent variables are internal energy (U), velocity (v) and volume fraction (α) for each of the six fields in addition to the pressure (P). The primary variables are grouped into two vectors. Thermodynamic properties make up the $\overline{x}$ vector, and the velocities are in the $\overline{v}$ vector.

$$\overline{x} = \begin{bmatrix} U_1 \\ \vdots \\ U_6 \\ \alpha_2 \\ \vdots \\ \alpha_6 \\ P \end{bmatrix} \tag{6.1}$$

$$\overline{v} = \begin{bmatrix} v_1 \\ \vdots \\ v_6 \end{bmatrix} \tag{6.2}$$

All primary variables used in the formulation must be independent of each other. Since the six volume fractions (α) sum to 1, they are not all independent. One (α_1) is eliminated from the $\overline{x}$ vector, making the remaining variables independent of one another. The α_1 term is solved for once the other volume fraction terms are known.

6.1.2 Mass Equations

The mass equations are used to track the exchange of mass between the fields due to physical displacement (i.e. droplets entrained into the vapor flow) or phase change (evaporation of the liquid in the vicinity of the wall, forming bubbles). These equations must track the mass exchange between each field and it's "neighbors" (such as the continuous vapor field and large and small droplets).

There are four primary physical interactions between fields: entrainment, de-entrainment, coalescence, and droplet/bubble breakup. These four interactions exchange mass between

fields. Entrainment and de-entrainment are interactions between the discrete fields and the continuous field. The coalescence and breakup interactions exchange mass between large and small discrete fields (bubbles or droplets). Coalescence joins particles of the smaller field to become particles of the larger field. The breakup mechanism works in reverse. Source terms used in the governing equations that represent the physical interactions between fields are noted as $S_{k,m}$, where the mass is transferred from field k to field m.

Similar notation is also used for phase change between fields, where $\Gamma_{i,k,m}$ indicates the mass rate of change from field k to field m at the interface. The mass rate of change at the wall is represented by $\Gamma_{w,k,m}$.

Basic Equations and Expansion in Time

The basic mass balance equations are first shown as a summation. The Γ and S terms are all non-negative, except $\Gamma_{i,1,4} = -\Gamma_{i,4,1}$. In the equation for field k, the Γ and S terms with k as the second subscript indicate that mass is transferring to field k, so those terms are added in the equation. The terms with k as the first subscript indicate that mass is lost from field k to the other field, so these terms are subtracted.

$$\frac{\partial}{\partial t}\left(\alpha_k \rho_k\right) + \frac{1}{A}\frac{\partial}{\partial x}\left(\alpha_k \rho_k v_k A\right) = -\sum_m \Gamma_{i,k,m} - \sum_r \Gamma_{w,k,r} + \sum_s \left(S_{s,k} - S_{k,s}\right) \tag{6.3}$$

Where:

- α_k - volume fraction of field k
- ρ_k - density of field k
- v_k - velocity of field k
- Γ - volumetric mass exchange rate (phase change)

Some terms on the right-hand side of Eqn. 6.3 are zero for some values of k. The values of sets m, r, and s for k of 1 through 6 are summarized in the table below.

Table 6.2: Summation Sets for Values of k

k	m	r	s
1	4, 5, 6	5, 6	2, 3
2	4	-	1, 3
3	4	-	1, 2
4	1, 2, 3	2, 3	5, 6
5	1	1	4, 6
6	1	1	4, 5

Using the table, the summations in Eqn. 6.3 can be determined based on the value of k. If k is 1, then the summation is performed over the terms where $k = 1$ and m equals 4, 5 and 6. This same method is used for all subscripted terms. The possible subscript values are set by the value of the subscript k.

Integration of Mass Equations in Space

The next step in the process will integrate the mass equations in space. It will be seen that after this integration, some scalar values are needed at cell edges. These edge values will be donored, bringing in "upstream" values as needed. Upstream values are used for improved stability in the calculation.

Fig. 6.1 represents a generic control volume nodalization. Scalar quantities are located at cell centers (K and L), and vector quantities (such as velocities) are located at cell edges (j and j+1).

The donoring calculation uses values from the cell centers and the velocity at the boundary between those cells to obtain the scalar value at the cell boundary. The equation for a donored property of field k is:

$$\dot{\phi}_{j,k} = \frac{1}{2}\left(\phi_{K,k} + \phi_{L,k}\right) + \frac{1}{2}\frac{|v_{j,k}|}{v_{j,k}}\left(\phi_{K,k} - \phi_{L,k}\right) \tag{6.4}$$

Where K and L are locations defined as shown in Fig. 6.1, $v_{j,k}$ is the velocity of field k at

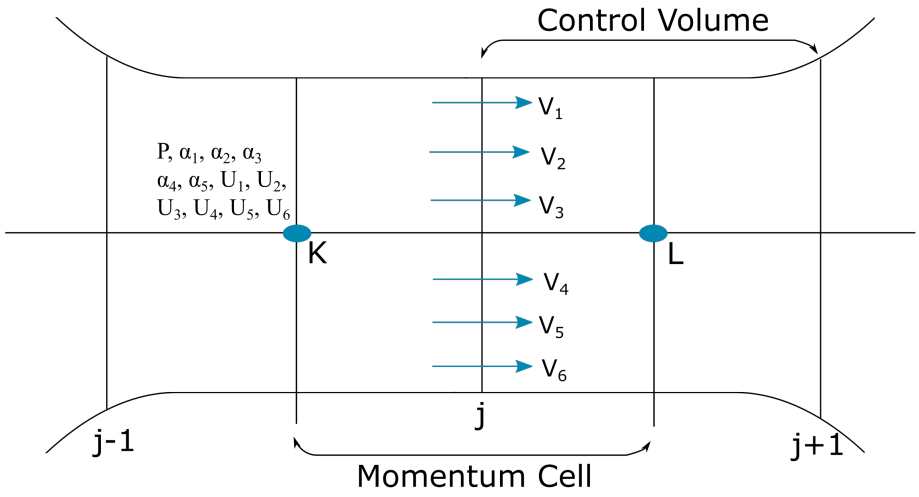

Figure 6.1: Cell Nodalization Diagram

junction j, and ϕ is any parameter. The overdot ($\dot{\phi}$) notation will be used to indicate that a scalar property has been "donored" at the current junction.

Integration of the mass equations with respect to the spatial variable x from the junction at x_j to the one at x_{j+1} gives:

$$\left(\rho_{k,L}\frac{\partial \alpha_{k,L}}{\partial t} + \alpha_{k,L}\frac{\partial \rho_{k,L}}{\partial t}\right) V_L + \left[\left(\dot{\alpha}_{k,j+1}\dot{\rho}_{k,j+1}v_{k,j+1}A_{j+1}\right) - \left(\dot{\alpha}_{k,j}\dot{\rho}_{k,j}v_{k,j}A_j\right)\right] = \\ - V_L\sum_m \Gamma_{i,k,m} - V_L\sum_r \Gamma_{w,k,r} + V_L\sum_s \left(S_{s,k} - S_{k,s}\right) \tag{6.5}$$

The mass exchange between phases must be considered separately for each interface between fields. A mass exchange equation at the interface between fields that is consistent Eqn. 3.1-33 of Reference [22] and represents volumetric vapor generation rate from field k to field m ($\Gamma_{i,k,m}$) is:

$$\Gamma_{i,k,m} = -\frac{H_{k,m}\left[T^s - T_m\right] + H_{m,k}\left[T^s - T_k\right]}{h_m^* - h_k^*} \tag{6.6}$$

Where:

- $\Gamma_{k,m}$ - Volumetric phase change rate from k, m
- T^s - Saturation temperature
- T_m - Temperature of field m
- T_k - Temperature of field k
- $H_{i,j}$ - Interface heat transfer coefficient per unit volume from field i to field j
- h_k^* - Specific enthalpy of field k (for bulk interface mass transfer)
- h_m^* - Specific enthalpy of field m (for bulk interface mass transfer)

The specific enthalpies for bulk mass transfer across the interface are determined by whether the liquid is vaporizing or condensing at the interface:

$$h_k^* = h_k^{sat} \tag{6.7}$$

$$h_m^* = h_m \tag{6.8}$$

Where k and m are as defined in Table 6.2. For example, if small droplets in a vapor field are vaporizing, k would be 4, and m would be 3. This means that the enthalpy of the vapor at saturation would be used for h_4^*, and the enthalpy of the droplets would be h_3^*.

Note that Eqn. 6.6 represents the phase change at any of the interfaces in the six-field model. It also provides for the possibility that the droplet fields will not only have different temperatures from the continuous liquid field, but they may also have different temperatures from each other.

Discretization of Mass Equations

The mass and energy inventories are of great importance to the solution. Since the mass inventory must be conserved, the density and void fraction are critical parameters. These parameters will be conserved by discretizing them in time.

Terms that are important in sonic wave propagation and phenomena with small time constants are evaluated implicitly (terms are at "new" time). This includes the velocity terms and the terms on the RHS of Eqn. 6.5.

The following equations will adopt some additional notation. Variables that are superscripted $n+1$ are at "new" time. Those superscripted n are at "old" time. A "$\sim$" indicates that the variable is provisional, between n and $n+1$.

Equation 6.9 is the "un-expanded" version of the mass balance equation.

$$\begin{aligned}
&\left[(\alpha\rho)_{k,L}^{n+1} - (\alpha\rho)_{k,L}^{n}\right] V_L + \left(\dot{\alpha}_{k,j+1}^{n}\dot{\rho}_{k,j+1}^{n} v_{k,j+1}^{n+1} A_{j+1} - \dot{\alpha}_{k,j}^{n}\dot{\rho}_{k,j}^{n} v_{k,j}^{n+1} A_j\right)\Delta t = \\
&\quad \sum_m \left\{ -\frac{V_L \Delta t}{(h_k^* - h_m^*)_L^n} \left[(H_{m,k})_L^n \left(T_L^{s,\sim n+1} - T_{k,L}^{\sim n+1}\right) + (H_{k,m})_L^n \left(T_L^{s,\sim n+1} - T_{m,L}^{\sim n+1}\right)\right]\right\} + \\
&\quad V_L \Delta t \sum_r \left(\Gamma_{w,k,r}^n\right) + V_L \Delta t \sum_s \left(S_{s,k}^n - S_{k,s}^n\right)
\end{aligned} \tag{6.9}$$

Substituting the appropriate versions of Eqn. 6.6 into Eqn. 6.5 and discretizing as described yields:

$$\begin{aligned}
&\left[\rho_{k,L}^n \left(\alpha_{k,L}^{n+1} - \alpha_{k,L}^n\right) + \alpha_{k,L}^n \left(\rho_{k,L}^{n+1} - \rho_{k,L}^n\right)\right] V_L + \left(\dot{\alpha}_{k,j+1}^{n}\dot{\rho}_{k,j+1}^{n} v_{k,j+1}^{n+1} A_{j+1} - \dot{\alpha}_{k,j}^{n}\dot{\rho}_{k,j}^{n} v_{k,j}^{n+1} A_j\right)\Delta t = \\
&\quad \sum_m \left\{ -\frac{V_L \Delta t}{(h_k^* - h_m^*)_L^n} \left[(H_{m,k})_L^n \left(T_L^{s,\sim n+1} - T_{k,L}^{\sim n+1}\right) + (H_{k,m})_L^n \left(T_L^{s,\sim n+1} - T_{m,L}^{\sim n+1}\right)\right]\right\} + \\
&\quad V_L \Delta t \sum_r \left(\Gamma_{w,k,r}^n\right) + V_L \Delta t \sum_s \left(S_{s,k}^n - S_{k,s}^n\right)
\end{aligned} \tag{6.10}$$

The right-hand side of the discretized mass equation for $k = 1$ is shown as an example of how the data in Table 6.2 are applied to the summation terms in Eqn. 6.10.

$k = 1$:

$$\sum_{m=4}^{6} \left\{ -\frac{V_L \Delta t}{(h_1^* - h_m^*)_L^n} \left[(H_{1,m})_L^n \left(T_L^{s,\sim n+1} - T_{m,L}^{\sim n+1} \right) + (H_{m,1})_L^n \left(T_L^{s,\sim n+1} - T_{1,L}^{\sim n+1} \right) \right] \right\} +$$
$$\left(S_{2,1}^n - S_{1,2}^n + S_{3,1}^n - S_{1,3}^n - \Gamma_{w,1,5}^n - \Gamma_{w,1,6}^n \right) V_L \Delta t \tag{6.11}$$

Note from Eqn. 6.10 that there are some density, volume fraction, and velocity terms that are needed at "new time" $(n+1)$. There are also some donored volume fraction and density terms that are kept at old time. Donored properties must be kept at old time, because at the time in the calculation where those terms will be needed, the flow direction at new time is unknown. This makes it impossible to compute the donored properties correctly. Thus, donored values are kept at old time.

The density and temperature values at new time that appear in Eqn. 6.10 are secondary dependent variables. These new time values must be expressed in terms of primary dependent variables (Eqn. 6.1) in order to proceed with the calculation. The density terms can be resolved with linearized state relations about the "old-time" values in a process described in Section 6.2. Eventually, all the "old-time" values will be on the right-hand side and the "new-time" values will be on the left. These "new-time" values on the left will consist only of temporal differences of the primary variables, perhaps modified by time-independent multipliers.

6.1.3 Momentum Equations

Basic Equations and Expansion in Time

The momentum equations will be discretized using the same methods that were used for the mass equations. The resulting generalized momentum conservation equation is shown below.

$$\begin{aligned}\alpha_k\rho_k A\frac{\partial v_k}{\partial t}+\frac{1}{2}\alpha_k\rho_k A\frac{\partial v_k^2}{\partial x}=&-\alpha_k A\frac{\partial P}{\partial x}+\alpha_k\rho_k B_x A-\left(\alpha_k\rho_k A\right)FW_k\cdot v_k+\\&\sum_m\left[s_k\Gamma_{i,k,m}A\left(v_{i,k,m}-v_k\right)\right]-\sum_m\left[\left(\alpha_k\rho_k A\right)FI_{k,m}\left(v_k-v_m\right)\right]+\\&\sum_s\left(S_{s,k}v_s-S_{k,s}v_k\right)-C\sum_m\left[\alpha_k\alpha_m\rho_{mk}A\frac{\partial(v_k-v_m)}{\partial t}\right]\end{aligned}\tag{6.12}$$

Where k, m, and s, are defined as before, P denotes the pressure in the control volume, and C is the coefficient of virtual mass that is dependent upon the flow regime. The assumption that all fields are at the same pressure results in a single pressure term in Eqn. 6.12. A similar assumption is made for many system codes in use today. These codes rely on artificial viscosity to obtain a well-posed model that can be solved. Ransom and Scofield [123] showed that a two-pressure solution (for a two-field model) compared very well to a single-pressure model that included artificial viscosity. Any model that includes more than one pressure must also verify the pressures used for the different fields are sensible. Current techniques for measuring pressures in multi-field systems are limited, and it is unlikely that it would be possible to verify pressures in a flow field that included multiple bubbles or droplets.

The phase multiplier (s_k) is in place to handle the necessary sign change on the volumetric mass exchange rate. For vapor phases (k is 4, 5, or 6), s_k is 1. The liquid phases (k is 1, 2, or 3) set s_k equal to -1.

The mixture density term in Eqn. 6.12 (ρ_{mk}) is defined as the mixture of field k and m:

$$\rho_{mk} = \frac{\alpha_k \rho_k + \alpha_m \rho_m}{\alpha_k + \alpha_m} \tag{6.13}$$

Where k and m are as defined in Table 6.2. The interfacial velocity term ($v_{i,k,m}$) in Eqn. 6.12 is defined as:

$$v_{i,k,m} = \lambda v_k + (1 - \lambda)\, v_m \tag{6.14}$$

The λ in Eqn. 6.14 is 0 for positive values of the vapor generation rate (Γ) for vapor field k and +1 for negative values of vapor generation rate for field k. With these definitions of λ, the interfacial velocity is essentially a donor formulation. In the case of vaporization of liquid field m to the vapor field k, the velocity used in the momentum conservation equation for the interface comes from the liquid field velocity (field m). For condensation, the velocity is the vapor field velocity (field k).

The virtual mass term in Eqn. 6.12 has been simplified by neglecting the spatial derivative portion. Approximations that are used to compute the spatial derivative, combined with the relatively coarse nodalizations used in system code analyses introduce inaccuracies that lead to non-physical solutions [22], so the spatial derivatives are neglected.

The details of the right-hand sides of the various forms of Eqn. 6.12 follow the patterns established by the mass conservation equations, and so will not be provided at this stage.

Discretization of Momentum Equations

The process of integration and discretization of the momentum equations follows the same general guidelines that were used for the mass conservation equations. A key variation is that the momentum control volumes are located between the cell centers of the mass/energy control volumes (e.g. “K” and “L” in Fig. 6.1).

Recall that scalar values are located at cell centers and vector quantities are on cell edges

(see Fig. 6.1). This has the effect of offsetting the momentum control volumes from the mass and energy control volumes. Thus, any average properties from the mass/energy control volumes must be interpolated or donored to get an appropriate value for the momentum cell centers, which are the junctions of the mass/energy control volumes.

Values like pressure that are needed as an average momentum control volume value are obtained by linear interpolation between mass/energy control volume centers. The momentum control volume is located between the centers of the mass/energy control volumes, so the integration in space is done from cell center to cell center ("K" to "L" in Fig. 6.1).

The momentum flux values are located on the edges of the momentum control volume, which are at the centers of the mass/energy control volume. Values that are needed for the momentum flux calculation (velocities, etc.) are obtained using a donor-like formulation. This formulation gives a velocity term at the mass/energy control volume center and a viscous-like term (numerical or artificial viscosity). Accounting for these adjustments and following the guidelines used for the mass conservation equations, the finite difference momentum equation for field k is:

$$
\begin{aligned}
&(\alpha_k\rho_k)_j^n\, v_{k,j}^{n+1}\Delta x_j + (\alpha_k\rho_k FW_k)_j^n\,(v_k)_j^{n+1}\,\Delta x_j\Delta t + \\
&\quad \sum_m \left\{(C\alpha_m\alpha_k\rho_{mk})_j^n\left(v_k^{n+1}-v_m^{n+1}\right)\right\}\Delta x_j + (\dot{\alpha}_k\dot{\rho}_k HLOSSK)_j^n\, v_{k,j}^{n+1}\Delta t - \\
&\quad \sum_m \left[s_k^n\,(\Gamma_{i,k,m})_j^n\,(v_{i,k,m}-v_k)_j^{n+1} - (\alpha_k\rho_k FI_{k,m})_j^n\,(v_k-v_m)_j^{n+1}\right]\Delta x_j\Delta t = \\
&\quad -(\dot{\alpha}_k)_j^n\,(P_L-P_K)^{n+1}\,\Delta t + (\alpha_k\rho_k)_j^n\, v_{k,j}^n\Delta x_j - \frac{1}{2}\,(\dot{\alpha}_k\dot{\rho}_k)_j^n\left[\left(v_k^2\right)_L^n - \left(v_k^2\right)_K^n\right]\Delta t + \\
&\quad (\alpha_k\rho_k)_j^n\, B_x\Delta x_j\Delta t + \frac{1}{2}\,(\dot{\alpha}_k\dot{\rho}_k\,(VIS_k))_j^n\,\Delta t - \\
&\quad \sum_m \left\{(C\alpha_m\alpha_k\rho_{mk})_j^n\,(v_m^n-v_k^n)\right\}\Delta x_j + \sum_s (S_{s,k}v_s - S_{k,s}v_k)\,\Delta x_j\Delta t
\end{aligned}
\tag{6.15}
$$

The terms with an overdot are donored as before. If the term is multiplied by Δx_j, then the scalar variables are interpolated between neighboring cell values.

The pressure gradient in the momentum equations are at new time because they fall under the category of terms that are responsible for the sonic wave propagation time step limit and phenomena with small time constants, so the implicit evaluation is used. Note that the only terms at new time are primary variables - velocity or pressure (v or P). The velocity squared terms are the exception. They are left at old time to avoid the need of an iterative solver. The momentum equations will be used in the solution of the remaining balance equations.

The HLOSS terms in the momentum equations result from dynamic flow losses resulting from abrupt area changes computed by the code or user-input loss values.

The artificial viscosity term, VIS_k is defined for field k below. Note that since this represents the artificial viscosity in the continuous fields, the values of k are either 1 or 4. VIS_k is zero for the remaining values of k.

$$(VIS_k)_j^n = \frac{1}{2}\left\{|v_{k,L}^n|\left[(v_k^n)_{j+1}\frac{A_{j+1}}{A_j} - (v_k^n)_j\right] - |v_{k,K}^n|\left[(v_k^n)_j - (v_k^n)_{j-1}\frac{A_{j-1}}{A_j}\right]\right\} \tag{6.16}$$

6.1.4 Energy Equations

Basic Equations and Expansion in Time

As previously stated, the noncondensable gas in the vapor field is neglected in this derivation. The result of this choice is that the term representing the heat transfer from the noncondensable gas to the vapor phase is eliminated from the energy balance equations.

The following simplifications are applicable to these equations (pg 52 in [22]):

- Reynolds heat flux is neglected
- Covariance terms are universally neglected
- Interfacial energy storage is neglected
- Internal phasic heat transfer is neglected

The energy conservation equation for field k is provided as Eqn. 6.17:

$$\begin{aligned}\frac{\partial}{\partial t}\left(\alpha_k \rho_k U_k\right) + \frac{1}{A}\frac{\partial}{\partial x}\left(\alpha_k \rho_k U_k v_k A\right) = -P\frac{\partial \alpha_k}{\partial t} - \frac{P}{A}\frac{\partial}{\partial x}\left(\alpha_k v_k A\right) + \\ \sum_{m=1}^{6}\left(Q_{i,m,k} + Q_{w,k}\right) - \sum_{m=1}^{6}\left(\Gamma_{i,k,m} h_k^* + \Gamma_{w,k,m} h_k^{'}\right) + \\ \sum_{m=1}^{6}\left(S_{m,k} h_m - S_{k,m} h_k\right) + DISS_k\end{aligned} \tag{6.17}$$

Where U_k is the internal energy of field k and Q is the volumetric heat addition rate. The phasic specific enthalpies in the bulk shown in the energy conservation equation (h_k^*, where k is any of the 6 fields) depend upon the heat transfer conditions as shown in Eqn. 6.7. The same is true for the phasic specific enthalpies associated with wall heat transfer in the thermal boundary layer.

$$h_k^{'} = h_k^{sat} \tag{6.18}$$

$$h_m^{'} = h_m \tag{6.19}$$

Where k and m are defined in Table 6.2 as before. The rates of interfacial heat transfer are then [22]:

$$Q_{i,4,1} = H_{4,1}\left(T^s - T_1\right) - \left(\frac{1+\epsilon}{2}\right)\left[\Gamma_{w,1,5}\left(h_5^{'} - h_1^{'}\right) + \Gamma_{w,1,6}\left(h_6^{'} - h_1^{'}\right)\right] \tag{6.20}$$

$$Q_{i,1,4} = H_{1,4}\left(T^s - T_4\right) - \left(\frac{1-\epsilon}{2}\right)\Gamma_{w,4,1}\left(h_4^{'} - h_1^{'}\right) \tag{6.21}$$

$$Q_{k,m} = H_{k,m}\left(T^s - T_m\right) \tag{6.22}$$

The terms in the above equations that include heat transfer coefficients (H) compute the heat transfer in the bulk coolant. The second term on the right-hand side of Eqns. 6.20 and

6.21 are for heat transfer that occurs at the wall. The ϵ is a wall vapor generation/condensation flag that is set to 1 for boiling in the boundary layer and -1 for condensation. Note in Eqn. 6.20 that there are two Γ terms representing bubble generation at the wall. The flow conditions determine whether large or small bubbles will be generated near the wall, so it is assumed that one of the two gamma terms will generally be near (or at) zero. Eqn. 6.22 represents the remaining interfacial heat transfer terms that are present in the complete set of energy governing equations.

The time derivative in the energy equation is expanded in time using the product rule, and then the expressions for $Q_{i,k,m}$ and $\Gamma_{i,k,m}$ (see Eqn. 6.6) are substituted into Eqn. 6.17 to obtain the generalized energy balance equation (after collecting all the H and $\frac{\partial \alpha_k}{\partial t}$ terms):

$$
\begin{aligned}
&\left(\rho_k U_k + P\right)\frac{\partial \alpha_k}{\partial t} + \alpha_k U_k \frac{\partial \rho_k}{\partial t} + \alpha_k \rho_k \frac{\partial U_k}{\partial t} + \\
&\quad \frac{1}{A}\left[\frac{\partial}{\partial x}\left(\alpha_k \rho_k U_k v_k A\right) + P\frac{\partial}{\partial x}\left(\alpha_k v_k A\right)\right] = \\
&\quad -\sum_m \left[\left(\frac{h_k^*}{h_m^* - h_k^*}\right) H_{k,m}\left(T^s - T_m\right) + \left(\frac{h_m^*}{h_m^* - h_k^*}\right) H_{m,k}\left(T^s - T_k\right)\right] + \\
&\quad \sum_r \left\{\left[\left(\frac{1+\epsilon}{2}\right) h_r{}' + \left(\frac{1-\epsilon}{2}\right) h_k{}'\right]\Gamma_{w,r,k}\right\} + \Gamma_{w,c,k} h_k' + Q_{w,k} + DISS_k + \\
&\quad \sum_s \left(S_{s,k} h_s - S_{k,s} h_k\right)
\end{aligned}
\tag{6.23}
$$

Where k, m, r and c are defined in Table 6.3. As with the mass equation, the expansion of the time derivative in the energy equations is useful for the solution of the system, but it is also helpful to have an unexpanded version of the energy balance equation. Equation 6.23 is the expanded version. The un-expanded and discretized version will be shown in the next section. The right-hand side of the energy balance equation for $k = 1$ is provided below.

Table 6.3: Summation Sets for Values of k in the Energy Equation

k	m	r	s	c
1	4, 5, 6	5, 6	2, 3	4
2	4	-	1, 3	-
3	4	-	1, 2	-
4	1, 2, 3	1	5, 6	-
5	1	-	4, 6	1
6	1	-	4, 5	1

$k = 1$:

$$
\begin{aligned}
&-\left(\frac{h_1^*}{h_4^* - h_1^*}\right) H_{1,4}\left(T^s - T_4\right) - \left(\frac{h_4^*}{h_4^* - h_1^*}\right) H_{4,1}\left(T^s - T_1\right) - \\
&\left(\frac{h_1^*}{h_5^* - h_1^*}\right) H_{1,5}\left(T^s - T_5\right) - \left(\frac{h_5^*}{h_5^* - h_1^*}\right) H_{5,1}\left(T^s - T_1\right) - \\
&\left(\frac{h_1^*}{h_6^* - h_1^*}\right) H_{1,6}\left(T^s - T_6\right) - \left(\frac{h_6^*}{h_6^* - h_1^*}\right) H_{6,1}\left(T^s - T_1\right) + \\
&\left[\left(\frac{1+\epsilon}{2}\right) h_5^{'} + \left(\frac{1-\epsilon}{2}\right) h_1^{'}\right] \Gamma_{w,5,1} + \left[\left(\frac{1+\epsilon}{2}\right) h_6^{'} + \left(\frac{1-\epsilon}{2}\right) h_1^{'}\right] \Gamma_{w,6,1} + \\
&\Gamma_{w,4,1} h_1^{'} + Q_{w,1} + DISS_1 + \\
&S_{2,1} h_2 - S_{1,2} h_1 + S_{3,1} h_3 - S_{1,3} h_1
\end{aligned}
\tag{6.24}
$$

Where the dissipation terms ($DISS_1$ above, $DISS_4$ for $k = 4$) are the sums of the effects of wall friction, pumps, and turbines. Other dissipation effects (interface mass transfer, interface friction, and any virtual mass) are neglected, as are the dissipation terms for the fragmented fields (bubbles, droplets). These terms are small in the energy equation. These interfacial friction terms are much more important in the mass and momentum equations, and are not neglected in those cases. The wall friction part of the dissipation for the vapor and gas phase are defined as:

$$DISS_1 = \alpha_1 \rho_1 FW_1 v_1^2 \tag{6.25}$$

$$DISS_4 = \alpha_4 \rho_4 FW_4 v_4^2 \tag{6.26}$$

Where FW_1 and FW_4 are the liquid and vapor wall drag coefficients.

Integration in Space and Discretization in Time

The energy equations are integrated in space (from j to $j+1$) as was done for the mass governing equations. They are also discretized in time, again as was done for the mass governing equations. Both of these steps followed the same processes that were outlined in more detail for the mass equations in Sections 6.1.2 and 6.1.2.

The un-expanded and expanded versions of the discretized energy equations are shown as Eqn. 6.27 and Eqn.6.28 respectively.

$$\begin{aligned}
&\left[(\alpha\rho U)_{k,L}^{n+1} - (\alpha\rho U)_{k,L}^{n}\right] V_L + \left[\dot{\alpha}_{k,j+1}^{n}\left(\dot{\rho}_{k,j+1}^{n}\dot{U}_{k,j+1}^{n} + P_L^n\right) v_{k,j+1}^{n+1} A_{j+1} - \right. \\
&\left. \dot{\alpha}_{k,j}^{n}\left(\dot{\rho}_{k,j}^{n}\dot{U}_{k,j}^{n} + P_L^n\right) v_{k,j}^{n+1} A_j\right] \Delta t = -\left(\alpha_{k,L}^{\sim n+1} - \alpha_{k,L}^{n}\right) V_L P_L^n \\
&- V_L \Delta t \sum_m \left[\left(\frac{h_k^*}{h_m^* - h_k^*}\right)_L^n (H_{k,m})_L^n \left(T_L^{\sim s,n+1} - T_{m,L}^{\sim n+1}\right) + \right. \\
&\left. \left(\frac{h_m^*}{h_m^* - h_k^*}\right)_L^n (H_{m,k})_L^n \left(T_L^{\sim s,n+1} - T_{k,L}^{\sim n+1}\right)\right] + \\
&V_L \Delta t \sum_r \left\{\left[\left(\frac{1+\epsilon}{2}\right) h_{r,L}{}', n + \left(\frac{1-\epsilon}{2}\right) h_{k,L}{}', n\right] (\Gamma_{w,r,k})_L^n\right\} + \\
&(\Gamma_{w,c,k})_L^n \, h_{k,L}^{',n} V_L \Delta t + (Q_{w,k})_L^n V_L \Delta t + DISS_{k,L}^n V_L \Delta t + \\
&V_L \Delta t \sum_s (S_{s,k} h_s - S_{k,s} h_k)
\end{aligned} \tag{6.27}$$

$$
\begin{aligned}
&\left[\left(\rho_k U_k + P\right)_L^n \left(\alpha_{k,L}^{\sim n+1} - \alpha_{k,L}^n\right) + \alpha_{k,L}^n U_{k,L}^n \left(\rho_{k,L}^{\sim n+1} - \rho_{k,L}^n\right) + \right. \\
&\left. \alpha_{k,L}^n \rho_{k,L}^n \left(U_{k,L}^{\sim n+1} - U_{k,L}^n\right)\right] V_L + \\
&\left[\dot{\alpha}_{k,j+1}^n \left(\dot{\rho}_{k,j+1}^n \dot{U}_{k,j+1}^n + P_L^n\right) v_{k,j+1}^{n+1} A_{j+1} - \dot{\alpha}_{k,j}^n \left(\dot{\rho}_{k,j}^n \dot{U}_{k,j}^n + P_L^n\right) v_{k,j}^{n+1} A_j\right] \Delta t = \\
&- V_L \Delta t \sum_m \left[\left(\frac{h_k^*}{h_m^* - h_k^*}\right)_L^n \left(H_{k,m}\right)_L^n \left(T_L^{\sim s,n+1} - T_{m,L}^{\sim n+1}\right) + \right. \\
&\left. \left(\frac{h_m^*}{h_m^* - h_k^*}\right)_L^n \left(H_{m,k}\right)_L^n \left(T_L^{\sim s,n+1} - T_{k,L}^{\sim n+1}\right)\right] + \\
&V_L \Delta t \sum_r \left\{\left[\left(\frac{1+\epsilon}{2}\right) h_{r,L}{}', n + \left(\frac{1-\epsilon}{2}\right) h_{k,L}{}', n\right] \left(\Gamma_{w,r,k}\right)_L^n\right\} + \\
&\left(\Gamma_{w,c,k}\right)_L^n h_{k,L}^{',n} V_L \Delta t + \left(Q_{w,k}\right)_L^n V_L \Delta t + DISS_{k,L}^n V_L \Delta t + \\
&V_L \Delta t \sum_s \left(S_{s,k} h_s - S_{k,s} h_k\right)
\end{aligned}
\tag{6.28}
$$

6.2 Linearized Approximations to New Time Variables

The only terms that should be at new time $(n+1)$ are the primary variables (U, P, α, v). There are some values in the preceding discretized governing equations that have variables at new time that are not primary variables. The additional variables at new time are the density and the temperatures.

The way to resolve this issue is to recognize that density and temperature can be written as functions of the primary variables. For this reason, they are often referred to as secondary variables. The Gibbs phase rule [124] states that for a given phase of uniform composition, only two intensive properties (temperature, pressure, etc.) can be varied without affecting one another or the other intensive properties. By treating each field in the flow as a separate component, the Gibbs rule allows the density and temperature to be determined by the pressure and internal energy. By the chain rule,

$$
\frac{d\psi\left(P,U\right)}{dt} = \frac{\partial \psi}{\partial P}\frac{\partial P}{\partial t} + \frac{\partial \psi}{\partial U}\frac{\partial U}{\partial t} \tag{6.29}
$$

6.2.1 Linearized State Equations

By replacing the derivative with respect to time of the primary variables with the discretized time values, an approximation to that derivative is obtained. This allows the new time value of the desired parameter (density, for example) to be written as an approximation of the sum of the parameter at old time and the multiple of the partial derivative of the parameter with respect to each primary variable multiplied by the change of that primary variable as in Equation 6.30.

$$\rho_{k,L}^{\sim n+1} = \rho_{k,L}^{n} + \left(\frac{\partial \rho_k}{\partial P}\right)_L^n \left(P_L^{n+1} - P_L^n\right) + \left(\frac{\partial \rho_k}{\partial U_k}\right)_L^n \left(U_{k,L}^{\sim n+1} - U_{k,L}^n\right) \tag{6.30}$$

Note that the approximation assumes that the change in density with respect to each of the primary variables considered is known. Note also that the pressure is assumed to be the same for all the modeled fields. The void fraction and velocity have also been eliminated from the calculation (even though they are primary variables), as those values have nothing to do with the density.

The provisional new time temperatures are developed in a similar way:

$$T_{k,L}^{\sim n+1} = T_{k,L}^{n} + \left(\frac{\partial T_k}{\partial P}\right)_L^n \left(P_L^{n+1} - P_L^n\right) + \left(\frac{\partial T_k}{\partial U_k}\right)_L^n \left(U_{k,L}^{\sim n+1} - U_{k,L}^n\right) \tag{6.31}$$

6.3 Source Terms and Stability

The source terms ($S_{k,m}$) that will be used in the six-field governing equations are documented in [119]. These terms are required for solution of the six-field model and represent the physical transfer of mass between the fields. The addition of these terms must be done with consideration to the overall stability of the model. Recall that the for a source term of $S_{k,m}$,

the notation indicates that the mass is moving from field k to field m.

6.3.1 Liquid Phase Source Terms

The source terms for the liquid phase should include representations of the physical mechanisms by which droplets are entrained, de-entrained, broken up, and coalesce. In the case of droplet entrainment, the orientation of the flow affects the entrainment rate. The orientations considered for the six-field model are upward annular flow, entrainment near a reflood quench front, and horizontal flow [119]. The function shown in Eqn. 6.32 indicates the parameters that are required for all three of these orientations. Not all parameters are needed for each orientation.

$$S_{1,2} = f_{1,2}\left(\rho_1, \rho_4, P_w, P_H, v_1, v_4, v_{4,crit}, \Gamma_{1,4}, A_f, \alpha_1, \lambda, \mu_1, \mu_4, \sigma, \pi, g, D_{hy}, P_p, W_{LF}, W_{LFC}, k_A^{'}\right) \tag{6.32}$$

The droplet entrainment functions, represented by the expression above, include non-linear terms. The methods used for linearization of the governing equations are ineffective on expressions that include powers of 7/8, which occur in some of the source term correlations. This non-linearity is the reason why the source terms are evaluated at old time in the six-field model. Many of the source term models presented in this section have similar issues with linearity.

The droplet de-entrainment models include two orientations: horizontal flow and vertical flow. These correlations use similar parameters to those used for the droplet entrainment, as shown in the expression below. Note that in horizontal flows, the gravity will act on the droplets, increasing the de-entrainment in the lower portions of the pipe. The correlation

selected will average those effects around the pipe circumference.

$$S_{3,1} = f_{3,1}\left(\sigma, \alpha_3, \rho_1, \rho_4, \mu_1, \mu_4, \gamma, D, V_{cell}, P_w, \Delta X, k_D, D_d, g, v_4, \varsigma, \zeta, \theta, S, Q_G, W_{LE}, L_{cell}\right) \tag{6.33}$$

No suitable models have been found for use in the droplet coalescence source terms. For purposes of the six-field model, the bubble coalescence correlations will be used until better droplet models become available. The droplet breakup models are based on three assumed mechanisms. Two are based on flow effects. These are bag-type breakup and shear breakup. In bag-type breakup, the droplets form large bag shapes and break up around the edges near the top of the "bag". For shear break-up, the droplets elongate until they disintegrate. The third mechanism for droplet breakup is for droplets that impact the spacer grid. As might be expected, that model will include dimensions of the grid and the rough probability of the droplets impacting the grid itself. These three options are represented by the expression:

$$S_{2,3} = f_{2,3}\left(\rho_1, \rho_4, v_4, v_2, \sigma, D_o, \alpha_2, v_{rel,1,d}\eta_e, A_g, A_c, m_E, V_{DI}^2, D_I, \alpha_e, A_{i,d}, V_{cell}\right) \tag{6.34}$$

6.3.2 Vapor Phase Source Terms

The vapor phase source terms include the physical effects of interaction for the bubble fields. Unfortunately, models for bubble entrainment, de-entrainment, and spacer grid breakup are not available for bubbles. Until such models become available, the correlations used for the droplet fields discussed in the previous section will be implemented.

Bubbles may coalesce into larger bubbles by random collision or wake entrainment. These mechanisms are notably more complex than those for the droplet interactions, with several

additional empirical constants. The random collision source terms are computed by correlations represented by the following expression:

$$S_{6,5} = f_{6,5}\left(\alpha_b, \alpha_{b,max}, A_{i,6}, \chi, C_{RC,k}, \rho_4, \rho_1, g, \sigma, G, W, V_c, r_k, C_{RC}^{(k)}, Rc_{max,b}, R_c^*\right) \tag{6.35}$$

Perhaps the most recognizable example of wake entrainment is where a small bubble is following in the wake of a larger bubble, but the opposite situation is also possible, where a larger bubble will be following a smaller bubble. The wake entrainment correlations are different for each case, but require similar parameters as input. The expression below encompasses both types of wake coalescence. Note that not all the parameters listed are used for every wake entrainment mechanism.

$$S_{6,5} = f_{6,5}\left(C_{WE}^{(k)}, v_{rel,l,b}, C_{D,k}, A_{i,k}, \alpha_{b,l}, \alpha_{b,T}, \rho_1, \rho_4, r_k, G, V_c, g, \sigma, R_{m,k}, R_c^*\right) \tag{6.36}$$

In a similar manner as droplets, bubbles may break up due to flow effects. Turbulent eddies may cause the bubbles to break up, as well as shear effects. The source terms related to these effects are computed using the parameters shown in the expression below:

$$S_{5,6} = f_{5,6}\left(C_{TI}^{(k)}, C_{SO}, C_d, \sigma, \rho_1, \rho_4, D_b, v_{rel,b,1}, G, R_c^*, R_{m,k}, R_{SO,c}\chi, \overline{u}_t, \alpha_k, \alpha_t, r_k, A_{i,k}, We_{c,TI,k}\right) \tag{6.37}$$

When bubbles break up due to size-related instability, the rate of that break up is expressed by a function that has the following input parameters:

$$S_{5,6} = f_{5,6}\left(C_{RC}^{(k)}, C_{RC,k}, C_{WE}^{(k)}, C_{D,k}, \sigma, \chi, \rho_4, \rho_1, G, g, W, r_k, R_{SO,c}, \alpha_k, r_k\right) \tag{6.38}$$

6.3.3 Stability

The formulation of the six field governing equations assumes that all the fields are at the same pressure. This single-pressure assumption results in an ill-posed problem. This is not a concern, however, because the addition of artificial viscosity mitigates the effects of the single-pressure choice [22].

Comparisons between a two-pressure model and the single-pressure system of RELAP5-3D showed that the differences between the two methods are more significant in the shorter wavelength components of the Fourier solution [22]. Neglecting these "shorter wavelength" components improves the results and the stability of the solution.

When the shorter wavelength components are removed, the ability of the model to resolve wave fronts in the solution is reduced. These wave fronts generally result from sudden changes in the model. Valves closing or opening, pressure pulses due to pipe ruptures, pumps starting up, and other sudden changes in the model. The six-field model introduces the additional possibility of solution wave fronts by the sudden appearance or disappearance of fields. When the shorter wavelength components of the Fourier solution are removed, these wave fronts are "smoothed". The corners of the wave front are not as sharp, and the wave front itself spreads out and attenuates.

In an attempt to better resolve the wave fronts, a user could reduce timestep sizes, but adequate accuracy is not obtained until the timestep is much less than the material Courant limit. Alternatively, the size of the control volumes can be reduced, but due to the fact that the wave front itself is finite, any volume size used will be an approximation, since the pressure within a volume is a single value.

The objectives of a typical plant analysis include minimizing runtime and model complexity. These goals are somewhat at odds of capturing the finer details of a wave front, but analyses of typical plants do not generally require that level of detail in wave front behavior.

The shorter wavelength components of the solution have been eliminated from this development in the interest of stability. In the case of the six-field model, all of the field source terms have been placed at old time. If included, the non-linear aspect of the source term correlations would introduce many short wavelength components to the solution.

6.4 Solution of the System

The mass, momentum, and energy governing equations describe the fluid behavior in every control volume in the model. The solution is obtained by formulating the mass and energy equations into a matrix equation so that they may be solved simultaneously. The momentum equations are arranged separately and solved for the velocities, which are then substituted into the mass and energy system.

The following sections will describe this process in greater detail.

6.4.1 Mass and Energy Matrix Formulation

Considering the mass and energy equations alone, there are 12 equations (six fields each for mass and energy equations) and 18 "primary" variable quantities at new time. The 18 terms at new time are the six velocities and the 12 derivatives of the remaining primary variables.

All of the terms that are multiplied by the difference between old-time and new time $\overline{x}$ terms are collected and arranged to be the elements of a coefficient matrix for control volume L ($\overline{\overline{A}}^n_L$). The n-time-level coefficients that are not multiplied by differences of primary variables or velocities at new time are collected on the right-hand side of the equations and make up the $\overline{b}^n_L$ vector. The terms that are multiplied by new-time velocities are collected into two vectors ($g^n_{k,j+1}$ and $g^n_{k,j}$) for each field – one at point $j+1$, the other at point j.

The matrix expression for the mass and energy governing equations for volume L is shown

in Eqn. 6.39.

$$\overline{\overline{A}}_L^n \Delta \overline{x}_L^{\sim n+1} = \overline{b}_L^n + \sum_{k=1}^{6} \left(g_{k,j+1}^n v_{k,j+1}^{n+1} + g_{k,j}^n v_{k,j}^{n+1} \right) \tag{6.39}$$

The $\overline{\overline{A}}$ array in Eqn. 6.39 is a 12 x 12 matrix made up of the coefficients from the mass and energy conservation equations. The structure of the A matrix is shown below.

$$\overline{\overline{A}}_L^n = \begin{bmatrix}
A_{1,1} & 0 & 0 & A_{1,4} & A_{1,5} & A_{1,6} & A_{1,7} & A_{1,8} & A_{1,9} & A_{1,10} & A_{1,11} & A_{1,12} \\
0 & A_{2,2} & 0 & A_{2,4} & 0 & 0 & A_{2,7} & 0 & 0 & 0 & 0 & A_{2,12} \\
0 & 0 & A_{3,3} & A_{3,4} & 0 & 0 & 0 & A_{3,8} & 0 & 0 & 0 & A_{3,12} \\
A_{4,1} & A_{4,2} & A_{4,3} & A_{4,4} & 0 & 0 & 0 & 0 & A_{4,9} & 0 & 0 & A_{4,12} \\
A_{5,1} & 0 & 0 & A_{5,4} & A_{5,5} & 0 & 0 & 0 & 0 & A_{5,10} & 0 & A_{5,12} \\
A_{6,1} & 0 & 0 & A_{6,4} & 0 & A_{6,6} & 0 & 0 & 0 & 0 & A_{6,11} & A_{6,12} \\
A_{7,1} & 0 & 0 & A_{7,4} & A_{7,5} & A_{7,6} & A_{7,7} & A_{7,8} & A_{7,9} & A_{7,10} & A_{7,11} & A_{7,12} \\
0 & A_{8,2} & 0 & A_{8,4} & 0 & 0 & A_{8,7} & 0 & 0 & 0 & 0 & A_{8,12} \\
0 & 0 & A_{9,3} & A_{9,4} & 0 & 0 & 0 & A_{9,8} & 0 & 0 & 0 & A_{9,12} \\
A_{10,1} & A_{10,2} & A_{10,3} & A_{10,4} & 0 & 0 & 0 & 0 & A_{10,9} & 0 & 0 & A_{10,12} \\
A_{11,1} & 0 & 0 & A_{11,4} & A_{11,5} & 0 & 0 & 0 & 0 & A_{11,10} & 0 & A_{11,12} \\
A_{12,1} & 0 & 0 & A_{12,4} & 0 & A_{12,6} & 0 & 0 & 0 & 0 & A_{12,11} & A_{12,12}
\end{bmatrix} \tag{6.40}$$

The time difference of the primary variables ($\Delta \overline{x}_L^{\sim n+1}$) vector in Eqn. 6.39 is the difference between the old-time and provisional new-time values of the primary variables. This is shown

in the $\Delta\overline{x}_L^{\sim n+1}$ vector.

$$\Delta\overline{x}_L^{\sim n+1} = \begin{bmatrix} U_{1,L}^{\sim n+1} - U_{1,L}^{n} \\ U_{2,L}^{\sim n+1} - U_{2,L}^{n} \\ U_{3,L}^{\sim n+1} - U_{3,L}^{n} \\ U_{4,L}^{\sim n+1} - U_{4,L}^{n} \\ U_{5,L}^{\sim n+1} - U_{5,L}^{n} \\ U_{6,L}^{\sim n+1} - U_{6,L}^{n} \\ \alpha_{2,L}^{\sim n+1} - \alpha_{2,L}^{n} \\ \alpha_{3,L}^{\sim n+1} - \alpha_{3,L}^{n} \\ \alpha_{4,L}^{\sim n+1} - \alpha_{4,L}^{n} \\ \alpha_{5,L}^{\sim n+1} - \alpha_{5,L}^{n} \\ \alpha_{6,L}^{\sim n+1} - \alpha_{6,L}^{n} \\ P_L^{n+1} - P_L^{n} \end{bmatrix} \tag{6.41}$$

The b vector in Eqn. 6.39 is a 12-value column vector that consists of the RHS terms of the governing equations that are not multiplied by a velocity or a primary variable. The terms multiplied by the velocities are formed into two 12-value column vectors that come from the coefficients of the velocity terms on the right-hand side of the governing equations. The coefficients in the A matrix are provided in Appendix A.

6.4.2 Momentum Matrix Solution Formulation

Eqn. 6.15 represents the time and space discretized momentum equation for all six fields. These equations are used to solve for the new-time velocity terms that are in the mass and energy equations.

Moving all the terms with a factor of new time velocity in Eqn. 6.15 to the left and all

other terms (including pressures) to the right results in the linear system shown in 6.42.

$$\overline{\overline{A}}^{n}_{v,j}\overline{v}^{n+1}_{j} = \overline{\overline{A}}^{n}_{p,j}\overline{P}^{n+1} + \overline{b}^{n}_{v,j} \tag{6.42}$$

Where the $\overline{\overline{A}}^{n}_{v,j}$ is a 6×6 matrix with coefficients that are the multipliers of the velocity terms in the momentum equation at point j. The $\overline{v}^{n+1}_{j}$ vector is made up of the six new time velocities. The matrix of pressure multipliers associated with grid point j is $\overline{\overline{A}}^{n}_{p,j}$. The pressure coefficient matrix is of dimension $6 \times N$, where N is the number of control volumes in the problem. The pressures in the N control volumes are in the $N \times 1$ vector $\overline{P}$. The remaining old-time terms are in the 6×1 $\overline{b}^{n}_{v,j}$ vector.

Since $\overline{\overline{A}}^{n}_{v,j}$ is nonsingular for sufficiently small values of Δt, so the velocity vector at new time is produced by multiplying all the terms in Eqn. 6.42 by $\left(\overline{\overline{A}}_{v,j}\right)^{-1}$. This gives an expression for the velocity vector at new time in terms of pressures, old-time quantities and $\overline{b}^{n}_{v,j}$, shown in Eqn. 6.43.

$$\overline{v}^{n+1}_{j} = \left(\overline{\overline{A}}^{n}_{v,j}\right)^{-1}\overline{\overline{A}}^{n}_{p,j}\overline{P}^{n+1} + \left(\overline{\overline{A}}^{n}_{v,j}\right)^{-1}\overline{b}^{n}_{v,j} \tag{6.43}$$

There are six rows in $\overline{v}^{n+1}_{j}$, each one for the velocity of a different field. The new time velocity for field k can be expressed as one of the rows of Eqn. 6.43:

$$v^{n+1}_{k,j} = \mathrm{row}_k\left[\left(\overline{\overline{A}}^{n}_{v,j}\right)^{-1}\overline{\overline{A}}^{n}_{p,j}\overline{P}^{n+1} + \left(\overline{\overline{A}}^{n}_{v,j}\right)^{-1}\overline{b}^{n}_{v,j}\right] \tag{6.44}$$

6.4.3 Solving the Matrix

As shown in Eqn. 6.44, the velocity at any junction within the model depends on the pressures in every volume in the model. This effectively links the 6×6 system of mass and energy governing equations for individual volumes represented by Eqn. 6.39 together into one large system. By arranging the system of equations represented by Eqn. 6.39 on the

diagonal of a larger matrix, a $12N \times 12N$ system is obtained, where N is the number of volumes in the problem. The matrix equation for the larger system is:

$$\overline{\overline{A}}^{*,n} \Delta \overline{X}^{\sim n+1} = \overline{b}^{*,n} + \sum_{k=1}^{6} \left\{ g_{k,j+1}^{n} \left(\text{row}_k \left[\left(\overline{\overline{A}}_{v,j+1}^{n} \right)^{-1} \overline{\overline{A}}_{p,j+1}^{n} \overline{P}^{n+1} + \left(\overline{\overline{A}}_{v,j+1}^{n} \right)^{-1} \overline{b}_{v,j+1}^{n} \right] \right) + g_{k,j}^{n} \left(\text{row}_k \left[\left(\overline{\overline{A}}_{v,j}^{n} \right)^{-1} \overline{\overline{A}}_{p,j}^{n} \overline{P}^{n+1} + \left(\overline{\overline{A}}_{v,j}^{n} \right)^{-1} \overline{b}_{v,j}^{n} \right] \right) \right\} \tag{6.45}$$

Where $\overline{\overline{A}}^{*,n}$ is the $12N \times 12N$ coefficient matrix made up of all N Eqn. 6.39 systems on the diagonal. The $\Delta \overline{X}^{\sim n+1}$ vector is an augmented vector from 1 to N that contains the $\Delta x_L^{\sim n+1}$ vectors from $L = 1$ to $L = N$. The same is true of the $\overline{b}^{*,n}$ vector.

The solution of Eqn. 6.45 are the values of the temporal differences in vector $\Delta \overline{X}^{\sim n+1}$ for all the volumes in the system, which can be used with the old-time values to obtain provisional new-time values for all the primary variables except pressure, which is obtained at new time.

6.4.4 Moving Primary Variables from Provisional New Time to New Time

To obtain the primary variables at "non-provisional" new time, the mass (Eqn. 6.9) is solved for $(\alpha\rho)_{k,L}^{n+1}$ using the provisional temperature terms that are obtained from the linearized approximations to new time variables shown in Section 6.2. This is done for each of the six fields.

The un-expanded energy equation (Eqn. 6.27) is then solved for $(\alpha\rho U)_{k,L}^{n+1}$. Dividing $(\alpha\rho U)_{k,L}^{n+1}$ by $(\alpha\rho)_{k,L}^{n+1}$ gives $U_{k,L}^{n+1}$ for each field.

The volume fraction of field k at new time $(\alpha_{k,L}^{n+1})$ can then be calculated from $(\alpha\rho)_{k,L}^{n+1}$

using:

$$\alpha_{k,L}^{n+1} = \frac{(\alpha\rho)_{k,L}^{n+1}}{\tilde{\rho}_{k,L}^{n+1}} \tag{6.46}$$

Where $\tilde{\rho}_{k,L}^{n+1}$ is as defined in Eqn. 6.30. Equation 6.46 can now be used to compute the volume fractions for each of the six fields. This completes the calculation of the set of primary variables at new time, and the calculation of the next timestep begins.

CHAPTER 7

Summary and Conclusions

The development of system analysis codes for nuclear systems is important to the advancement of the nuclear industry. These codes aid designers in efforts to develop safer, more efficient nuclear plants. Current system codes typically have only two fields, one for each phase (liquid and vapor). This simplification assumes that all the liquid (continuous liquid, large droplets, and small droplets) are modeled as one field having the same temperature, pressure, and velocity. The same approximation applies to the vapor field, where the continuous vapor as well as the large and small bubbles are represented by a single field and share a single velocity, temperature, and pressure.

Severe accident scenarios tax the capabilities of a two-field model. Many of the modern system codes are being expanded to include additional or new conservation equations to model additional fields. These changes have been found to improve the modeling capabilities of these codes.

This dissertation shows the development of two-phase, six-field conservation equations for six fields: liquid, small droplet, large droplet, vapor, small bubble, and large bubble. The two-phase six-field model includes six mass conservation equations that include source terms that represent the mass transfer from one field to another. This mass transfer can occur due to phase change, as well as physical mechanisms. These physical mechanisms include liquid and droplets interacting with the spacer grids and high velocity vapor flows causing droplet entrainment. Specific closure relationships are required to provide the value of these source terms in a full system analysis.

The six momentum continuity equations have been developed by including momentum exchange resulting from phase change and the same physical mechanisms that affect the mass continuity. The models capture the increase in momentum for the small droplet field when the large droplets break up due to vapor flow conditions or impacts with the spacer grids. The momentum of the continuous liquid field is reduced as droplets are entrained

into the vapor field. The current derivation is formulated to allow for the droplet fields to have different velocities from the continuous liquid, as well as different velocities for the two droplet fields.

Other system codes that have been modified to include additional fields have simplified the energy continuity equations by making the assumption that the droplet field is at the same temperature as the continuous liquid field. This allows for a single energy equation to represent all the liquid phase, including droplets and continuous liquid. The model presented here allows the droplet field to be at a different temperature from the continuous liquid. This requires additional energy conservation equations, which have been included in the derivation.

Closure models for two-field system codes account for a limited set of parameters in the governing equations. Since the governing equations in a two-field representation do not directly track bubbles or droplets, the closure models do not need to solve for the interactions between these fields. The governing equations must only account for mass, momentum, and energy exchange across a single interface. Accuracy is improved if the flow regime can be approximated (e.g. bubbly or annular) and appropriate heat transfer coefficients applied, but this is not necessary to close the system, where any reasonable model of the interfacial interactions will suffice.

The six-field governing equations outlined in Chapter 3 require specified closure models for interactions that arise from the increased detail of the six-field formulation. Since the governing equations must account for physical interactions that cause large droplets to break up and join the small droplet field, closure models are identified that represent that exchange. The closure models presented herein will complete the mass balance for the six-field two-phase flow model outlined in Chapter 3. These closure relationships provide the necessary input to solve the six-field governing equations, including the breakup of droplets due to flow effects and the spacer grids. Models have also been presented to account for bubble interactions (coalescence and breakup).

This dissertation shows the newly developed governing equations, justifications, and explanations for six fields. The six fields can provide a more realistic representation of the two-phase flows than one or two field models, which are commonly used in nuclear system codes. The primary variables for the six-field representation were also identified, which is also a unique contribution to the reactor analysis field. The number of variables was reduced using theorems and correlations before the equations were discretized spatially and temporally. Then, Taylor's theorem and the multi-dimensional chain rule were used to produce a set of equations with only the primary variables at new time. The resulting system was organized as matrix equations, and a method for solving the system was presented. This solution method was not previously available for solution of a six-field system of equations.

Future work in this field includes the code development of the proposed model. When the model has been implemented in a system code, it will be possible to test it against experimental results to evaluate the performance. It is difficult at this time to predict how much improvement in accuracy to expect, since the current codes that have added fields do not generally include the energy equations for the new fields, unlike the model proposed in this work. Additional future work includes the adaptation of the six-field model for vessel (3D) components and determining (by way of experiments if necessary) more of the closure models that are needed (such as droplet coalescence).

This work has developed an innovative, unique set of equations with applicable closure relationships that will model two-phase flows in more detail than has been attempted previously in a nuclear system code. The equations, closure models, identification of the primary variables and solution scheme constitute a novel application of the available theory that will provide useful capability to the existing system codes. The increased accuracy in reactor system modeling has the potential to reduce operational costs by increasing rated powers and improving accident response performance of the reactor system by removing uncertainties in the analysis.

References

[1] U.S. Nuclear Regulatory Commission, Washington, DC, TRACE V5.0 Theory Manual, 2008. Accession Number: ML120060218.

[2] Idaho National Laboratory, Idaho Falls, ID, RELAP5-3D Code Manual Volume IV: Models and Correlations, 2012. INEEL-EXT-98-00834.

[3] C. Frepoli et. all, Realistic LOCA Evaluation Methodology Applied to the Full Spectrum of Break Sizes (FULL SPECTRUM LOCA Methodology), Volume 1, Part 1. Westinghouse Electric Company, Cranberry Township, PA, 2010. WCAP-16996-NP.

[4] J.W. Spore et. all, TRAC-M/FORTRAN 90 Theory Manual. Los Alamos National Laboratory, Los Alamos, NM, 2001. NUREG/CR-6724.

[5] F. Bassenghi, Validation of the CFD Code NEPTUNE for a Full-Scale Simulator for Decay Heat Removal Systems With In-Pool Heat Exchangers. PhD Thesis, Universitá di Bologna, Bologna, IT, 2013. See also URL `http://amsdottorato.cib.unibo.it`.

[6] M. Ishii, "One-Dimensional Drift-Flux Model and Constitutive Equations for Relative Motion Between Phases in Various Flow Regimes," Internal Report ANL-77-47, Argonne National Laboratory, Fairfield, CT, March 1977.

[7] S. Ergun, Modeling of Dispersed Flow Film Boiling With Two Flow, Five Field Eulerian-Eulerian Approach and Effects of Spacer Grids on Heat Transfer. PhD Thesis, Pennsylvania State University, State College, PA, May 2006.

[8] K. H. Ardron and P. C. Hall, "Droplet hydrodynamics in the dispersed flow regime in bottom flooding," in Transient Two-Phase Flow: Proceedings of the Third CSNI Specialist Meeting (M. S. Plesset, N. Zuber, and I. Catton, eds.), (New York), pp. 205–225, Nuclear Energy Agency, Hemisphere Publishing Corporation, 1983.

[9] X. Sun, S. Kim, M. Ishii, and S. Beus, "Modeling of bubble coalescence and disintegration in confined upward two-phase flow," Nuclear Engineering and Design, vol. 230, pp. 3–26, May 2004.

[10] P. Saha and N. Zuber, "Point of net vapor generation and vapor void fraction in subcooled boiling," in Proceedings Fifth International Heat Transfer Conference, vol. **4**, (Tokyo, Japan), pp. 175–179, September 1974.

[11] R. Aris, Vectors, Tensors, and the Basic Equations of Fluid Mechanics. Toronto, Ontario: Dover, 1962.

[12] G. A. Roth and F. Aydogan, "Theory and implementation of nuclear safety system codes - part I: Conservation equations, flow regimes, numerics and significant assumptions," Progress in Nuclear Energy, vol. 76, pp. 160–182, September 2014.

[13] G. A. Roth and F. Aydogan, "Theory and Implementation of Nuclear Safety System Codes - Part II: System Code Closure Relations, Validation, and Limitations," Progress in Nuclear Energy, vol. 76, pp. 55–72, September 2014.

[14] S. Jayanti and M. Valette, "Prediction of dryout and post-dryout heat transfer at high pressures using a one-dimensional three-fluid model," International Journal of Heat and Mass Transfer, vol. 47, pp. 4895–4910, 2004.

[15] A. Guelfi and e. a. D. Bestion, "NEPTUNE: A New Software Platform for Advanced Nuclear Thermal Hydraulics," Nuclear Science and Engineering, vol. 156, pp. 281–324, 2007.

[16] S. Bajorek, "Trace development and status." Thermal-Hydraulic Codes News, March 2008. U.S. NRC publication.

[17] W. J. Shack, "Development of the TRACE Thermal-Hydraulic System Analysis Code." Personal Communication from W. J. Shack to D. E. Klein, September 2008. ML082540133.

[18] J. D. Talley, T. Worosz, S. Kim, S. M. Bajorek, and K. Tien, "Effect of Bubble Interactions on the Prediction of Interfacial Area in TRACE," Nuclear Engineering and Design, vol. 264, pp. 135–145, 2013.

[19] R. F. Kunz, B. W. Siebert, W. K. Cope, N. F. Foster, S. P. Antal, and S. M. Ettorre, "A Coupled Phasic Exchange Algorithm for Three-Dimensional Multi-Field Analysis of Heated Flows with Mass Transfer," Computers and Fluids, vol. 27, September 1998.

[20] G. L. Mesina, "A history of relap5 computer codes," Nuclear Science and Engineering, vol. 182, pp. v–ix, January 2016.

[21] J. W. Spore et al., TRAC-M/FORTRAN 90 (Version 3.0) Theory Manual. U.S. Nuclear Regulatory Commission, Washington, DC, 2001. NUREG/CR-6724.

[22] Idaho National Laboratory, Idaho Falls, ID, RELAP5-3D Code Manual Volume I: Code Structure, System Models and Solution Methods, 2012. INEEL-EXT-98-00834.

[23] D. Anders, R. Berry, D. Gaston, R. Martineau, J. Peterson, H. Zhang, H. Zhao, and L. Zou, "RELAP-7 Level 2 Milestone Report: Demonstration of a Steady State Single Phase PWR Simulation with RELAP-7," Internal Report INL/EXT-12-25924, Idaho National Laboratory (INL), Idaho Falls, ID, 2012.

[24] H. Zhang, H. Zhao, L. Zou, D. Anders, J. Peterson, R. Berry, and R. Martineau, "RELAP-7: Demonstrating Seven-Equation, Two-Phase Flow Simulation in a Single-Pipe, Two-Phase Reactor Core and Steam Separator/Dryer," Internal Report INL/EXT-13-28750, Idaho National Laboratory (INL), Idaho Falls, ID, 2013.

[25] R. A. Berry, R. Saurel, and O. LeMetayer, "The discrete equation method (dem) for fully-compressible two-phase flows in ducts of spatially varying cross-section," Nuclear Engineering and Design, vol. 240, pp. 3797–3818, 2010.

[26] Gesellschaft fur Anlagen-und Reaktorsicherheit (GS) mbH, ATHLET Mod 2.1 Cycle A - Models and Methods, 2006. GRS-P-1 - Vol 4.

[27] D. Bestion, "The physical closure laws in the cathare code," Nuclear Engineering and Design, vol. 124, pp. 229–245, 1990.

[28] Y. Taitel, B. Barnea, and A. E. Dukler, "Modeling Flow Pattern Transitions for Steady Upward Gas-Liquid Flow in Vertical Tubes," AIChE Journal, vol. 26, pp. 345–354, 1980.

[29] D. R. L. et al., "TRAC-PF1/MOD1 Correlations and Models," Technical Report NUREG/CR-5069, Los Alamos National Laboratory, Los Alamos, NM, Dec 1988.

[30] F. Barre and M. Bernard, "The cathare code strategy and assessment," Nuclear Engineering and Design, vol. 124, pp. 257–284, 1990.

[31] G. B. Wallis, One-dimensional Two-phase flow. New York: McGraw-Hill, 1969.

[32] M. Ishii and T. C. Chawla, "Local Drag Laws in Dispersed Two-Phase Flow," Internal report ANL-79-105, Argonne National Laboratory, Argonne, IL, December 1979. NUREG/CR-1230.

[33] B. Chexal and G. Lellouche, "A Full-Range Drift-Flux Correlation for Vertical Flows (Revision 1)," Internal Report EPRI NP-3989-SR, Electric Power Research Institute, Palo Alto, CA, September 1986.

[34] B. C. et. al., "The Chexal-Lellouche Void Fraction Correlation for Generalized Applications," Internal Report NSAC-139, Electric Power Research Institute, Palo Alto, CA, April 1991.

[35] B. C. et. al., "Void Fraction Technology for Design and Analysis," Internal Report TR-106326, Electric Power Research Institute, Palo Alto, CA, March 1997.

[36] P. Griffith, "The prediction of low-quality boiling voids," Transactions of the ASME, Journal of Heat Transfer, vol. 86, pp. 327–333, 1964.

[37] J. M. Putney, "Development of a new bubbly-slug interfacial friction model for relap5," Nuclear Engineering and Design, vol. 131, pp. 223–240, 1991.

[38] I. Kataoka and M. Ishii, "Drift flux model for large diameter pipe and new correlation for pool void fraction," International Journal of Heat and Mass Transfer, vol. 30, pp. 1927–1939, 1987.

[39] N. Zuber and J. Findlay, "Average volumetric concentrations in two-phase flow systems," Transactions of the ASME, Journal of Heat Transfer, vol. 87, pp. 453–568, 1965.

[40] N. Z. et. al., "Steady-State and Transient Void Fraction in Two-Phase Flow Systems," Internal Report GEAP-5417, General Electric Company, Argonne, IL, 1967.

[41] J. F. Lime, "Memorandum on Interfacial Drag from M. Ishii to R. Nelson," Internal Memo LA-RA-01-1591, Los Alamos National Laboratory, Los Alamos, NM, 28 July 1987.

[42] J. F. Wilson, R. J. Grenda, and J. F. Patterson, "Steam volume fraction in a bubbling two phase mixture," Transactions of the American Nuclear Society, vol. 4, no. 2, pp. 356–357, 1961.

[43] H. G. Sonnenburg, "Calculating the phase difference and rate of water vapor in different geometric bounded channels," Internal Report GRS-109, Gesellschaft fur Anlagen-und Reaktorsicherheit (GS) mbH, Cologne, Germany, 1994. Berechnung der Phasendif-

ferenzgeschwindigkeit von Wasser und Dampf in geometrisch unterschiedlich berandeten Kanalen.

[44] S. Nukiyama and Y. Tanasawa, "The cathare code strategy and assessment," Transactions of the Society of Mechanical Engineers (Japan), vol. 5, no. 18, p. 63, 1969.

[45] R. A. Riemke, "Modification to Unal's Subcooled Flow Boiling Bubble Model," Nuclear Technology, vol. 102, pp. 416–417, 1993.

[46] H. Unal, "Maximum Bubble Diameter, Maximum Bubble-Growth Time and Bubble Growth Rate During the Subcooled Nucleate Flow Boiling of Water up to 17.7 MN/m^2," International Journal of Heat and Mass Transfer, vol. 19, pp. 643–649, 1976.

[47] M. S. Plesset and S. A. Zwick, "Growth of vapor bubbles in superheated liquids," Journal of Applied Physics, vol. 25, no. 4, pp. 493–500, 1954.

[48] K. Lee and D. J. Ryley, "The evaporation of water droplets in superheated steam," Transactions of the ASME, Journal of Heat Transfer, vol. 90, pp. 445–451, 1968.

[49] G. Brown, "Heat Transmission of Condensation of Steam on a Spray of Water Drops," in Proceedings of the General Discussion on Heat Transfer, pp. 49–52, Institution of Mechanical Engineers, 1951.

[50] T. G. Theofanous, "Modeling of Basic Condensation Processes," in Proceedings, (Silver Springs, MD), 1979. The Water Reactor Safety Research Workshop on Condensation.

[51] E. Ranz and W. Marshall, "Evaporation from Droplets: part I and II," Chemical Engineering Progress, vol. 48, pp. 141–146, 173–180, 1952.

[52] R. Kronig and J. Brink, "On the theory of extraction from falling droplets," Applied Scientific Research, vol. A2, pp. 142–154, 1950.

[53] G. Ryskin, "Heat and mass transfer from a moving drop - some approximate relations for the nusselt number," Int. Comm. Heat Mass Transfer, vol. 14, pp. 741–749, 1987.

[54] M. Renksizbulut and M. C. Yuen, "Experimental study of droplet evaporation in a high-temperature air stream," Journal of Heat Transfer, vol. 105, no. 2, pp. 384–388, 1983.

[55] R. T. Lahey and F. J. Moody, The Thermal-Hydraulics of a Boiling Water Nuclear Reactor. Washington, D.C.: American Nuclear Society, 1977.

[56] S. Z. Kuhn, V. E. Schrock, and P. F. Peterson, "Final Report on U. C. Berkeley Single Tube Condensation Studies," Report UCB-NE-4201, U. C. Berkeley, Berkeley, CA, August 1994.

[57] K. K. Fung, Subcooled and Low Quality Film Boiling of Water in Vertical Flow at Atmospheric P PhD Thesis, University of Ottawa, Ottawa, Ontario, 1981.

[58] M. J. L. et. al., "PWR FLECHT-SEASET Unblocked Bundle, Forced and Gravity Reflood Task Data Report," Data Report NUREG/CR-1532, USNRC, Washington, DC, June 1980.

[59] Y. M. Chen and F. Mayinger, "Measurement of heat transfer at the phase interface of condensing bubbles," International Journal of Multiphase Flow, vol. 18, no. 6, pp. 877–890, 1992.

[60] S. G. Bankoff, "Some condensation studies pertinent to light water safety," International Journal of Multiphase Flow, vol. 6, pp. 51–67, 1980.

[61] J. G. M. Andersen, "REMI/HEAT COOL, a Model for Evaluation of Core Heat Up and Emergency Core Spray Cooling System Performance for Light Water Cooled Nuclear Power Reactors," Report 296, RISO National Lab Denmark, 1973.

[62] R. P. Forslund and W. M. Rohsenow, "Dispersed flow film boiling," Journal of Heat Transfer, vol. 90, pp. 399–407, November 1967.

[63] J. H. Linehan, M. Petrick, and M. M. El-Wakil, "The condensation of saturated vapor on a subcooled film during stratified flow," Chem. Eng. Symp. Series, vol. 66, no. 102, pp. 11–20, 1972.

[64] S. Whittaker, "Forced convection heat transfer correlations for flows in pipes, past flat plates, single cylinder, single sphere, and flows in packed beds and tube bundles," AIChE Journal, vol. 18, pp. 361–371, March 1972.

[65] M. C. Yuen and L. W. Chen, "Heat transfer measurements of evaporating liquid," Journal of Heat and Mass Transfer, vol. 21, pp. 537–542, May 1978.

[66] C. Unal, K. Tuzla, C. A. Tuzla, and J. C. Chen, "Vapor generation model for dispersed drop flow," in ANS Proceedings 1989 National Heat Transfer Conference, p. 56, American Nuclear Society, August 1989. HTC-Vol.4.

[67] K. Pasamehmetoglu and R. Nelson, "Transient direct-contact condensation on liquid droplets," Nonequilibrium Transport Phenomena, vol. 77, pp. 47–56, 1987.

[68] R. Pernica and J. Cizek, "PG General Correlation of CHFR and Statistical Evaluation Results," Report UJV-10156-T, NRI, 1994.

[69] R. Pernica and J. Cizek, "General correlation for prediction of critical heat flux ratio," in Proceedings of the 7^{th} International Meeting on Nuclear Reactor Thermal-Hydraulics, (Washington, DC), USNRC, U.S. Nuclear Regulatory Commission, September 1995. NUREG/CP-0142.

[70] J. C. Chen, R. K. Sundaram, and F. T. Ozkaynak, A Phenomenological Correlation for Post-CHF Heat Transfer. Washington, D.C.: U.S. Nuclear Regulatory Commission, 1977.

[71] J. C. Stewart and D. C. Groeneveld, "Low-quality and subcooled film boiling of water at elevated pressures," Nuclear Engineering Design, vol. 67, pp. 259–272, 1981.

[72] T. A. Bjornard and P. Griffith, "Pwr blowdown heat transfer," Thermal and Hydraulic Aspects of Nuclear Reactor Safety, vol. 1, pp. 17–41, 1977.

[73] L. B. et. al, "Studies on burnout, part 3," Energia Nucleare, vol. 14, no. 9, pp. 530–536, 1967.

[74] R. E. Henry, "A correlation for the minimum film boiling temperature," AICHE Symposium Series, vol. 138, pp. 81–90, 1974.

[75] L. S. Tong, "Prediction of departure from nucleate boiling for one axially non-uniform heat flux distribution," Journal of Nuclear Energy, vol. 21, pp. 241–248, 1967.

[76] B. C. Silfer and J. E. Hench, "Loss-of-Coolant Accident and Emergency Core Cooling Models for General Electric BWR," Technical Report NEDO-10329, General Electric Co., San Jose, CA, 1971.

[77] Israel, Casterline, and Matzner, "Critical heat flux measurements in 16 rod simulation of a bwr fuel assembly," Journal of Heat Transfer, pp. 34–36, August 1969.

[78] N. Z. et al., "The hydrodynamic crisis in pool boiling of saturated and subcooled liquids," International Development in Heat Transfer, Part II, no. 27, 1961.

[79] C. F. Avedisian and P. Griffith Technical Report 80620-84, MIT, Boston, MA, 1974.

[80] e. a. Y. A. Bezrukov, "Experimental investigations and statistical analysis of chf data obtained in models of vver fuel assemblies," Teploenergetika, vol. N2, pp. 80–82, 1976.

[81] V. S. Osmachkin Technical Report Preprint IAE-2345, Kurtschatov Institute, Moscow, 1974.

[82] V. K. Ivanov and L. L. Kobzar, "Calculation of critical heat flux in rod bundles with local turbulators," Atomnaya Energiya, vol. 54, pp. 395–399, June 1983.

[83] S. Mirshak, W. S. Durant, and R. H. Towell, "Heat Flux at Burn-out," Technical Report DP-355, Savannah River Laboratory, February 1959.

[84] V. E. Doroschuk, L. L. Levitan, and F. P. Lantzman, "Tabular data for calculating burnout when boiling water in uniformly heated round tubes," Teploenergetika, vol. 23, pp. 90–92, September 1976.

[85] D. C. Groeneveld and J. C. Stewart, "The minimum film boiling temperature for water during film boiling collapse," in Proceedings of the 7^{th} International Heat Transfer Conference (U. G. et. al., ed.), Hemisphere Publishing Corporation, 1982.

[86] D. C. Groeneveld, S. C. Cheng, and T. Doan, "1986 aecl-uo critical heat flux lookup table," Heat Transfer Engineering, vol. 7, pp. 46–62, 1986.

[87] G. T. Analytis, "Developmental assessment of relap5/mod3.1 with separate effect and integral test experiments: Model changes and options," Nuclear Engineering and Design, vol. 163, pp. 125–148, September 1996.

[88] J. Weisman, "Studies of Transition Boiling Heat Transfer at Pressure from 1-4 Bar," Internal Report EPRI NP-1899, Electric Power Research Institute, Palo Alto, CA, 1981.

[89] L. A. Bromley, "Heat transfer in stable film boiling," Chemical Engineering Progress, vol. 46, pp. 221–227, 1950.

[90] K. H. Sun, J. M. Gonzalez-Santalo, and C. L. Tien, "Calculations of combined radiation and convection heat transfer in rod bundles under emergency cooling conditions," Transactions of the ASME, Journal of Heat Transfer, vol. 98, pp. 414–420, 1976.

[91] N. Zuber, M. Tribus, and T. W. Westwater, "The hydrodynamic crisis in pool boiling of saturated and subcooled liquids," in International Developments in Heat Transfer: Proceedings of the 1961-62 Heat Transfer Conference, (New York), pp. 230–236, American Society of Mechanical Engineers, August 1963.

[92] R. Semeria and B. Martinet, "Calefaction spots on a heating wall: Temperature distribution and resorption," Proceedings of the Institute of Mechanical Engineers, vol. 180, 1966.

[93] A. Yamanouchi, "Effect of core spray cooling in transient state after loss of cooling accident," Nuclear Science and Technology, vol. 5, no. 11, 1968.

[94] D. Juhel, "A study of interfacial and wall heat transfer downstream of a quench front," in European Two-Phase Flow Group Meeting, June 1984. Rome.

[95] P. Clement and P. Regnier, "Heat transfer modeling at the quench front during reflooding phase in a loca - interpretation of experimental results," in European Two-Phase Flow Group Meeting, 1978. Stockholm.

[96] R. Shumway, "Consolidation of TRAC Codes: Task CHAN ," Internal Report SCIE-NRC-375-99, Scientech, Idaho Falls, ID, January 1999. ADAMS Accession No. ML071710042.

[97] T. Group, "CSNI Code Validation Matrix of Thermo-Hydraulic Codes for LWR LOCA and Transients," Internal Report CSNI Report 132, OECD-CSNI, Paris, France, March 1987.

[98] N. Aksan, F. D'Auria, H. Glaeser, J. Lillington, R. Pochard, and A.Sjoberg, "Evaluation of the Separate Effects Tests (SET) Validation Matrix," Internal Report OECDE/GD(97)9, OECD-CSNI, Paris, France, November 1996. NEA/CSNI/R(96)16.

[99] N. Aksan, "Overview on CSNI Separate Effects Test Facility Matrices for Validation of Best Estimate Thermal-Hydraulic Computer Codes," in Proceedings of THICKET 2008, (Switzerland), pp. 23–43, Paul Scherrer Institut (PSI), 2008. Session III - Paper number 03.

[100] Idaho National Laboratory, Idaho Falls, ID, RELAP5-3D Code Manual Volume III: Developmental Assessment, 2012. INEEL-EXT-98-00834.

[101] "Transient and Accident Analysis Methods," Regulatory Guide 1.203, USNRC, December 2005.

[102] A. Gelman, J. B. Carlin, H. S. Stern, D. B. Dunson, A. Vehtari, and D. B. Rubin, Bayesian Data Analysis. Boca Raton, FL: CRC Press, 2014.

[103] A. Bui, N. Dinh, and B. Williams, "Validation and Calibration of Nuclear Thermal Hydraulics Multiscale Multiphysics Models - Subcooled Boiling Study," Report INL/EXT-13-30293, Idaho National Laboratory (INL), Idaho Falls, ID, 2013.

[104] M. Ishii and T. Hibiki, Thermo-Fluid Dynamics of Two-Phase Flow. New York, NY: Springer, 2006.

[105] V. H. Ransom, "Couse A - Numerical Modeling of Two-Phase Flows For Presentation at Ecole d'Ete d'Analyse Numerique," Informal Report EGG-EAST-8546, EG&G Idaho, Idaho Falls, ID, May 1989.

[106] G. A. Roth and F. Aydogan, "Derivation of new mass, momentum, and energy conservation equations for two-phase flows," Progress in Nuclear Energy, vol. 80, pp. 90–101, April 2015.

[107] M. J. Holowach, A Physical Model for Predicting Droplet Entrainment in Transient Two-Phase Fluid Flow and Heat Transfer Systems Analysis Computer Codes. PhD Thesis, Pennsylvania State University, State College, PA, December 2002.

[108] N. Lee, S. Wong, H. Yeh, and L. Hochreiter, "Pwr flecht seaset unblocked bundle, forced gravity reflood task data evaluation and analysis report," Tech. Rep. WCAP 9891, Westinghouse Electric Corporation, Monroeville, PA, February 1982. EPRI NP-2013/NUREG CR-2256.

[109] M. Denham, "Heat Transfer Near the Quench Front in Single Tube Reflooding Experiments," Tech. Rep. AEEW-R-1436, Atomic Energy Establishment, Winfrith, England, May 1981.

[110] M. Denham, D. Elliot, and K. Shawyer, "Fundamental Studies of the Reflooding of an Inconel Tube in the REFLEX Rig," Tech. Rep. AEEW-R-1353, Atomic Energy Establishment - Reactor Development Division, Winfrith, Dorchester, England, August 1980.

[111] L. Pan and T. J. Hanratty, "Correlation of entrainment for annular flow in horizontal pipes," International Journal of Multiphase Flow, vol. 28, pp. 385–408, March 2002.

[112] I. Kataoka, M. Ishii, and K. Mishima, "Generation and Size Distribution of Droplets in Gas-Liquid Annular Two-Phase Flow," Journal of Fluids Engineering, vol. 105, pp. 230–238, June 1983.

[113] K. A. Williams, Numerical Fluid Dynamics of Nonequilibrium Steam-Water Flows with Droplets. PhD Thesis, University of New Mexico, May 1983.

[114] E. Rosal et al., "The pennsylvania state university and u.s. nuclear regulatory commission rod bundle heat transfer facility," in Proceedings of the 6^{th} ASME-JSME Thermal Engineering Joint Conference, March 2003.

[115] C. Y. Paik, L. E. Hochreiter, J. M. Kelly, and R. J. Kohrt, "Analysis of FLECHT-SEASET 163-Rod Blocked Bundle Data Using COBRA-TF," Report NUREG/CR-4166, USNRC, Washington, DC, October 1985.

[116] J. Qian and C. Law, "Regimes of coalescence and separation in droplet collision," Journal of Fluid Mechanics, vol. 331, no. 9, pp. 59–80, 1997.

[117] L. Williams, L. Dykhno, and T. Hanratty, "Droplet flux distributions and entrainment in horizontal gas-liquid flows," International Journal of Multiphase Flow, vol. 22, no. 1, pp. 1–18, 1996.

[118] X. Sun, Two-Group Interfacial Area Transport Equation for a Confined Test Section. PhD Thesis, Perdue University, West Lafayette, IN, 2001.

[119] G. A. Roth and F. Aydogan, "Mass closure models for a system code based on six fields," Progress in Nuclear Energy, vol. 94, pp. 147–1161, 2017.

[120] R. T. Lahey, "A Mechanistic Subcooled Boiling Model," in Proceedings of the 6th International Heat Transfer Conference, Toronto, Canada, vol. 1, (Toronto, Canada), pp. 293–297, August 1978.

[121] R. Situ, T. Hibiki, M. Ishii, and M. Mori, "Bubble lift-off size in forced convective subcooled boiling flow," International Journal of Heat and Mass Transfer, vol. 48, pp. 5536–5548, December 2005.

[122] L. Z. Zeng, J. F. Klausner, D. M. Bernhard, and R. Mei, "A unified model for the prediction of bubble detachment diameters in boiling systems – II. Flow boiling," International Journal of Heat and Mass Transfer, vol. 36, no. 9, pp. 2271–2279, 1993.

[123] V. H. Ransom and M. P. Schofield, "Two-pressure hydrodynamic model for two-phase separated flow," Tech. Rep. SRD-50-76, Idaho National Engineering Laboratory, Idaho Falls, ID, February 1976.

[124] J. W. Gibbs, The Scientific Papers of J.Willard Gibbs, Vol. 1: Thermodynamics. Mineola, NY: Dover Publications, 1961.

APPENDIX A

Linearized Governing Equations

This Appendix shows the linearized governing equations in their final form for matrix solution. Note that each equation is annotated to indicate the parts of the equation that are coefficients in the A matrix (Eqn. 6.40), b vector, or g vectors. The equations are arranged in the same order as the rows of the $\overline{\overline{A}}$ matrix in Eqn. 6.40. Thus, the energy equations for fields 1 through 6 come first, followed by the mass balance equations for fields 1 through 6.

A.1 Energy Equations in Terms of Primary Variables

Eqn. A.1 is the energy balance equation for the continuous liquid field, and constitutes the first row in the final matrix expression. Note that there are terms on the LHS of the equation that are differences of the primary variables at new time and old time (e.g. $P_L^{n+1} - P_L^n$). The coefficients in front of the primary variable differences are the values that will be in the $\overline{\overline{A}}$ matrix of the solution. The difference expressions will be in the $\Delta\overline{x}$ vector that is multiplied by the $\overline{\overline{A}}$ matrix. Boxes have been drawn around the coefficients, and the notation added to the box indicates which matrix or vector position that term will have. For example, the notation of $A_{1,1}$ adjacent to a boxed section of the equation indicates that the expression inside the box is located in the top left position in the $\overline{\overline{A}}$ matrix.

Continuous Liquid ($k = 1$):

$$\boxed{\left[-\Delta t\left(H_{1,4}\frac{h_1^*}{h_4^*-h_1^*}\right)_L^n\left(\frac{\partial T^s}{\partial U_4}-\frac{\partial T_4}{\partial U_4}\right)_L^n-\Delta t\left(H_{4,1}\frac{h_4^*}{h_4^*-h_1^*}+H_{6,1}\frac{h_6^*}{h_6^*-h_1^*}+\right.\right.}$$
$$\boxed{\left.\left.H_{5,1}\frac{h_5^*}{h_5^*-h_1^*}+H_{1,6}\frac{h_1^*}{h_6^*-h_1^*}+H_{1,5}\frac{h_1^*}{h_5^*-h_1^*}\right)_L^n\left(\frac{\partial T^s}{\partial U_4}\right)_L^n\right]}^{A_{1,4}}\boxed{\left(U_{4,L}^{\sim n+1}-U_{4,L}^n\right)}^{x_4}+$$
$$\boxed{\left[\left(\alpha_1U_1\frac{\partial\rho_1}{\partial U_1}\right)_L^n+(\alpha_1\rho_1)_L^n+\Delta t\left(H_{4,1}\frac{h_4^*}{h_4^*-h_1^*}+H_{6,1}\frac{h_6^*}{h_6^*-h_1^*}+H_{5,1}\frac{h_5^*}{h_5^*-h_1^*}\right)_L^n\right.}$$
$$\boxed{\left.\left(\frac{\partial T_1}{\partial U_1}\right)_L^n\right]}^{A_{1,1}}\boxed{\left(U_{1,L}^{\sim n+1}-U_{1,L}^n\right)}^{x_1}+\boxed{\Delta t\left(H_{1,5}\frac{h_1^*}{h_5^*-h_1^*}\frac{\partial T_5}{\partial U_5}\right)_L^n}^{A_{1,5}}$$
$$\boxed{\left(U_{5,L}^{\sim n+1}-U_{5,L}^n\right)}^{x_5}+\boxed{\Delta t\left(H_{1,6}\frac{h_1^*}{h_6^*-h_1^*}\frac{\partial T_6}{\partial U_6}\right)_L^n}^{A_{1,6}}\boxed{\left(U_{6,L}^{\sim n+1}-U_{6,L}^n\right)}^{x_6}+$$
$$\boxed{(\rho_1U_1+P)_L^n}^{A_{1,7}}\boxed{\left(\alpha_{2,L}^{\sim n+1}-\alpha_{2,L}^n\right)}^{x_7}+\boxed{(\rho_1U_1+P)_L^n}^{A_{1,8}}$$
$$\boxed{\left(\alpha_{3,L}^{\sim n+1}-\alpha_{3,L}^n\right)}^{x_8}+\boxed{(\rho_1U_1+P)_L^n}^{A_{1,9}}\boxed{\left(\alpha_{4,L}^{\sim n+1}-\alpha_{4,L}^n\right)}^{x_9}+\boxed{(\rho_1U_1+P)_L^n}^{A_{1,10}}$$
$$\boxed{\left(\alpha_{5,L}^{\sim n+1}-\alpha_{5,L}^n\right)}^{x_{10}}+\boxed{(\rho_1U_1+P)_L^n}^{A_{1,11}}\boxed{\left(\alpha_{6,L}^{\sim n+1}-\alpha_{6,L}^n\right)}^{x_{11}}+$$
$$\boxed{\left[\left(\alpha_1U_1\frac{\partial\rho_1}{\partial P}\right)_L^n-\Delta t\left(H_{1,4}\frac{h_1^*}{h_4^*-h_1^*}\right)_L^n\left(\frac{\partial T^s}{\partial P}-\frac{\partial T_4}{\partial P}\right)_L^n-\Delta t\left(H_{4,1}\frac{h_4^*}{h_4^*-h_1^*}+\right.\right.} \tag{A.1}$$
$$\boxed{\left.\left.H_{6,1}\frac{h_6^*}{h_6^*-h_1^*}+H_{5,1}\frac{h_5^*}{h_5^*-h_1^*}\right)_L^n\left(\frac{\partial T^s}{\partial P}-\frac{\partial T_1}{\partial P}\right)_L^n-\Delta t\left(H_{1,6}\frac{h_1^*}{h_6^*-h_1^*}\right)_L^n\right.}$$
$$\boxed{\left(\frac{\partial T^s}{\partial P}-\frac{\partial T_6}{\partial P}\right)_L^n-\Delta t\left(H_{1,5}\frac{h_1^*}{h_5^*-h_1^*}\right)_L^n\left(\frac{\partial T^s}{\partial P}-\frac{\partial T_5}{\partial P}\right)_L^n\right]}^{A_{1,12}}\boxed{\left(P_L^{n+1}-P_L^n\right)}^{x_{12}}=$$
$$\boxed{\Delta t\left(H_{1,4}\frac{h_1^*}{h_4^*-h_1^*}\right)_L^n(T^s-T_4)_L^n+\Delta t\left(H_{4,1}\frac{h_4^*}{h_4^*-h_1^*}+H_{6,1}\frac{h_6^*}{h_6^*-h_1^*}+\right.}$$
$$\boxed{\left.H_{5,1}\frac{h_5^*}{h_5^*-h_1^*}+\right)_L^n(T^s-T_1)_L^n+\Delta t\left(H_{1,6}\frac{h_1^*}{h_6^*-h_1^*}\right)_L^n(T^s-T_6)_L^n+\Delta t\left(H_{1,5}\frac{h_1^*}{h_5^*-h_1^*}\right)_L^n}$$
$$\boxed{(T^s-T_5)_L^n-\Delta t\left[\left(\frac{1+\epsilon}{2}\right)h_6^{'n}+\left(\frac{1-\epsilon}{2}\right)h_1^{'n}\right]_L\Gamma_{w,6,1}^n-\Delta t\left[\left(\frac{1+\epsilon}{2}\right)h_5^{'n}+\right.}$$
$$\boxed{\left.\left(\frac{1-\epsilon}{2}\right)h_1^{'n}\right]_L\Gamma_{w,5,1}^n+\Delta t\left(\Gamma_{w,4,1}h_1^{'}+Q_{w,1}+DISS_1+S_{2,1}h_2-S_{1,2}h_1+S_{3,1}h_3-\right.}$$
$$\boxed{\left.S_{1,3}h_1\right)_L^n}^{b_1}-\boxed{\frac{\Delta t}{V_L}\dot{\alpha}_{1,j+1}^nA_{j+1}\left(\dot{\rho}\dot{U}+P_L\right)_{1,j+1}^n}^{g_{1,1}}\boxed{v_{1,j+1}^{n+1}}+$$
$$\boxed{\frac{\Delta t}{V_L}\dot{\alpha}_{1,j}^nA_j\left(\dot{\rho}\dot{U}+P_L\right)_{1,j}^n}^{g_{1,2}}\boxed{v_{1,j}^{n+1}}$$

Large Droplet ($k = 2$):

$$\boxed{\left[-\Delta t\left(H_{4,2}\frac{h_4^*}{h_4^*-h_2^*}\frac{\partial T^s}{\partial U_4}\right)_L^n-\Delta t\left(H_{2,4}\frac{h_2^*}{h_4^*-h_2^*}\right)_L^n\left(\frac{\partial T^s}{\partial U_4}-\frac{\partial T_4}{\partial U_4}\right)_L^n\right]}^{A_{2,4}}\times$$
$$\boxed{\left(U_{4,L}^{\sim n+1}-U_{4,L}^n\right)}^{x_4}+\boxed{\left[\left(\alpha_2U_2\frac{\partial\rho_2}{\partial U_2}\right)_L^n+\alpha_{2,L}^n\rho_{2,L}^n+\Delta t\left(H_{4,2}\frac{h_4^*}{h_4^*-h_2^*}\frac{\partial T_2}{\partial U_2}\right)_L^n\right]}^{A_{2,2}}\times$$
$$\boxed{\left(U_{2,L}^{\sim n+1}-U_{2,L}^n\right)}^{x_2}+\boxed{(\rho_2U_2+P)_L^n}^{A_{2,7}}\boxed{\left(\alpha_{2,L}^{\sim n+1}-\alpha_{2,L}^n\right)}^{x_7}+$$
$$\boxed{\left[\left(\alpha_2U_2\frac{\partial\rho_2}{\partial P}\right)_L^n-\Delta t\left(H_{4,2}\frac{h_4^*}{h_4^*-h_2^*}\right)_L^n\left(\frac{\partial T^s}{\partial P}-\frac{\partial T_2}{\partial P}\right)_L^n-\right.}$$
$$\boxed{\left.\Delta t\left(H_{2,4}\frac{h_2^*}{h_4^*-h_2^*}\right)_L^n\left(\frac{\partial T^s}{\partial P}-\frac{\partial T_4}{\partial P}\right)_L^n\right]}^{A_{2,12}}\boxed{\left(P_L^{n+1}-P_L^n\right)}^{x_{12}}= \tag{A.2}$$
$$\boxed{-\frac{\Delta t}{V_L}\dot{\alpha}_{2,j+1}^nA_{j+1}\left(\dot{\rho}\dot{U}+P_L\right)_{2,j+1}^n}^{g_{2,1}}\boxed{v_{2,j+1}^{n+1}}+\boxed{\frac{\Delta t}{V_L}\dot{\alpha}_{2,j}^nA_j\left(\dot{\rho}\dot{U}+P_L\right)_{2,j}^n}^{g_{2,2}}\boxed{v_{2,j}^{n+1}}+$$
$$\boxed{\Delta t\left(H_{4,2}\frac{h_4^*}{h_4^*-h_2^*}\right)_L^n(T^s-T_2)_L^n+\Delta t\left(H_{2,4}\frac{h_2^*}{h_4^*-h_2^*}\right)_L^n(T^s-T_4)_L^n+}$$
$$\boxed{\Delta t\left(S_{3,2}h_3^{'}-S_{2,3}h_2^{'}+S_{1,2}h_1^{'}-S_{2,1}h_2^{'}-S_{LD,DE}h_{LD}^{'}\right)_L^n}^{b_2}$$

Small Droplet ($k = 3$):

$$\boxed{\left[-\Delta t\left(H_{4,3}\frac{h_4^*}{h_4^*-h_3^*}\frac{\partial T^s}{\partial U_4}\right)_L^n-\Delta t\left(H_{3,4}\frac{h_3^*}{h_4^*-h_3^*}\right)_L^n\left(\frac{\partial T^s}{\partial U_4}-\frac{\partial T_4}{\partial U_4}\right)_L^n\right]}^{A_{3,4}}\times$$
$$\boxed{\left(U_{4,L}^{\sim n+1}-U_{4,L}^n\right)}^{x_4}+\boxed{\left[\left(\alpha_3U_3\frac{\partial\rho_3}{\partial U_3}\right)_L^n+\alpha_{3,L}^n\rho_{3,L}^n+\Delta t\left(H_{4,3}\frac{h_4^*}{h_4^*-h_3^*}\frac{\partial T_3}{\partial U_3}\right)_L^n\right]}^{A_{3,3}}\times$$
$$\boxed{\left(U_{3,L}^{\sim n+1}-U_{3,L}^n\right)}^{x_3}+\boxed{(\rho_3U_3+P)_L^n}^{A_{3,8}}\boxed{\left(\alpha_{3,L}^{\sim n+1}-\alpha_{3,L}^n\right)}^{x_8}+$$
$$\boxed{\left[\left(\alpha_3U_3\frac{\partial\rho_3}{\partial P}\right)_L^n-\Delta t\left(H_{4,3}\frac{h_4^*}{h_4^*-h_3^*}\right)_L^n\left(\frac{\partial T^s}{\partial P}-\frac{\partial T_3}{\partial P}\right)_L^n-\right.}$$
$$\boxed{\left.\Delta t\left(H_{3,4}\frac{h_3^*}{h_4^*-h_3^*}\right)_L^n\left(\frac{\partial T^s}{\partial P}-\frac{\partial T_4}{\partial P}\right)_L^n\right]}^{A_{3,12}}\boxed{\left(P_L^{n+1}-P_L^n\right)}^{x_{12}}= \tag{A.3}$$
$$\boxed{-\frac{\Delta t}{V_L}\dot{\alpha}_{3,j+1}^nA_{j+1}\left(\dot{\rho}\dot{U}+P_L\right)_{3,j+1}^n}^{g_{3,1}}\boxed{v_{3,j+1}^{n+1}}+\boxed{\frac{\Delta t}{V_L}\dot{\alpha}_{3,j}^nA_j\left(\dot{\rho}\dot{U}+P_L\right)_{3,j}^n}^{g_{3,2}}\boxed{v_{3,j}^{n+1}}+$$
$$\boxed{\Delta t\left(H_{4,3}\frac{h_4^*}{h_4^*-h_3^*}\right)_L^n(T^s-T_3)_L^n+\Delta t\left(H_{3,4}\frac{h_3^*}{h_4^*-h_3^*}\right)_L^n(T^s-T_4)_L^n+}$$
$$\boxed{\Delta t\left(S_{2,3}h_2^{'}-S_{3,2}h_3^{'}+S_{1,3}h_1^{'}-S_{3,1}h_3^{'}\right)_L^n}^{b_3}$$

The continuous vapor energy equation follows the same pattern as before.

Continuous Vapor ($k = 4$):

$$
\begin{aligned}
&\boxed{\left[\left(\alpha_4 U_4 \frac{\partial \rho_4}{\partial U_4} + \alpha_4 \rho_4\right)_L^n + \Delta t \left(H_{1,4} \frac{h_1^*}{h_4^* - h_1^*} + H_{3,4} \frac{h_3^*}{h_4^* - h_3^*} + \right.\right.} \\
&\boxed{\left.\left. H_{2,4} \frac{h_2^*}{h_4^* - h_2^*}\right)_L^n \left(\frac{\partial T^s}{\partial U_4} - \frac{\partial T_4}{\partial U_4}\right)_L^n + \Delta t \left(H_{1,4} \frac{h_4^*}{h_4^* - h_1^*} + H_{3,4} \frac{h_4^*}{h_4^* - h_3^*} + \right.\right.} \\
&\boxed{\left.\left. H_{4,2} \frac{h_4^*}{h_4^* - h_2^*}\right)_L^n \frac{\partial T^s}{\partial U_4}\right]}^{A_{4,4}} \boxed{\left(U_{4,L}^{\sim n+1} - U_{4,L}^n\right)}^{x_4} - \\
&\boxed{\Delta t \frac{\partial T_f}{\partial U_1} \left(H_{4,1} \frac{h_4^*}{h_4^* - h_1^*}\right)_L^n}^{A_{4,1}} \boxed{\left(U_{1,L}^{\sim n+1} - U_{1,L}^n\right)}^{x_1} - \\
&\boxed{\Delta t \frac{\partial T_3}{\partial U_3} \left(H_{4,3} \frac{h_4^*}{h_4^* - h_3^*}\right)_L^n}^{A_{4,3}} \boxed{\left(U_{3,L}^{\sim n+1} - U_{3,L}^n\right)}^{x_3} - \\
&\boxed{\Delta t \frac{\partial T_2}{\partial U_2} \left(H_{4,2} \frac{h_4^*}{h_4^* - h_2^*}\right)_L^n}^{A_{4,2}} \boxed{\left(U_{2,L}^{\sim n+1} - U_{2,L}^n\right)}^{x_2} + \boxed{(\rho_4 U_4 + P)_L^n}^{A_{4,9}} \boxed{\left(\alpha_{4,L}^{\sim n+1} - \alpha_{4,L}^n\right)}^{x_9} + \\
&\boxed{\left[\left(\alpha_4 U_4 \frac{\partial \rho_4}{\partial P}\right)_L^n + \Delta t \left(H_{1,4} \frac{h_1^*}{h_4^* - h_1^*} + H_{3,4} \frac{h_3^*}{h_4^* - h_3^*} + H_{2,4} \frac{h_2^*}{h_4^* - h_2^*}\right)_L^n \left(\frac{\partial T^s}{\partial P} - \frac{\partial T_4}{\partial P}\right)_L^n + \right.} \\
&\boxed{\left. \Delta t \left(H_{4,1} \frac{h_4^*}{h_4^* - h_1^*}\right)_L^n \left(\frac{\partial T^s}{\partial P} - \frac{\partial T_1}{\partial P}\right)_L^n + \Delta t \left(H_{4,3} \frac{h_4^*}{h_4^* - h_3^*}\right)_L^n \left(\frac{\partial T^s}{\partial P} - \frac{\partial T_3}{\partial P}\right)_L^n + \right.} \\
&\boxed{\left. \Delta t \left(H_{4,2} \frac{h_4^*}{h_4^* - h_2^*}\right)_L^n \left(\frac{\partial T^s}{\partial P} - \frac{\partial T_2}{\partial P}\right)_L^n\right]}^{A_{4,12}} \boxed{\left(P_L^{n+1} - P_L^n\right)}^{x_{12}} = \\
&\boxed{-\Delta t \left[\left(H_{1,4} \frac{h_1^*}{h_4^* - h_1^*} + H_{3,4} \frac{h_3^*}{h_4^* - h_3^*} + H_{2,4} \frac{h_2^*}{h_4^* - h_2^*}\right)_L^n (T^s - T_4)_L^n + \right.} \\
&\boxed{\left. \left(H_{4,1} \frac{h_4^*}{h_4^* - h_1^*}\right)_L^n (T^s - T_1)_L^n + \left(H_{4,3} \frac{h_4^*}{h_4^* - h_3^*}\right)_L^n (T^s - T_3)_L^n + \right.} \\
&\boxed{\left. \left(H_{4,2} \frac{h_4^*}{h_4^* - h_2^*}\right)_L^n (T^s - T_2)_L^n\right] + } \\
&\boxed{\Delta t \left[\left(\frac{1+\epsilon}{2}\right) h_{1,L}^{',n} + \left(\frac{1-\epsilon}{2}\right) h_{4,L}^{',n}\right] (\Gamma_{w,1,4})_L^n + \Delta t Q_{w,4,L}^n + \Delta t DISS_{4,L}^n + } \\
&\boxed{\Delta t \left(S_{5,4} h_5 - S_{4,5} h_4 + S_{6,4} h_6 - S_{4,6} h_4\right)}^{b_4} \\
&\boxed{-\frac{\Delta t}{V_L} \dot{\alpha}_{g,j+1}^n A_{j+1} \left(\dot{\rho} \dot{U} + P_L\right)_{g,j+1}^n}^{g_{4,1}} \boxed{v_{g,j+1}^{n+1}} + \boxed{\frac{\Delta t}{V_L} \dot{\alpha}_{g,j}^n A_j \left(\dot{\rho} \dot{U} + P_L\right)_{g,j}^n}^{g_{4,2}} \boxed{v_{g,j}^{n+1}}
\end{aligned}
\tag{A.4}
$$

Large Bubble ($k = 5$):

$$\boxed{\Delta t \left(\frac{\partial T^s}{\partial U_4}\right)_L^n \left(H_{1,5}\frac{h_1^*}{h_5^* - h_1^*} + H_{5,1}\frac{h_5^*}{h_5^* - h_1^*}\right)_L^n}^{A_{5,4}} \boxed{\left(U_{4,L}^{\sim n+1} - U_{4,L}^n\right)}^{x_4} -$$

$$\boxed{\Delta t \frac{\partial T_1}{\partial U_1}\left(H_{5,1}\frac{h_5^*}{h_5^* - h_1^*}\right)_L^n}^{A_{5,1}} \boxed{\left(U_{1,L}^{\sim n+1} - U_{1,L}^n\right)}^{x_1} -$$

$$\boxed{\left[\left(\alpha_5^n U_5^n \frac{\partial \rho_5}{\partial U_5}\right) - \alpha_5\rho_5 - \Delta t\left(H_{1,5}\frac{h_1^*}{h_5^* - h_1^*}\frac{\partial T_5}{\partial U_5}\right)_L^n\right]}^{A_{5,5}} \boxed{\left(U_{5,L}^{\sim n+1} - U_{5,L}^n\right)}^{x_5} +$$

$$\boxed{(\rho_5 U_5 + P)_L^n}^{A_{5,10}} \boxed{\left(\alpha_{5,L}^{\sim n+1} - \alpha_{5,L}^n\right)}^{x_{10}} +$$

$$\boxed{\left[\left(\alpha_5 U_5 \frac{\partial \rho_5}{\partial P}\right)_L^n + \Delta t\left(H_{1,5}\frac{h_1^*}{h_5^* - h_1^*}\right)_L^n \left(\frac{\partial T^s}{\partial P} - \frac{\partial T_5}{\partial P}\right)_L^n +\right.} \tag{A.5}$$

$$\boxed{\left.\Delta t\left(H_{5,1}\frac{h_5^*}{h_5^* - h_1^*}\right)_L^n \left(\frac{\partial T^s}{\partial P} - \frac{\partial T_1}{\partial P}\right)_L^n\right]}^{A_{5,12}} \boxed{\left(P_L^{n+1} - P_L^n\right)}^{x_{12}} =$$

$$\boxed{-\Delta t\left(H_{1,5}\frac{h_1^*}{h_5^* - h_1^*}\right)_L^n (T^s - T_5)_L^n - \Delta t\left(H_{5,1}\frac{h_5^*}{h_5^* - h_1^*}\right)_L^n (T^s - T_1)_L^n +}$$

$$\boxed{(\Gamma_{w,1,5})_L^n h_{5,L}^{'n}\Delta t + \Delta t\left(S_{6,5}h_6 - S_{5,6}h_5 + S_{4,5}h_4 - S_{5,4}h_5\right)}^{b_5} -$$

$$\boxed{\frac{\Delta t}{V_L}\dot{\alpha}_{5,j+1}^n A_{j+1}\left(\dot{\rho}\dot{U} + P_L\right)_{5,j+1}^n}^{g_{5,1}} \boxed{v_{5,j+1}^{n+1}} + \boxed{\frac{\Delta t}{V_L}\dot{\alpha}_{5,j}^n A_j\left(\dot{\rho}\dot{U} + P_L\right)_{5,j}^n}^{g_{5,2}} \boxed{v_{5,j}^{n+1}}$$

Small Bubble ($k = 6$):

$$\boxed{\Delta t\left(\frac{\partial T^s}{\partial U_4}\right)_L^n\left(H_{1,6}\frac{h_1^*}{h_6^*-h_1^*}+H_{6,1}\frac{h_6^*}{h_6^*-h_1^*}\right)_L^n}^{A_{6,4}}\boxed{\left(U_{4,L}^{\sim n+1}-U_{4,L}^n\right)}^{x_4}-$$
$$\boxed{\Delta t\frac{\partial T_1}{\partial U_1}\left(H_{6,1}\frac{h_6^*}{h_6^*-h_1^*}\right)_L^n}^{A_{6,1}}\boxed{\left(U_{1,L}^{\sim n+1}-U_{1,L}^n\right)}^{x_1}-$$
$$\boxed{\left[\left(\alpha_6^n U_6^n\frac{\partial\rho_6}{\partial U_6}\right)-\alpha_6\rho_6-\Delta t\left(H_{1,6}\frac{h_1^*}{h_6^*-h_1^*}\frac{\partial T_6}{\partial U_6}\right)_L^n\right]}^{A_{6,6}}\boxed{\left(U_{6,L}^{\sim n+1}-U_{6,L}^n\right)}^{x_6}+$$
$$\boxed{(\rho_6U_6+P)_L^n}^{A_{6,11}}\boxed{\left(\alpha_{6,L}^{\sim n+1}-\alpha_{6,L}^n\right)}^{x_{11}}+$$
$$\boxed{\left[\left(\alpha_6U_6\frac{\partial\rho_6}{\partial P}\right)_L^n+\Delta t\left(H_{1,6}\frac{h_1^*}{h_6^*-h_1^*}\right)_L^n\left(\frac{\partial T^s}{\partial P}-\frac{\partial T_6}{\partial P}\right)_L^n+\right.}\quad(A.6)$$
$$\boxed{\left.\Delta t\left(H_{6,1}\frac{h_6^*}{h_6^*-h_1^*}\right)_L^n\left(\frac{\partial T^s}{\partial P}-\frac{\partial T_1}{\partial P}\right)_L^n\right]}^{A_{6,12}}\boxed{\left(P_L^{n+1}-P_L^n\right)}^{x_{12}}=$$
$$\boxed{-\Delta t\left(H_{1,6}\frac{h_1^*}{h_6^*-h_1^*}\right)_L^n(T^s-T_6)_L^n-\Delta t\left(H_{6,1}\frac{h_6^*}{h_6^*-h_1^*}\right)_L^n(T^s-T_1)_L^n+}$$
$$\boxed{(\Gamma_{w,1,6})_L^n\,h_{6,L}^{'n}\Delta t+\Delta t\left(S_{5,6}h_5-S_{6,5}h_6+S_{4,6}h_4-S_{6,4}h_6\right)}^{b_6}-$$
$$\boxed{\frac{\Delta t}{V_L}\dot{\alpha}_{6,j+1}^nA_{j+1}\left(\dot{\rho}\dot{U}+P_L\right)_{6,j+1}^n}^{g_{6,1}}\boxed{v_{6,j+1}^{n+1}}+\boxed{\frac{\Delta t}{V_L}\dot{\alpha}_{6,j}^nA_j\left(\dot{\rho}\dot{U}+P_L\right)_{6,j}^n}^{g_{6,2}}\boxed{v_{6,j}^{n+1}}$$

A.1.1 Mass Equations in Terms of Primary Variables

The same procedure that was used to develop the energy conservation equations with only primary variables at new time can be used on the mass equations represented by Eqn. 6.10. The liquid mass equation can be written as shown in Eqn. A.8. The coefficients of the matrix and vectors are marked as before.

Recall that the continuous liquid mass equation was derived with a volume fraction of the continuous liquid (α_1). The result of this was a term in the equation that had the difference of the liquid volume fraction at new and old time ($\alpha_{1,L}^{\sim n+1}-\alpha_{1,L}^n$) on the LHS of the equation. As outlined previously, the void fraction terms in the system of equations can

be made independent by replacing the continuous liquid volume fraction with:

$$\alpha_1 = 1 - (\alpha_2 + \alpha_3 + \alpha_4 + \alpha_5 + \alpha_6) \tag{A.7}$$

This substitution eliminates the α_1 term from the expression, leaving the remaining void fraction terms independent of one another. This substitution has been made for Eqn. A.8 below.

Note that the remaining α_1 terms in Eqn. A.8 will also be substituted as described, but since the remaining terms will not be part of the X vector in the matrix equation, the α_1 terms have been left in for simplicity.

Continuous Liquid $k = 1$:

$$
\begin{aligned}
&\boxed{\left\{-\frac{\Delta t}{\left(h_4^* - h_1^*\right)_L^n}\left[H_{1,4,L}\left(\frac{\partial T^s}{\partial U_4} - \frac{\partial T_4}{\partial U_4}\right)_L^n + H_{4,1,L}^n\left(\frac{\partial T^s}{\partial U_4}\right)_L^n\right] -\right.} \\
&\boxed{\frac{\Delta t}{\left(h_5^* - h_1^*\right)_L^n}\left[H_{1,5}\left(\frac{\partial T^s}{\partial U_4}\right)_L^n + H_{5,1}^n\left(\frac{\partial T^s}{\partial U_4}\right)_L^n\right] -} \\
&\boxed{\left.\frac{\Delta t}{\left(h_6^* - h_1^*\right)_L^n}\left[H_{1,6}\left(\frac{\partial T^s}{\partial U_1}\right)_L^n + H_{6,1}^n\left(\frac{\partial T^s}{\partial U_4}\right)_L^n\right]\right\}}^{A_{7,4}}\boxed{\left(U_{4,L}^{\sim n+1} - U_{4,L}^n\right)}^{x_4} + \\
&\boxed{\left\{\alpha_{1,L}^n\left(\frac{\partial \rho_1}{\partial U_1}\right)_L^n + \frac{\Delta t}{\left(h_4^* - h_1^*\right)_L^n}H_{4,1,L}^n\left(\frac{\partial T_1}{\partial U_1}\right)_L^n + \frac{\Delta t}{\left(h_5^* - h_1^*\right)_L^n}H_{5,1}^n\left(\frac{\partial T_1}{\partial U_1}\right)_L^n +\right.} \\
&\boxed{\left.\frac{\Delta t}{\left(h_6^* - h_1^*\right)_L^n}H_{6,1}^n\left(\frac{\partial T_1}{\partial U_1}\right)_L^n\right\}}^{A_{7,1}}\boxed{\left(U_{1,L}^{\sim n+1} - U_{1,L}^n\right)}^{x_1} - \boxed{\rho_{1,L}^n}^{A_{7,9}}\boxed{\left(\alpha_{4,L}^{\sim n+1} - \alpha_{4,L}^n\right)}^{x_9} - \\
&\boxed{\rho_{1,L}^n}^{A_{7,8}}\boxed{\left(\alpha_{3,L}^{\sim n+1} - \alpha_{3,L}^n\right)}^{x_8} - \\
&\boxed{\rho_{1,L}^n}^{A_{7,7}}\boxed{\left(\alpha_{2,L}^{\sim n+1} - \alpha_{2,L}^n\right)}^{x_7} + \boxed{\frac{\Delta t}{\left(h_5^* - h_1^*\right)_L^n}H_{1,5}^n\left(\frac{\partial T_5}{\partial U_5}\right)_L^n}^{A_{7,5}} \\
&\boxed{\left(U_{5,L}^{\sim n+1} - U_{5,L}^n\right)}^{x_5} - \boxed{\rho_{1,L}^n}^{A_{7,10}}\boxed{\left(\alpha_{5,L}^{\sim n+1} - \alpha_{5,L}^n\right)}^{x_{10}} + \\
&\boxed{\frac{\Delta t}{\left(h_6^* - h_f^*\right)_L^n}H_{1,6}^n\left(\frac{\partial T_6}{\partial U_6}\right)_L^n}^{A_{7,6}}\boxed{\left(U_{6,L}^{\sim n+1} - U_{6,L}^n\right)}^{x_6} - \boxed{\rho_{1,L}^n}^{A_{7,11}}\boxed{\left(\alpha_{6,L}^{\sim n+1} - \alpha_{6,L}^n\right)}^{x_{11}} + \qquad \text{(A.8)} \\
&\boxed{\left\{\alpha_{1,L}^n\left(\frac{\partial \rho_1}{\partial P}\right)_L^n - \frac{\Delta t}{\left(h_4^* - h_1^*\right)_L^n}\left[H_{1,4,L}^n\left(\frac{\partial T^s}{\partial P} - \frac{\partial T_4}{\partial P}\right)_L^n + H_{4,1,L}^n\left(\frac{\partial T^s}{\partial P} - \frac{\partial T_1}{\partial P}\right)_L^n\right] -\right.} \\
&\boxed{\frac{\Delta t}{\left(h_5^* - h_1^*\right)_L^n}\left[H_{1,5}^n\left(\frac{\partial T^s}{\partial P} - \frac{\partial T_5}{\partial P}\right)_L^n + H_{5,1}^n\left(\frac{\partial T^s}{\partial P} - \frac{\partial T_1}{\partial P}\right)_L^n\right] -} \\
&\boxed{\left.\frac{\Delta t}{\left(h_6^* - h_1^*\right)_L^n}\left[H_{1,6}^n\left(\frac{\partial T^s}{\partial P} - \frac{\partial T_6}{\partial P}\right)_L^n + H_{6,1}^n\left(\frac{\partial T^s}{\partial P} - \frac{\partial T_1}{\partial P}\right)_L^n\right]\right\}}^{A_{7,12}}\boxed{\left(P_L^{n+1} - P_L^n\right)}^{x_{12}} = \\
&\boxed{-\left(\dot{\alpha}\dot{\rho}A\right)_{1,j+1}^n\frac{\Delta t}{V_L}}^{g_{7,1}}\boxed{v_{1,j+1}^{n+1}} + \\
&\boxed{\left(\dot{\alpha}\dot{\rho}A\right)_{1,j}^n\frac{\Delta t}{V_L}}^{g_{7,2}}\boxed{v_{1,j}^{n+1}} + \boxed{\frac{\Delta t}{\left(h_4^* - h_1^*\right)_L^n}\left[H_{1,4,L}^n\left(T_L^{s,n} - T_{4,L}^n\right) +\right.} \\
&\boxed{\left.H_{4,1,L}^n\left(T_L^{s,n} - T_{1,L}^n\right)\right] + \frac{\Delta t}{\left(h_5^* - h_1^*\right)_L^n}\left[H_{1,5}^n\left(T_L^{s,n} - T_{5,L}^n\right) + H_{5,1}^n\left(T_L^{s,n} - T_{1,L}^n\right)\right] +} \\
&\boxed{\frac{\Delta t}{\left(h_6^* - h_f^*\right)_L^n}\left[H_{1,6}^n\left(T_L^{s,n} - T_{6,L}^n\right) + H_{6,1}^n\left(T_L^{s,n} - T_{1,L}^n\right)\right] +} \\
&\boxed{\left(S_{2,1} - S_{1,2} + S_{3,1} - S_{1,3} - \Gamma_{w,5} - \Gamma_{w,6}\right)\Delta t}^{b_7}
\end{aligned}
$$

Two of the terms on the RHS of Eqn. A.8 include a vapor velocity variable at new-time (shown in blue). The velocities are called for at different locations (j, $j+1$). The coefficients are the terms that are multiplied by the velocity terms, and make up the right-hand side of the matrix expression. The terms on the RHS that are not multiplied by the velocities are part of the b vector as indicated.

The same procedure outlined above is followed for the remaining mass balance equations. This results in the following equations for the large and small droplet fields:

Large Droplet $k = 2$:

$$\boxed{-\frac{\Delta t}{\left(h_4^* - h_2^*\right)_L^n}\left[H_{2,4}\left(\frac{\partial T^s}{\partial U_4} - \frac{\partial T_4}{\partial U_4}\right)_L^n + H_{4,2}^n\left(\frac{\partial T^s}{\partial U_4}\right)_L^n\right]}^{A_{8,4}} \boxed{\left(U_{4,L}^{\sim n+1} - U_{4,L}^n\right)}^{x_4} +$$

$$\boxed{\left[\alpha_{2,L}^n\left(\frac{\partial \rho_2}{\partial U_2}\right)_L^n + \frac{\Delta t}{\left(h_4^* - h_2^*\right)_L^n} H_{4,2}^n\left(\frac{\partial T_2}{\partial U_2}\right)_L^n\right]}^{A_{8,2}} \boxed{\left(U_{2,L}^{\sim n+1} - U_{2,L}^n\right)}^{x_2} +$$

$$\boxed{\rho_{2,L}^n}^{A_{8,7}} \boxed{\left(\alpha_{2,L}^{\sim n+1} - \alpha_{2,L}^n\right)}^{x_7} +$$

$$\boxed{\left\{\alpha_{2,L}^n\left(\frac{\partial \rho_2}{\partial P}\right)_L^n - \frac{\Delta t}{\left(h_4^* - h_2^*\right)_L^n}\left[H_{2,4}^n\left(\frac{\partial T^s}{\partial P} - \frac{\partial T_4}{\partial P}\right)_L^n + H_{4,2}^n\left(\frac{\partial T^s}{\partial P} - \frac{\partial T_2}{\partial P}\right)_L^n\right]\right\}}^{A_{8,12}} \times \tag{A.9}$$

$$\boxed{\left(P_L^{n+1} - P_L^n\right)}^{x_{12}} =$$

$$\boxed{-\left(\dot{\alpha}\dot{\rho}A\right)_{2,j+1}^n \frac{\Delta t}{V_L}}^{g_{8,1}} \boxed{v_{2,j+1}^{n+1}} + \boxed{\left(\dot{\alpha}\dot{\rho}A\right)_{2,j}^n \frac{\Delta t}{V_L}}^{g_{8,2}} \boxed{v_{2,j}^{n+1}} +$$

$$\boxed{\frac{\Delta t}{\left(h_4^* - h_2^*\right)_L^n}\left[H_{2,4}^n\left(T_L^{s,n} - T_{4,L}^n\right) + H_{4,2}^n\left(T_L^{s,n} - T_{2,L}^n\right)\right] + \left(S_{1,2} - S_{2,1} + S_{3,2} - S_{2,3}\right)\Delta t}^{b_8}$$

Small Droplet $k = 3$:

$$\boxed{-\frac{\Delta t}{\left(h_4^* - h_3^*\right)_L^n}\left[H_{3,4}\left(\frac{\partial T^s}{\partial U_4} - \frac{\partial T_4}{\partial U_4}\right)_L^n + H_{4,3}^n\left(\frac{\partial T^s}{\partial U_4}\right)_L^n\right]}^{A_{9,4}} \boxed{\left(U_{4,L}^{\sim n+1} - U_{4,L}^n\right)}^{x_4} +$$

$$\boxed{\rho_{3,L}^n}^{A_{9,8}} \boxed{\left(\alpha_{3,L}^{\sim n+1} - \alpha_{3,L}^n\right)}^{x_8} +$$

$$\boxed{\left[\alpha_{3,L}^n\left(\frac{\partial \rho_3}{\partial U_3}\right)_L^n + \frac{\Delta t}{\left(h_4^* - h_3^*\right)_L^n} H_{4,3}^n\left(\frac{\partial T_3}{\partial U_3}\right)_L^n\right]}^{A_{9,3}} \boxed{\left(U_{3,L}^{\sim n+1} - U_{3,L}^n\right)}^{x_3} +$$

$$\boxed{\left\{\alpha_{3,L}^n\left(\frac{\partial \rho_3}{\partial P}\right)_L^n - \frac{\Delta t}{\left(h_4^* - h_3^*\right)_L^n}\left[H_{3,4}^n\left(\frac{\partial T^s}{\partial P} - \frac{\partial T_4}{\partial P}\right)_L^n + H_{4,3}^n\left(\frac{\partial T^s}{\partial P} - \frac{\partial T_3}{\partial P}\right)_L^n\right]\right\}}^{A_{9,12}} \times \tag{A.10}$$

$$\boxed{\left(P_L^{n+1} - P_L^n\right)}^{x_{12}} =$$

$$\boxed{-\left(\dot{\alpha}\dot{\rho}A\right)_{3,j+1}^n \frac{\Delta t}{V_L}}^{g_{9,1}} \boxed{v_{3,j+1}^{n+1}} + \boxed{\left(\dot{\alpha}\dot{\rho}A\right)_{3,j}^n \frac{\Delta t}{V_L}}^{g_{9,2}} \boxed{v_{3,j}^{n+1}} +$$

$$\boxed{\frac{\Delta t}{\left(h_4^* - h_3^*\right)_L^n}\left[H_{3,4}^n\left(T_L^{s,n} - T_{4,L}^n\right) + H_{4,3}^n\left(T_L^{s,n} - T_{3,L}^n\right)\right] + \left(S_{1,3} - S_{3,1} + S_{2,3} - S_{3,2}\right)\Delta t}^{b_9}$$

The development of the equation for the continuous vapor field is the same as was shown for the continuous liquid field.

Continuous Vapor ($k = 4$):

$$\boxed{\left\{\alpha_{4,L}^{n}\left(\frac{\partial\rho_4}{\partial U_4}\right)_L^n+\frac{\Delta t}{(h_4^*-h_1^*)_L^n}\left[H_{1,4,L}^{n}\left(\frac{\partial T^s}{\partial U_4}-\frac{\partial T_4}{\partial U_4}\right)_L^n+H_{4,1,L}^{n}\left(\frac{\partial T^s}{\partial U_4}\right)_L^n\right]+\right.}$$
$$\boxed{\frac{\Delta t}{(h_4^*-h_2^*)_L^n}\left[H_{2,4}^{n}\left(\frac{\partial T^s}{\partial U_4}-\frac{\partial T_4}{\partial U_4}\right)_L^n+H_{4,2}^{n}\left(\frac{\partial T^s}{\partial U_4}\right)_L^n\right]+}$$
$$\boxed{\left.\frac{\Delta t}{(h_4^*-h_3^*)_L^n}\left[H_{3,4}^{n}\left(\frac{\partial T^s}{\partial U_4}-\frac{\partial T_4}{\partial U_4}\right)_L^n+H_{4,3}^{n}\left(\frac{\partial T^s}{\partial U_4}\right)_L^n\right]\right\}}^{A_{10,4}}\boxed{\left(U_{4,L}^{\sim n+1}-U_{4,L}^{n}\right)}^{x_4}-$$
$$\boxed{\frac{\Delta t}{(h_4^*-h_1^*)_L^n}H_{4,1,L}^{n}\left(\frac{\partial T_1}{\partial U_1}\right)_L^n}^{A_{10,1}}\boxed{\left(U_{1,L}^{\sim n+1}-U_{1,L}^{n}\right)}^{x_1}-$$
$$\boxed{\frac{\Delta t}{(h_4^*-h_2^*)_L^n}H_{4,2}^{n}\left(\frac{\partial T_2}{\partial U_2}\right)_L^n}^{A_{10,2}}\boxed{\left(U_{2,L}^{\sim n+1}-U_{2,L}^{n}\right)}^{x_2}-$$
$$\boxed{\frac{\Delta t}{(h_4^*-h_3^*)_L^n}H_{4,3}^{n}\left(\frac{\partial T_3}{\partial U_3}\right)_L^n}^{A_{10,3}}\boxed{\left(U_{3,L}^{\sim n+1}-U_{3,L}^{n}\right)}^{x_3}+\boxed{\rho_{4,L}^{n}}^{A_{10,9}}\boxed{\left(\alpha_{4,L}^{\sim n+1}-\alpha_{4,L}^{n}\right)}^{x_9}+$$
$$\boxed{\left\{\alpha_{4,L}^{n}\left(\frac{\partial\rho_4}{\partial P}\right)_L^n+\frac{\Delta t}{(h_4^*-h_1^*)_L^n}\left[H_{1,4,L}^{n}\left(\frac{\partial T^s}{\partial P}-\frac{\partial T_4}{\partial P}\right)_L^n+H_{4,1,L}^{n}\left(\frac{\partial T^s}{\partial P}-\frac{\partial T_1}{\partial P}\right)_L^n\right]+\right.} \tag{A.11}$$
$$\boxed{\frac{\Delta t}{(h_4^*-h_2^*)_L^n}\left[H_{2,4}^{n}\left(\frac{\partial T^s}{\partial P}-\frac{\partial T_4}{\partial P}\right)_L^n+H_{4,2}^{n}\left(\frac{\partial T^s}{\partial P}-\frac{\partial T_2}{\partial P}\right)_L^n\right]+}$$
$$\boxed{\left.\frac{\Delta t}{(h_4^*-h_3^*)_L^n}\left[H_{3,4}^{n}\left(\frac{\partial T^s}{\partial P}-\frac{\partial T_4}{\partial P}\right)_L^n+H_{4,3}^{n}\left(\frac{\partial T^s}{\partial P}-\frac{\partial T_3}{\partial P}\right)_L^n\right]\right\}}^{A_{10,12}}\boxed{\left(P_L^{n+1}-P_L^{n}\right)}^{x_{12}}=$$
$$\boxed{-\left(\dot{\alpha}\dot{\rho}A\right)_{4,j+1}^{n}\frac{\Delta t}{V_L}}^{g_{10,1}}\boxed{v_{4,j+1}^{n+1}}+\boxed{\left(\dot{\alpha}\dot{\rho}A\right)_{4,j}^{n}\frac{\Delta t}{V_L}}^{g_{10,2}}\boxed{v_{4,j}^{n+1}}-$$
$$\boxed{\frac{\Delta t}{(h_4^*-h_1^*)_L^n}\left[H_{1,4,L}^{n}\left(T_L^{s,n}-T_{4,L}^{n}\right)+H_{4,1,L}^{n}\left(T_L^{s,n}-T_{1,L}^{n}\right)\right]-}$$
$$\boxed{\frac{\Delta t}{(h_4^*-h_2^*)_L^n}\left[H_{2,4}^{n}\left(T_L^{s,n}-T_{4,L}^{n}\right)+H_{4,2}^{n}\left(T_L^{s,n}-T_{2,L}^{n}\right)\right]-}$$
$$\boxed{\frac{\Delta t}{(h_4^*-h_3^*)_L^n}\left[H_{3,4}^{n}\left(T_L^{s,n}-T_{g,L}^{n}\right)+H_{4,3}^{n}\left(T_L^{s,n}-T_{3,L}^{n}\right)\right]+\left(S_{5,4}-S_{4,5}+S_{6,4}-S_{4,6}\right)\Delta t}^{b_{10}}$$

Eqn. A.11 is the discretized vapor continuity equation. Note that the primary variable terms that will be in the X vector of the matrix expression are again highlighted in yellow. The velocity terms at new time that are on the right-hand side of the expression are again highlighted in blue. The non-highlighted terms are part of the A matrix or vectors as indicated. The discretized vapor mass equation is the sixth row of the A matrix.

The large and small bubble equations can be obtained by following the same process previously outlined.

Large Bubble $k = 5$:

$$\begin{aligned}
&\boxed{\left\{\frac{\Delta t}{(h_5^* - h_1^*)_L^n}\left[H_{1,5}^n\left(\frac{\partial T^s}{\partial U_4}\right)_L^n + H_{5,1}^n\left(\frac{\partial T^s}{\partial U_4}\right)_L^n\right]\right\}}^{A_{11,4}}\boxed{\left(U_{4,L}^{\sim n+1} - U_{4,L}^n\right)}^{x_4} - \\
&\boxed{\frac{\Delta t}{(h_5^* - h_1^*)_L^n}H_{5,1}^n\left(\frac{\partial T_1}{\partial U_1}\right)_L^n}^{A_{11,1}}\boxed{\left(U_{1,L}^{\sim n+1} - U_{1,L}^n\right)}^{x_1} + \\
&\boxed{\left[\alpha_{5,L}^n\left(\frac{\partial \rho_5}{\partial U_5}\right)_L^n - \frac{\Delta t}{(h_5^* - h_1^*)_L^n}H_{1,5}^n\left(\frac{\partial T_5}{\partial U_5}\right)_L^n\right]}^{A_{11,5}}\boxed{\left(U_{5,L}^{\sim n+1} - U_{5,L}^n\right)}^{x_5} + \\
&\boxed{\rho_{5,L}^n}^{A_{11,10}}\boxed{\left(\alpha_{5,L}^{\sim n+1} - \alpha_{5,L}^n\right)}^{x_{10}} + \\
&\boxed{\left\{\alpha_{5,L}^n\left(\frac{\partial \rho_5}{\partial P}\right)_L^n + \frac{\Delta t}{(h_5^* - h_1^*)_L^n}\left[H_{1,5}^n\left(\frac{\partial T^s}{\partial P} - \frac{\partial T_5}{\partial P}\right)_L^n + H_{5,1}^n\left(\frac{\partial T^s}{\partial P} - \frac{\partial T_1}{\partial P}\right)_L^n\right]\right\}}^{A_{11,12}} \times \\
&\boxed{\left(P_L^{n+1} - P_L^n\right)}^{x_{12}} = \boxed{-\left(\dot{\alpha}\dot{\rho}A\right)_{5,j+1}^n\frac{\Delta t}{V_L}}^{g_{11,1}}\boxed{v_{5,j+1}^{n+1}} + \boxed{\left(\dot{\alpha}\dot{\rho}A\right)_{5,j}^n\frac{\Delta t}{V_L}}^{g_{11,2}}\boxed{v_{5,j}^{n+1}} - \\
&\boxed{\frac{\Delta t}{\left(h_5^* - h_f^*\right)_L^n}\left[H_{1,5}^n\left(T_L^{s,n} - T_{5,L}^n\right) + H_{5,1}^n\left(T_L^{s,n} - T_{1,L}^n\right)\right]} + \\
&\boxed{\left(S_{6,5} - S_{5,6} + S_{4,5} - S_{5,4} + \Gamma_{w,5}\right)\Delta t}^{b_{11}}
\end{aligned} \tag{A.12}$$

Small Bubble $k = 6$:

$$\begin{aligned}
&\boxed{\left\{\frac{\Delta t}{(h_6^* - h_1^*)_L^n}\left[H_{1,6}^n\left(\frac{\partial T^s}{\partial U_4}\right)_L^n + H_{6,1}^n\left(\frac{\partial T^s}{\partial U_4}\right)_L^n\right]\right\}}^{A_{12,4}}\boxed{\left(U_{4,L}^{\sim n+1} - U_{4,L}^n\right)}^{x_4} - \\
&\boxed{\frac{\Delta t}{(h_6^* - h_1^*)_L^n}H_{6,1}^n\left(\frac{\partial T_1}{\partial U_1}\right)_L^n}^{A_{12,1}}\boxed{\left(U_{1,L}^{\sim n+1} - U_{1,L}^n\right)}^{x_1} + \\
&\boxed{\left[\alpha_{6,L}^n\left(\frac{\partial \rho_6}{\partial U_6}\right)_L^n - \frac{\Delta t}{(h_6^* - h_1^*)_L^n}H_{1,6}^n\left(\frac{\partial T_6}{\partial U_6}\right)_L^n\right]}^{A_{12,6}}\boxed{\left(U_{6,L}^{\sim n+1} - U_{6,L}^n\right)}^{x_6} + \\
&\boxed{\rho_{6,L}^n}^{A_{12,11}}\boxed{\left(\alpha_{6,L}^{\sim n+1} - \alpha_{6,L}^n\right)}^{x_{11}} + \\
&\boxed{\left\{\alpha_{6,L}^n\left(\frac{\partial \rho_6}{\partial P}\right)_L^n + \frac{\Delta t}{(h_6^* - h_1^*)_L^n}\left[H_{1,6}^n\left(\frac{\partial T^s}{\partial P} - \frac{\partial T_6}{\partial P}\right)_L^n + H_{6,1}^n\left(\frac{\partial T^s}{\partial P} - \frac{\partial T_1}{\partial P}\right)_L^n\right]\right\}}^{A_{12,12}} \times \\
&\boxed{\left(P_L^{n+1} - P_L^n\right)}^{x_{12}} = \boxed{-\left(\dot{\alpha}\dot{\rho}A\right)_{6,j+1}^n\frac{\Delta t}{V_L}}^{g_{12,1}}\boxed{v_{6,j+1}^{n+1}} + \boxed{\left(\dot{\alpha}\dot{\rho}A\right)_{6,j}^n\frac{\Delta t}{V_L}}^{g_{12,2}}\boxed{v_{6,j}^{n+1}} - \\
&\boxed{\frac{\Delta t}{(h_6^* - h_1^*)_L^n}\left[H_{1,6}^n\left(T_L^{s,n} - T_{6,L}^n\right) + H_{6,1}^n\left(T_L^{s,n} - T_{1,L}^n\right)\right] + } \\
&\boxed{\left(S_{5,6} - S_{6,5} + S_{4,6} - S_{6,4} + \Gamma_{w,6}\right)\Delta t}^{b_{12}}
\end{aligned} \tag{A.13}$$

A.1.2 Momentum Equations in Terms of Primary Variables

The momentum equations are not used directly in the A matrix, but are part of the solution. Eqn. 6.15 shows that the only primary variables in the momentum equations are velocities and pressures.

Continuous Liquid ($k = 1$):

$$
\begin{aligned}
(\dot{\alpha}_1)_j^n \Delta t \left(P_L - P_K\right)^{n+1} = & \left[(\alpha_1\rho_1 FI_{1,4})_j^n \Delta x_j \Delta t + (C\alpha_4\alpha_1\rho_{mk})_j^n \Delta x_j\right] v_{4,j}^{n+1} + \\
& \Big[-(\alpha_1\rho_1)_j^n \Delta x_j - (\alpha_1\rho_1 FWF + \Gamma_{4,1} + \Gamma_{5,1} + \Gamma_{6,1} - \alpha_1\rho_1 FI_{1,4} - \alpha_1\rho_1 FI_{1,5} - \\
& \alpha_1\rho_1 FI_{1,6})_j^n \Delta x_j \Delta t - (C\alpha_4\alpha_1\rho_{mk})_j^n \Delta x_j - (C\alpha_5\alpha_1\rho_{mk})_j^n \Delta x_j - (C\alpha_6\alpha_1\rho_{mk})_j^n \Delta x_j - \\
& (\dot{\alpha}_1\dot{\rho}_1 HLOSSG)_j^n \Delta t\Big] v_{1,j}^{n+1} + \left[(\alpha_1\rho_1 FI_{1,5})_j^n \Delta x_j \Delta t + (C\alpha_5\alpha_1\rho_{mk})_j^n \Delta x_j\right] v_{5,j}^{n+1} + \\
& \left[(\alpha_1\rho_1 FI_{1,6})_j^n \Delta x_j \Delta t + (C\alpha_6\alpha_1\rho_{mk})_j^n \Delta x_j\right] v_{6,j}^{n+1} + (\alpha\rho v)_{1,j}^n \Delta x_j + \\
& \left[(\alpha_1\rho_4)_j^n B_x - (\Gamma_4)_j^n \left(v_{i,1,4}\right)_j^{n+1} - (\Gamma_{5,1})_j^n \left(v_{i,1,5}\right)_j^{n+1} - (\Gamma_{6,1})_j^n \left(v_{i,1,6}\right)_j^{n+1}\right] \Delta x_j \Delta t - \\
& \frac{1}{2}(\dot{\alpha}_1\dot{\rho}_1)_j^n \left[\left(v_f^2\right)_L^n - \left(v_f^2\right)_K^n\right] \Delta t + \frac{1}{2}(\dot{\alpha}_1\dot{\rho}_1 VIS_1)_j^n \Delta t + (C\alpha_4\alpha_1\rho_{mk})_j^n \left(v_1^n - v_4^n\right)_j \Delta x_j + \\
& (C\alpha_5\alpha_f\rho_{mk})_j^n \left(v_1^n - v_5^n\right)_j \Delta x_j + (C\alpha_6\alpha_f\rho_{mk})_j^n \left(v_1^n - v_6^n\right)_j \Delta x_j + \\
& \left(S_{2,1}v_2 - S_{1,2}v_1 + S_{3,1}v_3 - S_{1,3}v_1\right) \Delta x_j \Delta t
\end{aligned}
\tag{A.14}
$$

Note that the only primary variable term remaining is the pressure difference. As before, it is located on the left-hand side of the equation. The velocity terms at new time are again located on the right-hand side of the equation. The interface velocity term ($v_{i,k,m}$) is computed using the method described in Reference [22] and shown below.

$$
v_{i,k,m} = \lambda v_k + (1 - \lambda)\, v_m \tag{A.15}
$$

Where λ is 0 for positive values of $\Gamma_{m,k}$ and 1 for negative values of $\Gamma_{m,k}$, which has the effect of making it a donor formulation.

The droplet, vapor, and bubble momentum equations follow the same process, and are as shown below:

Large Droplet ($k = 2$):

$$\begin{aligned}\dot{\alpha}_{2,j}^{n}\Delta t(P_L - P_K)^{n+1} = &\left[(\alpha_2\rho_2 FI_{2,4})_j^n \Delta x_j \Delta t + (C\alpha_4\alpha_2\rho_{mk})_j^n \Delta x_j\right] v_{4,j}^{n+1} - \left[(\alpha_2\rho_2)_j^n \Delta x_j + \right.\\ &\left.(\alpha_2\rho_2 FI_{2,4} - \Gamma_{4,2})_j^n \Delta x_j \Delta t + (C\alpha_4\alpha_2\rho_{mk})_j^n \Delta x_j + (\dot{\alpha}_2\dot{\rho}_2 HLOSS)_j^n \Delta t\right] V_{2,j}^{n+1} - \\ &(\Gamma_{4,2})_j^n \Delta x_j \Delta t (v_{i,2})_j^{n+1} + (\alpha_2\rho_2)_j^n B_x \Delta x_j \Delta t - (C\alpha_4\alpha_2\rho_{mk})_j^n \Delta x_j v_4^n + \\ &(C\alpha_4\alpha_2\rho_{mk} + \alpha_2\rho_2)_j^n \Delta x_j v_2^n - \frac{1}{2}(\dot{\alpha}_2\dot{\rho}_2)_j^n \left(v_{2,L}^2 - v_{2,K}^2\right)^n \Delta t + \\ &(S_{1,2}v_1 - S_{2,1}v_2 + S_{3,2}v_3 - S_{2,3}v_2)\Delta x_j \Delta t\end{aligned} \tag{A.16}$$

Small Droplet ($k = 3$):

$$\begin{aligned}\dot{\alpha}_{3,j}^{n}\Delta t(P_L - P_K)^{n+1} = &\left[(\alpha_3\rho_3 FI_{3,4})_j^n \Delta x_j \Delta t + (C\alpha_4\alpha_3\rho_{mk})_j^n \Delta x_j\right] v_{4,j}^{n+1} - \left[(\alpha_3\rho_3)_j^n \Delta x_j + \right.\\ &\left.(\alpha_3\rho_3 FI_{3,4} - \Gamma_{4,3})_j^n \Delta x_j \Delta t + (C\alpha_4\alpha_3\rho_{mk})_j^n \Delta x_j + (\dot{\alpha}_3\dot{\rho}_3 HLOSS)_j^n \Delta t\right] V_{3,j}^{n+1} - \\ &(\Gamma_{4,3})_j^n \Delta x_j \Delta t (v_{i,3,4})_j^{n+1} + (\alpha_3\rho_3)_j^n B_x \Delta x_j \Delta t - (C\alpha_4\alpha_3\rho_{mk})_j^n \Delta x_j v_4^n + \\ &(C\alpha_4\alpha_3\rho_{mk} + \alpha_3\rho_3)_j^n \Delta x_j v_3^n - \frac{1}{2}(\dot{\alpha}_3\dot{\rho}_3)_j^n \left(v_{3,L}^2 - v_{3,K}^2\right)^n \Delta t + \\ &(S_{1,3}v_1 - S_{3,1}v_3 + S_{2,3}v_2 - S_{3,2}v_3)\Delta x_j \Delta t\end{aligned} \tag{A.17}$$

Continuous Vapor ($k = 4$):

$$
\begin{aligned}
(\dot{\alpha}_4)_j^n \Delta t (P_L - P_K)^{n+1} = \Big[& - (\alpha_4\rho_4)_j^n \Delta x_j - (\alpha_4\rho_4 FWG - \Gamma_{1,4} - \Gamma_{2,4} - \Gamma_{3,4} - \\
& \alpha_4\rho_4 FI_{4,1} - \alpha_4\rho_4 FI_{4,2} - \alpha_4\rho_4 FI_{4,3})_j^n \Delta x_j \Delta t - (C\alpha_1\alpha_4\rho_{mk})_j^n \Delta x_j - \\
& (C\alpha_2\alpha_4\rho_{mk})_j^n \Delta x_j - (C\alpha_3\alpha_4\rho_{mk})_j^n \Delta x_j - (\dot{\alpha}_4\dot{\rho}_4 HLOSSG)_j^n \Delta t \Big] v_{4,j}^{n+1} + \\
& \Big[(\alpha_4\rho_4 FI_{4,1})_j^n \Delta x_j \Delta t + (C\alpha_1\alpha_4\rho_{mk})_j^n \Delta x_j \Big] v_{1,j}^{n+1} + \\
& \Big[(\alpha_4\rho_4 FI_{4,2})_j^n \Delta x_j \Delta t + (C\alpha_2\alpha_4\rho_{mk})_j^n \Delta x_j \Big] v_{2,j}^{n+1} + \\
& \Big[(\alpha_4\rho_4 FI_{4,3})_j^n \Delta x_j \Delta t + (C\alpha_3\alpha_4\rho_{mk})_j^n \Delta x_j \Big] v_{3,j}^{n+1} + \\
& (\alpha\rho v)_{4,j}^n \Delta x_j + \Big[(\alpha_4\rho_4)_j^n B_x + (\Gamma_{1,4})_j^n (v_{i,4,1})_j^{n+1} + \\
& (\Gamma_{2,4})_j^n (v_{i,4,2})_j^{n+1} + (\Gamma_{3,4})_j^n (v_{i,4,3})_j^{n+1} \Big] \Delta x_j \Delta t - \\
& \frac{1}{2} (\dot{\alpha}_4\dot{\rho}_4)_j^n \left[\left(v_4^2\right)_L^n - \left(v_4^2\right)_K^n \right] \Delta t + \frac{1}{2} (\dot{\alpha}_4\dot{\rho}_4 VIS_4)_j^n \Delta t + \\
& (C\alpha_1\alpha_4\rho_{mk})_j^n (v_4^n - v_1^n)_j \Delta x_j + (C\alpha_2\alpha_4\rho_{mk})_j^n (v_4^n - v_2^n)_j \Delta x_j + \\
& (C\alpha_3\alpha_4\rho_{mk})_j^n (v_4^n - v_3^n)_j \Delta x_j + (S_{5,4}v_5 - S_{4,5}v_4 + S_{6,4}v_6 - S_{4,6}v_4) \Delta x_j \Delta t
\end{aligned}
\tag{A.18}
$$

Large Bubble ($k = 5$):

$$
\begin{aligned}
\dot{\alpha}_{5,j}^n \Delta t (P_L - P_K)^{n+1} = & \Big[(\alpha_5\rho_5 FI_{5,1})_j^n \Delta x_j \Delta t + (C\alpha_1\alpha_5\rho_{mk})_j^n \Delta x_j \Big] v_{1,j}^{n+1} - \Big[(\alpha_5\rho_5)_j^n \Delta x_j + \\
& (\alpha_5\rho_5 FI_{5,1} + \Gamma_{1,5})_j^n \Delta x_j \Delta t + (C\alpha_1\alpha_5\rho_{mk})_j^n \Delta x_j + (\dot{\alpha}_5\dot{\rho}_5 HLOSSG)_j^n \Delta t \Big] v_{5,j}^{n+1} + \\
& (\Gamma_5)_j^n \Delta x_j \Delta t (v_{i,5,1})_j^{n+1} + (\alpha_5\rho_5)_j^n B_x \Delta x_j \Delta t - (C\alpha_1\alpha_5\rho_{mk})_j^n \Delta x_j v_1^n + \\
& (C\alpha_1\alpha_5\rho_{mk} + \alpha_5\rho_5)_j^n \Delta x_j v_5^n - \frac{1}{2} (\dot{\alpha}_5\dot{\rho}_5)_j^n \left(v_{5,L}^2 - v_{5,K}^2 \right)^n \Delta t + \\
& (S_{4,5}v_4 - S_{5,4}v_5 + S_{6,5}v_6 - S_{5,6}v_5) \Delta x_j \Delta t
\end{aligned}
\tag{A.19}
$$

Small Bubble ($k = 6$):

$$\begin{aligned}\dot{\alpha}^n_{6,j}\Delta t(P_L - P_K)^{n+1} = &\left[(\alpha_6\rho_6 FI_{6,1})^n_j \Delta x_j \Delta t + (C\alpha_1\alpha_6\rho_{mk})^n_j \Delta x_j\right] v^{n+1}_{1,j} - \Big[(\alpha_6\rho_6)^n_j \Delta x_j + \\ &(\alpha_6\rho_6 FI_{6,1} + \Gamma_{1,6})^n_j \Delta x_j \Delta t + (C\alpha_1\alpha_6\rho_{mk})^n_j \Delta x_j + (\dot{\alpha}_6\dot{\rho}_6 HLOSSG)^n_j \Delta t\Big] v^{n+1}_{6,j} + \\ &(\Gamma_{1,6})^n_j \Delta x_j \Delta t (v_{i,6,1})^{n+1}_j + (\alpha_6\rho_6)^n_j B_x \Delta x_j \Delta t - (C\alpha_1\alpha_6\rho_{mk})^n_j \Delta x_j v^n_1 + \\ &(C\alpha_1\alpha_6\rho_{mk} + \alpha_6\rho_6)^n_j \Delta x_j v^n_6 - \frac{1}{2}(\dot{\alpha}_6\dot{\rho}_6)^n_j \left(v^2_{6,L} - v^2_{6,K}\right)^n \Delta t + \\ &(S_{4,6}v_4 - S_{6,4}v_6 + S_{5,6}v_5 - S_{6,5}v_6)\Delta x_j \Delta t\end{aligned} \tag{A.20}$$